

Fibrillin-1 controls microRNAs important for cell function and the pathogenesis of thoracic aortic aneurysms

Rong-Mo Zhang

Department of Anatomy and Cell Biology,
Faculty of Medicine and Health Science,
McGill University, Montreal, Canada

April, 2021

A thesis submitted to McGill University in partial fulfillment of the requirements of the degree
of Doctor of Philosophy (Ph.D.)

© Rong-Mo Zhang, 2021

Table of Contents

Table of Contents	i
List of Figures	vi
List of Tables	ix
Abbreviations	x
Abstract	xi
Résumé.....	xiii
Acknowledgments.....	xv
Preface.....	xvii
Original Contribution to Knowledge	xviii
Contribution of Authors	xix
CHAPTER 1 LITERATURE REVIEW AND INTRODUCTION	1
1.1 Overview of extracellular matrix	2
1.2 Fibrillins and microfibrils	2
1.2.1 Domain organization of fibrillins	2
1.2.2 RGD integrin binding site	4
1.2.3 Heparin/heparan sulfate binding sites	7
1.2.2 Fibrillin-containing microfibrils.....	8
1.3 Fibrillinopathies and thoracic aortic aneurysms	9
1.3.1 Fibrillinopathies and mouse models.....	9
1.3.2 Thoracic aortic aneurysms.....	12
1.4 Dysregulated signaling related to fibrillinopathies and thoracic aortic aneurysms	13
1.4.1 Focal adhesion kinase.....	13
1.4.2 Ras-ERK signaling cascade.....	15
1.4.3 Inflammation responses.....	16
1.4.4 Hypoxia-inducible factor 1 α regulatory signaling.....	17
1.5 microRNA	18
1.5.1 miR-612.....	20
1.5.2 miR-3185.....	20
1.5.3 miR-1208.....	20
1.5.4 miR-122.....	21
1.6 Rationale, hypotheses, goals and objectives	22

CHAPTER 2 THE FIBRILLIN-1 RGD INTEGRIN BINDING SITE REGULATES GENE EXPRESSION AND CELL FUNCTION THROUGH MICRORNAS	24
2.1 Preface:.....	26
2.2 Abstract	27
2.3 Introduction	29
2.4 Results	32
2.4.1 RGD-mediated fibrillin-1 ligation alters mRNA expression of growth factors, actin-binding-proteins and integrins	32
2.4.2 Analysis of miRNA expression patterns after RGD ligation	34
2.4.3 The miRNA signature is specific to RGD-mediated fibrillin-1 ligation	35
2.4.4 Fibrillin-1-induced miRNAs target mRNAs for growth factors, actin binding proteins and integrins.....	36
2.4.5 Fibrillin-1 and miR-503 regulate canonical TGF- β signaling.....	37
2.4.6 miR-612 and miR-3185 regulate fibrillin-1-mediated focal adhesion formation.....	38
2.5 Discussion	41
2.6 Materials and Methods	46
2.6.1 Generation of recombinant expression plasmids.....	46
2.6.2 Production of recombinant proteins	47
2.6.3 Purification of recombinant proteins	48
2.6.4 Cell Culture	49
2.6.5 Electric Cell Substrate Impedance Sensing	50
2.6.6 RNA extraction.....	51
2.6.7 Microarray analysis	51
2.6.8 Quantification of miRNA and mRNA.....	53
2.6.9 Interaction studies between miRNAs and mRNAs	54
2.6.10 Indirect immunofluorescence	56
2.6.11 Quantification of p-Smad2 and focal adhesions.....	57
2.7 Acknowledgements	58
2.8 Figures and Tables	59
CHAPTER 3 THE FIBRILLIN-1 RGD MOTIF POST-TRANSCRIPTIONALLY REGULATES ERK1/2 SIGNALING AND FIBROBLAST PROLIFERATION VIA MIR-1208	83
3.1 Preface	85
3.2 Abstract	86
3.3 Introduction	88

3.4 Materials and Methods	91
3.4.1 Production and purification of recombinant proteins	91
3.4.2 Cell Culture	92
3.4.3 RNA extraction and quantification of miRNA and mRNA	93
3.4.4 microRNA transfection into fibroblasts	94
3.4.5 Inhibitor treatment of fibroblasts.....	95
3.4.6 Dual luciferase assay	95
3.4.7 Indirect immunofluorescence	96
3.4.8 Western blotting	97
3.4.9 Data analyses	98
3.5 Results	99
3.5.1 Interactions with the RGD motif of fibrillin-1 promote fibroblast proliferation and downregulate miR-1208.....	99
3.5.2 Fibroblast interaction with the fibrillin-1 RGD motif elevates the mRNA and protein levels of ERK1/2 and MEK1/2.....	99
3.5.3 The RGD cell binding-controlled miRNA miR-1208 targets ERK2 and MEK1.....	100
3.5.4 Functional consequences of miR-1208 on target mRNA levels	102
3.5.5 miR-1208 inhibits ERK1/2 protein levels and phosphorylation	102
3.5.6 miR-1208 inhibits MEK1/2 protein level and phosphorylation.....	103
3.5.7 miR-1208 negatively regulates fibroblast proliferation	104
3.5.8 ERK1/2 inhibition abrogates the effect of miR-1208 on proliferation.....	104
3.5.9 Inhibitors of JNK and Src kinase stimulate miR-1208 expression.....	105
3.6 Discussion	107
3.7 Acknowledgements	114
3.8 Figures and Tables	115
CHAPTER 4 GENETIC PROFILING OF THORACIC AORTIC ANEURYSMS REVEALS THE ROLE OF MIR-122 IN PATHOGENETIC INFLAMMATORY PATHWAYS.....	134
4.1 Preface:.....	136
4.2 Abstract	137
4.3 Introduction	140
4.4 Results	144
4.4.1 Characterization of the ascending aortic aneurysms in <i>Fbn1</i> ^{mgR/mgR} mice	144
4.4.2 Time-dependent miRNA profiling of ascending aortae of <i>Fbn1</i> ^{mgR/mgR} mice.....	145

4.4.3 mRNA profiling of ascending aortae of <i>Fbn1^{mgR/mgR}</i> mice.....	146
4.4.4 RNA-seq analyses of TAA tissues from human patients	147
4.4.5 Correlative analyses between miRNAs and mRNAs expression in aneurysm tissues	148
4.4.6 Functional analyses of miR-122 on inflammatory responses.....	149
4.4.7 Deficient fibrillin-1 in the ECM downregulates miR-122 via decreased c-Src kinase.....	150
4.4.8 Hypoxic conditions suppress miR-122 expression and fibrillin-1 network formation.....	151
4.4.9 ERK1/2 inhibition elevated miR-122 levels.....	152
4.5 Discussion	153
4.6 Materials and Methods	158
4.6.1 Mice and aortic tissue preparation.....	158
4.6.2 <i>Ex vivo</i> aorta culture	159
4.6.3 Mouse smooth muscle cell explant.....	159
4.6.4 RNA extraction and reverse transcript PCR.....	159
4.6.5 Microarray analysis of mouse ascending aorta	160
4.6.6 Human sample collections and RNA isolation.....	161
4.6.7 RNA sequencing.....	161
4.6.8 Pathway enrichment analyses.....	162
4.6.9 Cell Culture	163
4.6.10 Generation of fibroblast-derived matrix.....	164
4.6.11 microRNA transfection into cells and <i>ex vivo</i> aorta culture	165
4.6.12 Quantification of miRNA and mRNA.....	165
4.6.13 Inhibitor treatment of smooth muscle cells	166
4.6.14 Western blotting	166
4.6.15 Indirect immunofluorescence of aortae	167
4.6.16 Indirect immunofluorescence of cells	167
4.6.17 miR-122 in situ hybridization of aorta	168
4.6.18 Enzyme-linked immunosorbent assay	169
4.7 Figures and Tables	170
CHAPTER 5 QUANTIFICATION OF EXTRACELLULAR MATRIX FIBER SYSTEMS RELATED TO ADAMTS PROTEINS	185
5.1 Preface.....	187
5.2 Abstract	188

5.3 Introduction	188
5.4 Materials	189
5.5 Methods	190
5.5.1 Quantification Procedures in Cell Culture	190
5.5.2 Quantification Procedures of Tissue Sections	197
5.5.3 Explanation of Quantification Parameters.....	201
5.6 Notes.....	202
5.7 Figures	205
CHPATER 6 CONCLUSION AND DISCUSSION	210
REFERENCES	218
APPENDIX.....	242

List of Figures

Chapter 1

Fig. 1.1 The fibrillin protein family	4
Fig. 1.2 Schematic representation of human integrins.....	7
Fig. 1.3 Mouse models altering the structure of fibrillin-1.....	12

Chapter 2

Fig. 2.1 Comparative analysis of fibroblast mRNA expression levels.....	59
Fig. 2.2 Comparative analysis of fibroblast miRNA expression levels.....	60
Fig. 2.3 Specificity of fibrillin-1 mediated miRNA regulation	61
Fig. 2.4 TGF- β signaling upon interaction with fibrillin-1 and overexpression of miR-503	63
Fig. 2.5 Consequences of fibroblast interaction with fibrillin-1 and of miRNA modulation on focal adhesion formation.....	65
Fig. 2.6 Rescue experiments of fibrillin-1 regulated miRNA on focal adhesion formation.....	67
Fig. S2.1 Representation and purification of fibrillin-1 and fibronectin and their recombinant fragments	69
Fig. S2.2 Analysis of endogenous fibrillin-1 and fibronectin levels of HSF.....	70
Fig. S2.3 Concentration dependency in real-time electric cell substrate impedance sensing (ECIS).....	71
Fig. S2.4 Analysis of HSF interaction with the recombinant fibrillin-1 and fibronectin fragments	72
Fig. S2.5 Interactions between miRNAs and growth factor mRNAs	73
Fig. S2.6 Interactions between miRNAs and mRNAs of actin-binding proteins	74
Fig. S2.7 Interactions between miRNAs and ITGB3 mRNA.....	75

Chapter 3

Fig. 3.1 Comparative analysis of fibroblast proliferation, miR-1208 expression and the levels of total and phosphorylated ERK1/2 and MEK1/2 upon interaction with the RGD motif in fibrillin-1.	116
Fig. 3.2 Prediction and validation of the molecular interaction between miR-1208 and the 3'UTR of <i>ERK2</i> and <i>MEK1</i>	118
Fig. 3.3 Functional analysis of miR-1208 on the regulation of <i>ERK</i> and <i>MEK</i> mRNA levels.	119
Fig. 3.4 Consequences of miR-1208 modulation on ERK1/2 and pERK1/2 levels	120
Fig. 3.5 Consequences of miR-1208 modulation on MEK1/2 and pMEK1/2 levels	121
Fig. 3.6 Functional analysis of miR-1208 on fibroblast proliferation	123
Fig. 3.7 ERK1/2 signaling is required for miR-1208 regulated proliferation.....	125
Fig. 3.8 Identification of integrin-activated signaling pathways that regulate miR-1208 expression and cell proliferation.....	127
Fig. 3.9 The fibrillin-1 RGD motif activates ERK1/2 signaling and cell proliferation	128
Fig. S3.1 Comparative analysis of ERK1/2 and MEK1/2 in MSU1.1 upon fibrillin-1 RGD motif binding.....	132
Fig. S3.2 ERK1/2 signaling is required for miR-1208 regulated proliferation under serum-free condition	133

Chapter 4

Fig. 4.1 Characterization of the ascending aortic aneurysms in <i>Fbn1^{mgR/mgR}</i> mice.....	171
Fig. 4.2 Time-dependent miRNA profiling of ascending aortae of <i>Fbn1^{mgR/mgR}</i> mice	172
Fig. 4.3 Global mRNA analyses and selected protein levels relevant to inflammation in the ascending aortae of 10-week old <i>Fbn1^{mgR/mgR}</i> versus wild-type mice	174
Fig. 4.4 RNA-seq analyses of human TAA patients and its comparison with <i>Fbn1^{mgR/mgR}</i>	176

Fig. 4.5 Comparative analyses between the miRNAs and mRNAs expression in mouse tissues	178
Fig. 4.6 Upstream regulators of miR-122	180

Chapter 5

Fig. 5.1 Processing of DAPI-stained nuclei.....	205
Fig. 5.2 Skeletonization of fibronectin fibers and quantification results	206
Fig. 5.3 Image processing after focal adhesion kinase staining and quantification results.....	207
Fig. 5.4 Immunofluorescence staining of fibrillin-1 in the descending aorta of an 8-day old mouse using Cy5 labeled secondary antibodies	208
Fig. 5.5 Immunohistochemical staining of fibrillin-1 in the descending aorta of an 8-month old mouse	209

List of Tables

Chapter 2

Table 2.1 KEGG pathway analysis for the mRNA and miRNA microarray	76
Table 2.2 Predictions of interactions between miRNAs and mRNAs	78
Table 2.3 Experimentally validated interactions between miRNAs and mRNAs	80
Table 2.4 Quantification of focal adhesion (FA) formation of HSFs seeded on rF1M-WT and rF1M-RGA coated Y-shaped micropatterns.....	82

Chapter 3

Table S3.1 Sequences of the inserts into pmirGLO vector for dual luciferase assays	129
Table S3.2 Primers used for mRNA qPCR.....	131

Chapter 4

Table S4.1 Information of the five TAA patients, from which the TAA tissues were used for RNAseq.....	183
Table S4.2 Information of the seven MFS patients, from which skin fibroblasts were used to generate cell-derived matrices	184

Abbreviations

AAA	Abdominal aortic aneurysm
AD	Acromicric dysplasia
BMP	Bone morphogenetic proteins
cbEGF	Calcium binding EGF-like domain
CCA	Congenital contractual arachnodactyly
EBP	Elastin-binding protein
ECM	Extracellular matrix
EGF domain	Epidermal growth factor-like domain
ERK	Extracellular signal-regulated kinase
FAK	Focal adhesion kinase
FIH	Factor-inhibiting HIF-1
GD	Geleophysic dysplasia
GT-8 mouse	Green truncated-8 mouse
HIF-1 α	Hypoxia-inducible factor 1 α
LTBP	Latent transforming growth factor β binding protein
MFS	Marfan syndrome
miRNA	microRNA
RGA	Arginine-Glycine-Alanine
RGD	Arginine-Glycine-Aspartic acid
RGD	Arginine-Glycine-Glutamic acid
RISC	RNA-induced silencing complex
SSS	Stiff skin syndrome
TAA	Thoracic aortic aneurysms
TB domain	Transforming growth factor-beta-binding protein-like domain
TGF- β	Transforming growth factor- β
Tsk mouse	Tight skin mouse
UTR	Untranslated regions
WMS	Dominant Weill-Marchesani syndrome

Abstract

Introduction: Fibrillin-1 constitutes the backbone of microfibrils in the extracellular matrix of connective tissues, including skin and aorta. It harbors an evolutionarily conserved RGD amino acid sequence mediating fibrillin-1-cell interaction. Mutations in the RGD-containing domain can cause stiff skin syndrome (SSS) and Marfan syndrome (MFS). Compromised fibrillin-1-cell interaction caused by a RGD to RGE substitution leads to skin fibrosis in a SSS mouse model. A hypomorph fibrillin-1 mutant MFS mouse model (*Fbn1^{mgR/mgR}*) presents with thoracic aortic aneurysms (TAA) and defective smooth muscle cell attachment to elastic laminae. These data indicate critical roles of fibrillin-1-cell interactions in dermal and aortic tissue homeostasis. microRNA (miRNA) microarrays previously performed in the Reinhardt laboratory identified a subset of miRNAs regulated by fibrillin-1-fibroblast interactions. Based on this data, the current project explored whether and how these fibrillin-1-controlled miRNAs regulate focal adhesion formation and fibroblast proliferation. The study further investigated differentially regulated miRNAs and pathways during TAA pathogenesis of *Fbn1^{mgR/mgR}* mice.

Results: To quantify the immunofluorescence staining of focal adhesions, cell nuclei, and extracellular matrix fibers in cell cultures and tissue sections, customized ImageJ-based methods were developed. Quantification of focal adhesion staining in human skin fibroblasts revealed that downregulated miR-612 and miR-3185 contributed to fibrillin-1-promoted focal adhesion formation. Furthermore, Ki67-positive nuclei quantification revealed that fibrillin-1 RGD-cell interaction promoted fibroblast proliferation. The c-Src–JNK signaling was shown to mediate downregulation of miR-1208 triggered by the fibrillin-1-cell interaction. Interestingly, different from the classical RAS-ERK1/2 activation, downregulated miR-1208 elevated the phosphorylated

MEK1/2 and ERK1/2 levels by post-transcriptionally increasing their mRNA and protein levels, which in turn promoted fibroblast proliferation.

In the ascending aortae of *Fbn1^{mgR/mgR}* mice, upregulated inflammatory responses were first predicted based on the altered miRNA profile, and then validated by mRNA microarrays, immunofluorescence, and Western blotting. Inflammatory pathways were also upregulated in human TAA tissues, as shown by RNAseq analyses. miR-122 was the most downregulated miRNA in the TAA tissues of *Fbn1^{mgR/mgR}* mice. This miRNA could post-transcriptionally regulate the expression of the pro-inflammatory cytokines *Ccl2* and *Il1 β* in aorta organ cultures, correlating with elevated levels of these cytokines. Additionally, hypoxic conditions and elevated ERK1/2 signaling, previously reported in TAA tissues of *Fbn1^{mgR/mgR}* mice, downregulated miR-122 in smooth muscle cells and aorta organ cultures.

Conclusion: This project provided novel miRNA-based mechanisms by which fibrillin-1 RGD-cell interaction regulates focal adhesion formation, ERK1/2 activation, and fibroblast proliferation. The study also provided new data how fibrillin-1-controlled miRNAs regulate pro-inflammatory cytokines during TAA progression.

Résumé

Introduction: La fibrilline-1 est la principale composante des microfibrilles de la matrice extracellulaire (MEC) des tissus conjonctifs tels la peau et l'aorte. Sa séquence peptidique contient un domaine RGD hautement conservé et responsable de l'interaction entre les protéines de fibrilline-1 et les cellules. Des mutations dans le domaine RGD sont donc néfastes, provoquant des pathologies tels le syndrome de la peau raide (*stiff skin syndrome*, SSS) et le syndrome de Marfan (*Marfan syndrome*, MFS). Dans un modèle murin de SSS, compromettre l'interaction fibrilline-1-cellule, via une substitution de RGD à RGE, conduit à une fibrose cutanée. Dans un modèle murin du MFS, des mutations conduisant à un phénotype hypomorphe pour la fibrilline-1 (*Fbn1^{mgR/mgR}*) peut mener à des anévrismes de l'aorte thoracique (AAT) et à un attachement déficient des cellules musculaires lisses aux lames élastiques. Ces données démontrent les rôles critiques des interactions fibrilline-1-cellule dans l'homéostasie des tissus dermiques et aortiques. Les puces à ARN de microARN (miARN) ont préalablement identifiés des miARN régulés par les interactions entre la fibrilline-1 et les fibroblastes. Sur la base de ces données, ce projet a voulu confirmer si ces miARN régulent la formation d'adhérence focale et la prolifération des fibroblastes et si c'est le cas, d'en explorer le mécanisme. Plus précisément, l'étude s'est penchée sur l'identification des miARN et des voies de signalisations régulées de manière différentielle au cours de la pathogenèse du TAA des souris *Fbn1^{mgR/mgR}*.

Résultats: Des méthodes utilisant le logiciel ImageJ furent développées pour la quantification des résultats d'immunofluorescence relatifs aux adhérences focales, prolifération (Ki67) et à la MEC. Dans les fibroblastes cutanés humains, la régulation à la baisse de miR-612 et de miR-3185 contribue à la formation accrue d'adhésions focales par le biais de fibrilline-1. De plus, la quantification des noyaux positifs pour Ki67 a révélé que l'interaction entre le domaine RGD de

la fibrilline-1 et les fibroblastes favorisait leur prolifération. La voie de signalisation c-Src-JNK régule négativement l'expression de miR-1208 déclenchée par l'interaction fibrilline-1 et les cellules. Fait intéressant, contrairement à la voie classique de RAS-ERK1/2, la régulation à la baisse de miR-1208, mène à une augmentation des niveaux de MEK1/2 et ERK1/2 phosphorylés en augmentant post-transcriptionnellement leurs niveaux (ARNm et protéines), favorisant ainsi la prolifération des fibroblastes.

Dans les aortes ascendantes des souris *Fbn1^{mgR/mgR}*, les réponses inflammatoires régulées à la hausse ont d'abord été prédites sur la base du profil de miARN altéré, puis validées par une approche combinée comprenant des puces à ARNm, d'expériences d'immunofluorescence et d'immunobuvardage. L'analyse par séquençage ARN a aussi démontré and plusieurs voies de signalisation inflammatoires étaient régulées à la hausse dans les tissus humains de TAA. Le miARN montrant la plus forte régulation à la baisse dans les tissus TAA des souris *Fbn1^{mgR/mgR}* était miR-122. Ce miARN pourrait ainsi réguler l'expression des cytokines pro-inflammatoires Ccl2 et Il1 β dans les cultures d'organes de l'aorte, ce corrèle avec des niveaux élevés de ces cytokines. De plus, des conditions hypoxiques et une signalisation ERK1/2 élevée, précédemment signalées dans les tissus TAA de souris *Fbn1^{mgR/mgR}*, ont mené à une régulation à la baisse miR-122 dans les cellules musculaires lisses et les cultures d'organes de l'aorte.

Conclusion: Ce projet a identifié de nouveaux mécanismes de régulation des adhérences focales, de l'activation de ERK1/2 et la prolifération des fibroblastes impliquant des miARN et l'interaction entre le domaine RGD de la fibrilline-1 . L'étude a également fourni de nouvelles données sur la manière dont les miARN contrôlés par la fibrilline-1 régulent les cytokines pro-inflammatoires au cours de la progression de l'AAT.

Acknowledgments

First, I would like to express my deepest appreciation and sincerest gratitude to the continuous and unlimited supports from my supervisor, Dr. Dieter P. Reinhardt. Pursuing Ph.D. degree in Reinhardt laboratory is one of the most rewarding periods in my early academic career. Dr. Reinhardt provided the students a well-organized environment for doing research. I had the freedom to explore what I was curious about and interested in, with everything in place. More importantly, as a senior researcher, Dr. Reinhardt has always been open to discussion and provided professional guidance, to make sure the experimental design to be on the right track, and the progress in proper pace. Dr. Reinhardt also set a good role model on working ethic, which are very important for my life-long career. I was entrusted to supervisor master and undergraduate student, and participate in grant application. Other than that, Dr. Reinhardt always supported and encouraged students to attend conference, which were great opportunities for us to discuss science and share our work to fellow scientists. These experiences are very helpful for my future career.

The nice and supportive lab members made my six years of Ph.D. study full of joy. Muthu, who came to Reinhardt laboratory around the same time as me, was very warm hearted, caring, and professional. Heena, a previous senior student in the lab, was always open to discuss science and generously provided perceptive opinion. Karina, the co-first author of my first publication in Ph.D. study, was also very organized and professional. Based on her important pilot studies, I could start and develop this Ph.D. project. I also want to acknowledge Jason, the previous lab manager, who instructed me the bench techniques when I just joined in the lab. Hana, a professional, generous, and strong female. In addition to her lab work, her cakes and cookies were also very nice. Ling was the lab manager and a good friend to all the lab members. She has always been ready to help others. As a former surgeon, she generously taught me the techniques on mouse

dissection. I also want to thank the students I supervised, Nadine, Yiyun and Prana. Nadine and Yiyun provided important figures for my second paper during Ph.D. study. Additionally, Yiyun also took care of the mice colony well. Teaching was a mutual beneficial process. The supervising experience also helped me to become a mature scientist. Dr. Blaise from Université de Reims Champagne-Ardenne, Dr. Boucher and Mr. Laroche helped for the French abstract of the thesis. Many thanks to all other past and present lab members I met, including Valentin, Neha, Cori, Iram, Elahe, Lisa, Tom, Shaynah, Jamie, Joe, Merve, JC, Domenico, Elaine, Rajpreet, Olivia, and Isaac, as well as the nice people I met in our department.

To have the progress, the advisors, comments and supports from my advisory committee and comprehensive committee are very critical. Here I would like to extend my sincere thanks to Dr. Autexier, Dr. Haglund, Dr. Presley Dr. Philip, Dr. Rocheal, and Dr. Nantel. They appreciated my work, provided professional guidance and pointed out the aspects I need to improve, all of which were very important for my learning process. Dr. Autexier, who was also my mentor, has seen and helped my growth from starting the first several months I entered McGill. During this process, she has always been ready to help me and provide professional advice.

I would like to thank the department of Anatomy and Cell Biology at McGill University for providing such a great environment to pursue my Ph.D. study.

Last, but certainly not least, I would like to thank my family, who know me the best and trust me the most. They have always been supportive to all the choices and decisions I made. Gratitude also extends to all the friends I met here in Montreal during this period.

Preface

The work described in this thesis has been published, accepted or to be submitted as follows:

Chapter 2

The fibrillin-1 RGD integrin binding site regulates gene expression and cell function through microRNAs

Karina A. Zeyer, # **Rong-Mo Zhang**, # Heena Kumra, Amani Hassan, and Dieter P. Reinhardt

#co-first authors

Journal of Molecular Biology (2019) 431: 401-421

Chapter 3

The fibrillin-1 RGD motif post-transcriptionally regulates ERK1/2 signaling and fibroblast proliferation via miR-1208

Rong-Mo Zhang, Karina A. Zeyer, Nadine Odenthal, Yiyun Zhang, and Dieter P. Reinhardt

FASEB Journal (accepted, on March 31th, 2021)

Chapter 4

Genetic profiling of thoracic aortic aneurysms reveals the role of miR-122 in pathogenetic inflammatory pathways

Rong-Mo Zhang, Bhama Ramkhelawon, and Dieter P. Reinhardt

Manuscript in preparation

Chapter 5

Quantification of Extracellular Matrix Fiber Systems Related to ADAMTS Proteins

Rong-Mo Zhang, Heena Kumra, and Dieter P. Reinhardt

ADAMTS Proteases. Methods in Molecular Biology (2020) 2043:237-250

Original Contribution to Knowledge

This thesis presents original discoveries contributing to the novel outside-in cell signaling triggered by fibrillin-1-cell interaction, with the involvement of microRNAs. Additionally, the role of a fibrillin-1-controlled microRNA was identified in the pathogenesis of thoracic aortic aneurysm pathogenesis in a Marfan syndrome mouse model. The detailed key contributions are:

1. Identified the fibrillin-1-controlled microRNAs (miR-612 and miR-3185) involved in focal adhesion formation in human skin fibroblasts.
2. Discovered that the fibrillin-1 RGD motif promoted fibroblast proliferation by activating ERK1/2 signaling.
3. Revealed a novel mechanism how a fibrillin-1-controlled microRNA (miR-1208) post-transcriptionally activated ERK1/2 signaling.
4. Determined time-dependent microRNA profiles in the ascending aortae of *Fbn1^{mgR/mgR}* mice.
5. Uncovered similarities between the genetic profiles of TAA tissues from *Fbn1^{mgR/mgR}* mice and human TAA patients.
6. Demonstrated that downregulation of a fibrillin-1-controlled microRNA (miR-122) elevates *Ccl2* and *Il1 β* expression in aorta cultures.
7. Identified that hypoxic conditions and activated ERK1/2 signaling downregulates miR-122.
8. Developed novel quantification methods of microscopic images based on the ImageJ software.

Contribution of Authors

Dr. Dieter P. Reinhardt is the project director and was involved in all aspects and phases of the work.

Chapters 1 and 6: The text and the figures compiled in chapters 1 and 6 were generated by me and reviewed and edited by Dr. Reinhardt.

Chapter 2: The study conception was designed by Ms. Zeyer and by me. I performed experiments for Figs. 2.3c, 2.5, 2.6 and S2.1. I designed the fibronectin fragments (FN-WT and FN-RGA, Fig. S2.1B), performed cell morphology and qPCR analyses of fibroblasts seeded on FN-WT, as compared to FN-RGA (Fig. 2.3 A and C). miRNA transfection experiments for focal adhesion kinase staining in Figs. 2.5 and 2.6 were also performed by me. Additionally, I performed the electric cell substrate impedance sensing (ECIS) experiments of fibroblasts seeded on FN-WT and FN-RGA fragments (Figs. S2.2B and S2.3B and D). Ms. Hassan designed the fibrillin-1 fragments (rF1M-WT and rF1M-RGA, Fig. S2.1b). Ms. Zeyer performed miRNA and mRNA microarrays, qPCR and ECIS experiments of fibroblasts seeded on rF1M-WT and rF1M-RGA. Ms. Zeyer also generated Fig. 2.4 on the functional aspects of miR-503 on pSmad2. Ms. Zeyer, I and Dr. Kumra participated in analyzing and interpreting the data. The manuscript draft was provided by Ms. Zeyer and by me. All the authors were involved in the revision of the paper.

Chapter 3: The concept, experimental design and acquisition of the data were mostly from me. I analyzed the data and generated all the figures. Ms. Zeyer contributed to Fig. 3.1 a-c. Ms. Odenthal and Ms. Zhang performed part of the experiments for Figs. 3.4 b, d, f and 3.5 under my supervision, as exchange student or summer volunteer in the Reinhardt laboratory. The manuscript draft was assembled by me.

Chapter 4: The study presented in chapter 4 was conceptualized and planned by me. Dr. Ramkhelawon performed the RNA-seq analysis for TAA tissue from human patients, and provided the profiles of all the differentially expressed mRNA transcripts. All figures were generated by me. The manuscript draft was compiled by me.

Chapter 5: The methods for Figs. 5.1-5.3 were developed and written by me. Dr. Kumra provided Figs. 5.4 and 5.5 and helped with the writing of the corresponding methods.

CHAPTER 1 LITERATURE REVIEW AND INTRODUCTION

1.1 Overview of extracellular matrix

The extracellular matrix (ECM) is a dynamic three-dimensional network secreted and assembled by cells. It constitutes a core part of all tissues in multicellular organisms. ECM proteins are comprised of various proteins, including glycoproteins, glycosaminoglycans and proteoglycans [1,2]. After secretion by the cells, these ECM proteins assemble, cross-link and/or polymerize to form organized structures conferring strength and integrity to tissues [3]. The ECM and cells reciprocally regulate and influence each other. The ECM not only provides adhesive substrates for cells critical for function and survival, but also enables communications between cells and tissues through cell-surface receptors, and through mechanical forces [4-6]. Properties of the ECM define the functional status of tissues and the fate of the cells, which is important for maintaining tissue homeostasis. In addition to direct cell-ECM interactions, the ECM is also a reservoir for numerous growth factors, controlling their bioavailability and release, which in turn governs a wide spectrum of cell activities [7]. Smaller parts of ECM proteins released during maturation or degradation can also serve as small-molecule hormones or cytokines [8,9]. Failure in ECM organization or mutations in ECM proteins could lead to disorders affecting multiple connective tissues, including skin, aorta, bone and eye [10-12].

1.2 Fibrillins and microfibrils

1.2.1 Domain organization of fibrillins

The fibrillin family constitutes three highly homologous multi-domain glycoproteins of about 350 kDa in mass, fibrillin-1 (encoded on human chromosome 15), fibrillin-2 (chromosome 5) and fibrillin-3 (chromosome 19) (Fig. 1.1). Fibrillins are conserved throughout evolution from invertebrates to *Homo sapiens* [13]. Structures similar to human fibrillin-1 are also found in invertebrate species, including jellyfish [14], sea cucumber [15], lobster and whelk [16]. This remarkable conservation indicates the importance of fibrillins in tissue organization of metazoan

organisms. As multi-domain proteins, fibrillins are mainly composed of epidermal growth factor-like (EGF) domains and transforming growth factor-beta-binding protein-like (TB) domains. There are 47 EGF domains in fibrillin-1 and -2 and 46 in fibrillin-3 (Fig. 1.1). Each of the EGF domains are stabilized by three disulfide bonds, formed between the six cysteine residues in a C1-C3, C2-C4 and C5-C6 pattern [17,18]. The majority of these EGF domains are calcium binding EGF (cbEGF) domains, containing a consensus sequence for direct ligation of calcium ions. Calcium is critical for the protection of fibrillins against proteolysis [19], the control of self-interaction [20], and the interaction with several other ECM components, such as microfibril-associated glycoprotein-1 and heparin/heparan sulfate [21-23]. There are 43 cbEGF domains in fibrillin-1 and fibrillin-2, and 42 in fibrillin-3 [17,19]. The second most common domain in fibrillins are the seven TB domains [24], which are stabilized by four disulfide bonds in a C1-C3, C2-C6, C4-C7 and C5-C8 pattern [25]. Fibrillins further contain two hybrid (hyb) domains, with a similar sequence of TB domains in their N-terminus and of EGF domains in their C-terminus [26];Pereira, 1993 #446}. The hyb domain contains four inter-domain disulfide bonds arranged in a C1-C3, C2-C5, C4-C6 and C7-C8 pattern [27]. Additionally, there is a unique domain in all fibrillins following the 1st TB domain. It is proline-rich domain in fibrillin-1, glycine-rich domain in fibrillin-2, and proline/glycine-rich domain in fibrillin-3 [26,28]. The N- and C-terminal domains in fibrillins are also unique, which are processed by furin convertases [29-31]. All three isoforms are globally expressed, including but not limited to blood vessels, skin, heart, perichondrium, developing bronchi, pancreas, kidney, and testis. Fibrillin-1 is expressed throughout life, while fibrillin-2 and -3 are primarily present during embryonic development [32,33].

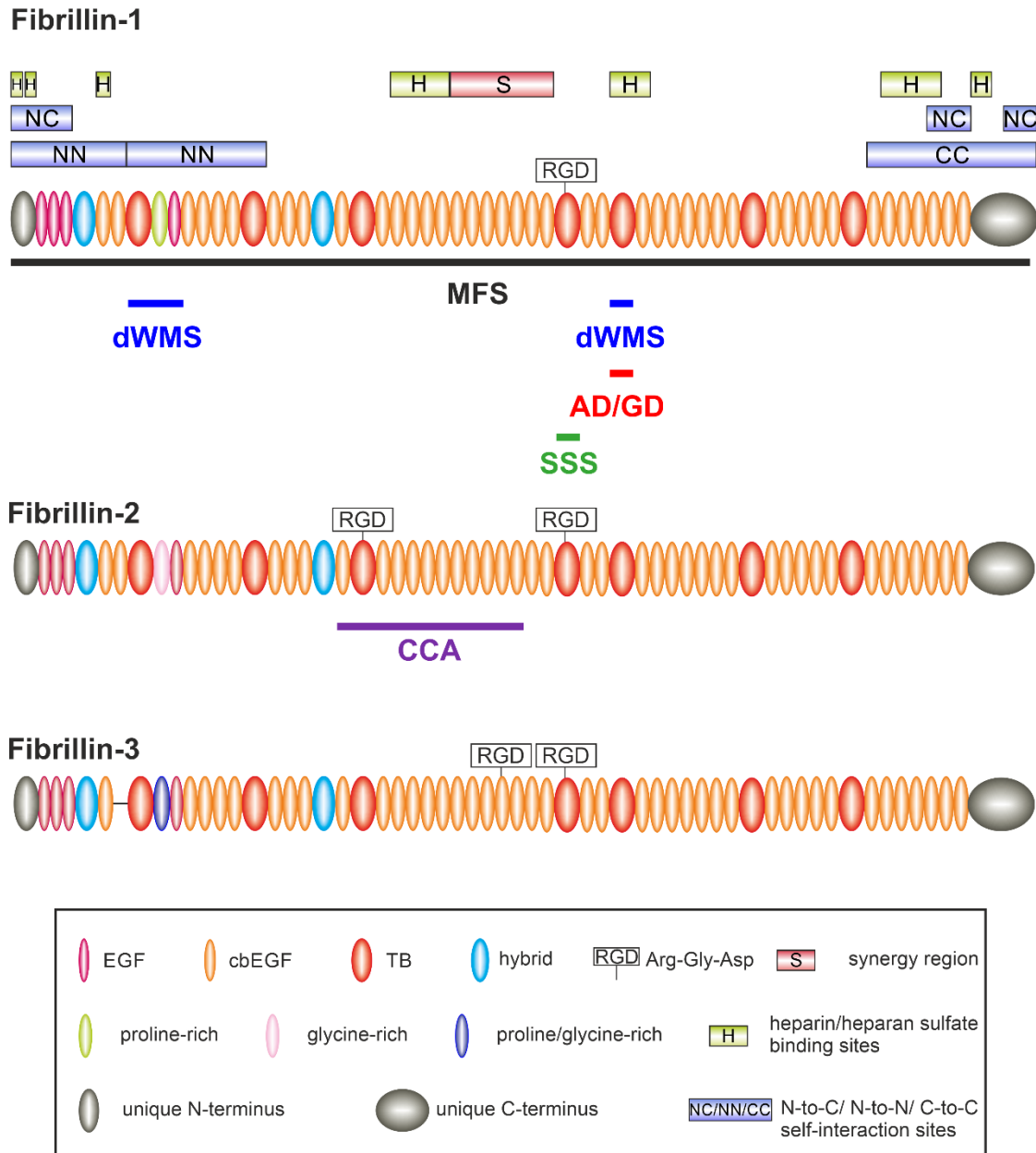


Fig. 1.1 The fibrillin protein family

The domain organizations of human fibrillin-1, -2 and -3 are shown. The RGD sites, the synergy region (S), heparin/heparan sulfate binding sites (H), and self-interaction sites (NN, NC, CC) are indicated. The regions of the mutations causing various fibrillinopathies are marked for fibrillin-1 and 2.

1.2.2 RGD integrin binding site

Arginine-glycine-aspartic acid (RGD) is an evolutionally conserved sequence present in many ECM proteins. It can mediate the ECM-cell interaction via integrin heterodimer

transmembrane proteins. The RGD motif was first discovered in fibronectin by Pierschbacher and Ruoslahti in 1984 [34]. Later an RGD motif was identified in numerous ECM proteins, including fibrillins, vitronectin, thrombospondin, laminin, entactin, tenascin, among others [35-37]. To engage in integrin binding, the RGD sequence must be available at a conformation that is compatible for interaction, typically an exposed loop conformation. Multiple factors can influence RGD-integrin interactions. For example, if proline follows the RGD sequence in a short peptide, the cells cannot attach [38]. Replacement of the critical aspartic acid with glutamic acid or alanine abrogates its interactions with integrin [39,40]. The steric conformation of the aspartic acid is also important: The L-form of aspartic acid in the peptide is active but not the D-form, whereas the steric conformation of the arginine residue does not affect binding activities [38]. Integrin ligand interactions are usually divalent cation-dependent [41], and aspartic acid contributes to divalent cation binding via the acidic side chain, explaining the importance of aspartic acid in RGD-dependent integrin binding. The domains around the RGD sequence can also contribute to integrin binding. For example, the synergy site located upstream of the RGD-containing domain in fibronectin promotes cell adhesion [42]. An RGD motif is localized in the TB4 domain in all fibrillins. There is one additional RGD motif present in the TB3 domain in fibrillin-2 and the cbEGF18 domain in fibrillin-3 (Fig. 1.1). X-ray crystallographic structural analysis of the cbEGF22-TB4-cbEGF23 recombinant fibrillin-1 fragment revealed that the RGD site is present in an exposed flexible loop conformation, which is favorable for integrin binding [43].

Integrins are single pass transmembrane cell surface receptors, composed of two non-covalently associated subunits, α and β [44]. The size of the subunits varies between 90-180 kDa, with >1600 amino acid residues positioned on the extracellular side and only 20-50 amino acid residues composing the C-terminal intracellular portion. Integrin activation can be elicited as

inside-out or outside-in bi-directional signal transductions [44,45]. In the inside-out manner, cytosolic talin binds to the cytoplasmic domain of the integrin β -subunit, leading to conformational changes in the extracellular domains and priming the receptor-ligand interaction [46,47]. Some integrins like α IIb β 3, α v β 3, α L β 2 and α X β 2 are shown to undergo this conformation changes initiated by this inside-out manner [44,45]. Among them, integrins α IIb β 3, α v β 3 can bind to RGD (Fig. 1.2). Integrins α L β 2 and α X β 2 are leukocyte specific [48], which indicate the inside-out activation is critical for the regulation of immune cell migration. However, not all integrins undergo conformation changes upon intracellular activation. Integrin α 5 β 1, for example, only exists as an extended conformer [49]. Integrin can also be activated by the interaction with ECM proteins or mimetic peptides containing integrin binding sequences, Mn^{2+} ions, as well as through integrin clustering and lateral diffusion of receptors (reviewed by Calderwood [50]). Changes in integrin expression patterns also contribute to the control of integrin-mediated adhesion. Initiated by extracellular ligands or by other transmembrane receptors, the cytoplasmic domain will recruit multiple proteins and trigger signaling. These proteins include focal adhesion kinase (FAK), src-family kinases, and ERK1/2 signaling, as discussed in chapter 1.4.

There are 18 α subunits and 8 β subunits in human, which can combine to form 24 integrin heterodimers [44]. 8 of these integrins can interact with the RGD motif, the others recognize different but related motifs. Integrins α 5 β 1, α v β 3 and α v β 6 have been reported to interact with the RGD motif in fibrillin-1 [35,51-53] (Fig. 1.2). Similar to fibronectin, a synergy site assisting RGD binding to integrins (e.g. α 5 β 1) are located in the region between cbEGF16 and cbEGF22 [40] (Fig. 1.1).

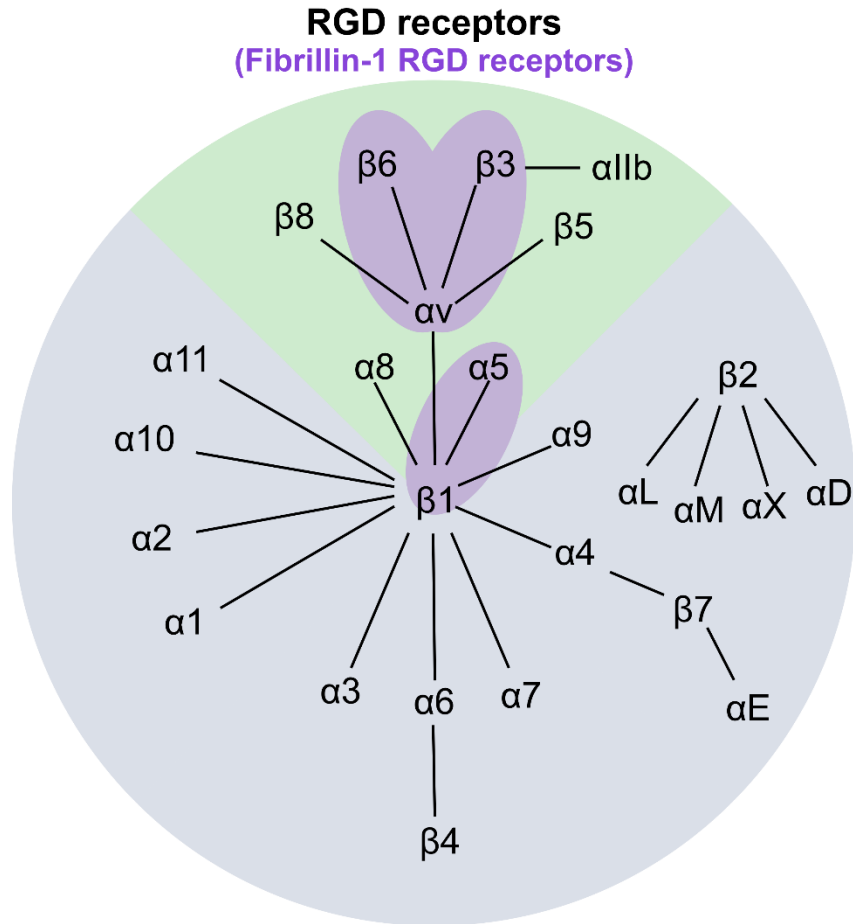


Fig. 1.2 Schematic representation of human integrins

Representation of the 24 human integrins (modified from Barczyk, *et al.*, 2010 [48]). The green sector indicates the RGD binding integrins. Purple ellipses highlight integrins $\alpha 5\beta 1$, $\alpha v\beta 3$ and $\alpha v\beta 6$, which can interact with the fibrillin-1 RGD motif.

1.2.3 Heparin/heparan sulfate binding sites

Fibrillin-1 is a major heparin/heparan sulfate interacting molecule harboring seven binding regions spanning from N to C-terminus (Fig. 1.1) [22,54,55]. These heparin/heparan sulfate binding sites are demonstrated to assist RGD-integrin interaction by promoting focal adhesion formation [40]. The transmembrane receptor for fibrillin-1 heparin/heparan sulfate binding sites has not been identified yet. However, Syndecans, a group of transmembrane heparan sulfate proteoglycans, are likely to participate in this interaction, as fibroblasts from syndecan-4 null mice

are defective in focal adhesion formation on fibrillin-1 fragments that encompass the RGD-containing domain [40]. Additionally, fibrillin-1 heparin/heparan sulfate interactions with fibrillin-1 can regulate fibrillin-1 microfibril formation. Either addition of heparin/heparan sulfate or, inhibition of sulphation and biosynthesis of heparan sulfate sulfation or the biosynthesis of heparan sulfate can also suppress fibrillin network formation by human skin fibroblasts [22].

1.2.2 Fibrillin-containing microfibrils

Fibrillins self-assemble in a head to tail manner, displaying a bead-on-a-string configuration visible by electron microscopy. The diameter of fibrillin-containing microfibrils is about 10–12 nm, with an average untensioned periodicity of 56 nm [56-58]. Microfibrils provide the deposition scaffold for tropoelastin, the precursor of mature elastic fibers [59]. Fibrillin microfibrils closely regulate the elastic fiber formation with an extensive inventory of microfibril-associated molecules, including fibulins, latent transforming growth factor β binding proteins (LTBPs) and microfibril-associated glycoproteins [60-62]. In mature elastic fibers, microfibrils primarily locate at the surface of the elastin core [63]. Mice with a complete ablation of fibrillin-1, die within 2-week of age with ruptured aortae and impaired pulmonary function, owing to disorganized elastic fibers [64]. Fibrillins can also form isolated fibrillin bundles without the presence of elastin, in tissues including superficial regions of the skin, the ciliary zonules of the eye, and the kidney and [65-67].

In addition to the structural role, fibrillins microfibrils sequester growth factors directly or indirectly, and govern their bioavailability to the cells. Both fibrillin-1 and fibrillin-2 can directly bind to bone morphogenetic proteins (BMPs). BMP dysregulations are observed in fibrillin-1 and fibrillin-2 knockout mice [68]. Transforming growth factor- β s (TGF- β s) are secreted in large latent complexes, in which TGF- β propeptide are associated with LTBPs. After

secretion, these large latent complexes are deposited onto the fibrillins microfibrils [69]. Abnormally elevated TGF- β is associated with disrupted fibrillin-1 microfibrils in the aorta and lung of patients or mice with fibrillin-1 mutations [70,71].

1.3 Fibrillinopathies and thoracic aortic aneurysms

1.3.1 Fibrillinopathies and mouse models

Fibrillinopathies are heritable autosomal-dominant syndromic connective tissue disorders caused by mutations in fibrillin-1 and fibrillin-2. Fibrillinopathies caused by fibrillin-1 mutations include Marfan syndrome (MFS) [12], stiff skin syndrome (SSS) [11], dominant Weill-Marchesani syndrome (WMS) [72,73] and acromicric and geleophysic dysplasia (AD and GD) [74]. Mutations in fibrillin-2 can lead to congenital contractual arachnodactyly (CCA) [75]. No pathogenic mutations have been identified in the fibrillin-3 gene until now. The regions where fibrillinopathies-causing mutations occur in fibrillin-1 and -2 are indicated in Fig. 1.1.

Mutations in the RGD-encoding TB4 domain of fibrillin-1 can cause both, SSS and MFS. Particularly, all the SSS-causing mutations are localized to the TB4 domain of fibrillin-1. Other mutations in fibrillin-1 that causes GD, AD and WMS, where patients exhibit fibrotic skin phenotypes are also present in close vicinity to the TB4 domain of fibrillin-1. This suggests a potential role of the RGD motif in these disorders. SSS is characterized by congenital scleroderma in association with dermal fibrosis, and is usually present throughout the body [11]. Heterozygous substitutions of RGD to RGE (D1545E) and W1572C in the TB4 domain of mouse fibrillin-1 (*Fbn1*^{RGE/+} and *Fbn1*^{W1572C/+}) phenocopy SSS with excessive microfibrillar aggregates and elevated phosphorylated extracellular signal-regulated kinase 1/2 (pERK1/2) signaling in the dermis [76]. Abnormally active integrins $\alpha\beta3$ and $\alpha5\beta1$ were found in fibroblasts isolated from

Fbn1^{RGE/+} mice and SSS patients [76]. Antibody treatments either to activate β 1 integrin or deactivate β 3 integrin ameliorate skin fibrosis in *Fbn1*^{RGE/+} and *Fbn1*^{W1572C/+} mice [76]. A large in-frame duplication of cbEGFs 7-24 (exons 17-40), including the RGD-containing TB4 domain in fibrillin-1 results in tight skin (Tsk), with accumulation of microfibrils in the loose connective tissue in the heterozygous mice [77]. Homozygous Tsk mice die in utero at day 7-8 of gestation. Increased proteolytic susceptibility of fibrillin-1 in Tsk mice lead to a decrease of fully functional microfibrils [78].

MFS, the most prevalent fibrillinopathy, affects about 1 in 3,000-5,000 individuals [79]. There are more than 3,000 known MFS-causing mutations in fibrillin-1, located throughout the gene and protein [80] (Fig. 1.1). Clinical manifestations include thoracic aortic aneurysms (TAA), lens dislocation, long bone overgrowth, among others [12]. Aortic rupture caused by progressive TAA is the primary cause of mortality in MFS. Various molecular consequences can be initiated by fibrillin-1 mutations, including retention in the secretory pathway [81], reduced microfibril assembly [82], and enhanced proteolytic degradation [83,84]. However, independent of the underlying mechanistic details, the common consequence of MFS mutations in fibrillin-1 is a general reduction in the amount of fully functional tissue microfibrils leading to reduced cell interactions, activated TGF- β signaling, elevated ERK1/2 signaling and increased matrix degradation [71]. Consistently, fibroblasts isolated from MFS patients typically, but not always, are characterized by less fibrillin-1 deposition in the ECM [85]. Several mouse models modifying fibrillin-1 were developed to mimic the phenotypes of MFS. *Fbn1*^{mg Δ /mg Δ} mice have a deletion of the 8th cbEGF- 3rd TB domains in fibrillin-1, caused by an in-frame deletion of exons 19-24 [86]. *Fbn1*^{mg Δ /mg Δ} express fibrillin-1 at ~10% of wild-type level, and die at around 3-weeks of age, with cardiovascular complications including aortic dilation and dissection. Although heterozygous

Fbn1^{mgΔ/+} show no phenotype, heterozygous mice still harboring the PGK neo-cassette flanked by lox-P, *Fbn1*^{mgΔloxPneo/+}, present with MFS phenotypes, including defective microfibrillar deposition, emphysema, deterioration of aortic wall and kyphosis [87]. ~78% fibrillin-1 mRNA is transcribed in embryonic fibroblasts derived from *Fbn1*^{mgΔloxPneo/+} mice. *Fbn1*^{mgΔloxPneo/+} mice shows spine deformation at 2-month of age and typically die by 3-month of age from hemothorax, likely resulting from an aortic rupture. Homozygous mice with mgΔloxPneo allele die 4-8 days after birth. *Fbn1*^{mgR/mgR} mice, with the insertion of PGK neo-cassette in the intron between exons 18 and 19, express 20-25% of normal fibrillin-1 [86]. Mimicking severe MFS manifestations, *Fbn1*^{mgR/mgR} mice develop TAA and die around 12-16 weeks of age together with skeletal and pulmonary manifestations, including long bone overgrowth, kyphosis and emphysema. *Fbn1*^{C1039G/+} mice with a heterozygous missense mutation in fibrillin-1 are characterized by haploinsufficiency of functional microfibrils in the aortic wall [88]. Another MFS mouse model generated is the GT-8 model, where fibrillin-1 is truncated after cbEGF17 and tagged with green fluorescent protein [89]. Homozygous GT-8 pups die postnatally between 9-18 days, whereas heterozygous GT-8 mice survive up to 1 year. The aortic wall deteriorates with elastic laminae fragmentation starting from 2 months after birth in heterozygous mice. The expression level of truncated fibrillin-1 is normal, but it exerts a dominant negative effect on wild-type fibrillin-1 assembly (Fig. 1.3).

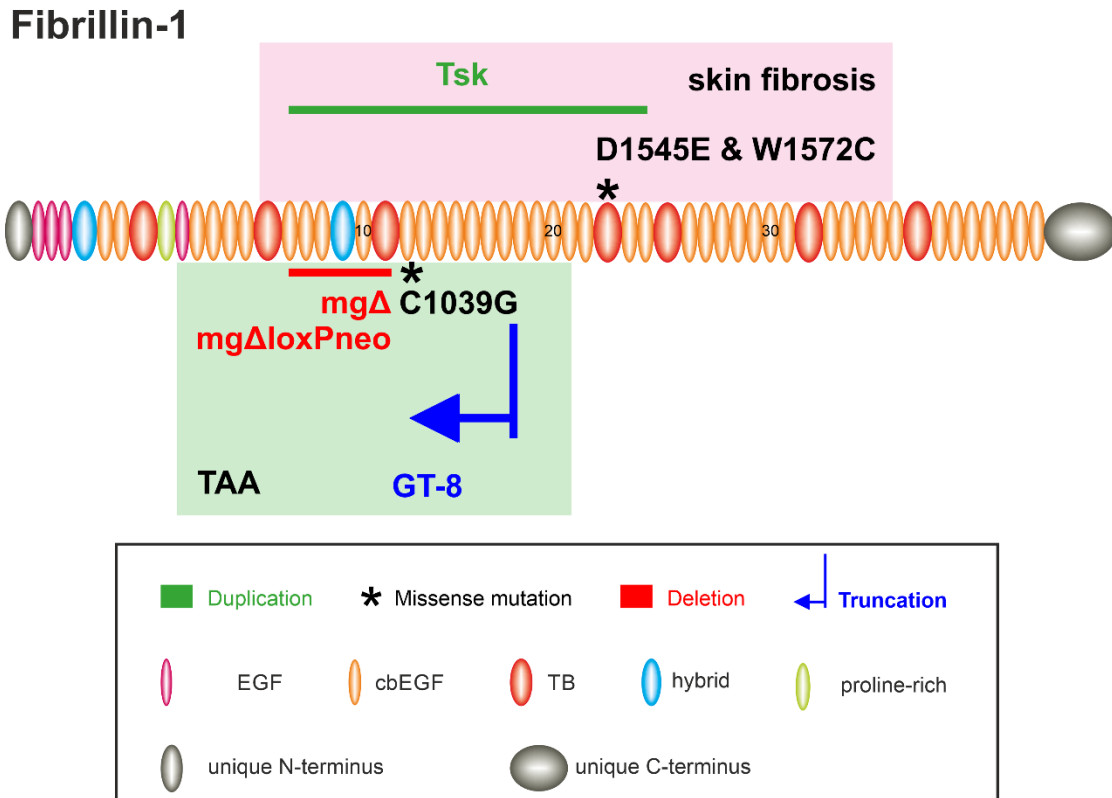


Fig. 1.3 Mouse models altering the structure of fibrillin-1

Domains altered in the respective mouse models, with the 10th, 20th and 30th cbEGF domain marked on the schematic drawing of fibrillin-1. The Tsk mouse model contains an in-frame duplication from cbEGF 7-24 (exons 17-40); the C1039G mutation occurs in cbEGF11; the D1545E (RGD to RGE substitution) and W1572C occur in TB4; mgR modification results to reduced expression (20-25%) of normal fibrillin-1; both mgΔ and mgΔloxPneo cause deletion of cbEGF8-TB3 (exons 19-24); the GT-8 mouse model contains a N-terminal half of truncated fibrillin-1 up to cbEGF17. Tsk, *Fbn1*^{RGE/+}(D1545E) and *Fbn1*^{W1572C/+} mice present with fibrotic skin (pink box). *Fbn1*^{C1039G/+}, *Fbn1*^{mgΔ/mgΔ}, *Fbn1*^{mgΔloxPneo/+} and GT-8 mice develop TAA (green box).

1.3.2 Thoracic aortic aneurysms

TAA is the hall mark and the most fatal manifestation in MFS. It was previously called cystic medial necrosis, due to its histopathologic degeneration in the tunica media, with fragmented elastic laminae, and proteoglycan accumulation [90,91]. TAA is usually detected incidentally and below the threshold for surgical repair (5.0–5.5 cm) [92]. Current treatments using β-blockers,

such as atenolol, show a beneficial effect in reducing, but not preventing, TAA progression [93,94]. The only options to prevent aneurysm rupture are endovascular repair or open surgery. No effective interventions can prevent aneurysm progression. Thus, identifying the molecular mechanism and the genetic basis underlying TAA pathogenesis remains a critical endeavor. Besides fibrillin-1, deficiencies of several other ECM proteins can also lead to TAA, such as COL3A1[95], MFAP5 [96], LOX [97] and FLNA [98]. Mutations disrupting smooth muscle cell contraction or TGF- β signaling can also lead to TAA. These genes include MYH11[99], ACTA2[100], TES [101], PRKG1 [102], TGFB2/3 [103,104] and TGFBR1/2 [105]. The involvement of multiple genes in the pathogenesis of TAA shows the complex nature of this disorder. Recently, the response of smooth muscle cells to the hemodynamic load on a structurally defective aorta was proposed to be the primary driver of TAA [106], which highlights the importance of cell-ECM interactions in TAA pathogenesis.

1.4 Dysregulated signaling related to fibrillinopathies and thoracic aortic aneurysms

1.4.1 Focal adhesion kinase

FAK was first identified by Schaller et al., 1992 in chicken embryo cells binding to fibronectin [107]. FAK is a nonreceptor tyrosine kinase recruited by integrins at their cytosolic side, which assembles with several other proteins into focal adhesions, from which FAK gained its name. Integrin interacted bound to ECM proteins initiate the formation of adhesomes where FAK localizes to a membrane-proximal signaling layer containing integrin cytoplasmic tails, talin, kindlin and paxillin. Through these focal adhesion component, FAK is recruited to indirectly interact with integrins [108,109]. Among these integrin binding molecules, talin is a structural adaptor that links the conserved β subunits of integrins indirectly to the cytoskeleton, except of integrin $\alpha_6\beta_4$, which interacts with intermediate filaments [110]. Paxillin and vinculin are scaffolding adaptors which bridge focal adhesion proteins [111]. Furthermore, composition of

ECM ligands can also regulate focal adhesion formation. Presence of heparin/heparin sulfate binding sites in the TB5 domain, which is located three-domain downstream of RGD-containing TB4 domain in fibrillin-1 (Fig. 1.1), was shown to promote focal adhesion formation initiated by RGD-integrin interaction [40]. Focal adhesion formation is also regulated by intracellular signaling in myofibroblasts. Stress fibers are reported to be necessary for focal adhesion maturation in fibroblasts [112]. Antagonists of myosin contraction provoke the dispersion of focal adhesion [113].

With the help of components in focal adhesion complex, FAK regulates multiple cell activities, including cell migration, mechanosensing, cell proliferation, and ECM organization. FAK regulates cell migration via Rho/Rac activation cycles [114], and via associating with growth factor receptors [115]. Independent of the kinase activities, interactions of integrin, focal adhesion complex and actin filaments can constitute a molecular clutch, by which cytoskeletally generated forces are transmitted to the integrin and direct cell migrations, via focal adhesion complex [116,117]. FAK-deficient cells displayed reduced mobility on ECM substrates in response to chemotactic and haptotactic signals [115,118,119]. The differentiation of fibroblasts into the contractile phenotype, the α -smooth muscle actin positive myofibroblasts, is also regulated by FAK. Absence of FAK disrupt fibroblast growth factor and heparin induced myofibroblast differentiation [120]. FAK activated by integrin ligation autophosphorylates on tyrosine-397 residue. This induces an interaction with Src that stabilizes the active conformation of Src, leading to increased catalytic activity [121,122]. The Src-FAK complex activate PAK1, which in turn phosphorylates and activates MEK1 and RAF, the upstream kinase for ERK1/2 activation [123]. The kinases recruited by FAK have been shown to be responsible for sustaining the ERK1/2 activation after adhesion of many cell types, including fibroblasts [124,125]. Other than regulating

intracellular molecules, ECM organization is also regulated by FAK. For example, reduced formation of extracellular fibronectin fibrils, a master organizer of ECM, was observed in the mesoderm of *FAK* knockout embryos and in isolated fibroblasts [126].

Focal adhesion is closely involved in the pathogenesis of SSS and TAA. Isolated SSS dermal fibroblasts are characterized by reduced activity of FAK [11]. Variants in focal adhesion proteins, including testin (*TES*), talin and zyxin are significantly enriched in isolated TAA tissues obtained from sporadic patients [101]. *Tes*^{Y249H} and *Tes*^{-/-} mice present with spontaneous aortic dilations [101]. Impaired mechano-signaling and perturbed focal adhesions, with decreased number and increased size of FAK staining, were observed in the vascular smooth muscle cells isolated from *Fbn1*^{mgAloxPneo/+} TAA mice [127].

1.4.2 Ras-ERK signaling cascade

Integrin activation is one of the multiple stimuli that can activate the RAS-ERK signaling cascade. These stimuli include growth factors, Angiotensin II, G-protein coupled receptor signaling, cytokines and osmotic stress among others

[128,129]. In this central signaling cascade, RAS activates RAF kinases by promoting RAF dimer formation. Active RAF in turn phosphorylates and activates MEK1/2, which further phosphorylates their only known physiological substrates, ERK1/2 [129]. Integrin activates ERK1/2 signaling primarily through FAK-Src complex (as discussed in chapter 1.4.1) and Shc kinase, which can directly activate RAS [45]. ERK1/2 signaling can regulate a wide spectrum of cell activities, including mRNA transcription, cell cycle progression, cell survival, migration, cytoskeletal remodeling, and differentiation (reviewed by Roskoski [129]). This thesis focused on the activated ERK1/2 in fibrillinopathies and TAA pathogenesis.

Elevated pERK1/2 was identified in isolated SSS dermal fibroblasts [11]. Suppression of ERK1/2 is one of the beneficial effects of integrin modulation therapies in SSS mice and isolate mouse fibroblasts [76]. Treatment of SSS mice (*Fbn1*^{RGE/+} and *Fbn1*^{W1572C/+}) with either the ERK1/2 signaling inhibitor RDEA119 or with TGF- β neutralizing antibodies prevented aggressive skin fibrosis [76]. ERK1/2 levels are also upregulated in MFS mouse models, *Fbn1*^{C1039G/+} and *Fbn1*^{mgR/mgR} [70,130]. Inhibition of ERK1/2 signaling using RDEA119 or doxycycline, can delay TAA progression in these MFS mouse models. ERK1/2 activation in fibrillinopathies is thought to be the consequence of elevated TGF- β and angiotensin II signaling, while the relationship between ERK1/2 and ECM-cell interaction is not fully explored.

1.4.3 Inflammation responses

Inflammation is a complex set of interactions among soluble factors and cells that can occur in all tissues in response to various stimuli. The initial purpose of inflammatory responses is to adapt to tissue stress and restore the tissue to a homeostatic state. However, physiological problems occur if inflammation fails to subside and crosses the homeostatic set points. Other than the well-characterized stimuli, such as microbial and non-microbial foreign bodies, inflammation can also be triggered by cytokines, tissue malfunction, abnormal cell contacts, cell death, and proteolyzed ECM proteins (reviewed by Medzhitov [131]).

Stiff skin syndrome (SSS) is a non-inflammatory disorder, whereas inflammation plays an important role in thoracic aortic aneurysm (TAA) pathogenesis. *In vivo* studies using the fibrillin-1 hypomorphic mouse model *Fbn1*^{mgR/mgR} and in human TAA have previously demonstrated the presence of inflammatory immune cells and elevated cytokines in the tunica adventitia at aneurysmal lesions. Monocyte infiltration into the tunica media of the aorta can be observed as early as 8-weeks of age in the *Fbn1*^{mgR/mgR} mice [86]. Macrophage infiltration into the adventitia

is also observed in aortic specimens obtained from MFS patients, along with elastolysis of the media and a fibroproliferative response [132]. Pro-inflammatory cytokines, including IL-1 β , IL-3, IL-6 and CCL2 are reported to be elevated in the affected tissues or serum of various TAA mouse models or in patient-derived tissues [133-136]. Some trials using anti-inflammatory agents inhibiting IL-6 [135,137], IL-3 [134], IL-1 β [133,138] or deletion of the respective genes have been shown to ameliorate progression of TAA in these mouse models. In addition to cytokines, elastin and recombinant fibrillin-1 fragments harboring an elastin-binding protein (EBP) recognition sequence, XGXXPG, can also act as chemotactic stimuli for monocytes in *Fbn1*^{mgR/mgR} mice [139,140]. Chemotaxis was significantly diminished when macrophages were pretreated with XGXXPG, or by a mutation of the EBP recognition sequence in fibrillin-1 fragments [140,141]. These data demonstrate the importance of inflammatory responses in TAA pathogenesis and progression. However, how the inflammatory cytokines are regulated, and the exact role of inflammatory responses *in vivo* requires further investigations.

1.4.4 Hypoxia-inducible factor 1 α regulatory signaling

Hypoxia-inducible factor 1 α (HIF-1 α) is a transcription factor and a master regulator of oxygen homeostasis. HIF-1 α protects the cells under hypoxic conditions by controlling angiogenesis, erythropoiesis, and glycolysis [142]. Under well-oxygenated conditions, HIF-1 α is hydroxylated by prolyl hydroxylases that generates a binding site for the von Hippel-Lindau protein, a constituent of the ubiquitin ligase complex, which in turn triggers proteasomal degradation [143]. Factor-inhibiting HIF-1 (FIH) is an enzyme that inhibits HIF-1 α by hydroxylating a conserved asparaginyl residue in HIF-1 α , which also requires oxygen as a substrate [144]. Thus, HIF-1 α is protected from ubiquitination under hypoxic conditions or in the presence of factors inhibiting hydroxylases, including CoCl₂ and iron chelators.

Although HIF-1 α induced signaling is not investigated in fibrillinopathies with fibrotic skin, studies using systemic sclerosis fibroblasts show that hypoxia induces the ECM production via elevating TGF- β or connective tissue growth factor signaling [145,146]. Elevated HIF-1 α is also observed in TAA tissue on the mRNA and protein levels [147]. Inhibition of HIF-1 α using rapamycin can ameliorate TAA progression in *Fbn1*^{C1039G/+}, via suppressing ERK1/2 signaling [148]. However, a smooth muscle cell specific *Hif-1 α* knockout displayed detrimental effects on β -aminopropionitrile and angiotensin II-induced TAA formation by reducing lysyl oxidase and tropoelastin mRNA expression [149]. These data suggest that elevated HIF-1 α is closely associated with aneurysm development, but the underpinning mechanisms need to be determined.

1.5 microRNA

microRNA (miRNA) represents a large family of genomically encoded single-stranded short non-coding RNAs of 21-23 nucleotides in length. miRNAs function as post-transcriptional regulators of gene expression in metazoans and plants. Endogenous pri-miRNAs are processed by Drosha-DGCR8 in the nucleus, and are then exported to the cytoplasm as pre-miRNAs, which are then cleaved by Dicer, an endo-ribonuclease necessary for the miRNA maturation, to generate dsRNA duplexes. One strand of the duplex guides the RNA-induced silencing complex (RISC) to bind to the 3' untranslated regions (UTRs), or sometimes the coding region, of specific target mRNAs. This binding can promote mRNA degradation as a result of deadenylation, or suppresses mRNA translation [150]. Among them, mRNA degradation explains 66%-90% of the overall repression [151]. miRNA-mRNA binding requires Watson-Crick pairing of mRNAs to the 2nd-8th nucleotide of the miRNA seeding region [152]. Bioinformatic tools, such as microT-CDS and TargetScan, can predict miRNA-mRNA pairing based on the Watson-Crick pairing in each binding site [152,153].

As important post-transcriptional regulators, miRNAs are predicted to target around 60% of mammalian mRNAs and various processes, including cell proliferation and ECM protein secretion [154,155]. A constitutive knockout of *Dicer* leads to embryonic lethality at E7.5 [156]. A vascular smooth muscle cell-specific *Dicer* knockout results in lethality at E16 due to severe hemorrhage and dilated vessels [157]. Specific miRNAs are dysregulated in connective tissue disorders including skin fibrosis and aneurysms [158,159]. These miRNAs closely regulate multiple processes including cell survival and ECM synthesis. For example, upregulation of miR-21 in lesional areas of systemic sclerosis and fibroblasts of human patients can prevent fibroblast apoptosis [160]. miR-21 was also found to be upregulated in aneurysmal aortae of pancreatic elastase-infused and angiotensin II-induced abdominal aortic aneurysm (AAA) mouse models [161]. This served as a rescue mechanism to decrease apoptosis in the aortic wall via phosphatase and tensin homolog protein. Lentiviral overexpression of miR-21 slows AAA progression also via phosphatase and tensin homolog [161]. miR-29b, upregulated in the TAA lesion of *Fbn1*^{C1039G/+} mice, contributes to aneurysmal development [159]. Inhibition of miR-29b in *Fbn1*^{C1039G/+} mice using locked nucleic acid oligonucleotides rescued the aneurysmal progression. These data emphasize the important regulatory roles of miRNAs in the connective tissue disorders. However, it is not clear whether and how ECM-cell interaction regulates miRNAs in fibrillinopathies. Thus, elucidating the miRNA profiles and upstream regulators as well as functional consequences in these disorders are important. Previous miRNA microarrays performed in the Reinhardt laboratory identified a subset of fibrillin-1-controlled miRNAs. My project further investigated the targets, the functional consequences, and the upstream regulators of four fibrillin-1-controlled microRNAs: miR-612, miR-3185, miR-1208 and miR-122.

1.5.1 miR-612

miR-612 is encoded on human Ch11q13.1, and is only present in primates [162]. As a tumor suppressor, miR-612 was shown to suppress epithelial to mesenchymal transition in hepatocellular carcinoma cells [163]. It can also suppress stemness of hepatocellular carcinoma cells via targeting Wnt/ β -catenin signaling [164]. Study using bladder cancer cells reveals miR-612 cell growth, colony formation, migration, invasion and epithelial-mesenchymal transition via regulating pro-oncogenic malic enzyme 1 [165].

1.5.2 miR-3185

The DNA sequence coding for miR-3185 is only reported to be present on human Ch17q21.32, but not in other species [162]. Upregulation of miR-3185 is observed in cardiac tissues with mechanical asphyxia. miR-3185 suppresses the *CYP4A11*, which is associated with several oxygen-related functions by influencing nicotinamide adenine dinucleotide phosphate-dependent metabolism [166].

1.5.3 miR-1208

miR-1208 is transcribed from human chromosome Ch8q24.21, and is also reported only in primates [162]. miR-1208 is expressed at low levels in Burkitt's lymphoma, breast cancer, and colon cancer cell lines [167], but it is upregulated in gastric cancer [168]. Recently, Kim *et al.* reported that miR-1208 acts as a tumor suppressor by targeting the 3'UTR mRNA coding for the TBC1 domain containing kinase [169]. This in turn suppressed proliferation and induced apoptosis of a renal carcinoma Caki-1 cells.

1.5.4 miR-122

miR-122 is encoded on human chromosome Ch18q21.31. Unlike miR-612, miR-3185 and miR-1208, miR-122 is evolutionally conserved, and is detected in zebrafish [170]. miR-122 level occupies 70% of total miRNA expression in human liver [171]. miRNA-122 is well characterized to control multiple aspects of liver functions, including fibrosis, inflammation, hepatocyte growth, lipid metabolism, hepatic phenotype maintenance, as well as viral infection and proliferation (reviewed by Wen [172]). Knockout of miR-122 in mice result in progressive hepatic fibrosis, inflammation, and higher incidence of hepatocellular carcinoma [173]. miR-122 regulates collagen maturation by targeting the prolyl 4-hydroxylase mRNA *P4HAI*, which controls the proper three-dimensional folding of procollagen chains [174]. Inflammation is elevated in the liver of miR-122 knockout mice, owing to the increased infiltration of immune cells, which can also promote fibrosis. miR-122 regulates chemotaxis of immune cells by targeting the mRNA of two important pro-inflammatory cytokines, *Ccl2* and *Il1 β* [173]. miR-122 can also directly activate natural killer cells through Toll-like receptor signaling [175].

miR-122 is further reported to be upregulated in the aortic tunica intima and the serum of high fat diet fed *ApoE*^{-/-} mice, with elevated endothelial to mesenchymal transition in atherosclerotic lesions. Lentiviral inhibition of miR-122 suppressed the endothelial apoptosis and endothelial to mesenchymal transition in this experimental system [176,177]. Vascular injury can elevate miR-122 in the rat aortic tunica adventitia [178], inhibition of which prevents apoptosis and oxidative stress caused by angiotensin II induction, via suppressing the SIRT6-ELA-ACE2 signaling.

1.6 Rationale, hypotheses, goals and objectives

Previous studies from the Reinhardt lab identified a subclass of miRNAs and mRNAs regulated by fibrillin-1 RGD-fibroblast interactions, using two fibrillin-1 fragments harboring either the wild-type RGD or the non-cell binding RGA sequence. Some molecular interaction between these regulated miRNAs and mRNAs were identified previously, which are central to fibrillin-1 RGD controlled TGF- β signaling.

Building on these previous data, **it is hypothesized that the fibrillin-1 controlled miRNAs also participate in other important cell activities, including focal adhesion formation and cell proliferation. Thus, the first overarching goal of my project was to further investigate whether and how the fibrillin-1-controlled miRNAs are involved in focal adhesion formation and cell proliferation, and how these miRNAs are controlled by the interactions of fibroblast with fibrillin-1.** To achieve this, the following specific objectives were performed:

1. Use bioinformatic tools to predict mRNA targets of the fibrillin-1-controlled miRNAs that are relevant for focal adhesion formation and fibroblast proliferation.
2. Experimentally determine the miRNA-mRNA interaction sites using dual luciferase reporter assays.
3. Study the function of the fibrillin-1 dysregulated miRNAs on focal adhesion formation and fibroblast proliferation, by overexpressing or inhibition of relevant miRNAs.
4. Identify the upstream regulators mediating the control of fibrillin-1 on these miRNAs.

Upon identification of the regulation of fibrillin-1-controlled miRNAs in fibroblasts, we explored whether miRNAs were dysregulated in the aortae of fibrillin-1 haploinsufficient *Fbn1*^{mgR/mgR} mice. Fibrillin-1 containing microfibrils connect smooth muscle cells with elastic laminae in the aortic tunica media. As *Fbn1*^{mgR/mgR} mice develop TAA with loss of fibrillin-1

microfibrils in the tunica media and with altered smooth muscle phenotypes, **it is hypothesized that miRNAs are differentially regulated in the aortic smooth muscle cells of wild-type and *Fbn1^{mgR/mgR}* mice. Thus, the second overarching goal was to understand whether and how miRNAs are derailed in pathological TAA, and to identify the core regulatory miRNA(s) and their role in key pathways during TAA pathogenesis.** The following detailed objectives were performed:

1. Determine time-dependent miRNA profiles in the ascending aortae of *Fbn1^{mgR/mgR}* mice.
2. Compare the mRNA profiles in TAA tissues of *Fbn1^{mgR/mgR}* mice with TAA tissues from patients, and identify the commonly dysregulated pathways.
3. Discover the functional role of the core miRNA(s) on regulating pathways identified in 2, using primary smooth muscle cell and *ex vivo* aorta organ cultures.
4. Elucidate the upstream regulators of the core miRNA(s).

Additionally, unbiased and automated quantification methods of immunostaining or *in situ* hybridization were required. **The hypothesis was that the currently existing quantification methods can be significantly improved and adopted to ECM fiber systems. The third goal of my project was thus to develop and customize ImageJ-based quantification methods for the present study, and for ECM-related applications in general.** The following detailed objectives were performed:

1. Improve quantification methods for focal adhesions.
2. Optimize quantification methods for cell proliferation.
3. Customize quantification methods for ECM fiber formation.
4. Expand quantification methods for tissue staining.

**CHAPTER 2 THE FIBRILLIN-1 RGD INTEGRIN BINDING SITE REGULATES GENE
EXPRESSION AND CELL FUNCTION THROUGH MICRORNAS**

**The fibrillin-1 RGD integrin binding site regulates gene expression and cell
function through microRNAs**

Karina A. Zeyer,^{1,#} Rong-Mo Zhang,^{1,#} Heena Kumra,¹ Amani Hassan,¹ and Dieter P.
Reinhardt^{1,2,*}

¹ Faculty of Medicine, McGill University, Montreal, Canada

² Faculty of Dentistry, McGill University, Montreal, Canada

contributed equally to this work

* Correspondence to Dieter P. Reinhardt: Department of Anatomy and Cell Biology, McGill
University, 3640 University Street, Montreal, Quebec, H3A 0C7, Canada. Phone: +1
514.398.4243. E-mail: dieter.reinhardt@mcgill.ca

2.1 Preface:

RGD motif is the primary mediator for fibrillin-1-cell interaction, via integrin bindings. Mutations from RGD to RGA, RGE and RGG have been shown to abrogate cell adhesion to RGD-containing proteins or peptides. Mutations in and around the RGD-containing TB4 domain in human fibrillin-1 can cause fibrotic skin in SSS, GD, AD and WMS in human. Tsk mice with structural alteration of fibrillin-1 central cell binding domains, presents with fibrotic skin. RGD to RGE substitution in mouse fibrillin-1 phenocopies SSS. Skin fibrosis can be ameliorated with integrin modulating treatment. These lines of evidence strongly suggest the involvement of fibrillin-1 RGD-fibroblast interaction in the pathogenesis of skin fibrosis. Several miRNAs have been reported to be dysregulated in fibrotic skin, such as miR-21 and miR-29b. However, it was not clear whether disrupted fibrillin-1-cell interaction regulates miRNAs. To answer this question, gene expression profiling of miRNAs and mRNAs were performed in this chapter, comparing skin fibroblasts seeded on RGD-containing fibrillin-1 fragment (rF1M-WT) to those on RGA non-integrin binding controls (rF1M-RGA). Functionally analyses of these differentially regulated miRNA were investigated, with the focus on TGF- β signaling and focal adhesion formation.

2.2 Abstract

Fibrillins are the major components of microfibrils in the extracellular matrix of elastic and non-elastic tissues. Fibrillin-1 contains one evolutionarily conserved RGD sequence which mediates cell-matrix interactions through cell-surface integrins. Here, we present a novel paradigm how extracellular fibrillin-1 controls cellular function through integrin-mediated microRNA regulation. Comparative mRNA studies by global microarray analysis identified growth factor activity, actin binding and integrin binding as the most important functional groups that are regulated upon fibrillin-1 ligation with dermal fibroblasts. Many of these mRNAs are targets of miRNAs that were identified when RNA from the fibrillin-1-ligated fibroblasts was analyzed by a miRNA microarray. The expression profile was specific to fibrillin-1 ligation since interaction with fibronectin displayed a partially distinct profile. The importance of selected miRNAs for the regulation of the identified mRNAs was suggested by bioinformatics prediction and the interactions between miRNAs and mRNAs were experimentally validated. Functionally, we show that miR-503 controls p-Smad2 dependent TGF- β signaling, and that miR-612 and miR-3185 are involved in the focal adhesion formation regulated by fibrillin-1. In conclusion, we demonstrate that fibrillin-1 ligation with fibroblasts regulate miRNA expression profiles which in turn control critical cell functions.

Keywords: fibrillin; integrin; microRNA; cell signaling; extracellular matrix; connective tissue

Abbreviations used:

BMP, bone morphogenetic protein; cbEGF, calcium-binding epidermal growth factor-like domain; DAVID, the database for annotation, visualization and integrated discovery; DIANA, DNA intelligent analysis; DMEM, Dulbecco's modified Eagle's medium; ECIS, electric-cell substrate impedance sensing; FAK, focal adhesion kinase; FDR, false discovery rate; HEK293, human embryonic kidney 293; HSFs, human skin fibroblasts; KEGG, Kyoto encyclopedia of genes and genomes; LTBP, latent TGF- β binding protein; MAPK, mitogen-activated protein kinase; miRNA, micro ribonucleic acid; p-Smad2, phosphorylated Sma and Mad related protein 2; TB, transforming growth factor-beta-binding protein-like domain; TBS, Tris-buffered saline; TGF- β , transforming growth factor-beta; UTR, untranslated region

2.3 Introduction

The fibrillin family consists of three highly homologous, evolutionarily conserved ~350 kDa glycoproteins, fibrillin-1, -2 and -3 [13,28,179,180]. Fibrillin-1 is the main form in postnatal life, whereas fibrillin-2 and -3 are primarily expressed during development [33,181,182]. Fibrillins are multi-domain proteins composed of common and unique domains, depicted in Supplemental Figure S2.1A [24,26]. The most frequently occurring domains are calcium-binding epidermal growth factor-like (cbEGF) domains [17], and transforming growth factor-beta binding protein-like (TB) domains [25].

The fourth TB domain contains the sole RGD cell binding site in fibrillin-1. RGD sequences represent integrin receptor recognition sites that tether extracellular proteins to cells and mediate numerous cellular functions including cell attachment, focal adhesion formation and intracellular signaling [44,183]. This interaction is essential for cells to sense and react to their extracellular microenvironment [184,185]. Specifically, fibrillin-1 interacts with integrins $\alpha_5\beta_1$, $\alpha_v\beta_3$ and $\alpha_v\beta_6$ [35,51-53]. Fibrillin-1 adhesion to integrin $\alpha_5\beta_1$ and cell migration is enhanced by an upstream synergy site, comprised by an cbEGF array [40]. In addition, fibrillin-1 is a major heparin/heparan sulfate interacting protein, containing seven binding regions [22,54,55,186,187]. One heparan sulfate binding site, located immediately downstream of TB4, supports focal adhesion formation [40]. Supplemental Figure S2.1A shows the RGD cell binding site, the synergy region and the heparan sulfate binding regions relative to the full-length fibrillin-1 protein.

Secreted fibrillins first associate with the cell surface [188], and then multimerize into supramolecular microfibrils in the extracellular matrix of elastic and non-elastic tissues. During development, microfibrils act as a scaffold for tropoelastin deposition in skin, blood vessels and lung [63]. Microfibrils also occur independently of elastic fibers, for example in ciliary zonules of

the ocular system, or along basement zones in various tissues [66,67]. Importantly, microfibrils play a major fibrillin-1-associated role in regulating the bioavailability of growth factors of the transforming growth factor-beta (TGF- β) superfamily [71,189]. Whereas TGF- β s interact with fibrillin-1 and microfibrils indirectly in the extracellular matrix through interactions with the latent TGF- β binding proteins (LTBP)-1, -3 and -4 [69], bone morphogenetic protein (BMP)-2, -4, -7, and -10 interact directly with fibrillin-1 [189].

The importance of microfibrils in the development and homeostasis of tissues is highlighted by a variety of autosomal dominant connective tissue disorders caused by mutations in fibrillin-1, most importantly Marfan syndrome [12], but also other disorders such as stiff skin syndrome [11], acromicric and geleophysic dysplasia [74], and dominant Weill-Marchesani syndrome [72]. Deregulation of TGF- β is an important contributor to the pathogenesis in Marfan syndrome and related disorders [71,190].

Micro ribonucleic acids (miRNAs) have been identified as important regulators of gene expression [191]. They represent single-stranded short non-coding RNAs that are about 21-23 nucleotides in length. Most miRNAs regulate gene expression on the mRNA level by binding directly to the 3' untranslated regions (UTRs) of specific target mRNAs. This leads to the inhibition of translation through either mRNA cleavage or translational repression, or decreased mRNA stability as a result of deadenylation [150]. Inhibition of miRNAs maturation by ablating the RNaseIII catalytic domain of Dicer leads to stem cell depletion and embryonic lethality [156]. miRNAs are essential for the regulation of cellular activity. As key regulators of gene expression of many cellular processes, miRNA can regulate 30-60% of human genes [154]. miRNAs have been demonstrated to be involved in the regulation of extracellular matrix proteins and their receptors including collagens, fibronectin and integrins [192], growth factor bioavailability [193], and cytoskeletal

dynamics [194]. Directly related to fibrillin-1, it was shown that miR-29b regulates aortic wall apoptosis and extracellular matrix abnormalities in the *Fbn1*^{C1039G/+} Marfan syndrome mouse model [159]. An initial biological proof of concept study demonstrated that silencing miR-29b in these mice can prevent early aneurysm formation [195].

The relationship between miRNAs, fibrillin-1 and integrin ligation is currently not understood. This study identifies several miRNAs and delineates their role in cell functions triggered by cell-fibrillin-1 interactions. Unraveling the downstream pathways that are regulated upon fibrillin-1 ligation allows to understand the physiological function of fibrillin-1-mediated cell-matrix interactions at an early stage of microfibril assembly and pathology.

2.4 Results

2.4.1 RGD-mediated fibrillin-1 ligation alters mRNA expression of growth factors, actin-binding-proteins and integrins

Directly after secretion, fibrillin-1 associates with the cell surface where it co-localizes with fibronectin [188], prior to forming higher molecular weight assemblies [196]. We intended to mimic this early stage of fibrillin-1 cell association to analyze the cellular consequences of fibrillin-1 ligation on mRNA expression by microarray analysis (Affymetrix Human Gene 2.0 chips). For this reason, we produced two recombinant human fibrillin-1 fragments encompassing domains cbEGF10 to cbEGF31 (Supplemental Figure S2.1A). The wild-type rF1M-WT fragment was designed to include the RGD integrin binding site in the TB4 domain, as well as the upstream located synergy region and two heparin-binding regions, to analyze the RGD cell binding site in its sequence context needed to properly mediate cell attachment and cell binding to fibrillin-1 [40]. The rF1M-RGA mutant fragment is identical to rF1M-WT except one point mutation (p.Asp1587Ala), which has been previously shown to abolish interaction with integrins [40,53]. This fragment was used as a non-cell interacting control. The microarray was conducted with RNA preparations obtained from human skin fibroblasts (HSFs) grown for 24 h on rF1M-WT and the rF1M-RGA control.

Upon ligation of HSFs with fibrillin-1, 520 differentially regulated mRNAs with an false determination rate (FDR)-adjusted p-value of <0.05 were detected that were at least 2-fold significantly up-or downregulated (Figure 2.1A). This demonstrates that fibrillin-1 ligation via the RGD site triggers a broad cellular response. To predict enriched functional themes, gene ontology analysis of the selected gene products was employed using the database for annotation, visualization and integrated discovery (DAVID) Bioinformatics Resources, which identified growth factor activity, actin binding and integrin binding as relevant enriched groups, among

others (Figure 2.1B). These three groups were of particular interest for the following reasons. Growth factor regulation by the extracellular matrix is well established for growth factors of the TGF- β superfamily that are known to be sequestered by microfibrils. Two members of this group, *TGFB2* and *BMP2* mRNA, were identified in the microarray. Moreover, other growth factor mRNAs such as three members of the CCN gene family (*CTGF*, *CYR61*, *NOV* mRNAs) were found to be differentially regulated in the microarray analysis. Actin binding and integrin binding represent two important groups as the interaction of the RGD site with integrins results in changes in cell shape and adhesion compared to the RGA control (Supplemental Figure S2.4A,C). Actin-binding proteins are likely relevant for these different phenotypes.

The Kyoto encyclopedia of genes and genomes (KEGG) pathway bioinformatic analysis narrows down the general description of the molecular function to a list of defined pathways. Table 2.1 displays a list of differentially regulated pathways relevant to fibrillin-1 binding and signaling. These include growth factor pathways such as TGF- β , mitogen-activated protein kinases (MAPK), Wnt, Hedgehog and Notch signaling, focal adhesions, and the regulation of the actin cytoskeleton. mRNAs from these selected functional groups with relevance to fibrillin biology and/or with the highest fold changes upon fibrillin ligation were validated by real-time qPCR using HSFs from two different human donors (Figure 2.1C-E). One cell ID was identical to the one used for the microarray analysis (ID 595), and another one (ID 222) was used to determine the conservation of the observed mRNA regulation among HSFs from different donors. Within the three groups, 10 out of 14 mRNAs (*BMP2*, *TGFB2*, *CTGF*, *CYR61*, *NOV*, *AFAP1*, *CNN1*, *TAGLN*, *ITGA6* and *ITGB3*) could be validated in HSFs from both donors.

2.4.2 Analysis of miRNA expression patterns after RGD ligation

The differentially regulated mRNAs upon fibrillin-1 ligation raised the question how these changes are regulated. One potent mechanism in gene regulation are miRNAs. The same 24 h RNA preparations were thus used for a miRNA microarray (Affymetrix miRNA 3.0) to identify miRNAs involved in regulating the differentially expressed mRNAs for growth factors, actin binding-proteins and integrins. We identified 129 differentially expressed miRNAs with an FDR-adjusted p-value of <0.05 (Figure 2.2A).

To determine common pathways regulated by these 129 miRNAs, pathway prediction analysis was conducted using the DNA intelligent analysis (DIANA) miRPath v.2.0 tool [197] (Table 2.1). The list of pathways was almost identical to the ones identified in the mRNA pathway analysis. This indicates that the differentially regulated miRNAs and mRNAs act together in the same pathways including the TGF- β , MAPK, Wnt, and Hedgehog signaling pathways, as well as focal adhesions and the regulation of the actin cytoskeleton.

Ten miRNAs were chosen for further analysis based on their level of differential expression, their high statistical significance and their importance in regulating the relevant functional groups identified in the mRNA microarray. These miRNAs were validated by qPCR. For the upregulated miRNAs, the results from the microarray were confirmed for 4 of 5 miRNAs (Figure 2.2B). Similarly, 4 of 5 downregulated miRNAs could be validated (Figure 2.2C). Time course analyses of the validated miRNAs were performed to determine at what time point the expression levels were consistently up- or downregulated between 2-24 h after exposure to fibrillin-1 (Figure 2.2D). Most tested miRNAs (miR-4521, miR-612, miR-1208, miR1231, miR-3185) consistently changed expression levels a short time (2-8 h) after HSF binding to rF1M-WT. Three of the miRNAs (miR-

29b-1*, miR-424*, miR-503) required longer (24 h) for a consistent upregulation. This data helps explain why 24 h after fibrillin-1 ligation, profound changes in mRNA expression can occur.

2.4.3 The miRNA signature is specific to RGD-mediated fibrillin-1 ligation

To exclude the possibility that the mRNA and miRNA expression patterns observed by microarrays were induced by mechanical stress triggered by the atypical shape of HSFs seeded on the RGA-containing fibrillin-1 fragment (Supplemental Figure S2.4A), controls with cells seeded on poly-D-lysine were included. Poly-D-lysine is a positively charged amino acid polymer widely used as an effective non-integrin attachment factor for cultured monolayer cells. HSFs seeded on poly-D-lysine-coated plates had a similar phenotypic appearance as cells seeded on rF1M-WT (Figure 2.3A). Therefore, potential differences in miRNA regulation observed between HSFs seeded on poly-D-lysine and the fibrillin-1 wild-type fragment can be attributed to RGD-mediated signaling events and not to mechanical stress-induced signaling pathways. If the observed miRNA regulation patterns are simply a consequence of the differences in shape or adherence to the culture dish, then no differences in miRNA levels should be observed between HSFs seeded on rF1M-WT and poly-D-lysine. All tested miRNAs (miR-29b-1*, miR-424, miR-503, miR-4521) upregulated upon interaction with the RGD-containing rF1M-WT relative to rF1M-RGA were also upregulated relative to poly-D-lysine (Figure 2.3B, left panel). Downregulation of selected miRNAs (miR-612, miR-1208, miR-1231, miR-3185) upon interaction with rF1M-WT as compared the RGA control was even stronger (2.0-3.6-fold) for HSFs seeded on rF1M-WT relative to poly-D-lysine (Figure 2.3B, right panel). In summary, the differential up- or downregulation was conserved for all tested miRNAs, demonstrating that the induction or repression of the respective miRNAs are confidently mediated by the RGD sequence in fibrillin-1.

Various extracellular matrix proteins contain an RGD cell binding site. To address specificity for the fibrillin-1 RGD site, we have produced and analyzed two fibronectin fragments encompassing either the RGD or an inactive RGA motif in the 10th fibronectin type III (FNIII-10) domain and the synergy site in the FNIII-9 domain (Supplemental Figure S2.1A). As expected, FN-WT promoted cell attachment whereas FN-RGA did not (Supplemental Figure S2.4B, D). Interaction of HSFs with fibronectin resulted in both similar and distinct miRNA expression patterns compared to the interaction with fibrillin-1 (compare Figure 2.3B and C). Cell ligation with FN-WT also resulted in the upregulation of miR-29b-1*, miR-503, and miR-4521, but not of miR-424. For the downregulated miRNAs, only miR-1208 and miR-1231 show a similar expression upon fibrillin-1 and fibronectin ligation, whereas miR-612 is upregulated and miR-3185 remains unchanged when cells are ligated to fibronectin.

2.4.4 Fibrillin-1-induced miRNAs target mRNAs for growth factors, actin binding proteins and integrins

Since growth factor activity, actin binding and integrin binding are three of the most relevant groups identified by the mRNA microarray, we explored the miRNA-dependent regulation of their mRNA levels. First, bioinformatics analysis using the miRanda algorithm was conducted to predict interactions between miRNAs and mRNAs [198]. Specifically, the interaction between all 8 miRNAs validated by qPCR (miR-29b-1*, miR-424*, miR-503, miR-612, miR-1208, miR-1231, miR-3185 and miR-4521) and validated mRNAs relevant for growth factor activity, actin or integrin binding (*TGFB2*, *BMP2*, *CTGF*, *CYR61*, *NOV*, *AFAP1*, *CNN1*, *TAGLN*, and *ITGB3*) was assessed (Table 2.2). The six dysregulated mRNAs in the focal adhesion group reported in Table 2.1 were not in the predicted target list of the 8 selected miRNAs, and thus were not further analyzed. This analysis predicted some miRNAs as potent regulators of a number of potential and

relevant targets, and provided a candidate list for the subsequent experimental confirmation. To validate these targets, we used the established method of overexpressing a mutant GW182 protein that normally plays an important role in miRNA-mediated gene silencing [199-201]. GW182 proteins directly interact with Argonaute proteins [202], are recruited to miRNA targets, and promote their silencing. The overexpression in the human fibroblast cell line MSU1.1 enabled the locking of miRNAs and their targets in the RISC complex. We focused on the miRNAs with 3 or more predicted targets, and thus miR-424 and miR-4521 were not included in the experimental validation. The experimentally validated interactions of miR-29b-1*, miR-503, miR-612, miR-1208, miR-1231, and miR-3185 with growth factor, actin binding-proteins and integrin binding mRNAs are summarized in Table 2.3. In total, 17 (58%) of the 29 algorithm-based prediction of the miRNA-mRNA interactions could be validated. Experimental details are shown in Supplemental Figures S2.5, S2.6 and S2.7. Five of the 9 tested mRNAs (*TGFB2*, *CTGF*, *NOV*, *AFAP1*, *CNN*) were validated as targets for ≥ 4 of the 6 most dysregulated miRNAs. Among them, *TGFB2* is validated to be regulated by all the 6 tested miRNAs. These data indicate that the fibrillin-1 ligation-controlled miRNAs indeed act in these functional groups.

2.4.5 Fibrillin-1 and miR-503 regulate canonical TGF- β signaling

Since fibrillin-1 is involved in the regulation of TGF- β bioavailability and activity through its interaction with the LTBPs, we explored whether the interaction of fibrillin-1 with fibroblasts directly affects TGF- β signaling pathways. HSFs displayed differential activities of the canonical TGF- β signaling pathway, depending on the substrate they were seeded on, as evidenced by immunofluorescence staining for phosphorylated Sma and Mad related protein 2 (p-Smad2) (Figure 2.4A). The pathway was more active 24 h after HSFs were seeded on the mutant RGA-

containing fragment as shown by a stronger p-Smad2 signal intensity (149%) relative to the Tris-buffered saline (TBS) control. Contrary, interaction with the wild-type fibrillin-1 fragment led to reduced TGF- β signaling to about 55% of the control after 24 h. This correlates with downregulated *TGFB2* mRNA levels upon integrin ligation to rF1M-WT, as observed in the microarray (Figure 2.1C). TGF- β 1 control treatment for 24 h induced the strongest activation (197% of the control) of the TGF- β signaling pathway. In summary, fibrillin-1 ligation with HSFs controls the canonical TGF- β pathway by dampening its activity.

Since all tested fibrillin-1 ligation-controlled miRNAs target *TGFB2* mRNA (Table 2.3), we performed functional analysis on the TGF- β signaling pathway. The role of miR-503 was of particular interest because the upregulation of miR-503 in HSFs on rF1M-WT correlates with the downregulation of *TGFB2* mRNA in the microarray and qPCR. HSFs seeded on TBS control wells were transfected with miR-503 mimics and p-Smad2 activity was analyzed after 48 h by immunofluorescence (Figure 2.4B). A significant reduction in the p-Smad2 intensity to 64% was observed when miR-503 was overexpressed compared to the non-transfected control. This explains the situation when HSFs are seeded on rF1M-WT, resulting in upregulation of miR-503 and downregulation of p-Smad2 dependent TGF- β activity. In conclusion, miR-503 contributes to the reduced TGF- β signaling observed upon binding of HSFs to fibrillin-1.

2.4.6 miR-612 and miR-3185 regulate fibrillin-1-mediated focal adhesion formation

Since focal adhesion formation is one of the important downstream events after fibrillin-1 integrin binding to fibroblasts [40], the focal adhesion kinase (FAK) activity was assessed by immunofluorescence for phosphorylated FAK. To facilitate this analysis, HSFs were seeded on

either rF1M-WT or rF1M-RGA coated Y-shaped micropatterns ($1600 \mu\text{m}^2$) that provided a defined area and shape for the cells to attach (Figure 2.5A). HSFs seeded on rF1M-WT frequently occupied the entire available area, whereas cells seeded on the rF1M-RGA did often not occupy the entire area. The number, average area and total area of focal adhesions per cell was significantly higher in HSFs seeded on rF1M-WT as compared to the rF1M-RGA control (Table 2.4).

Since rF1M-WT ligation with HSFs resulted in upregulation of miR-29b-1* and miR-503, and downregulation of miR-612, miR-1208, miR-1231, and miR-3185 (see Figure 2.1), we transfected HSFs with miRNA mimics and inhibitors, respectively, to analyze whether these miRNAs are mediators of focal adhesion formation (Figure 2.5B and C). miR-29b-1* overexpression did not change the number of focal adhesions per cell, but led to a significantly decreased average size. miR-503 overexpression resulted in significantly lower number and average size of focal adhesions (Figure 2.5B). Thus, miR-29b-1* and miR-503 cannot be mediators of the fibrillin-1-promoted focal adhesion formation. For miR-612, miR-1208, miR-1231, or miR-3185, only inhibition of miR-612 showed a significant increase in both, number and average size of focal adhesions, whereas inhibition of miR-3185 resulted in an increased average size of focal adhesions (Figure 2.5C). Inhibition of miR-1208 decreased the focal adhesion number.

This result indicates that miR-612 and miR-3185 mediate the fibrillin-1 induced focal adhesion formation. To further prove this possibility, miR-612 or miR-3185 were overexpressed in HSF seeded on rF1M-WT (Figure 2.6A), demonstrating that the miR-3185 mimic could downregulate the total area of focal adhesion per cell. Furthermore, rescue experiments to inhibit miR-612 or miR-3185 on HSF seeded on rF1M-RGA (Figure 2.6B) showed that the miR-612 inhibitor can rescue the total area of focal adhesion per cell.

In conclusion, miR-612 and miR-3185 contribute to the fibrillin-1 mediated regulation of focal adhesion formation in HSFs.

2.5 Discussion

miRNAs are key regulators of gene expression of cellular processes, including the regulation of the extracellular matrix. However, how extracellular matrix proteins regulate the expression of miRNAs and associated downstream cell functions is currently very little explored. Many extracellular matrix proteins interact with cells via RGD-dependent integrin receptors. Here, we use fibrillin-1 as a model protein because of its importance in tissue and organismal development. We and others have shown that the RGD sequence in fibrillin-1 provides the molecular basis for cell adhesion via integrin $\alpha 5\beta 1$, $\alpha v\beta 3$ and $\alpha v\beta 6$ [35,40,51-53]. In the present study, we provide for the first time a comprehensive analysis of how fibrillin-1-integrin ligation regulates miRNA expression and downstream cell function using dermal fibroblasts as a model system. Furthermore, our study significantly extends the repertoire of how miRNAs act in several miRNA-mediated regulatory pathways, most importantly the TGF- β signaling pathway and focal adhesion formation.

Integrin-mediated fibrillin-1 interaction with dermal fibroblasts resulted in profound changes of mRNA and miRNA expression patterns. Global microarray analysis revealed differential expression of 520 mRNAs and 129 miRNAs after 24 h of interaction of fibroblasts with fibrillin-1. Independent pathway analysis for mRNA and miRNA expression demonstrated significant overlaps. The differentially expressed mRNAs and miRNAs act together in signaling pathways mediated by TGF- β , Wnt, MAPK, or Hedgehog, and in pathways for cytoskeletal organization. These are pathways hitherto not directly associated with the interaction between fibrillin-1 and cells, and they are potentially involved in the pathogenesis of some of the fibrillin-1 associated disorders. None of the identified miRNAs has been described previously in regard to fibrillin-1 mediated cell signaling.

We have analyzed the specificity of fibrillin-1 regulated miRNA expression in two ways. Firstly, we tested whether the different cell shapes of HSFs seeded on rF1M-WT compared to rF1M-RGA could cause the differential miRNA regulation. However, we have observed similar patterns of up- or down-regulated miRNAs when HSFs were seeded on rF1M-WT compared to either rF1M-RGA or to cells seeded on poly-D-lysine, a substrate that HSFs readily attach to and spread on, excluding this possibility. Secondly, we have analyzed the specificity for the RGD binding site in fibrillin-1. Analyzing a selected set of miRNAs with HSFs seeded on a fibronectin control fragment containing the RGD sequence in the 10th type III domain revealed similarities and differences compared to the rF1M-RGD-seeded HSFs. While the overall pattern was similar, miR-612 and miR-3185 for example were downregulated in cells seeded on rF1M-WT and either upregulated (miR-612) or unchanged (miR-3185) in cells seeded on fibronectin. While we have not addressed the molecular cause for these protein-specific responses, it is possible that they originate from different affinities of fibrillin-1 and fibronectin for specific integrins or from a different set of integrins interacting with both proteins. Fibrillin-1 and fibronectin RGD sites share binding with $\alpha 5\beta 1$ and $\alpha v\beta 3$ integrins expressed on fibroblasts. For fibrillin-1, binding to $\alpha 5\beta 1$ was reported of relative low affinity, whereas $\alpha 5\beta 1$ interacts with fibronectin with high affinity [53,203]. Different synergy sites upstream of the RGD sites in both proteins may also contribute to the modulation of the downstream signaling [40,204]. In addition, fibronectin may involve additional RGD-binding integrins that are not shared with the known set of fibrillin-1 interacting integrins [205].

It is well documented that fibrillin-1 is involved in the regulation of TGF- β bioavailability via its interaction with several LTBPs [69,206]. Here, we demonstrate an additional mechanism how fibrillin-1 controls TGF- β . Fibrillin-1 ligation with HSFs controls the canonical TGF- β pathway by dampening p-Smad2 activity. One of the miRNAs that are upregulated when fibrillin-1 interacts

with HSFs is miR-503, and overexpression of miR-503 in HSFs reduces p-Smad2 activity. We also have determined that *TGFB2* mRNA is a direct target of miR-503 (Table 2.3), which will be downregulated when miR-503 is elevated. Potentially, miR-503 also targets other critical mRNAs in the TGF- β signaling pathway in fibroblasts, not tested in the present study. These data extend the current concepts how fibrillins and microfibrils are involved in the regulation of TGF- β , demonstrating a regulatory mechanism via integrin-mediated and miRNA-dependent gene expression.

Previous *in vivo* studies demonstrated that heterozygous mice with an RGD to RGE substitution in fibrillin-1 (*Fbn1*^{RGE/+}) displayed diffuse skin fibrosis including increased deposition of collagen and microfibrils, similar to stiff skin syndrome patients that carry mutations in the TB4 domain [11,76]. Enhanced TGF- β bioavailability contributed to increased TGF- β activity in these mutant mice. Importantly, that study showed increased total (latent and free) TGF- β 2 in the dermis of mutant mice, but no difference in free TGF- β . These findings correlate directly with our observation of *TGFB2* mRNA downregulation when HSFs interact with the wild-type fibrillin-1 fragment, and therefore upregulation when HSFs are grown on the integrin-binding deficient fibrillin-1 RGA mutant. Fibroblasts from patients with systemic sclerosis showed decreased levels of miR-29a *in vitro* [76]. The miR-29 family members are known to be repressed by TGF- β and inhibit the expression of multiple matrix components in fibroblasts and suppress fibrosis [207,208]. Integrin-modulating therapies and TGF- β antagonism restored miR-29a levels in patient-derived fibroblasts [76]. miR-29a targets genes related to extracellular matrix, such as fibrillin-1, integrins, collagens, and laminins [209]. Although miR-29b-1* has a different seed region compared to miR-29a, and thus different targets, miR-29a and miR-29b-1* are co-expressed from the same cluster [154,210]. In the present study, we show miR-29b-1* to be

significantly upregulated when HSFs bind to wild-type fibrillin-1, while miR-29b-1 remains unchanged. Furthermore, TGFB2 mRNA, which we have experimentally determined as a direct target of miR-29b-1*, and p-Smad2-dependent TGF- β signaling are also kept at a low level when HSFs binds to rF1M-WT. These results suggest that miR-29b-1* is involved, in addition to miR-503, in fibrillin-1 mediated dampening of TGF- β activity. However, this likely occurs on a network level, as overexpression of miR-29b-1* alone in HSFs did not result in reduced TGF- β activity (not shown).

Integrin ligation with extracellular proteins stimulates the assembly of focal adhesions at the cell membrane. The integrin/focal adhesion complex serves as a crucial element for mechanotransduction [211], and is essential for the activation of TGF- β [212]. Focal adhesion formation triggered by RGD-containing fibrillin-1 fragments was previously shown for keratinocytes mediated through integrin $\alpha v \beta 6$ [53]. Bax et al. reported that the TB5-cbEGF25 domains support the formation of focal adhesions [40]. However, the contribution of the RGD site alone to focal adhesion formation was not tested. HSFs seeded on the rF1M-WT developed significantly more focal adhesions and can spread better than HSFs seeded on the rF1M-RGA control. However, HSFs seeded on the rF1M-RGA fragments still develop focal adhesions to some extent (Figure 2.5A). It is possible that the described supporting role of the heparin/heparan sulfate binding site located in TB5 does not entirely dependent on the interaction of integrins with the RGD site in TB4 [40].

Regardless of whether or not non-RGD sites in fibrillin-1 have independent separate roles in focal adhesion formation, we have identified two miRNAs, miR-612 and miR-3185, as important regulators for fibrillin-1-mediated focal adhesion formation for the following reasons. These miRNAs are both downregulated when HSFs are seeded on rF1M-WT. miR-612 and miR-3185

inhibition in HSFs led to significantly more focal adhesions or more developed focal adhesions. Rescue experiments showed that focal adhesion formation in HSFs could be enhanced by miR-612 inhibition in HSFs grown on rF1M-RGA, or inhibited by miR-3185 overexpression in HSFs seeded on rF1M-WT. Calponin 1, which we have validated as a target for miR-612, is a myofibroblast and smooth muscle cell marker [213]. The level of calponin 1 mRNA was elevated in the microarray and qPCR when HSFs were grown on rF1M-WT, concomitant with the downregulation of miR-612. This indicates that HSFs seeded on fibrillin-1 have differentiated into smooth muscle α -actin expressing myofibroblast, which promotes focal adhesion maturation [214]. The regulation of calponin 1 by miR-612 could be one of the underlying mechanisms of HSF focal adhesion assembly regulated by extracellular fibrillin-1, via regulating myofibroblast differentiation.

Virtually no information is available in the literature about the function of miR-3185. Despite the fact that we were not able to identify and validate a target for miR-3185 in the actin-binding group or the focal adhesion group that is dysregulated in the mRNA microarray more than 2-fold, we demonstrate here that it acts in the pathway of fibrillin-1-regulated focal adhesion formation as shown by the cell culture rescue experiments. Re-inspection of the mRNA microarray data comparing HSFs seeded on rF1M-WT versus rF1M-RGA using a lower threshold (>1.4 fold change) revealed two possible candidates involved in focal adhesion formation/stability, talin 1 (1.45-fold upregulated) and vinculin (1.53-fold upregulated). Both mRNAs are predicted targets of miR-3185 using TargetScan. Although the relative changes are low, collaboratively, these two targets could potentially account for the regulation of focal adhesions [215].

In summary, the present study shows that ligation of fibroblasts with the RGD site in fibrillin-1 controls the expression of many mRNAs and miRNAs in pathways relevant to fibrillin function.

We have identified 28 new mRNA targets for several of the fibrillin-1 regulated miRNAs, and have shown that some are involved in the regulation of TGF- β signaling and in focal adhesion formation. This work shows that matrix proteins (fibrillin-1 and fibronectin) can regulate the levels of miRNAs through their interaction with integrins. These findings may prove relevant in the future for some connective tissue disorders that are caused by fibrillin-1 deficiencies, including stiff skin syndrome and Marfan syndrome.

2.6 Materials and Methods

2.6.1 Generation of recombinant expression plasmids

Full-length fibrillin-1 has the propensity to aggregate and is thus difficult to purify [216]. Due to the modular domain organization, smaller correctly folded fibrillin-1 fragments are often used to study the functional properties of different regions in fibrillin-1 [17,83,216-218]. To recombinantly produce a central human fibrillin-1 fragment containing the RGD integrin binding site and the synergy site, but not the N-terminal and C-terminal self-interaction sites, the following expression plasmids were generated. A DNA sequence coding for human fibrillin-1 domains cbEGF10 to cbEGF31 including an N-terminal signal peptide from the BM40 protein and a C-terminal octa-histidine tag were prepared with appropriate oligonucleotides based on the pCEPSP-rF18H plasmid described previously [21]. The resulting plasmid pCEPSP-rF1M-WT codes for a protein (rF1M-WT) with the sequence APLAD⁹¹⁰-Q²⁰⁵⁴GRAWSHPQFEKGASGEHHHHHHHH (human fibrillin-1 sequence is underlined). To generate a plasmid that harbors an inactive integrin binding site, the pDNSP-rFBN1-RGA plasmid described previously [188], was amplified by PCR and a *PmlI* \times *NotI* restricted fragment was subcloned into pCEPSP-rF1M-WT, resulting in plasmid

pCEPSP-rF1M-RGA. This plasmid codes for a protein (rF1M-RGA) identical to rF1M-WT except an D¹⁵⁴³A mutation in the RGD motif.

Full length fibronectin contains multiple integrin binding sites. To exclude integrin binding sites other than the RGD in the 10th type III domain and to include the synergy site in the 9th type III domain, recombinant expression plasmids were produced coding for the amino acid sequence from the 8th to 11th type III domain (A¹³⁵⁶-T¹⁷²⁰) with either the wild-type RGD sequence (FN-WT) or a mutant RGA (FN-RGA). This region of fibronectin does not include any disulfide bonds or glycosylation sites. To facilitate identification and purification of the expressed recombinant fragments, the expression plasmids were designed to include sequences coding for a V5 tag and a hexa-histidine tag (5'-GGTAAGCCTATCCCTAACCCCTCTCCTCGGTCTCGATTCTAC-3') inserted after the 11th type III domain and prior to the stop codon. The recombinant cDNA was commercially synthesized as gBlocks (Integrated DNA Technologies) and inserted into the pET-22b bacterial expression plasmid using Gibson Assembly (New England Biolabs). The correct sequence of all expression plasmids were validated by Sanger sequencing.

2.6.2 Production of recombinant proteins

Recombinant fibrillin-1 fragments were produced as secreted proteins in human embryonic kidney 293 (HEK293)-Epstein-Barr virus nuclear antigen (EBNA) cells (Invitrogen) to ensure proper disulfide bond formation and glycosylation. The pCEPSP plasmid vectors to express the recombinant fibrillin-1 fragments (rF1M-WT and rF1M-RGA) were transfected into HEK293-EBNA for episomal expression. 250 µg/mL hygromycin B (Wisent) in cell culture medium was used to select and maintain the transfected population of HEK293-EBNA cells. The transfected HEK293-EBNA cells were cultured to confluency in triple-layer flasks (Thermo Fisher Scientific) in standard Dulbecco's modified Eagle's medium (DMEM) cell culture medium (Wisent),

supplemented with 10% fetal bovine serum (Wisent). After the cells reached confluency, they were washed with 20 mM 4-(2-hydroxyethyl)-1-piperazine-ethanesulfonic acid, 150 mM NaCl, 2.5 mM CaCl₂, pH 7.4 to remove serum proteins, and cultured in serum-free DMEM medium to produce conditioned medium containing the secreted proteins.

The fibronectin recombinant fragments were produced in *E. coli*, which was feasible due to the absence of disulfide-bonds and N-linked glycosylation in the recombinant proteins. The recombinant pET-22b plasmids were amplified in NEB-5 α (*recA1* negative; New England Biolabs). For protein production, the plasmids were transformed into BL21 (DE3) cells (Thermo Fisher Scientific). 2 mM of isopropyl- β -D-thiogalactoside (IPTG) was used to induce protein expression when the culture medium reached ~0.6-0.8 optical density at 600 nm.

2.6.3 Purification of recombinant proteins

The recombinant fibrillin-1 and fibronectin fragments were chromatographically purified to homogeneity in a two-step protocol as described previously [219]. Briefly, the histidine-tagged recombinant fragments were first purified by immobilized metal affinity chromatography using an increasing imidazole gradient for elution. The eluted recombinant fragments were further purified in a second step by gel filtration chromatography (Superose 12). The BCA protein assay kit (Thermo Fisher Scientific) was used to determine the concentration of the purified proteins. The recombinant fragments were analyzed by gel electrophoresis and Coomassie Blue staining under reducing and non-reducing conditions showing the expected molecular masses (Supplemental Figure S2.1B). Typical yields were ~1mg/L cell culture medium for the fibrillin-1 fragments and ~0.65mg/L culture medium for the fibronectin fragments.

2.6.4 Cell Culture

2.6.4.1 Human skin fibroblasts

HSFs were isolated from the foreskin of healthy boys (two to five years of age), following a standard circumcision procedure. This procedure was approved by the Montreal Children's Hospital Research Ethics Board (PED-06-054), and written consent of the patient's parents was obtained. Cells were cultured in DMEM, supplemented with 10% v/v fetal bovine serum, 100 µg/mL penicillin, 100 µg/mL streptomycin, and 2 mM glutamine (Wisent) at 37°C in a 5% CO₂ atmosphere. HSFs from two human donors were used between passages 4 and 8 throughout this study. For all experiments, ID 595 was used, and some experiments additionally included ID 222.

Prior to seeding HSFs for an experiment, the cells were serum-starved to remove all growth factors and other components in fetal bovine serum, as their presence might have interfered with cell signaling pathways. For this purpose, HSFs were washed twice with phosphate-buffered saline and thereafter kept on serum-free culture medium (DMEM with supplements) for 24 h. Cell culture plates or chamber slides were coated with the fibrillin-1 fragments rF1M-WT and rF1M-RGA at a concentration of 25 µg/mL in TBS overnight. This concentration was determined as optimal in promoting cell adhesion in a real-time cell attachment assay with increasing coating concentrations (Supplemental Figure S2.3). For some experiments, cell culture plates or chamber slides were coated with poly-D-lysine (100 µg/mL, Sigma), recombinant fibronectin fragments FN-WT and FN-RGA (25 µg/mL), or the culture medium was supplemented with TGF-β1 (5 ng/mL, PeproTech) as further controls.

For trypsinization, the HSFs were washed twice with phosphate-buffered saline and incubated with 0.25% trypsin-EDTA (Wisent) for exactly 3 min. Serum-free medium was added to the dissociated cells and the cell suspension was spun down for 5 min at $1,200 \times g$. The cell pellet was resuspended in serum-free medium and centrifuged for 5 min at $1,200 \times g$. The short incubation time with trypsin and the two centrifugation steps ensured limited enzymatic activity of trypsin under serum-free conditions to minimize proteolytic degradation of cell surface receptors. After coating, the plates were washed twice with TBS, and HSFs were seeded in serum-free media with supplements. Light microscopic images of HSFs were recorded using a PowerShot A640 digital camera (Canon).

2.6.4.2 MSU-1.1 cells

The experimental validation of interactions between miRNAs and mRNAs requires efficient transfection of two vectors together with miRNA mimics, which can be achieved with cell lines. We tested MSU-1.1, a human skin fibroblast cell line [220] by real-time qPCR for its mRNA expression pattern of relevant target genes compared to primary fibroblasts. Generally, the expression of the tested target mRNAs was similar to the expression by primary fibroblasts. Therefore, MSU-1.1 fibroblasts were utilized for the experimental miRNA target validation. The MSU-1.1 cells were cultured under conditions as described for primary fibroblasts.

2.6.5 Electric Cell Substrate Impedance Sensing

Electric-cell substrate impedance sensing (ECIS; ZTheta, Applied Biophysics) is a biophysical method to electronically monitor cell attachment and spreading in real-time [221]. As the cells attach to the coated protein, a change in impedance is measured to analyze cell attachment in real-

time. 40,000 HSFs were seeded per well in serum-free DMEM. The impedance was monitored over 6 h. All measurements were performed at a frequency of 32,000 and 64,000 Hz. To determine the optimal protein coating concentration for subsequent cell attachment and spreading assays, a concentration series from 0 to 50 $\mu\text{g/mL}$ rF1M-WT or FN-WT was used to coat 96W20idf plates (Applied Biophysics) overnight at 4°C (Supplemental Figure S2.3). 25 $\mu\text{g/mL}$ coating concentration produced optimal cell binding for both recombinant fragments, and thus this coating concentration was used for the experiments in this study.

2.6.6 RNA extraction

Total RNA was extracted from HSFs at various time points to study miRNA and mRNA levels by microarray and real-time quantitative polymerase chain reaction (qPCR). Total RNA includes miRNAs and mRNAs and the extraction was performed using the miRNeasy Mini Kit (Qiagen) according to the manufacturer's instructions. 1,000,000 HSFs were seeded on 10 cm in diameter cell culture dishes (Sarstedt) to ensure sufficient RNA yields.

2.6.7 Microarray analysis

Microarray analysis was performed for miRNAs and mRNAs using miRNA 3.0 and Human Gene 2.0 chips from Affymetrix, respectively. The miRNA 3.0 chips contained 19,724 probe sets from 153 different organisms, including 1,733 human mature miRNA and 1,658 human pre-miRNA probe sets. This covers all miRNA sequences in the miRNA database miRBase (Release 17, April 2011). The Human Gene 2.0 chips cover 30,654 human mRNA probe sets. The microarray analysis including RNA quality control, complementary DNA (cDNA) preparation and labeling and the

actual array were conducted at the Genome Quebec Innovation Centre at McGill University. RNA samples were prepared after 24 h of interaction between HSFs and the recombinant fibrillin-1 fragments rF1M-WT and rF1M-RGA. The same RNA samples were submitted in biological quadruplicates for the miRNA and mRNA microarray analysis. The raw data from the microarrays was normalized and quality control was performed using the Expression Console software (Affymetrix). The Transcriptome Analysis Console software (Affymetrix) was applied to perform statistical tests for differential expression of expressed genes and to visualize fold changes of miRNAs and mRNAs. Normalized intensities from rF1M-WT and rF1M-RGA were compared using one-way ANOVA. After executing ANOVA, multi-testing correction was performed using the Benjamini-Hochberg FDR-controlling procedure for all the expressed genes [222]. All p-values indicated refer to FDR-adjusted p-values.

The microarray data for this study have been submitted to the NCBI's Gene Expression Omnibus database <https://www.ncbi.nlm.nih.gov/geo> [223,224], and are accessible through GEO Series accession number GSE82085

<https://www.ncbi.nlm.nih.gov/geo/query/acc.cgi?token=wvsjockubnadrst&acc=GSE82085>.

To determine common pathways in which genes are controlled by the differentially regulated miRNAs, pathway analysis was conducted using the DIANA miRPath v.2.0 tool [197]. This bioinformatics tool searches the predicted target genes of the identified, differentially regulated miRNAs and analyzes their combinatorial effects in KEGG, a database resource for biological pathways. The DAVID Bioinformatics Resources 6.7 (david.abcc.ncifcrf.gov/) [225] allows searches of molecular functions of differentially expressed mRNAs to determine enriched themes and relevant KEGG pathways.

2.6.8 Quantification of miRNA and mRNA

For reverse transcription of miRNAs, the miScript II RT kit (Qiagen) was used, according to the manufacturer's instructions. 1 µg of total RNA was typically used for reverse transcription, if not limited by a low RNA yield. For reverse transcription of mRNAs, the Super Script III First-Strand Synthesis System for RT-PCR (Life Technologies) was used as detailed in the manual. 1 µg of total RNA was used, if RNA yield was sufficient.

For the quantification of miRNAs, real-time qPCR was performed using the miScript SYBR Green PCR Kit according to the manufacturer's instructions (Qiagen). miScript Primer Assays were obtained from Qiagen for human miR-29b-1* (cat. no. MS00009289), miR-424* (cat. no. MS00009688), miR-503 (cat. no. MS00033838), miR-612 (cat. no. MS00005047), miR-1208 (cat. no. MS00014196), miR-1231 (cat. no. MS00031290), miR-1914* (cat. no. MS00016548), miR-3185 (cat. no. MS00020930), miR-4443 (cat. no. MS00041272) and miR-4521 (cat. no. MS00040796). RNU6 (cat. no. MS00033740) and SNORD61 (cat. no. MS00033705) were used as reference genes. The real-time cycler (Applied Biosystems, Step-One™ Real-Time qPCR system) was programmed to an initial PCR activation step for 15 min at 95°C and 40 cycles of a 3-step cycling program: 1) Denaturation (94°C for 15 s), 2) Annealing (55°C for 30 s), 3) Extension (70°C for 34 s). Melt-curve analysis was performed after each run to determine the specificity of the detected product.

For quantification of mRNA, cDNA prepared using the Super Script III First-Strand Synthesis System was used for real-time qPCR with the SYBR Green Select Master Mix (5 µL) (Life Technologies), and 100-400 nM forward and reverse primers (Supplemental Table 2.1). GAPDH

and RPL13A were used as reference genes. The real-time cycler was programmed to an initial PCR activation step for 2 min at 50°C and afterwards 2 min at 95°C and 40 cycles of a 3-step cycling program: 1) Denaturation (95°C for 15 s), 2) Annealing (58°C for 15 s), 3) Extension (72°C for 1 min). Melt-curve analysis was performed after each run to determine the specificity of the detected product.

2.6.9 Interaction studies between miRNAs and mRNAs

2.6.9.1 Bioinformatics prediction

Bioinformatics analysis utilizing the miRanda algorithm was conducted to predict interactions between miRNAs and mRNAs [198]. This algorithm allows searches for the complementarity between miRNAs and 3' UTRs of mRNAs and integrates thermodynamics of the binding site as well as conservation across species. The predicted target sites were scored using a regression model, the mir support vector regression (mirSVR). mirSVR scores miRNAs according to their likelihood of mRNA downregulation. The regression model comprises features of the predicted miRNA/target site duplex, local and global context features. Local features include adenine/uracil composition near the target sites and secondary structure accessibility. Global features comprise the length of the UTR, relative position of the target sites relative to UTR ends as well as the conservation level of the block containing the target site.

2.6.9.2 Experimental validation

The well-established mirTrap system (Clontech) was used to experimentally validate predicted interactions between miRNAs and mRNAs [199-201]. The system uses a dominant-negative form of a subunit of RISC, which traps the miRNA and its mRNA targets. This mutant subunit contains

a FLAG epitope (DYKDDDDK) and thus the entire complex can be immunoprecipitated, and target mRNAs can subsequently be identified by real-time qPCR.

Transfection, lysis, immunoprecipitation and RNA isolation were performed according to the manufacturer's instructions. MSU-1.1 cells at a density of 1,500,000 cells/10 cm in diameter culture plates were used for transfection with miRNA mimics and the pMirTrap vector. The transfection efficiencies were controlled with miR-132 co-transfected with the pMirTrap Control and the pMirTrap vectors. The transfected control cells were used to analyze the fold enrichment of a fluorescent quantifiable miR-132 target coded on the pMirTrap control vector. After the immunoprecipitation, the RNA was isolated from the immunoprecipitated material bound to the anti-FLAG beads ("After IP") and from the pre-immunoprecipitation control ("Before IP") using the NucleoSpin RNA XS kit (Macherey-Nagel). The mRNAs of which the levels were ≥ 20 -fold more in "After IP" than in "Before IP" were considered to be bound by the transfected miRNA.

2.6.9.3 miRNA overexpression and inhibition studies

miRNA mimics and inhibitors were commercially obtained from Qiagen. 1) *Mimics*: Syn-hsa-miR-29b-1-5p (cat. no. MSY0004514), Syn-hsa-miR-503-5p (cat. no. MSY002874). 2) *Inhibitors*: Anti-hsa-miR-612 (cat. no. MIN0003280), Anti-hsa-miR-1208 (cat. no. MIN0005873), Anti-hsa-miR-1231 (cat. no. MIN0005586), Anti-hsa-miR-3185 (cat. no. MIN0015065). miRNA mimics and inhibitors were transfected either in 8-well chamber slides or in 12-well plates. The procedure is described in detail for the 8-well chamber slides. Alternate volumes or cell numbers for the transfection in 12-well plates are indicated in brackets. Shortly before the transfection, 10,000 (100,000) HSFs were seeded per well of an 8-well chamber slide in 250 (1,100) μL of serum-free DMEM. 19 ng (75ng) miRNA mimic or 190 ng (750 ng) inhibitor was diluted in 50 μL (100 μL) DMEM. This resulted in a final miRNA concentration of 5 nM (mimic) or 50 nM (inhibitor) after

adding the complexes to the cells. 1.5 μ L (6 μ L) of HiPerfect Transfection Reagent (Qiagen) were added to the diluted miRNA and incubated for 10 min at room temperature to allow for the formation of transfection complexes. These complexes were added drop-wise onto the cells. The cells were incubated with the transfection complexes under regular growth conditions and analyzed after 48 h.

2.6.10 Indirect immunofluorescence

Indirect immunofluorescence was performed as previously described [188]. Briefly, HSFs were grown in 8-well chamber glass slides (Thermo Fisher Scientific) at densities of 10,000 - 75,000 cells/well, depending on the experiment. After fixation with 70% methanol/30% acetone, and blocking with 10% v/v normal goat serum, the cells were incubated with one of the following primary antibodies. Mouse monoclonal anti- β -actin (1:200; Sigma, cat. no. A4700), rabbit monoclonal anti-phosphorylated FAK antibody (Tyr397) (1:400; Abcam, cat. no. ab81298), and anti-p-Smad2 antibodies (Ser465/467) (1:500, Millipore, cat. no. AB3849). Secondary antibodies used were 1:100 diluted goat anti-rabbit or goat anti-mouse conjugated to Alexa Fluor 488 (Life Technologies, cat. no. A11008 and A11029), and goat anti-rabbit or goat anti-mouse conjugated to Cy3 (Jackson ImmunoResearch Laboratories, cat. no. 111-165-003 and 111-166-003). Nuclear counterstaining was performed with 4', 6-diamidino-2-phenylindole (DAPI).

To unify the shape of HSFs, which can influence focal adhesion formation, Y-shape micropatterns with 1,600 μ m² area (Cytoo) were used. 25 μ g/mL rF1M-WT and rF1M-RGA were coated for 2 h at room temperature, prior to seeding 60,000 HSFs in 4 mL medium in 35mm petridishes. After 24 h, HSFs were fixed with 70% methanol/30% acetone and stained as described above.

All images were recorded with the Zen 2012 software (Zeiss) using an Axio Imager M2 microscope (Zeiss) equipped with an ORCA-flash4.0 camera (Hamamatsu).

2.6.11 Quantification of p-Smad2 and focal adhesions

Quantification of p-Smad2 and of focal adhesions were performed using the ImageJ software [226]. To quantify p-Smad2, the corrected total cell fluorescence was determined. An outline was drawn around each cell and area and mean fluorescence were measured. The background was determined in areas without cells. The corrected total cell fluorescence was calculated: CTCF = (mean fluorescence intensity of the cell - mean background intensity) \times area of selected cell.

The quantification of focal adhesion was based on an established procedure which was adjusted in the following manner [227]. To decrease the background, the images were processed using “*Subtract Background*” with the sliding paraboloid option and 50 pixels rolling ball radius. To enhance the local contrast, the CLAHE plugin (Contrast Limited Adaptive Histogram Equalization) was used with these parameters: block size = 19, histogram bins = 256, maximum slope = 6 [228]. To optimize the quality of images for particle quantification, “*Mathematical exponential*” (EXP), “*Brightness & Contrast*”, and “*Threshold*” were sequentially applied. The “*min and max*” values of “*Brightness & Contrast*” and “*Threshold*” were derived from the average of the automatic values obtained from multiple images. The average “*min and max*” values were applied to all images. Finally, “*Analyze Particles*” produced the number, the average size and the total area of focal adhesions.

Authors Contributions

Study conception and design: KAZ, RMZ, DPR; Acquisition of data: KAZ, RMZ, HK, AH;

Analysis and interpretation of data: KAZ, RMZ, HK, AH, DPR; Draft manuscript: KAZ, RMZ;

Critical revision: KAZ, RMZ, HK, AH, DPR;

Dieter P Reinhardt was the project director involved in all aspects and phases of the work.

Conflict of Interest

The authors do not have a conflict of interest.

2.7 Acknowledgements

This study was financially supported by the Natural Sciences and Engineering Research Council of Canada (RGPIN-2016-06278), the Heart and Stroke Foundation Canada (G-16-00014634), the Canadian Institutes of Health Research (MOP-137091), the Fonds de recherche du Québec – Nature et technologies, and the German Studienstiftung des Deutschen Volkes.

2.8 Figures and Tables

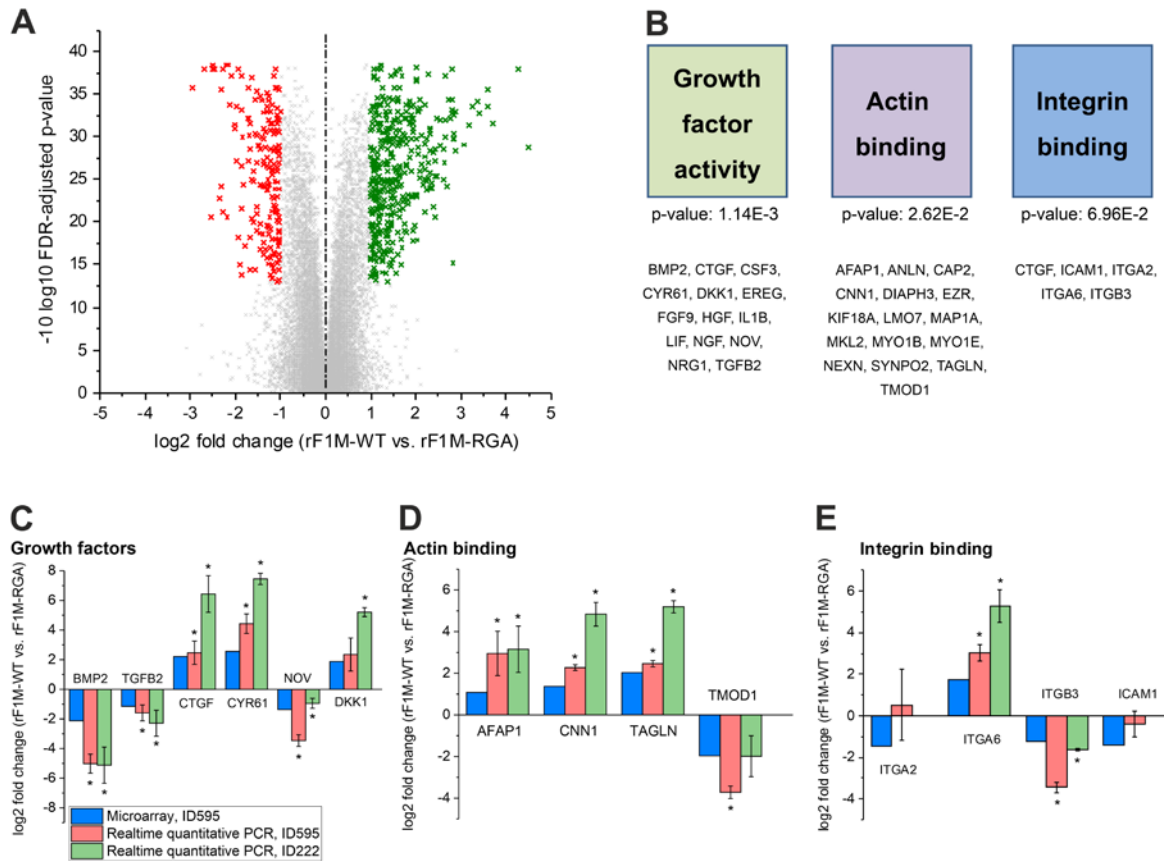


Fig. 2.1 Comparative analysis of fibroblast mRNA expression levels

(A) Microarray analysis was conducted for mRNAs in biological quadruplicates for each condition (rF1M-WT vs. rF1M-RGA) using the Gene Chips Human Gene 2.0 (Affymetrix). Differential mRNA expression between the two conditions after 24 h is shown as a volcano plot. Statistically significant upregulated mRNAs are shown in green and downregulated mRNAs in red. Only mRNAs with a fold change of <-2 or >2 are considered. 520 differentially regulated mRNAs were detected. (B) Functional annotation was conducted to identify enriched biological themes for the 520 differentially expressed mRNAs using DAVID Bioinformatics Resources 6.7 (david.abcc.ncifcrf.gov) [225]. A selection of Gene Ontology (GO) terms of molecular function is shown including the respective p-values. Dysregulated mRNAs within the respective GO groups are listed below. (C-E) Microarray validation by qPCR was conducted for selected mRNAs in each of the functional groups indicated in (B). The functional groups include growth factors (C), actin binding (D) and integrin binding (E). HSFs from two different human donors were used to validate the results of the microarray (ID 595, ID 222). ID 595 was used in the microarray. The mRNA levels are shown as log₂ fold changes of rF1M-WT vs. rF1M-RGA. Values are indicated as mean values of biological triplicates with three technical replicates each \pm standard error of the mean. Student's t-test was performed to assess statistical significance (* p-value < 0.05).

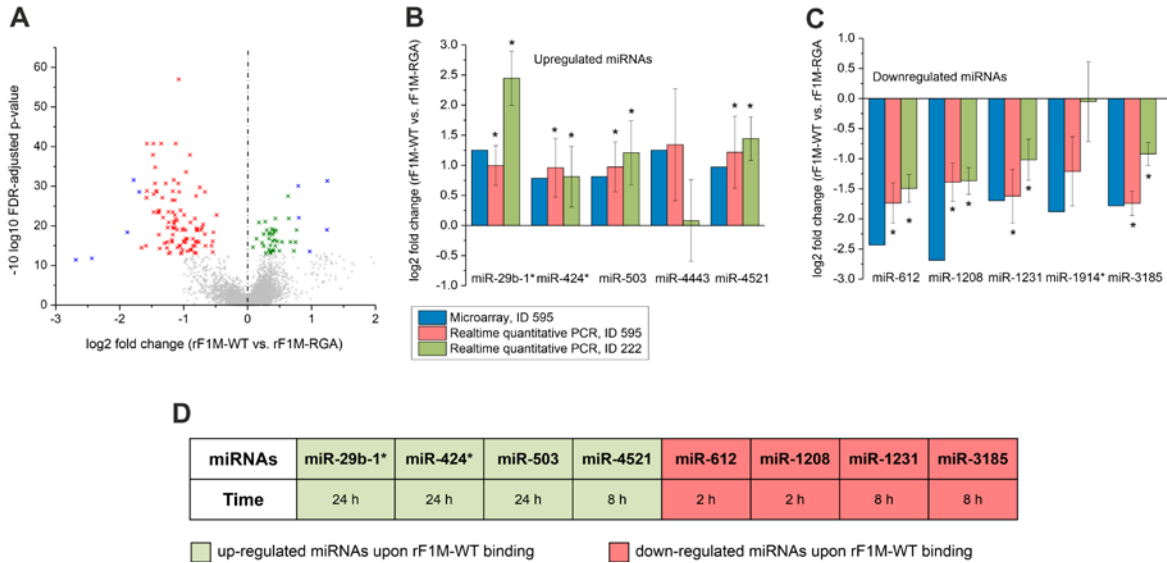


Fig. 2.2 Comparative analysis of fibroblast miRNA expression levels

(A) Microarray analysis of HSFs (ID 595) was conducted for miRNAs in biological quadruplicates for each condition using miRNA 3.0 chips (Affymetrix). RNA samples from the same HSFs (ID 595) exposed to the recombinant fibrillin-1 fragments for 24 h used for the mRNA microarray analysis (see Fig. 2.1A) were analyzed. Differential expression of miRNAs between the two conditions (rF1M-WT vs. rF1M-RGA) after 24 h of cell growth is shown as a volcano plot. Statistically significant upregulated miRNAs are shown in green and downregulated miRNAs in red. 129 differentially regulated miRNAs were detected. Ten miRNAs were chosen for further studies (highlighted in blue) based on high fold changes, statistical significance and relevant pathways. (B,C) Microarray data for the selected upregulated (B) and downregulated (C) miRNAs were validated by qPCR. HSFs from two different human donors were used to validate the microarray results (ID 595, ID 222). The miRNA levels are shown as log₂ fold changes of rF1M-WT vs. rF1M-RGA. Values are indicated as mean values of biological triplicates with three technical replicates each \pm standard error of the mean. Student's t-test was performed to assess statistical significance (* p-value < 0.05). (D) Time course analysis (2, 4, 8 and 24 h after cell seeding on rF1M-WT or rF1M-RGA) by qPCR for the selected differentially regulated miRNAs identified in the microarray. "Time" represents the starting time point when consistent and significant differential miRNA regulation occurred. Green boxes represent the up-regulated and red boxes the down-regulated miRNAs upon HSFs binding to rF1M-WT.

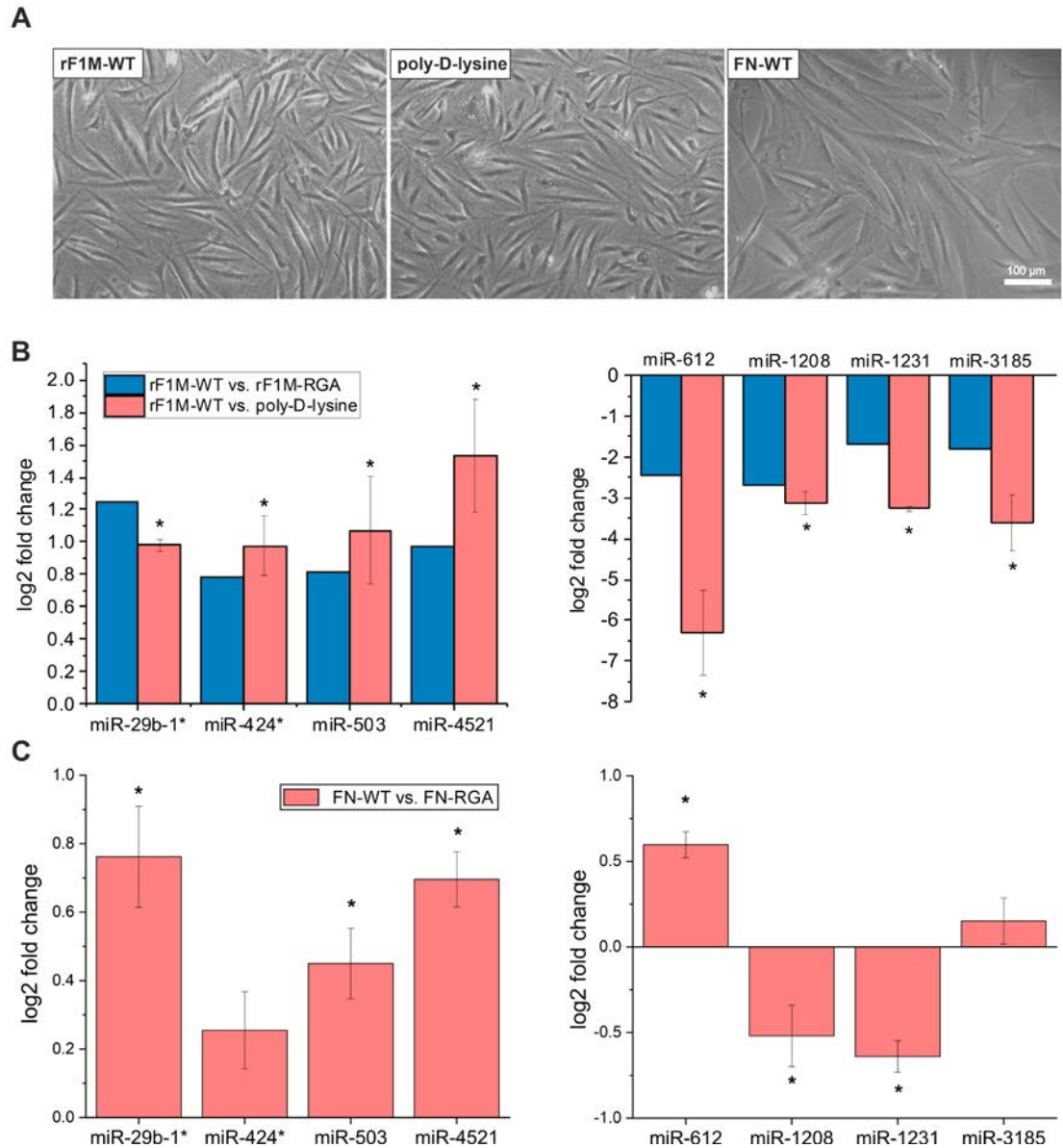


Fig. 2.3 Specificity of fibrillin-1 mediated miRNA regulation

(A) Light microscopic images of HSFs (ID 595) grown for 24 h on rF1M-WT, poly-D-lysine, or FN-WT coated culture dishes as indicated. (B) qPCR analysis to determine the specificity of miRNA regulation mediated by fibrillin-1 exemplified with selected miRNAs. miRNA levels were determined for HSFs grown for 24 h on rF1M-WT versus poly-D-lysine coated plates (red columns). For comparison, rF1M-WT versus rF1M-RGA data for 24 h are shown from the miRNA microarray in Figure 2.2A (blue columns). Upregulated miRNAs in the microarrays are shown on the left panel, downregulated miRNAs on the right panel. (C) Corresponding miRNAs level were determined 24 h after HSFs interacting with FN-WT compared to FN-RGA controls. The miRNA levels are shown as log₂ fold changes of rF1M-WT versus poly-D-lysine, rF1M-WT versus rF1M-RGA, and FN-WT versus FN-RGA, respectively. Values are indicated as mean values of biological triplicates with three technical replicates each \pm standard error of the mean. Student's t-test was performed to assess statistical significance (* p-value < 0.05).

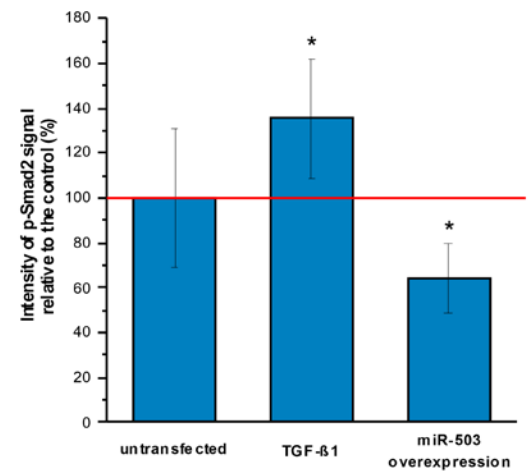
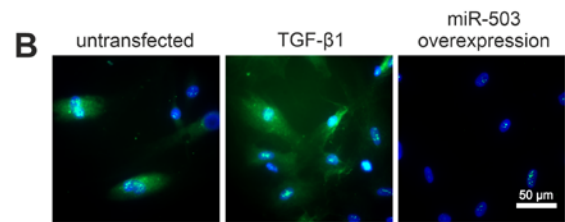
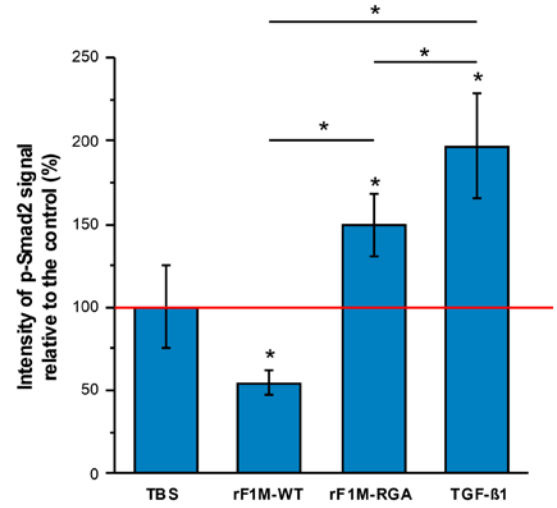
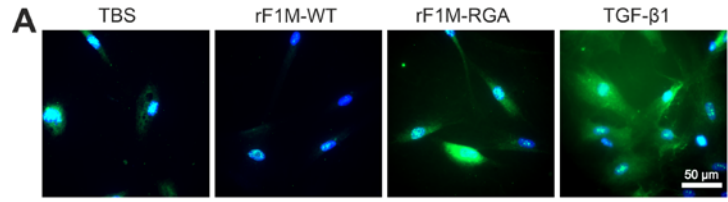


Fig. 2.4 TGF- β signaling upon interaction with fibrillin-1 and overexpression of miR-503

(A) Immunofluorescence staining for p-Smad2 was conducted at 24 h after cell seeding. 10,000 HSFs (ID 595) were seeded per well of an 8-well chamber slide coated with rF1M-WT or rF1M-RGA at 25 $\mu\text{g}/\text{mL}$ or TBS buffer as a control. As a positive control, cells were treated with TGF- β 1 (5 ng/mL) for 24 h. Representative images for each condition are shown. The intensity of the p-Smad2 signal 24 h after cell seeding was quantified in the lower panel. Each condition was analyzed in biological duplicates. Five different images were recorded for each duplicate. Untreated cells seeded on TBS control wells were used as reference set to 100% for comparison with all other conditions (red line). Statistical analysis was performed using Student's t-test (* p-value < 0.05). Statistical significance is indicated for each value relative to the control reference, indicated by asterisks above the error bars. Statistically significant differences between the rF1M-WT, rF1M-RGA and TGF- β 1 samples are indicated by asterisks above horizontal lines. (B) Immunofluorescence staining for p-Smad2 was conducted 48 h after cell seeding under conditions as in (A). Cells were transfected with miR-503 mimics at the time of seeding or treated with TGF- β 1 (5ng/mL) for 48 h. An untransfected control was included as indicated. Representative images for each condition are shown. Quantification of the intensity of the p-Smad2 signals are shown in the lower panel. Each condition was analyzed in biological duplicates. Five different images were recorded for each duplicate. Untransfected cells seeded on TBS control wells were used as a reference for comparison with the other conditions (100%; red line). Statistical analysis was performed using Student's t-test (* p-value < 0.05).

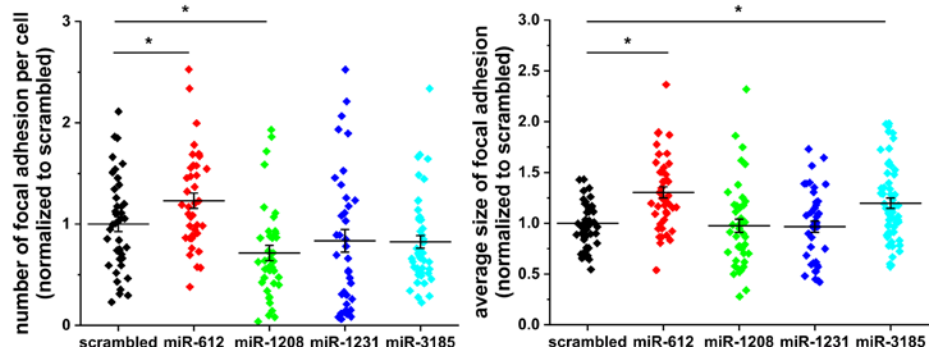
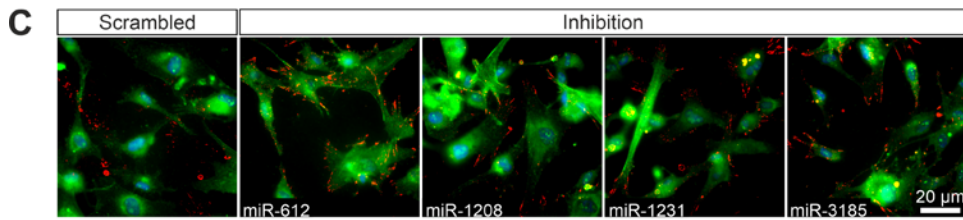
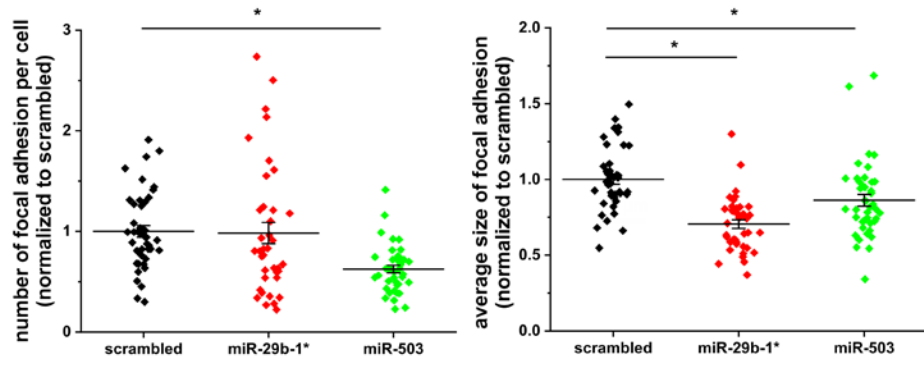
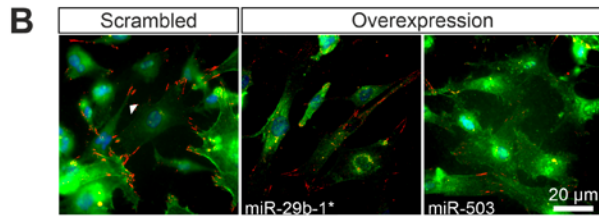
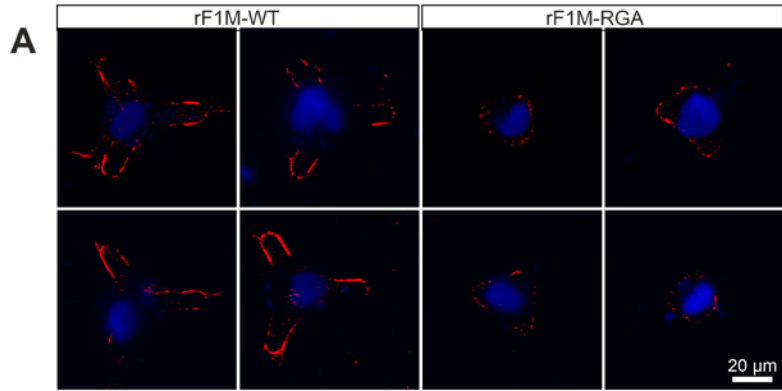


Fig. 2.5 Consequences of fibroblast interaction with fibrillin-1 and of miRNA modulation on focal adhesion formation

(A) Immunofluorescence staining of phosphorylated FAK (red) was conducted 24 h after HSF seeding on 1,600 μm^2 Y shape micropattern (Cytoo) coated with either rF1M-WT or rF1M-RGA at 25 $\mu\text{g}/\text{mL}$. Representative images for each condition are shown. (B) Immunofluorescence staining for actin (green) and phosphorylated FAK (red) was conducted after 48 h after HSF seeding on non-coated chamber slides. For each condition, cells were either transfected with miRNA mimics for miR-29b-1* and miR-503 or inhibitors for miR-612, miR-1208, miR-1231 and miR-3185 at the time of seeding. A scrambled control was included. Representative images for each condition are shown. Quantification of the number (left panels) and average sizes (right panels) of focal adhesion per cell normalized to the respective scrambled control are shown below each immunofluorescence panel. A total of 60 images from biological triplicates were quantified. Each bar represents the mean \pm standard error of the mean. Statistical analysis was performed using Student's t-test (* p-value < 0.05).

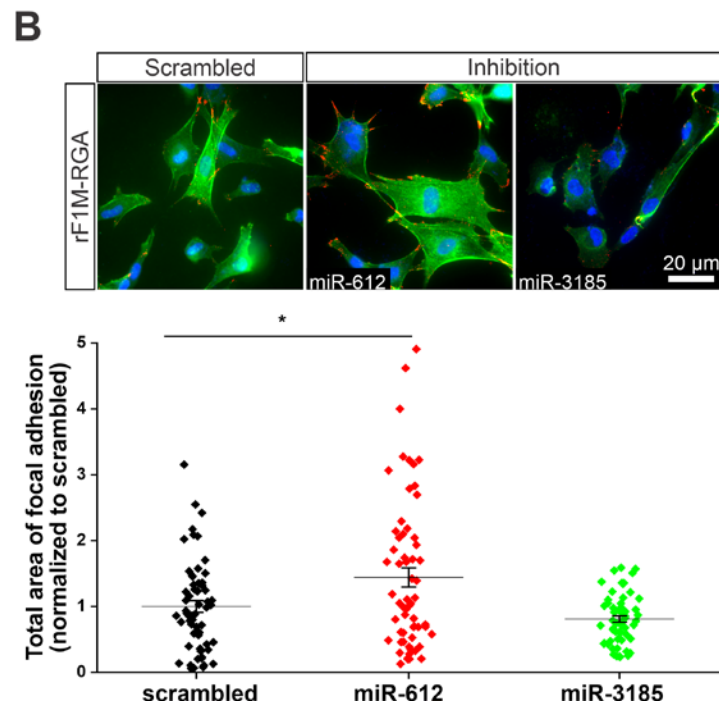
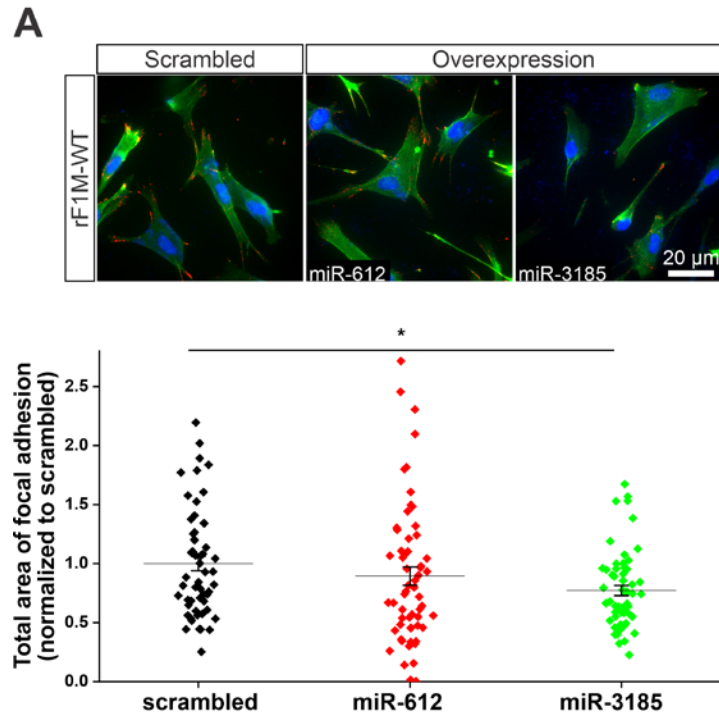


Fig. 2.6 Rescue experiments of fibrillin-1 regulated miRNA on focal adhesion formation

(A) HSFs seeded on rF1M-WT-coated chamber-slides (as described as Fig. 2.5) were transfected with miR-612 or miR-3185 mimics, or with a scrambled miRNA as control. (B) HSFs seeded on rF1M-RGA coated slides were transfected with inhibitors of miR-612, miR-3185, or a scrambled control. For both (A) and (B), immunofluorescence staining (top panels) for phosphorylated FAK (red) and actin (green) was conducted after 48 h, and the phosphorylated FAK signals were quantified (bottom panels) as total area of focal adhesions per cell normalized to the respective scrambled control. The data represent three independent experiments with HSFs from two different donors and different passage numbers. A total of 60 images for each condition were quantified. Each bar represents the mean \pm standard error of the mean. Statistical analysis was performed using Student's t-test (* p-value < 0.05).

Supplemental Figure S1

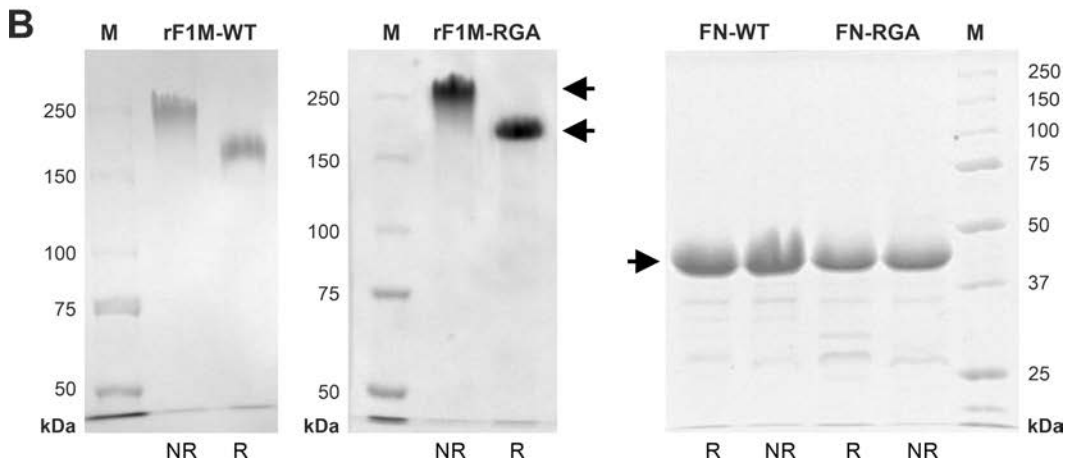
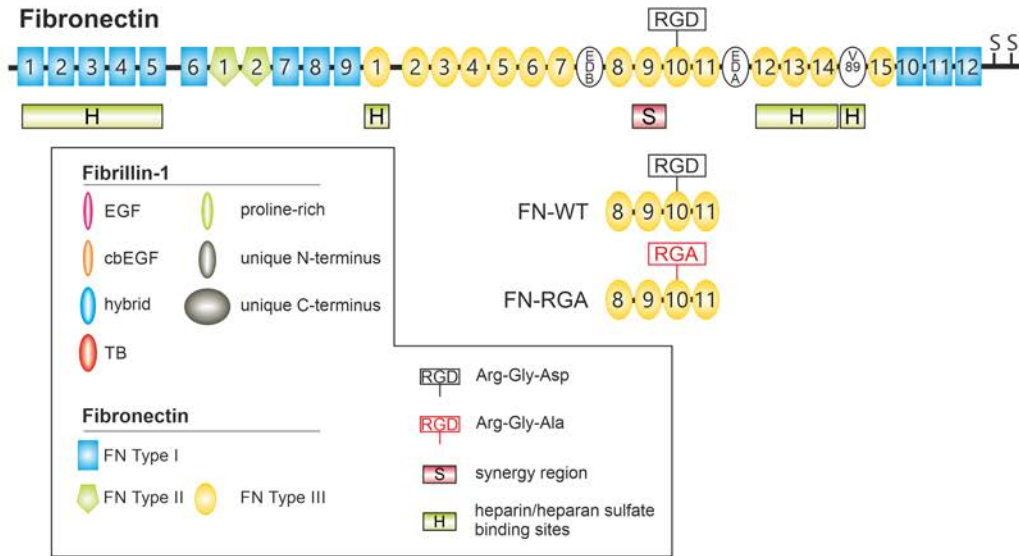
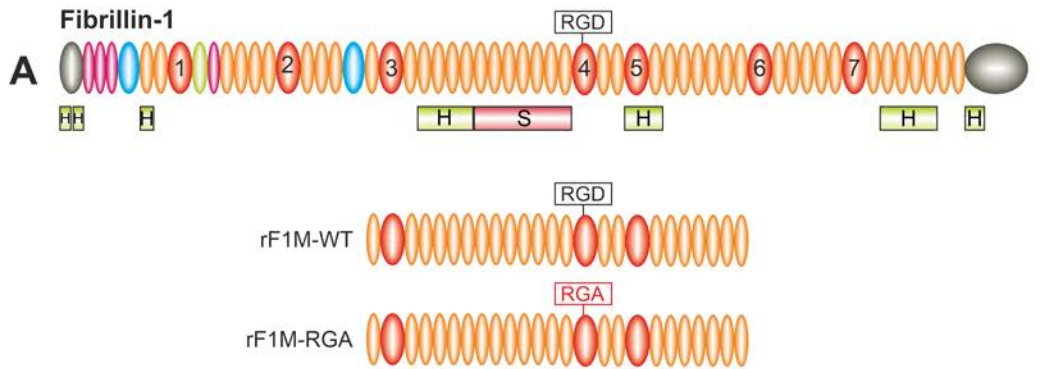


Fig. S2.1 Representation and purification of fibrillin-1 and fibronectin and their recombinant fragments

(A) The domain organization of human fibrillin-1 and fibronectin is shown. The RGD cell binding sites, the synergy region (S), and the heparin/heparan sulfate-binding sites (H) are indicated. The recombinant fibrillin-1 fragment and fibronectin control fragments used in this study are shown relative to the full-length proteins. Each pair consists of the wild-type fragment harboring an RGD integrin binding site, and an inactive RGA mutant control. **(B)** The purified fibrillin-1 (left panels) and fibronectin (right panel) fragments were analyzed on 6% or 10% SDS-PAGE, respectively, under non-reducing (NR) or reducing (R) conditions. Minor contaminating bands in the fibronectin fragment preparations are breakdown products of the fragments (validated by Western blotting).

Supplemental Figure S2

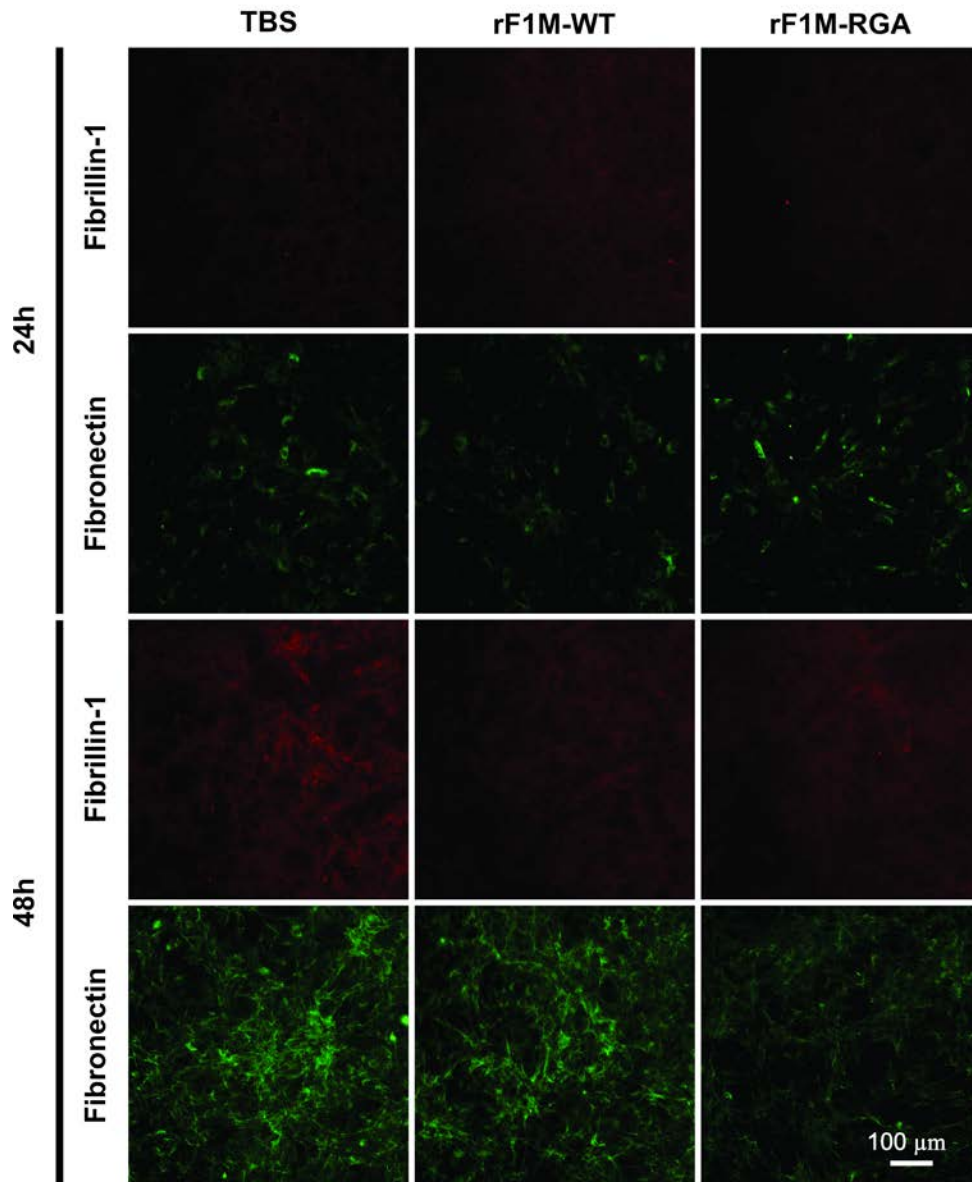


Fig. S2.2 Analysis of endogenous fibrillin-1 and fibronectin levels of HSF

To analyze the levels of endogenous fibrillin-1 and fibronectin levels under the experimental conditions used throughout this study, 75,000 serum-starved HSFs (ID 595) were seeded in 8-well chamber slides either uncoated (TBS) or coated with 25 $\mu\text{g}/\text{mL}$ rF1M-WT or rF1M-RGA and grown for 24 h or 48 h in serum-free DMEM medium. Indirect immunofluorescence with specific antibodies against fibrillin-1 (red) and fibronectin (green) was performed. Note the very low levels of fibrillin-1 and fibronectin staining and the complete absence of fibers at 24 h of cell growth.

Supplemental Figure S3

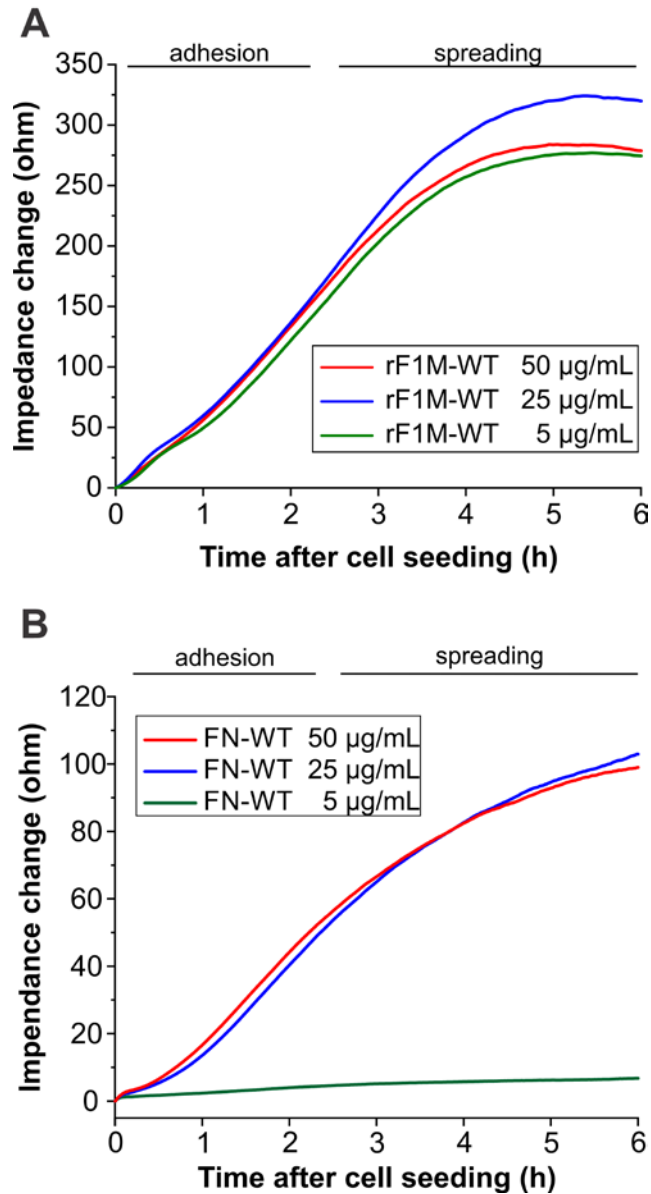


Fig. S2.3 Concentration dependency in real-time electric cell substrate impedance sensing (ECIS)

Real-time ECIS was used to determine the interaction between HSFs and (A) rF1M-WT or (B) FN-WT. 96 well plates were coated with rF1M-WT or FN-WT at concentrations from 5-50 µg/mL to determine the optimal concentration of the recombinant proteins to mediate cell attachment and spreading. Representative graphs are shown for 5, 25 and 50 µg/mL rF1M-WT or FN-WT with 40,000 cells per well. The estimated time of adhesion (0-2 h) and spreading (>2 h) is indicated.

Supplemental Figure S4

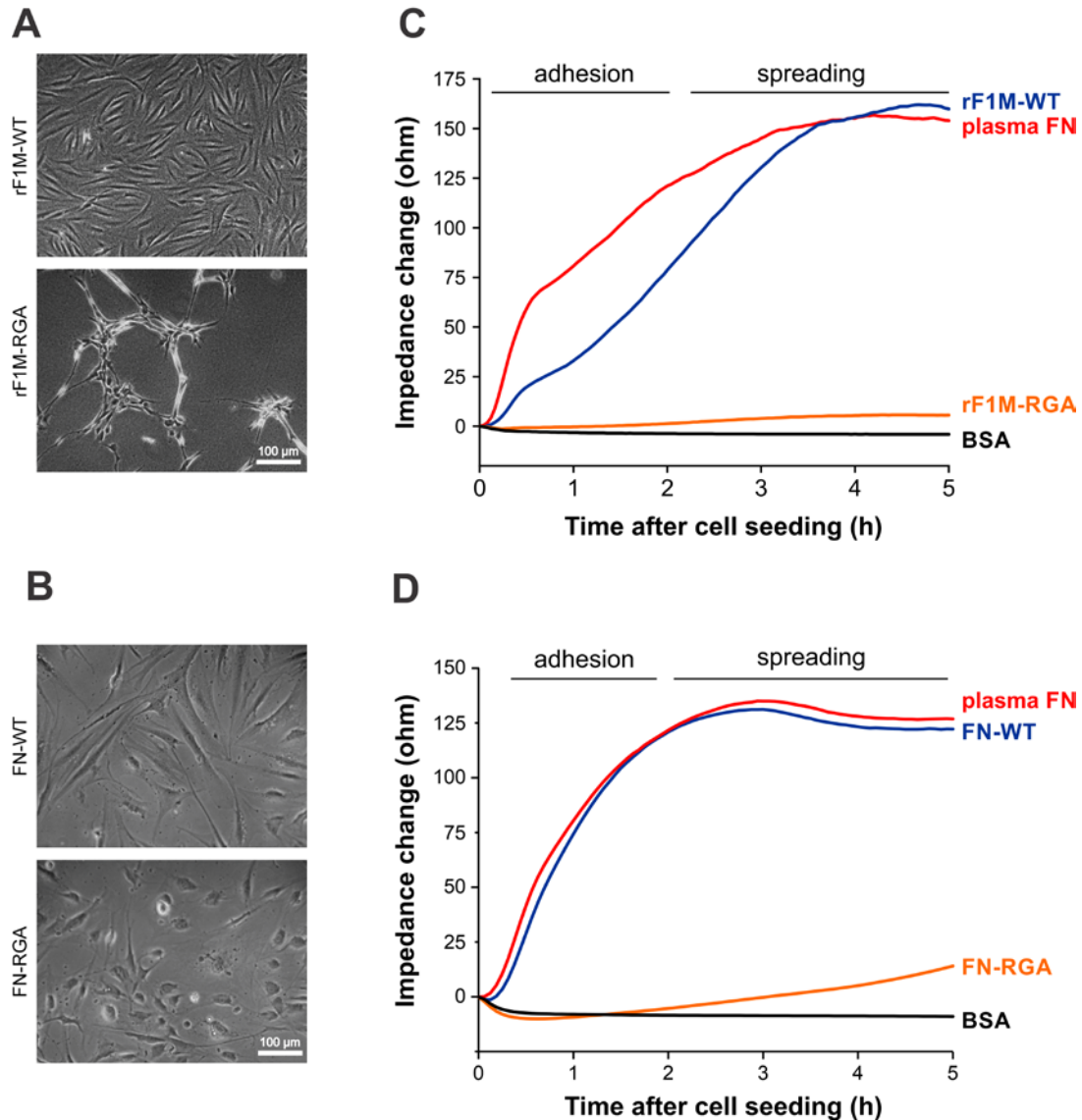


Fig. S2.4 Analysis of HSF interaction with the recombinant fibrillin-1 and fibronectin fragments.

(A, B) Cell morphologies of HSFs grown for 24 h on culture dishes coated with (A) rF1M-WT or rF1M-RGA, or (B) FN-WT or FN-RGA. (C, D) Quantification of HSF attachment and spreading by real-time ECIS analysis. 96-well plates were coated with (C) rF1M-WT or rF1M-RGA, or (D) FN-WT, FN-RGA, plasma fibronectin or BSA at a concentration of 25 $\mu\text{g/mL}$. 40,000 HSFs were seeded in each well. The estimated time of adhesion (0-2 h) and spreading (>2 h) is indicated on top.

Supplemental Figure S5

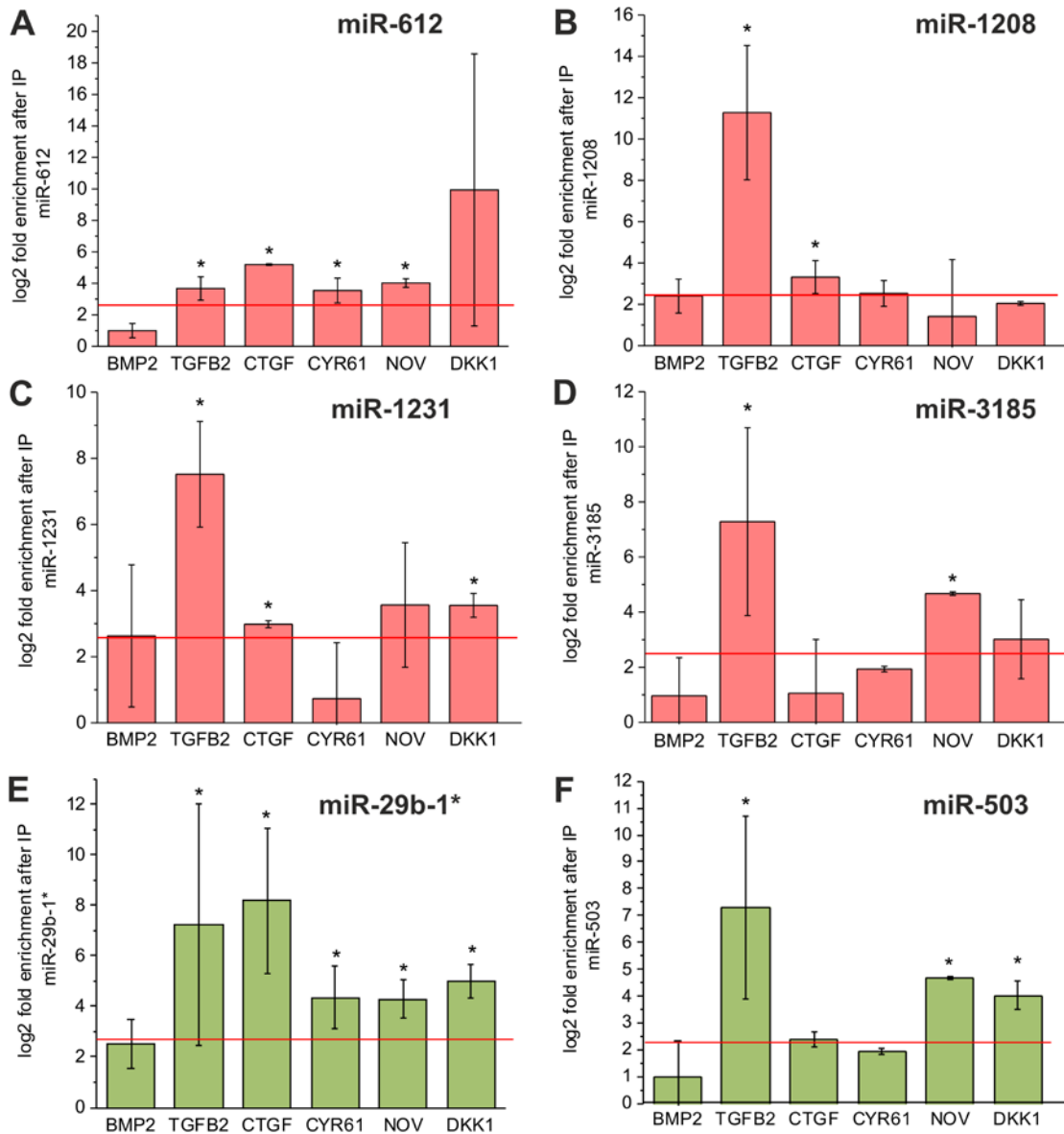


Fig. S2.5 Interactions between miRNAs and growth factor mRNAs

(A-F) The interactions between miR-612 (A), miR-1208 (B), miR-1231 (C), miR-3185 (D), miR-29b-1* (E) and miR-503 (F) with various growth factor mRNAs were experimentally assessed by the mirTrap assay. (A-D) The mRNA targets of downregulated miRNAs are depicted in red. (E, F) Targets of upregulated miRNAs are shown in green. The enrichment was determined by real-time qPCR of the mRNA samples before and after immunoprecipitation. Values are indicated on a log₂ scale as mean values \pm standard error of the mean of two independent experiments with technical triplicates each. A cut-off of 5-fold enrichment (2.3 on a log₂ scale) is indicated by a red line. Student's t-test was performed to assess statistical significance (* p-value < 0.05).

Supplemental Figure S6

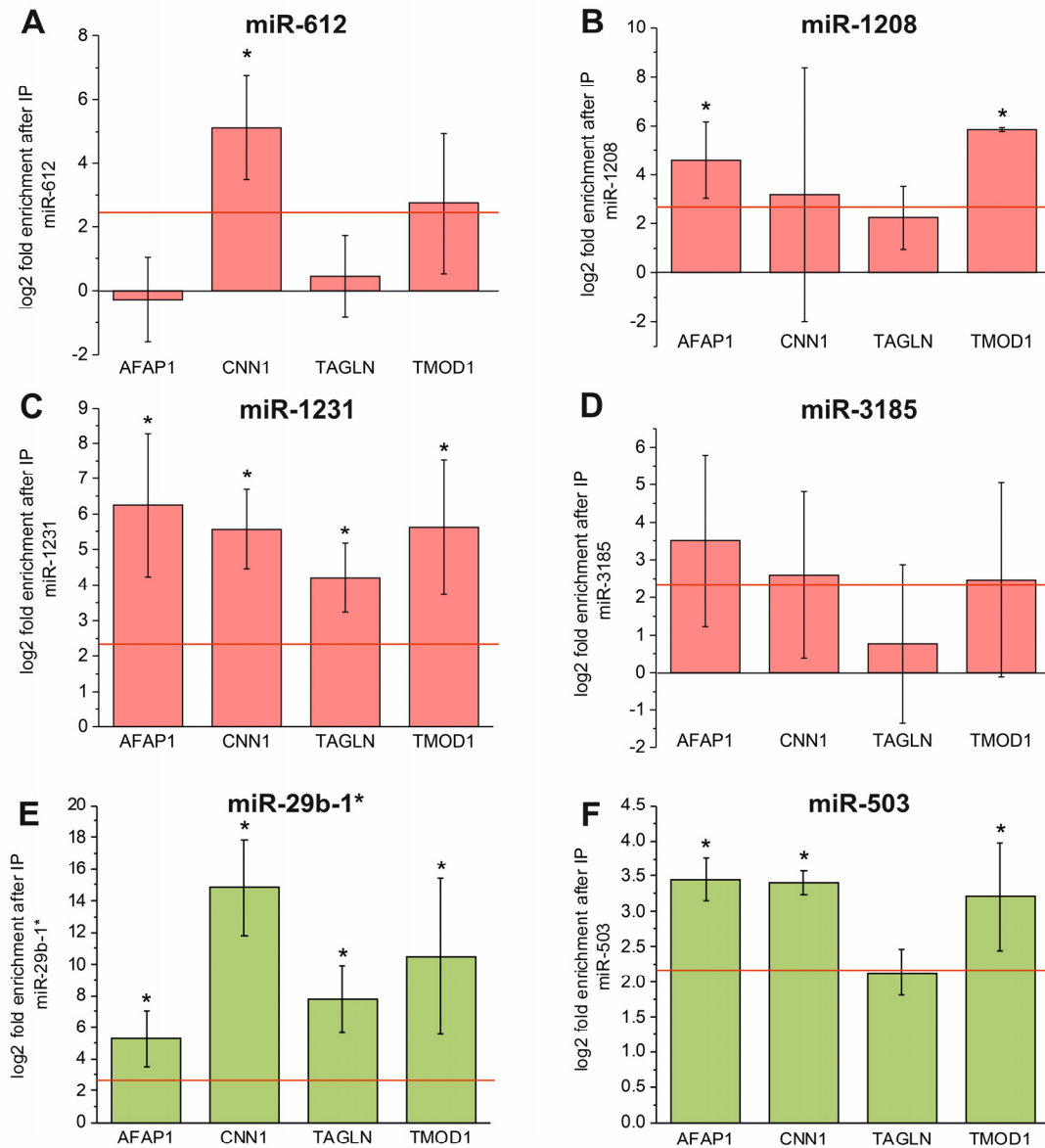


Fig. S2.6 Interactions between miRNAs and mRNAs of actin-binding proteins

(A-F) The interactions between miR-612 (A), miR-1208 (B), miR-1231 (C), miR-3185 (D), miR-29b-1* (E) and miR-503 (F) with various mRNAs of actin-binding proteins were experimentally assessed by the mirTrap assay. The mRNA targets of downregulated miRNAs are depicted in red (A-D), and targets of upregulated miRNAs are shown in green (E, F). The enrichment was determined by real-time qPCR of the mRNA samples before and after immunoprecipitation. Values are indicated on a log₂ scale as mean values \pm standard error of the mean of two independent experiments with technical triplicates each. A cut-off of 5-fold enrichment (2.3 on a log₂ scale) is indicated by a red line. Student's t-test was performed to assess statistical significance (* p-value < 0.05).

Supplemental Figure S7

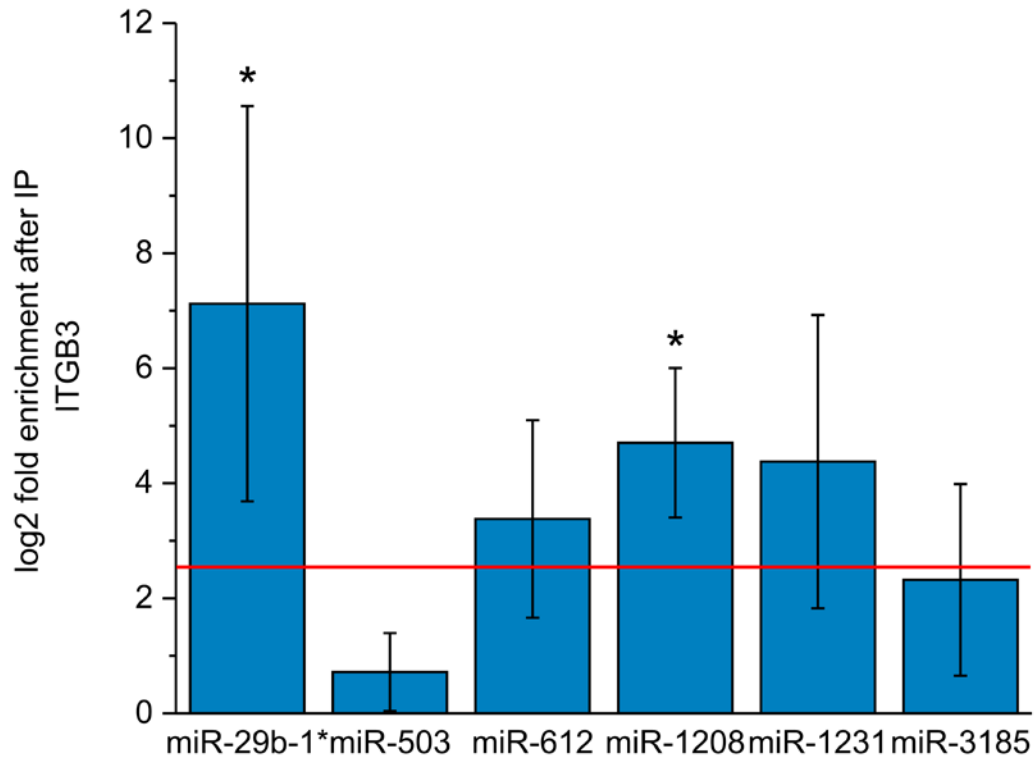


Fig. S2.7 Interactions between miRNAs and ITGB3 mRNA

The interactions between ITGB3 mRNA and various miRNAs were experimentally assessed by the mirTrap assay. The enrichment was determined by real-time qPCR of the mRNA samples before and after immunoprecipitation. Values are indicated on a log₂ scale as mean values \pm standard error of the mean of two independent experiments with technical triplicates each. A cut-off of 5-fold enrichment (2.3 on a log₂ scale) is indicated by a red line. Student's t-test was performed to assess statistical significance (* p-value < 0.05).

Table 2.1 KEGG pathway analysis for the mRNA and miRNA microarray

KEGG pathway	p-value mRNA microarray	# genes	p-value miRNA microarray	# miRNAs	# genes
TGF-β signaling pathway	1.14E-3	6	5.22E-4	29	36
MAPK signaling pathway	4.30E-2	8	2.52E-19	50	120
Wnt signaling pathway	1.01E-2	3	1.04E-10	39	73
Hedgehog signaling pathway	1.75E-2	2	2.96E-10	31	27
Notch signaling pathway	4.33E-2	2	not significant	-	-
Focal adhesion	2.62E-2	6	1.42E-37	47	105
Regulation of actin cytoskeleton	1.87E-3	10	8.18E-12	46	96

Analysis of Kyoto Encyclopedia of Genes and Genomes (KEGG) pathways using the data from the mRNA microarray (fold-change > 2-fold) was performed with the DAVID Bioinformatics Resources 6.7 [225,229], and using the data from the miRNA microarray with the DIANA miRPath v.2.0 [197]. A selection of relevant KEGG pathways is shown.

Table 2.2 Predictions of interactions between miRNAs and mRNAs

miRNA target mRNA	miR- 29b-1* ↑	miR- 424* ↑	miR- 503 ↑	miR- 612 ↓	miR- 1208 ↓	miR- 1231 ↓	miR- 3185 ↓	miR- 4521 ↑
Growth factors								
TGFB2 (transforming growth factor beta 2) ↓	++	-	+	-	++	+	-	-
BMP2 (bone morpho-genetic protein 2) ↓	++	-	-	-	-	++	++	-
CTGF (connective tissue growth factor) ↑	++	-	-	-	+	++	-	-
CYR61 (cysteine-rich protein 61) ↑	-	-	-	-	-	-	-	-
NOV (nephroblastoma overexpressed) ↓	++	-	+	-	-	+	-	-
Actin binding								
AFAP1 (actin filament associated protein 1) ↑	+	++	+	+	+	+	+	-
CNN1 (calponin 1) ↑	-	-	+	+	+	-	-	-
TAGLN (transgelin) ↑	+	-	-	+	-	-	-	-
Integrin binding								
ITGB3 (integrin beta 3) ↓	-	+	-	++	+	+	+	-

Bioinformatic prediction of interactions and regulation between miRNAs and mRNAs. The miRanda algorithm was used to assess the probability of interaction between a certain miRNA and a mRNA (microrna.org) [198]. ++ indicates highly probable interactions, + interactions with low probability, and – no predicted interactions. Upregulation of miRNAs and mRNAs as determined by the microarrays is indicated by up-pointing arrows, and downregulation by down-pointing arrows.

Table 2.3 Experimentally validated interactions between miRNAs and mRNAs

miRNA	miR-29b-1* ↑	miR-503 ↑	miR-612 ↓	miR-1208 ↓	miR-1231 ↓	miR-3185 ↓
target mRNA						
Growth factors						
TGFB2 (transforming growth factor beta 2) ↓	+	+	+	+	+	+
BMP2 (bone morphogenetic protein 2) ↓	-	-	-	-	-	-
CTGF (connective tissue growth factor) ↑	+	-	+	+	+	-
CYR61 (cysteine-rich, angiogenic inducer 61) ↑	+	-	+	-	-	-
NOV (nephroblastoma overexpressed) ↓	+	+	+	-	-	+
Actin binding						
AFAP1 (actin filament associated protein 1) ↑	+	+	-	+	+	-
CNN1 (calponin 1) ↑	+	+	+	-	+	-
TAGLN (transgelin) ↑	+	-	-	-	+	-
Integrin binding						
ITGB3 (integrin beta 3) ↓	+	-	-	+	-	-

The interactions between miR-29b-1*, miR-503, miR-612, miR-1208, miR-1231 and miR-3185 with mRNAs were experimentally validated. Student's t-test was performed to assess statistical significance (* p-value < 0.05). The overview table indicates experimentally validated interactions (+) and no interactions (-) between the miRNAs and the respective mRNAs. Upregulation of miRNAs and mRNAs as determined in the microarrays is indicated by up-pointing arrows, and downregulation by down-pointing arrows.

Table 2.4 Quantification of focal adhesion (FA) formation of HSFs seeded on rF1M-WT and rF1M-RGA coated Y-shaped micropatterns.

	Number of FAs per cell	Average area of FA	Total area of FAs per cell
rF1M-WT	94 ± 37	0.74 ± 0.14 μm ²	68.01 ± 25.90 μm ²
rF1M-RGA	52 ± 23	0.55 ± 0.10 μm ²	29.76 ± 16.43 μm ²
p-value	3.80E-05	5.02E-06	3.20E-07

The data are presented as average ± standard deviation. p-values were calculated comparing rF1M-WT versus rF1M-RGA using the two sample t-test. Number of cells analyzed: 32 cells for rF1M-WT, and 20 cells for rF1M-RGA.

**CHAPTER 3 THE FIBRILLIN-1 RGD MOTIF POST-TRANSCRIPTIONALLY
REGULATES ERK1/2 SIGNALING AND FIBROBLAST PROLIFERATION VIA MIR-
1208**

**The fibrillin-1 RGD motif post-transcriptionally regulates ERK1/2 signaling
and fibroblast proliferation via miR-1208**

Rong-Mo Zhang,¹ Karina A. Zeyer,¹ Nadine Odenthal,² Yiyun Zhang,¹ and Dieter P.

Reinhardt^{1,3,*}

¹ Faculty of Medicine and Health Sciences, McGill University, Montreal, Canada

² Department of Natural Science, University of Lübeck, Lübeck, Germany

³ Faculty of Dentistry, McGill University, Montreal, Canada

* Correspondence to Dieter P. Reinhardt: Department of Anatomy and Cell Biology, McGill

University, 3640 University Street, Montreal, Quebec, H3A 0C7, Canada. Phone: +1

514.398.4243. E-mail: dieter.reinhardt@mcgill.ca

3.1 Preface

Chapter 2 identified a subset of fibrillin-1-controlled miRNAs, and validated their involvements in pSmad2 signaling and focal adhesion formation. This chapter extended the study into another important cell activity, cell proliferation. RGD-containing fibrillin-1 fragments were shown to promote cell proliferation in mesangial and endothelial cells. However, to our best knowledge, whether fibrillin-1 RGD can regulate fibroblast proliferation has not been investigated. This chapter sought to investigate whether and how fibrillin-1 regulate fibroblast proliferation, and identified a novel regulatory mechanism of proliferation, via fibrillin-1 controlled miRNAs.

3.2 Abstract

Fibrillin-1 is an extracellular matrix protein which contains one conserved RGD integrin binding motif. It constitutes the backbone of microfibrils in many tissues, and mutations in fibrillin-1 cause various connective tissue disorders. Although it is well established that fibrillin-1 interacts with several RGD-dependent integrins, very little is known about the associated intracellular signaling pathways. Recent published evidence identified a subset of miRNAs regulated by fibrillin-1 RGD-cell adhesion, with miR-1208 among the most downregulated. The present study shows that the downregulated miR-1208 controls fibroblast proliferation. Inhibitor experiments revealed that fibrillin-1 RGD suppressed miR-1208 expression via c-Src kinase and the downstream JNK signaling. Bioinformatic prediction and experimental target sequence validation demonstrated four miR-1208 binding sites on the *ERK2* mRNA and one on the *MEK1* mRNA. ERK2 and MEK1 are critical proliferation-promoting kinases. Decreased miR-1208 levels elevated the total and phosphorylated ERK1/2 and MEK1/2 protein levels and the phosphorylated to total ERK1/2 ratio. Together, the data demonstrate a novel outside-in signaling mechanism explaining how fibrillin-1 RGD-cell binding regulates fibroblast proliferation.

Keywords: miR-1208; RGD; fibrillin-1; ERK1/2 signaling; fibroblasts, proliferation

Abbreviations

AD acromicric dysplasia

DAPI 4', 6-diamidino-2-phenylindole

FAK focal adhesion kinase

GD geleophysic dysplasia

PBS phosphate-buffered saline

RGD arginine-glycine-aspartic acid

SDS sodium dodecyl sulfate

SSc systemic sclerosis

SSS stiff skin syndrome

TB4 TGF- β binding domain 4

TBS Tris-buffered saline

UTR untranslated region

WMS Weill Marchesani syndrome

3.3 Introduction

Fibrillin-1, a 350 kDa extracellular multi-domain glycoprotein, constitutes the backbone of microfibrils in skin and other tissues [230], providing the scaffold for elastic fiber deposition [231]. Fibrillin-1 directly interacts with integrin cell surface trans-membrane receptors. These interactions are mainly mediated by an evolutionary conserved arginine-glycine-aspartic acid (RGD) sequence in the fourth TGF- β binding domain (TB4) of fibrillin-1 [13], which binds to integrins $\alpha v\beta 3$, $\alpha 5\beta 1$ and $\alpha v\beta 6$ [35,51-53]. Fibrillin-1 RGD-containing fragments were reported to promote proliferation of mesangial and endothelial cells [232,233], and although not previously shown this is also expected for fibroblasts. This study identified a novel intracellular mechanism involved in fibroblast proliferation governed by fibrillin-1 RGD.

Accumulated fibrillin-1 deposition in the extracellular matrix and activated ERK1/2 signaling, which is known to promote fibroblast proliferation [234-236], are associated with systemic sclerosis (SSc) characterized by skin fibrosis [237]. A large genomic rearrangement, resulting in an in-frame duplication of a central region of fibrillin-1 which includes the TB4 domain with the RGD motif, phenocopies SSc in tight skin mice [77]. Mutations of fibrillin-1 can cause multiple fibrillinopathies characterized by fibrotic skin, such as stiff skin syndrome (SSS) [11], geleophysic and acromicric dysplasia (GD and AD) [74], and dominant Weill Marchesani syndrome (WMS) [72]. Mutations resulting in SSS all localize to the RGD-containing TB4 domain of fibrillin-1, and typically lead to the accumulation of microfibrils and collagen fibers, as well as elevated ERK1/2 signaling in the dermis, which can potentially activate fibroblast proliferation [11]. Mutations causing GD, AD and WMS are located in close vicinity to the TB4 domain [72,74]. While no mutation has been associated directly with the fibrillin-1 RGD motif in human, the localization of mutations leading to these disorders in close vicinity suggests a role of the RGD-cell interaction

in skin abnormalities of these disorders. Importantly, heterozygous mice with an RGD to RGE inactivating substitution in fibrillin-1 (Fbn1RGE/+) phenocopies SSS with excessive microfibrillar aggregates and elevated pERK1/2 signaling in the dermis [76]. More active integrins $\alpha\beta3$ and $\alpha5\beta1$ were observed in fibroblasts isolated from Fbn1RGE/+ mice and SSc patients [76]. Antibody treatments to activate $\beta1$ integrin or deactivate $\beta3$ integrin ameliorate skin fibrosis in Fbn1RGE/+ mice, and normalize pERK1/2 induced by TGF- β in SSc fibroblasts [76]. The available data suggest a role of the fibrillin-1 RGD on ERK1/2 signaling and proliferation during dermal pathogenesis.

RGD-containing small chemically synthesized peptides [238-240], or fibronectin have been shown to promote cell proliferation [241-243]. Integrin binding can elicit ERK1/2 and JNK signaling via activation of focal adhesion kinase (FAK), c-Src kinase and Fyn kinase (reviewed in [44,244]). Fibrillin-1 RGD is reported to activate FAK [40,245], and FAK in turn can recruit and activate c-Src kinase [246]. Independent of FAK, $\beta3$ integrin can also activate c-Src kinase directly [247]. The fibrillin-1 binding integrins, primarily $\alpha\beta3$ and $\alpha5\beta1$, can associate with Fyn kinase [248]. Integrins $\alpha\beta3$ and $\alpha5\beta1$ can also physically associate with other transmembrane receptors, including TGF β R2 and platelet-derived growth factor receptor β [249,250], facilitating activation of downstream ERK1/2 signaling. All these pathways activate ERK1/2 signaling and consequently cell proliferation through the RAS-RAF-MEK1/2-ERK1/2 kinase cascade. Based on the existing literature, it would be expected that the RGD motif in fibrillin-1 can also stimulate cell proliferation via this classical RAS-ERK1/2 cascade.

In this study, we report a novel regulatory mechanism on ERK1/2 signaling and fibroblast proliferation mediated by fibrillin-1 RGD-controlled miRNA. miRNAs, a large family of single-

stranded short non-coding RNAs (21-23 nucleotides in length), target mRNAs for cleavage or translational repression (reviewed in [150,251]). A few miRNAs have been identified to play a role in regulating fibroblast proliferation. For example, miR-21 promotes fibroblast proliferation in fibrosis by relieving ERK1/2 signaling from its inhibitor, sprouty1 [252]. Serum-induced miR-22 suppresses the interferon genes, which are inhibitors for fibroblast proliferation [253]. Overexpression of let-7 and miR-125, which are upregulated in quiescent fibroblasts, slow cell cycle re-entry into the proliferating state, through an undefined mechanism [254]. However, upstream regulators of these proliferation-regulating miRNAs were not explored. Our previous study identified a subset of miRNAs regulated by fibrillin-1 RGD-cell interaction, with miR-1208 being one of the most downregulated miRNAs [245]. The current study explored the detailed role of miR-1208 in fibrillin-1 regulated fibroblast proliferation. Fibrillin-1 RGD suppresses miR-1208 expression through c-Src and JNK signaling, and miR-1208 in turn post-transcriptionally regulates activation of ERK1/2 signaling by controlling ERK2 and MEK1 levels. Since abnormalities in fibrillin-1 deposition in the extracellular matrix and in ERK1/2 signaling are involved in several fibrillinopathies, the results of this study may help to understand the underpinning pathogenetic mechanisms.

3.4 Materials and Methods

3.4.1 Production and purification of recombinant proteins

Detailed protocols to recombinantly produce the central human fibrillin-1 fragment rF1M-WT and rF1M-RGA were previously described [245]. Briefly, the fragments span the region from amino acid position 910-2054 of human fibrillin-1 with the wild-type RGD sequence (rF1M-WT) or a p.D1543A mutation (rF1M-RGA) inactivating the binding to integrins as shown previously [245]. The recombinant proteins were produced in HEK293 and secreted into the culture medium to ensure proper disulfide bond formation and glycosylation. Since the recombinant fragments contain a C-terminal hexa-histidine tag, nickel-chelating chromatography was used for purification. The eluted proteins were further purified using gel filtration chromatography (Superose 12). The purity of the recombinant proteins was verified to be >90% by gel electrophoresis and Coomassie Blue staining. Protein concentrations were determined with the BCA protein assay kit (Thermo Fisher Scientific, Waltham, MA, USA).

3.4.2 Cell Culture

Primary human skin fibroblasts used in the experiments were isolated from the foreskin of healthy boys (two to five years of age), following a standard circumcision procedure, approved by the Montreal Children's Hospital Research Ethics Board (PED-06-054). For all experiments, primary fibroblasts from two donors were used between passages 4 and 10. MSU1.1, a human skin fibroblast cell line, was used for some experiments [220]. HEK293 cells were employed for dual luciferase assays. Primary fibroblast and cell lines were cultured in DMEM medium, supplemented with 10% fetal bovine serum, 100 µg/mL penicillin, 100 µg/mL streptomycin, and 2 mM glutamine, at 37°C in a 5% CO₂ atmosphere.

For analyses of fibroblasts seeded on rF1M-WT and rF1M-RGA, cell culture plates or chamber slides were coated with the recombinant proteins at a concentration of 25 µg/mL in Tris-buffered saline (TBS) containing 2 mM Ca²⁺ overnight at 4 °C. This coating concentration was previously optimized for promoting cell adhesion [245]. For some experiments to facilitate cell adhesion for qPCR after 8 h of seeding (Fig. 3.1d and Supplementary Fig. 3.1), additional poly-D-lysine (100 µg/mL, Sigma) was coated (2 h at room temperature) after the recombinant proteins. We showed previously that poly-D-lysine does not affect integrin-triggered signaling [245]. The plates were then washed twice with serum-free DMEM medium, before cell seeding.

Fetal bovine serum contains plasma fibronectin, which may interfere with the fibrillin-1 RGD signaling. Thus, prior to cell experiments with coated recombinant proteins, fibroblasts were serum-starved for 24 h to remove residual plasma fibronectin from the medium. For the kinase inhibitor experiments conducted without coated recombinant proteins, serum-containing medium was used, because plasma fibronectin does not interfere with this experimental setup, and serum

promotes cell proliferation. For trypsinization, the fibroblast monolayer was first washed twice with phosphate-buffered saline (PBS), followed by incubation with 0.25% trypsin-EDTA (Wisent) for 3 min. DMEM medium was added to the dissociated cells and the cell suspension was centrifuged for 5 min at $1,200 \times g$. The cell pellet was resuspended in medium and centrifuged again for 5 min at $1,200 \times g$ to completely remove residual trypsin. The short incubation time with trypsin and the two centrifugation steps minimized proteolytic degradation of cell surface integrins. Light microscopic images of fibroblasts were recorded using a PowerShot A640 digital camera (Canon).

3.4.3 RNA extraction and quantification of miRNA and mRNA

Extraction of total RNA including both miRNAs and mRNAs were performed using the miRNeasy Mini Kit (Qiagen, Hilden, Germany, cat#217004) from 300,000 cells grown in 6-well plates (Corning, Tewksbury, MA, USA), according to the manufacturer's instructions. For reverse transcription of RNA into cDNA, 0.1-1 μg of total RNA was used. miScript II RT kit (Qiagen, cat#218160) was used to reverse transcribe miRNAs, according to the manufacturer's instructions. ProtoScript II First-Strand Synthesis System for RT-PCR (New England Biolabs, Ipswich, MA, USA, cat#E6560S) was used to reverse transcribe mRNAs as detailed in the supplier's manual.

For quantification of miRNAs, real-time qPCR was performed using the miScript SYBR Green PCR Kit (Qiagen, cat#218073), according to the manufacturer's instructions. miScript Primer Assays were obtained from Qiagen for human miR-1208 (cat#MS00014196). RNU6 (cat#MS00033740) was used as reference gene. The real-time cyclers (Applied Biosystems, Foster City, CA, USA, Step-OneTM Real-Time qPCR system) was programmed to an initial PCR

activation step for 15 min at 95°C and 40 cycles of a 3-step cycling program: 1) Denaturation (94°C for 15 s), 2) Annealing (55°C for 30 s), 3) Extension (70°C for 34 s). Melting curve analysis was performed after each run to determine the specificity of the amplified products. For quantification of mRNA, cDNA was used for real-time qPCR with the SYBR Green Select Master Mix (Applied Biosystems, cat#4472908), and 200 nM forward and reverse primers (Supplementary Table 3.2). GAPDH was used as a reference gene. The real-time cycler was programmed with an initial PCR activation step for 2 min at 50°C and afterwards 2 min at 95°C and 40 cycles of a 3-step cycling program: 1) Denaturation (95°C for 15 s), 2) Annealing (58°C for 15 s), 3) Extension (72°C for 1 min). Melting curve analysis was performed after each run to determine the specificity of the amplified products. The delta-delta Ct method was used to compare different groups.

3.4.4 microRNA transfection into fibroblasts

The mimic and inhibitor of miR-1208 were commercially obtained from Qiagen: Syn-hsa-miR-1208 (cat#MSY0005873) and Anti-hsa-miR-1208 (cat#MIN0005873). The mimic or the inhibitor was prepared with HiPerFect transfection reagent (Qiagen, cat#301704) in DMEM medium. The solution was then applied to the cells directly after seeding on 6-well plates or 8-well chamber slides, at a final concentration of 5 nM for the mimic and 50 µM for the inhibitor. 5 µg/mL actinomycin D was supplemented to the medium to eliminate newly expressed mRNAs. qPCR of *ERK1*, *ERK2*, *MEK1* and *MEK2* mRNAs were performed 24 h after transfection to test the changes upon miR-1208 mimic or inhibitor transfection, while immunofluorescence and Western blotting were performed 48 h after transfection to allow sufficient time to analyze consequences at the protein level.

3.4.5 Inhibitor treatment of fibroblasts

Inhibitors purchased from Selleckchem (Houston, TX, USA) were applied in the concentrations recommended by the manufacturer to fibroblasts directly after cell seeding: 10 μ M ERK1/2 inhibitor (SCH772984, cat#S7101), 10 μ M FAK inhibitor (PF573228 cat#S2013), 10 μ M CDC42 inhibitor (ML141, cat#S7686), 10 μ M pan-Src inhibitor (Saracatinib, cat#S1006), 100 nM c-Src inhibitor (Dasatinib, cat#S1021), 10 μ M Fyn inhibitor (PP2, cat#S7008) and 20 μ M JNK inhibitor (SP600125, cat#S1460). 1:1,000 v/v DMSO was used as buffer control. qPCR reactions were performed 24 h after treatment, and immunofluorescence analyses were performed 48 h after treatment to allow analysis of the protein level.

3.4.6 Dual luciferase assay

The sequences of the predicted binding sites for miR-1208 on the 3' untranslated region (UTR) of *ERK2* and *MEK1* were obtained using microT-CDS (http://diana.imis.athena-innovation.gr/DianaTools/index.php?r=microT_CDS/index) [153]. Double-stranded DNA fragments were annealed using two chemically synthesized single-stranded DNA sequences (Integrated DNA Technologies, Coralville, IA, USA) in Oligo Annealing Buffer (Promega, Madison, WI, USA, cat#C838A). Annealing resulted in double stranded fragments with sticky ends compatible with *XhoI* and *XbaI* restricted sites. To identify the specific binding site contributing to miR-1208 interaction, each insert contained only one predicted site. Additionally, a *BamHI* site was present in the inserts for screening correctly ligated sequences (Supplementary Table 3.1). The fragments were inserted in the *XhoI* \times *XbaI* restricted pmirGLO vector (Promega, cat#E133A), using T4 DNA ligase (Invitrogen, Waltham, MA, USA, cat#LS15224017). The *E.*

coli NEB5 α strain (New England Biolabs, cat#C2987) was used for transformation to amplify the ligated vector. The plasmids were purified using the NucleoSpin Plasmid Kit (Macherey-Nagel, Düren, Germany, cat#740588.250), followed by ethanol precipitation to sterilize the plasmids prior to transfection. Sanger sequencing was employed to validate the correct sequence of all inserts.

Each of the plasmids (2.5 ng/ μ L) and miR-1208 mimic or scrambled (100 nM) were co-transfected into 10,000 HEK293 cells per well of white 96-well plates (Greiner Bio-One, Frickenhausen, Germany, cat#655073) with lipofectamine 2000 (Invitrogen, cat#11668-019) in OPTI-MEM I Reduced Serum Media (Gibco, Waltham, MA, USA, Cat#31985-062) [255]. 48 h after transfection, the activities of firefly luciferase and *Renilla* luciferase were activated with the Dual-Luciferase Reporter Assay System (Promega, cat#E2920). Luminescence was measured using a luminescent plate reader (PerkinElmer 2030 workstation, Waltham, MA, USA). The firefly luminescence was normalized to the internal *Renilla* luminescence.

3.4.7 Indirect immunofluorescence

Indirect immunofluorescence was performed as previously described [188]. Briefly, cells were grown in 8-well chamber glass slides (Thermo Fisher Scientific) at densities of 20,000 cells/well. After fixation with 70% methanol/30% acetone, cells were blocked with 10% v/v normal goat serum. 1:500 dilution of primary antibodies of Ki67 (Abcam, Cambridge, MA, USA, cat#ab15580) was applied to the cells for 1.5 h at room temperature. Secondary antibody used was 1:200 diluted goat anti-rabbit conjugated to Cy3 (Jackson Immunoresearch Laboratories, West Grove, PA, USA, cat#111-165-003) for 1 h at room temperature. Nuclear counterstaining was performed with 4', 6-diamidino-2-phenylindole (DAPI). All images were recorded using an Axio Imager M2

microscope (Zeiss, Oberkochen, Germany) equipped with an ORCA-flash4.0 camera (Hamamatsu, Japan). Original images in the tiff format were exported for cell counting using ImageJ [226], as previously described [256].

3.4.8 Western blotting

Cells were seeded in 6-well plates, with 300,000 cells per well. The cells were washed twice with PBS, and then lysed in the plate using 200 μ L RIPA buffer (50mM Tris, 150mM NaCl, 0.5% sodium deoxycholate, 1% Triton X-100, 0.1% sodium dodecyl sulfate (SDS), pH 8) including 2% v/v protease inhibitor cocktail (Roche, Basel, Switzerland, cat#11697498001) and 1% v/v phosphatase inhibitor cocktail (Sigma, St. Louis, MO, USA, cat#P5726). The lysate was scraped and transferred immediately to cold 1.5 ml tubes and centrifuged at $9,300 \times g$ for 2 min to eliminate non-soluble cell debris and ECM. The supernatant was denatured in SDS containing sample buffer at 95°C for 5 min, then 50 μ L of the supernatant was loaded onto a 10% SDS-PAGE gel, electrophoresed, and then transferred in 10 mM sodium tetraborate onto a 0.45 μ m pore size nitrocellulose membrane (Bio-Rad, Berkeley, CA, cat#1620115). The blots were blocked with 5% non-fat dry milk for 1 h at room temperature. The blot was subjected to primary antibody incubation overnight at 4°C , followed by 3×5 min washes in TBST (TBS, pH 7.4 with 0.05% Tween-20). The blots were incubated with one of the following primary antibodies from Cell Signaling (Danvers, MA, USA) at a 1:1,000 dilution in 2% dry milk: anti-ERK1/2 (cat #4695), anti-pERK1/2 (cat#4377), anti-MEK1/2 (cat#9121), anti-pMEK1/2 (cat#4058), and anti-GAPDH (cat#2118). Horseradish peroxidase conjugated goat anti-rabbit secondary antibody (Jackson Immunoresearch Laboratories, cat#111-035-003) was used 1:800 diluted (2 h incubation at room temperature). Chemiluminescent Western blotting substrate (Thermo Fisher Scientific, cat#34580)

was used to detect the horseradish peroxidase substrate signal. The blots were imaged using a ChemiDoc imager (Bio-Rad). Band intensities were quantified using ImageJ and normalized to GAPDH staining on the same blot, as described previously [256]. The exposure times were adjusted for each experiment to ensure non-saturation of the bands.

3.4.9 Data analyses

Raw data of experiments were collected as described above, using primary fibroblasts from two donors, MSU1.1, or HEK cell lines. Repeats were performed with duplicates, triplicates or quadruplicates, depending on the experimental settings. Prior to the statistical analyses, outlier analysis was performed using Grubbs' test at a confidence level of 95%. Given that there was always one variable between compared datasets, statistical significance was determined using the two-tailed student's t-tests with 95% confidence level. Paired sample t-test, two-sample t-test or one-sample t-test were used depending on the distribution of the data. All data were expressed as mean values \pm standard deviation. In relative quantifications, the averages of the control groups were set to 1.

3.5 Results

3.5.1 Interactions with the RGD motif of fibrillin-1 promote fibroblast proliferation and downregulate miR-1208

Previous studies have revealed that the RGD site of fibrillin-1 mediates adhesion and spreading of various primary cells and cell lines [35,51,52,232,245]. To study the role of fibrillin-1 RGD on fibroblast proliferation, we used a recombinant RGD-containing wild-type fibrillin-1 fragment (rF1M-WT), and a RGA mutant control fragment (rF1M-RGA) that cannot interact with integrins (Fig. 3.1a). These fragments cover about 42% of fibrillin-1 in the central region omitting the N- and C-terminal ends, because they confer aggregation during purification [216]. The fragments were designed to encompass the RGD-containing TB4 domain and the upstream located synergy site which both mediate integrin binding. To determine whether the RGD motif of fibrillin-1 promotes primary skin fibroblast proliferation, Ki67 staining was performed after cell seeding on rF1M-WT and rF1M-RGA for 12, 24 and 48 h (Fig. 3.1b and c). Non-coated plates (TBS) were used as controls. Starting from 24 h, fibroblasts interacting with rF1M-WT showed 12% Ki67 positive staining, compared to only 2-3% when cells were seeded on rF1M-RGA or on non-coated flasks. After 48 h of interaction, 56% of fibroblasts seeded on rF1M-WT stained positively for Ki67, compared to 3-8% cells seeded on rF1M-RGA and non-coated flasks. Taken together, these results demonstrate that interaction of fibroblasts with the fibrillin-1 RGD motif promotes fibroblast proliferation.

3.5.2 Fibroblast interaction with the fibrillin-1 RGD motif elevates the mRNA and protein levels of ERK1/2 and MEK1/2

Since the ERK1/2 signaling cascade is important for proliferation, we extended the study to understand whether this pathway is activated upon interaction of fibroblasts with rF1M-WT.

Previous studies focused on the phosphorylated kinase levels, when studying the activation of the ERK1/2 signaling pathway. Interestingly, we found that mRNA levels of the key kinases in this cascade, *ERK2*, *MEK1* and *MEK2*, were elevated by 2.8 to 3-fold after 8 h of cell seeding on rF1M-WT (Fig. 3.1d). These observations were not restricted to primary fibroblasts, as similar observations were made with the fibroblast cell line MSU1.1, which showed upregulated *ERK2* and *MEK1* mRNA by 1.3 and 1.6-fold, respectively upon interacting with rF1M-WT (Supplementary Fig. 3.1).

Western blotting of total and phosphorylated protein of ERK1/2 and MEK1/2 was performed using cell lysates 24 h after seeding on rF1M-WT, when proliferation was elevated, and compared with the rF1M-RGA control (Fig. 3.1e). The quantification revealed that ERK1/2 protein levels were elevated by 2-fold relative to the rF1M-RGA control, and MEK1/2 protein levels were increased by 2.9-fold. pERK1/2 and pMEK1/2 levels were elevated 4-fold and 2.8-fold, respectively, by rF1M-WT. The ratio of phosphorylated ERK1/2 to total ERK1/2 ratio was 1.9-fold higher in cells seeded on rF1M-WT, whereas the phosphorylated MEK1/2 to total MEK1/2 ratio was not changed. In summary, the data show that the RGD motif in rF1M-WT upregulates both mRNA and protein levels of ERK1/2 and MEK1/2, leading to elevated pERK1/2 and pMEK1/2 levels.

3.5.3 The RGD cell binding-controlled miRNA miR-1208 targets ERK2 and MEK1

Previous work from the lab showed that miR-1208 was downregulated in primary fibroblasts as early as 2 h after rF1M-WT binding persisting up to 48 h [245]. In the present study, we confirmed these results showing that miR-1208 was downregulated to ~57% after 24 h interaction of fibroblasts with rF1M-WT, as compared to the rF1M-RGA control (Fig. 3.2a). Bioinformatic

analysis, using microT-CDS, predicted 14 binding sites for miR-1208 on the 3'UTR of *ERK2* (ENST00000215832, Ensemble), including two 8-mer, two 7-mer and ten 6-mer binding sites. Two binding sites were predicted on the 3'UTR of *MEK1* (ENST00000307102, Ensemble), one 7-mer and one 6-mer binding site (Fig. 3.2b). No binding sites for miR-1208 were predicted in *ERK1* or *MEK2*.

To identify which predicted binding sites in the 3'UTR of *ERK2* and *MEK1* contribute to miR-1208 interactions, dual luciferase assays were performed using the miRNA target expression vector pmirGLO. Each predicted binding site was inserted separately into the multiple cloning site located 3' of the sequence coding for the firefly luciferase protein (Supplementary Table 3.1). These plasmids were co-transfected into HEK293 cells together with either the miR-1208 mimic or a scrambled control. 48 h after transfection, firefly luciferase mediated luminescence was determined in the cell lysates and normalized to the *Renilla* luminescence internal control. The analysis demonstrated that miR-1208 could significantly reduce luciferase activity with the 3'UTR sequences #3 (8-mer, 29%), #4 (7-mer, 28%), #8 (6-mer, 16%) and #9 (6-mer, 78%) of *ERK2*, as compared to the scrambled control (Fig. 3.2c and green arrowheads in Fig. 3.2b). Analysis of the *MEK1* 3'UTR sequences revealed that miR-1208 can directly interact with sequence #1 (7-mer, 12%) (Fig. 3.2e and green arrowhead in Fig. 3.2b). The alignments of the identified mRNA sequences of *ERK2* and *MEK1* with miR-1208 are shown in Figs. 2d and 2f. The binding sites are not conserved between the mRNAs of the respective isoforms of ERK1/2 and MEK1/2. Overall, the data reveal four novel miR-1208 binding sites in the *ERK2* mRNA and one in the *MEK1* mRNA.

3.5.4 Functional consequences of miR-1208 on target mRNA levels

miRNA-mRNA interactions result in mRNA destabilization or translational repression, with mRNA degradation explaining 66%-90% of the overall consequences [151]. Thus, the levels of miRNA and the respective mRNA targets are typically inversely correlated. Here, we performed qPCR to determine the relative quantities of *ERK1*, *ERK2*, *MEK1* and *MEK2* mRNAs in fibroblasts after transfection with miR-1208 inhibitors or mimics. Based on the timeframe of the miR-1208 downregulation upon fibrillin-1 binding described above, the miR-1208 inhibitor was transfected into primary fibroblasts and analyzed by qPCR after 24 h. The inhibition of miR-1208 resulted in significant upregulation of *ERK2* (20%) and *MEK1* (7%) mRNAs, but not of *ERK1* and *MEK2* mRNAs (Fig. 3.3a). Complementing experiments using a miR-1208 mimic revealed that *ERK2* and *MEK1* mRNA levels were significantly suppressed by 20% and 16%, respectively (Fig. 3.3b). The fact that miR-1208 suppressed *ERK2* stronger than *MEK1* in fibroblast is consistent with the dual luciferase assays shown in Fig. 3.2, which demonstrated more miR-1208 binding sites on *ERK2* and stronger suppression of firefly luciferase activation. Surprisingly, *ERK1*, which was not a predicted target of miR-1208, was also significantly downregulated (35%) by the miR-1208 mimic. This indicates that either there is one or more miR-1208 binding sites present in the *ERK1* mRNA not predicted by bioinformatic tools, or alternatively, indirect effects of miR-1208 on *ERK1* mRNA levels. In summary, the results demonstrate that miR-1208 directly targets *ERK2* and *MEK1* mRNAs in primary fibroblasts.

3.5.5 miR-1208 inhibits ERK1/2 protein levels and phosphorylation

To further consolidate the functional consequence of miR-1208 on total and phosphorylated ERK1/2, the protein levels were quantified by Western blotting after fibroblast transfection with

miR-1208 inhibitors or mimics. Cell lysates 48 h after transfection showed 69% more ERK1/2 when miR-1208 was inhibited, compared to the scrambled control (Fig. 3.4a). Correspondingly, ERK1/2 levels were 41% lower when miR-1208 was overexpressed (Fig. 3.4b). The pERK1/2 level was elevated by 184% when miR-1208 was inhibited, and it decreased correspondingly by 87% when miR-1208 was overexpressed (Figs. 3.4c and d). To analyze whether the elevated pERK1/2 is the consequence of increased ERK1/2, the activation by upstream kinases, or both, we determined the pERK1/2 to ERK1/2 ratio. The pERK1/2 to ERK1/2 ratio was upregulated by 101% when miR-1208 was inhibited, and downregulated by 75% when miR-1208 was overexpressed (Fig. 3.4e and f). Together, these results show that both increased availability of ERK1/2 and higher upstream kinase activity contributed to the elevated pERK1/2 levels.

3.5.6 miR-1208 inhibits MEK1/2 protein level and phosphorylation

As MEK1/2 are upstream kinases that phosphorylate ERK1/2, and *MEK1* is a target of miR-1208, we investigated MEK1/2 and pMEK1/2 levels upon transfection of miR-1208 inhibitors or mimics in fibroblasts. Similar to the results for ERK1/2, both MEK1/2 and pMEK1/2 levels were upregulated by 53% and 80%, respectively, upon inhibition of miR-1208 (Fig. 3.5a and c). Consistent with these results, overexpression of miR-1208 downregulated MEK1/2 and pMEK1/2 levels by 51% and 54% respectively (Fig. 3.5b and d). Unlike the results for ERK1/2, the pMEK1/2 to MEK1/2 ratio did not significantly change upon miR-1208 inhibition or overexpression (Fig. 3.5 e and f). The data reveal that the altered pMEK1/2 levels upon miR-1208 transfection are the consequence of the changed availability of MEK1/2, but not altered upstream kinase activity.

3.5.7 miR-1208 negatively regulates fibroblast proliferation

The evidence presented above demonstrated that miR-1208 negatively regulates ERK1/2 signaling through post-transcriptional suppression of ERK1/2 and MEK1/2. Given the promoting role of ERK1/2 signals on cell proliferation, the results suggest that miR-1208 inhibits cell proliferation. To address this hypothesis, experiments were performed to rescue the reduced proliferation when cells were seeded on rF1M-RGA (see Fig. 3.1a and b), using the miR-1208 inhibitor. Ki67 immunostaining showed significantly increased fibroblast proliferation by 243% under these conditions (Fig. 3.6a and b). miR-1208 inhibition could also upregulate proliferation when fibroblasts were seeded on rF1M-WT (26%) or on non-coated wells (97%), albeit at lower levels (Fig. 3.6a and b). Complementing experiments using miR-1208 mimics showed downregulated proliferation levels of fibroblasts interacting with rF1M-WT (15%), whereas cells seeded on rF1M-RGA or on non-coated wells were unaffected (Fig. 3.6c and d).

The functional consequence of miR-1208 inhibition under rF1M-WT coated conditions is less than that under rF1M-RGA coated conditions. This is likely due to the relatively low levels of miR-1208 under rF1M-WT-conditions (42% reduction) (Fig. 3.2a). The same rationale explains the unchanged proliferation rate of rF1M-RGA seeded cells upon miR-1208 overexpression, because the miR-1208 level is already relatively high. Overall, the data reveal that miR-1208 negatively regulates fibroblast proliferation. Since miR-1208 is suppressed when fibroblasts interact with fibrillin-1, proliferation is upregulated through higher ERK1/2 and MEK1/2 levels.

3.5.8 ERK1/2 inhibition abrogates the effect of miR-1208 on proliferation

To elucidate whether the regulatory role of miR-1208 on proliferation exclusively depends on ERK1/2 signaling, we used a dual mechanism inhibitor of ERK1/2, SCH772984, which inhibits

both, the intrinsic kinase activity and ERK1/2 phosphorylation [257]. As expected, cell proliferation was significantly reduced to ~0.1 % upon 10 μ M SCH772984 treatment for 48 h, in both serum-containing and serum-free conditions (Fig. 3.7a and b, Supplementary Fig. 3.2a and b). Importantly, the promoting effect of miR-1208 inhibition on fibroblast proliferation was completely abolished in the presence of SCH772984. Since ERK1/2 signaling can regulate the expression levels of many transcription factors and miRNAs [258,259], it is possible that this observation results from alterations of endogenous miR-1208 expression levels. However, this possibility was excluded by qPCR analyses after 10 μ M SCH772984 treatment for 24 h, which showed that ERK1/2 signaling did not regulate miR-1208 expression. (Fig. 3.7c). These data demonstrate that active ERK1/2 signaling is required for the regulation of fibroblast proliferation by miR-1208.

3.5.9 Inhibitors of JNK and Src kinase stimulate miR-1208 expression

To investigate the upstream regulators involved in the RGD-dependent regulation of miR-1208, we employed a series of kinase inhibitors. Upon RGD-integrin interaction, FAK, CDC42 and Src kinases (c-Src and Fyn kinase) can be activated [45]. This stimulates downstream signaling cascades, including ERK1/2 and JNK signaling, which can regulate gene and miRNA expression [260]. Fibroblasts seeded on rF1M-WT were treated with FAK inhibitor (PF573228), CDC42 inhibitor (ML141), pan-Src kinase inhibitor (Saracatinib), c-Src kinase inhibitor (Dasatinib), Fyn kinase inhibitor (PP2), and JNK inhibitor (SP600125) for 24 h, and fibroblasts seeded on rF1M-RGA served as a negative control. qPCR results show that inhibition of pan-Src kinases, c-Src

kinase and JNK resulted in 25-35% higher miR-1208 levels, compared to the DMSO control, similar to the increases observed with the rF1M-RGA control (65%) (Fig. 3.8a). These results demonstrate that the activation of c-Src kinase and JNK control miR-1208 expression upon RGD ligation. Inhibition of FAK, CDC42 and Fyn kinase did not change or even downregulated miR-1208 levels, suggesting that these kinases did not play a critical regulating role on miR-1208 expression upon fibrillin-1 RGD binding. Ki67 immunofluorescence revealed that the inhibition of Src kinases and JNK kinase can downregulate fibroblast proliferation to various extents (Fig. 3.8b and c). Because miR-1208 levels are upregulated upon inhibition of Src kinases and JNK kinase, we performed miR-1208 inhibitor experiments to investigate whether fibroblast proliferation can be rescued upon inhibition of these kinases. Proliferation was rescued by miR-1208 inhibition in the presence of the pan-Src kinase inhibitor (75%), c-Src kinase inhibitor (102%), or JNK inhibitor (371%) (Fig. 3.8d and e). These rescue experiments further consolidate the upstream regulatory role of c-Src and JNK kinase on miR-1208 expression and in turn on fibroblast proliferation.

3.6 Discussion

We determined in this study the mechanism how fibrillin-1 controls cell proliferation through the regulation of miR-1208 levels. The data demonstrate that the interaction of extracellular fibrillin-1 with fibroblasts through the RGD motif downregulates miR-1208 via c-Src and downstream JNK signaling. miR-1208 post-transcriptionally regulates ERK1/2 activation, through modification of the *ERK2* and *MEK1* mRNA levels. We determined several binding sites of miR-1208 on the 3'UTR of the *ERK2* and *MEK1* mRNA, providing the basis for this regulation. Decreased miR-1208 levels upon fibroblasts interaction with fibrillin-1 elevates total ERK1/2 and MEK1/2, which leads to enhanced phosphorylation of these kinases, activating ERK1/2 signaling and fibroblast proliferation (Fig. 3.9).

Previous studies focused on the direct catalytic role of FAK, c-Src, Fyn kinase and CDC42 on the phosphorylation and activation of the RAS-RAF-MEK1/2-ERK1/2 signaling cascade upon integrin binding [45,261]. The level of activated pERK1/2 and pMEK1/2 can be principally controlled by two mechanisms: I) the activity of the respective upstream kinases, which is generally well understood (Fig. 3.9, black arrows); and II) by controlling the ERK1/2 and MEK1/2 protein levels, which is much less known (Fig. 3.9, green arrows). Phosphorylation of these kinases is a reversible reaction, with the forward reaction catalyzed by the upstream kinase and the reverse reaction catalyzed by the respective phosphatases. Therefore, an increase in the levels of non-phosphorylated substrate shifts the equilibrium of the reaction to the product side, resulting in increased phosphorylated and activated ERK1/2 and MEK1/2. In this scenario, the ratio of inactive non-phosphorylated kinase to activated phosphorylated kinase does not change. But the ratio does change when the respective upstream kinases are activated and phosphorylate their downstream

targets (e.g. activated MEK1/2 phosphorylates ERK1/2). We previously identified miR-1208 as one of the most down-regulated miRNAs when fibroblasts grow on fibrillin-1 [245]. Here we demonstrate that upon fibroblast interaction with fibrillin-1 RGD, the decreased miR-1208 levels elevated ERK1/2 signaling via post-transcriptionally upregulating the protein levels of ERK1/2 and MEK1/2. This led to increased levels of the phosphorylated forms (pERK1/2 and pMEK1/2), due to increased availability of the substrates (see mechanism II above). For ERK1/2, the elevated ratio of p/total ERK1/2 can be explained by additional activation of MEK1/2 (mechanism I). However, the ratio of p/total MEK1/2 was not changed, clearly indicating that the upstream kinase for MEK1/2 (RAF) was not activated by decreased miR-1208 levels (Fig. 3.9).

We used the DIANA-microT-CDS algorithm, which predicted 14 binding sites for miR-1208 on the 3'UTR of *ERK2* and two sites on *MEK1*. miRNA-mRNA binding requires Watson-Crick pairing of mRNA to the 5' nucleotides 2-7 seed region of miRNAs [152]. Nucleotide 1 and 8 can also contribute to binding efficacy, resulting in a hierarchy of binding efficacy: 8-mer>7-mer>6-mer with respect to the seed pairing. Dual luciferase assays validated four sites for *ERK2*, and one for *MEK1*. For *MEK1*, the binding efficacy between the two predicted miR-1208 binding sites matched this hierarchy [152], as the 7-mer binding site suppressed luciferase expression, but not the 6-mer. However, the binding efficacy of the determined miR-1208 binding sites in the *ERK2* 3'UTR did not strictly follow this hierarchy. The #9 binding site (6-mer) resulted in highest suppression of luciferase expression (78%), much higher than those of the #3 or #4 (8- or 7-mer) validated binding sites (29 and 28%, respectively). Several 8- or 7-mer predicted binding sites on the *ERK2* mRNA could not be validated for miR-1208 binding, suggesting that the sequence

downstream of the miR-1208 seed region can also influence miRNA-mRNA interaction. In fact, prior to mRNA target binding, the miRNA is likely bound in its entire length to Argonaute, to protect it from degradation by RNases [251]. Thus, successive pairing downstream of the seed region (nucleotides 9-12) can result in neutral or even disfavored effects on the miRNA-mRNA interaction, as it may require more energy to change the confirmation of miRNA-Argonaute interaction in RISC. Whereas pairing at nucleotides 13-16 enables additional favorable interactions without incurring the large conformational change [251]. This explains why the #9 site (6-mer) for *ERK2* showed the highest suppressive activity on the target mRNA, as this binding site does not match in the unfavorable position 9-12 and it contains 5 contiguous matching nucleotides in position 14-18, favoring RISC binding to the target mRNA. The three other validated binding sites in *ERK2* showed lower efficacies, because they either contained matches in the 9-12 region (#3 and #8), or did not contain any matches downstream of the seed region (#4). The identified 7-mer site on *MEK1* also contained three matching nucleotides in position 9-12, explaining the relatively low suppressive efficacy on luciferase expression (12%). Alignment between the 3'UTRs of human *ERK2* and *ERK1* and between *MEK1* and *MEK2* demonstrated that the respective binding sites are not conserved, further consolidating the notion that miR-1208 directly targets the *ERK2* and *MEK1* mRNAs (Fig. 3.9).

Identification of *ERK2* and *MEK1* targeted by miR-1208 is consistent with their known roles in proliferation. Human *ERK1* and *ERK2* are homologous isoforms ubiquitous in most of tissues, 84% identical at the amino acid level [262]. However, *ERK1* and *ERK2* are not entirely redundant in function. For example, ablation of the *Erk2* gene in mice is embryonic lethal, while *Erk1*-

deficient mice are viable and fertile [263,264], and ERK2 plays a more dominant role in proliferation than ERK1 [265-267]. We have shown that fibrillin-1 RGD-fibroblast interaction can elevate *ERK2* mRNA levels by downregulating miR-1208. Surprisingly, we also observed inhibitory potency of miR-1208 on *ERK1* mRNA levels, which was not bioinformatically predicted. It is possible that miR-1208 indirectly regulates *ERK1* mRNA level, and thus complements its direct mechanism on the *ERK2* mRNA. MEK1 and MEK2 have differential regulatory roles in cell cycle progression, in which MEK1 preferentially promotes cell proliferation, whereas MEK2 induces growth arrest [268,269]. Consistently, downregulation of miR-1208 by the fibrillin-1 RGD motif upregulated *MEK1* mRNA and in turn proliferation.

To further identify the mechanism how the RGD motif in fibrillin-1 suppresses miR-1208, we used inhibitors of ERK1/2, FAK, CDC42/Rac kinases, pan-Src kinases, c-Src kinase, Fyn kinase, and JNK, which are all activated by integrin binding to extracellular ligands (reviewed in [45,261]). We identified that RGD-cell interaction suppressed miR-1208 via activation of c-Src kinases and downstream JNK (Fig. 3.9). This in turn post-transcriptionally activated ERK1/2 signaling via mechanism II mentioned above and thus cell proliferation (Fig. 3.9 green arrows). JNK signaling is also a well-characterized proliferation-promoting pathway (reviewed in [270]). Our study complements the existing model, demonstrating the involvement of miR-1208 and providing a novel crosstalk between JNK and ERK1/2 signaling. Although ERK1/2 signaling regulates the transcription of multiple miRNAs [258,259], we excluded the possibility that direct ERK1/2 inhibition affects miR-1208 expression levels.

Upregulation of ERK1/2 signaling caused by dysregulated fibrillin-1 in the extracellular matrix is a hallmark of several fibrillinopathies, including SSc, SSS and Marfan syndrome [76,237,271]. Various ERK1/2 inhibiting strategies have been tested to treat fibrillinopathies in mouse models. For example, treatment of *Fbn1*^{RGE/+} mice harboring a heterozygous inactivation of the RGD motif, with either the MEK inhibitor RDEA119 or with TGF- β neutralizing antibody prevented aggressive skin fibrosis [76]. Both losartan, which suppresses ERK1/2 signaling, and RDEA119 were used to treat aortic aneurysm progression in MFS mice with mutated fibrillin-1 [70,271]. Given that miRNA-based RNA interference strategies have been successfully used in multiple pre-clinical and clinical trials [159,272], our findings suggest that miR-1208, which inhibits ERK1/2 and downstream cell proliferation, can potentially be exploited as a therapeutic candidate in fibrillinopathies characterized by elevated ERK1/2 and altered fibrillin-1 cell interaction. Integrin-modulating strategies using activating $\alpha 5$ integrin and deactivating $\beta 3$ integrin antibodies also showed therapeutic benefits in *Fbn1*^{RGE/+} mice and SSc fibroblasts to normalize pERK1/2 levels and skin fibrosis [76]. It is reported that elevated pERK1/2 signaling in scleroderma fibroblasts induce integrin $\alpha\beta 3$ expression which in turn sustains pro-fibrotic gene expressions, including $\alpha 2(I)$ collagen [273]. Anti-integrin $\alpha\beta 3$ antibody treatment reverses the SSc phenotype by inhibiting the autocrine TGF- β signaling *in vitro*, while not changing TGF- β expression [273]. These results suggest a cross-talk between fibrillin-1 binding and TGF- β signaling with activated pERK1/2 signaling as the point of convergence. Consistent with these data, our study demonstrates a novel mechanistic link between fibrillin-1 RGD-integrin binding and ERK1/2 signaling, by promoting the expression of the ERK1/2 and MEK1/2 kinases via decreased miR-1208.

miR-1208 is encoded on human chromosome 8q24 and expressed in primates, but not in mouse, fish, or invertebrates, preventing the use of such disease models for *in vivo* studies [162]. Thus, to study miR-1208 in pathological conditions, the only option is to use human patient-derived tissue or cells. This is especially pertinent for the fibrillin-1 related pathologies characterized by abnormal fibroblast proliferation and elevated ERK1/2 signaling, including SSc and SSS. This may provide further insight into how deficient fibrillin-1 microfibrils may lead to fibrotic phenotypes in these disorders. For other fibrillinopathies also characterized by thickened skin, such as GD, AD and WMS, it is less clear whether fibroblast proliferation and ERK1/2 signaling are involved in the pathogenesis. However, the underlying fibrillin-1 mutations in the TB5 domain which are in close vicinity to the RGD-containing TB4 domain suggest similar mechanisms. Since we show that miR-1208 is regulated by the fibrillin-1 RGD, it is possible that miR-1208 dysregulation is involved in these fibrillinopathies.

In line with our results on miR-1208's inhibitory effect on fibroblast proliferation, Kim *et al.* reported that miR-1208 inhibited proliferation of human renal cancer cells [169]. However, miR-1208 acts through the mTOR pathway in the cell line used, by targeting the TBC1-domain-containing-kinase. Furthermore, miR-1208 is also reported to be downregulated in cancer, including breast cancer and colon cancer cell lines [167]. Dysregulation of integrins $\alpha\beta3$, $\alpha5\beta1$ or $\alpha\beta6$, which all bind to fibrillin-1 RGD, and elevated pERK1/2 are hallmarks of these cancers [274-281]. Our study demonstrated miR-1208 suppression mediated by fibrillin-1 RGD motif increased both total and phosphorylated ERK1/2 level and cell proliferation. Taken together, these

studies suggest a possible connection of fibrillin-1 RGD-integrin binding, activated ERK1/2 signaling and cancer cell proliferation with decreased miR-1208.

In conclusion, the present study elucidates a novel mechanistic component of the outside-in signaling cascade of fibrillin-1 RGD-integrin interaction which regulates cell proliferation. The fibrillin-1 RGD motif suppresses miR-1208 via c-Src and JNK signaling. This promotes fibroblast proliferation via post-transcriptionally regulating the level of *ERK2* and *MEK1* mRNA. miR-1208 binding efficacies to all predicted binding sites on *ERK2* and *MEK1* were evaluated. These data provide a novel crosstalk between JNK and ERK1/2. The knowledge how fibrillin-1 RGD post-transcriptionally controls ERK1/2 further provides a novel basis to interpret disease mechanisms originating from deficiencies of fibrillin-1.

3.7 Acknowledgements

We thank Dr. J.M. Laberge (Montreal Children's Hospital) for supporting this project with expert advice. We are grateful for the financial support from the Canadian Institutes of Health Research (PJT-162099), the Marfan Foundation (USA), the Genetic Aortic Disorders Association Canada, the China Scholarship Council, and the Hector and Ada Ma Fellowship. We would like to thank Dr. John Presley, McGill University, for proof-reading the manuscript.

Availability of data and material

All data and material are available upon request from the corresponding author.

Contributions

Study conception and design: Rong-Mo Zhang, Dieter P. Reinhardt

Acquisition of data: Rong-Mo Zhang, Karina A. Zeyer, Nadine Odenthal, Yiyun Zhang

Analysis and interpretation of data: Rong-Mo Zhang, Dieter P. Reinhardt

Manuscript writing: Rong-Mo Zhang, Dieter P. Reinhardt

Declarations: The authors have no conflicts of interest.

3.8 Figures and Tables

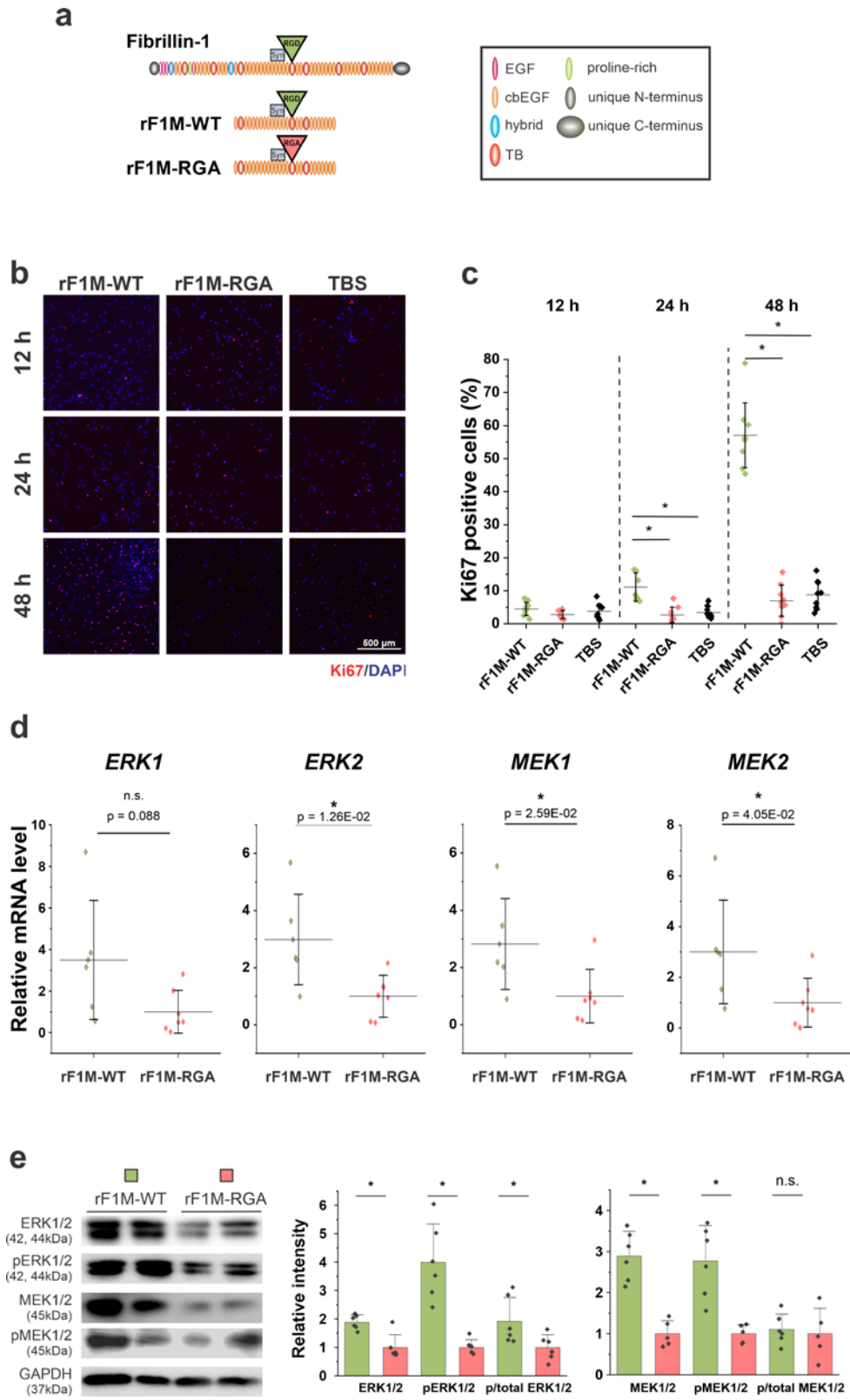


Fig. 3.1 Comparative analysis of fibroblast proliferation, miR-1208 expression and the levels of total and phosphorylated ERK1/2 and MEK1/2 upon interaction with the RGD motif in fibrillin-1.

(a) Recombinant fibrillin-1 fragments (rF1M) span from the cbEGF domains 10 to 31, lacking the N- and C-terminal self-assembly sites. The two fragments differ in the TB4 domain, where rF1M-WT harbors the conserved RGD cell binding sequence, which was mutated to RGA in rF1M-RGA. (b) Representative images of Ki67 staining (red) of fibroblasts seeded on the recombinant fragment-coated 8-well chamber slides for 12, 24 and 48 h. Nuclei were counter-stained with DAPI (blue). TBS buffer without protein was used as control. (c) Quantification of the Ki67 positive fibroblasts seeded under the conditions shown in (b). Triplicates of three experiments using primary fibroblasts from two different donors were quantified. The Y-axis shows the percentage of total cells \pm standard deviation. Two-sample t-test was used to determine significance. * represents p-value < 0.05 . n.s.; not significant. (d) qPCR of *ERK1*, *ERK2*, *MEK1* and *MEK2* mRNA in fibroblasts seeded on the recombinant fragments for 8 h. Comparative mRNA levels were normalized to those obtained on the rF1M-RGA control. Primary fibroblasts from two different donors were used, with triplicate analyses each. Two-sample t-test was performed to test significance. * represents p-value < 0.05 . (e) Representative Western blots of total and phosphorylated ERK1/2 and MEK1/2 protein levels, using lysates of fibroblasts cultured for 24 h on rF1M-WT or rF1M-RGA. Representative GAPDH images from the same blot of pMEK1/2 staining are shown. Western blotting of the fibroblast lysates from two different donors in triplicates were used for quantification and statistical analysis. The relative intensities were first normalized to GAPDH on the same blot, then normalized to respective rF1M-RGA controls. Y-axis data indicate the mean of ERK1/2, pERK1/2, p/total ERK1/2, MEK1/2, pMEK1/2 and p/total MEK1/2 \pm standard deviation, as compared to the control groups. Two sample t-test was used to test the significance (* p-value < 0.05). n.s.; not significant.

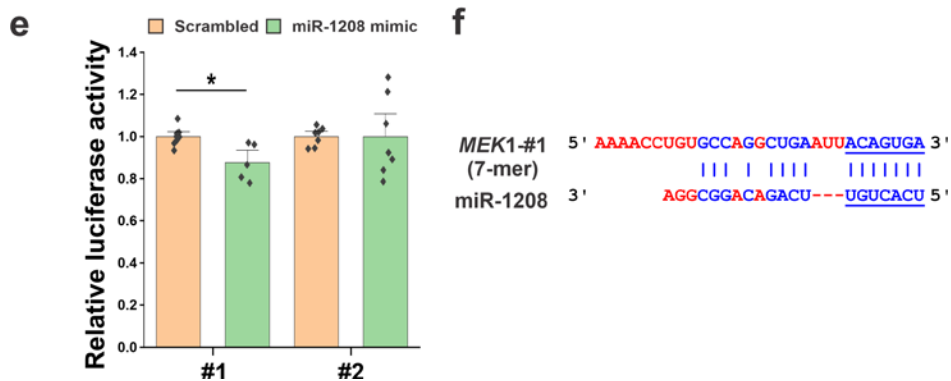
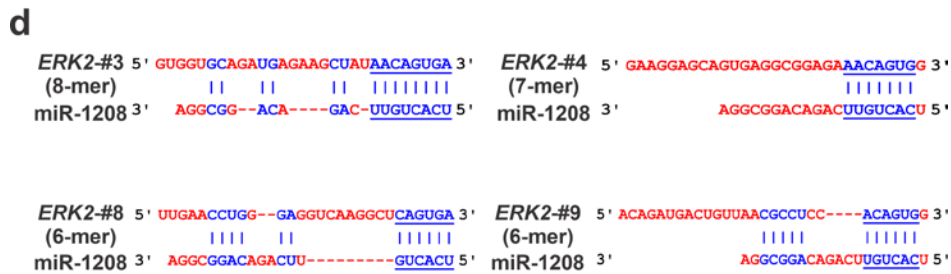
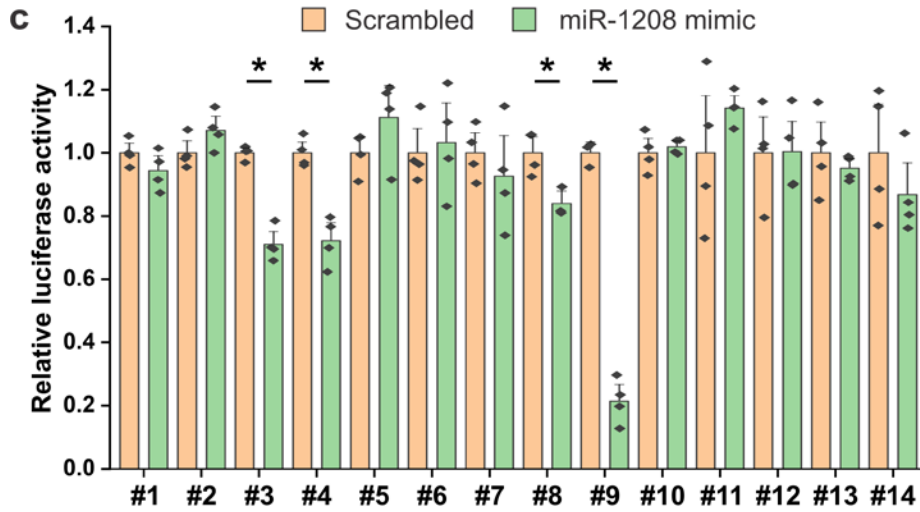
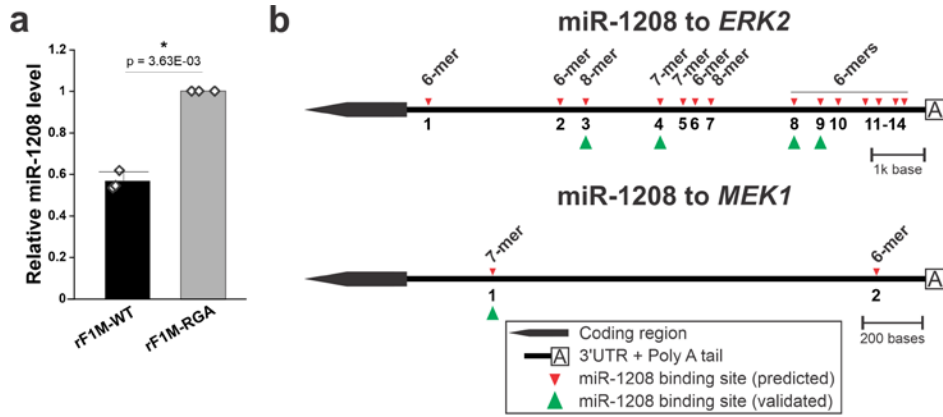


Fig. 3.2 Prediction and validation of the molecular interaction between miR-1208 and the 3'UTR of *ERK2* and *MEK1*.

(a) qPCR quantification of miR-1208 levels in primary fibroblasts seeded in triplicates on rF1M-WT (black bar) or the rF1M-RGA control (grey bar) for 24 h. The relative quantification values for rF1M-RGA were all set to 1. One-sample t-test was performed to test significance. * represents p-value < 0.05. (b) Molecular interaction prediction of miR-1208 binding sites on the 3'UTR of *ERK2* and *MEK1*, using microT-CDS, a module in the DIANA tools (http://diana.imis.athena-innovation.gr/DianaTools/index.php?r=microT_CDS/index). Black bars with poly-A tail (boxed A) represent the 3'UTR of *ERK2* and *MEK1*, thick black arrowheads represent the 3' end of the coding region. Red arrowheads indicate the predicted binding sites for miR-1208, with the numbers of matching nucleotides indicated. Green arrowheads indicate the validated miR-1208 binding sites from c and e. (c and e) Dual luciferase assay using the miRNA target expression vector pmirGLO in HEK293 cells co-transfected with either miR-1208 mimic (green bars) or scrambled control miRNA (orange bars) for 48 h. Each bar represents the results of the assay using one predicted miR-1208 target sequence in *ERK2* or *MEK1* cloned into pmirGLO. The numbers on the X-axes correlate to the numbers indicated in (b). Y-axes show the luciferase activities normalized to the internal control *Renilla* luminescence. The luciferase activity of the scrambled miRNA control was set to 1 for each sample. Quadruplicates were used in (c), octuplicates were quantified and analyzed in (e). Two-sample t-tests were performed to assess statistical significance (* p-value < 0.05). Validated targets sites are indicated by green arrowheads in (b). (d and f) Sequences and alignments of the validated miR-1208 binding sites in *ERK2* and *MEK1*. The matching nucleotides with miR-1208 are indicated in blue, non-matching nucleotides are in red. Matching nucleotides in the miR-1208 seed region are underlined.

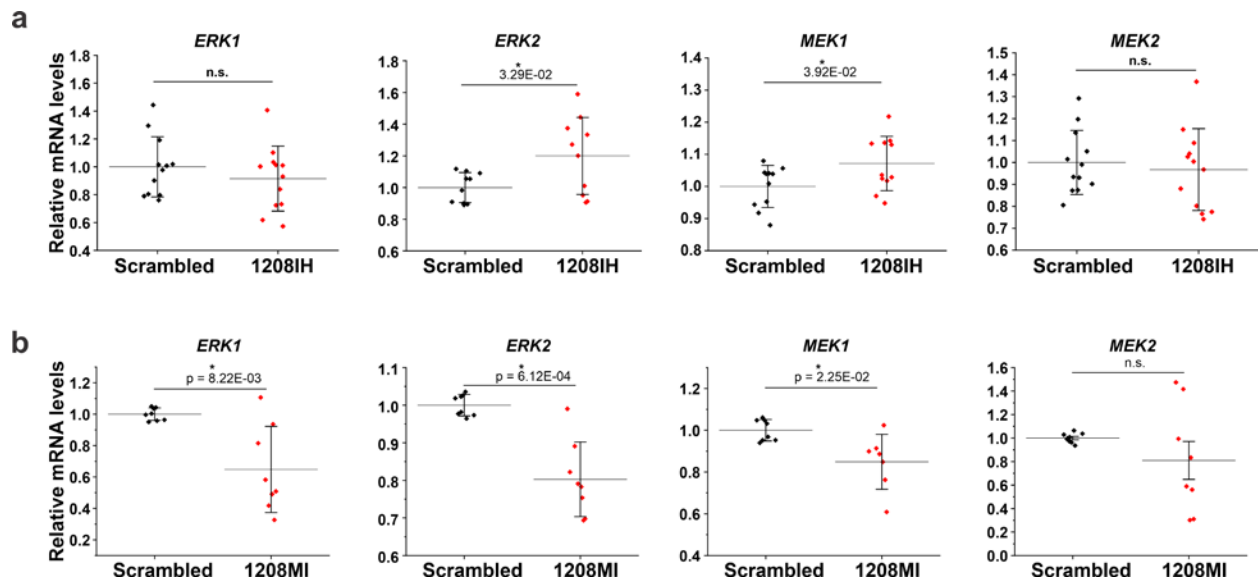


Fig. 3.3 Functional analysis of miR-1208 on the regulation of *ERK* and *MEK* mRNA levels. qPCR analysis of *ERK1*, *ERK2*, *MEK1* and *MEK2* mRNA levels upon miR-1208 inhibition (1208IH, **a**) or overexpression (1208MI, **b**) in primary human skin fibroblasts. 300,000 fibroblasts seeded in 6-well plates were treated for 24 h with 50 nM miR-1208 inhibitors or 5 nM mimics, and scrambled miR controls at the same concentrations. Four experiments using fibroblasts from two different donors and in different passage numbers were used in triplicates or duplicates for quantification. Y-axis values indicate the mean \pm standard deviation, as normalized to the scrambled transfected control. The mean of scrambled samples were set to 1. Two-sample t-test were performed to analyze statistical significance between the means of different groups (* p-value < 0.05).

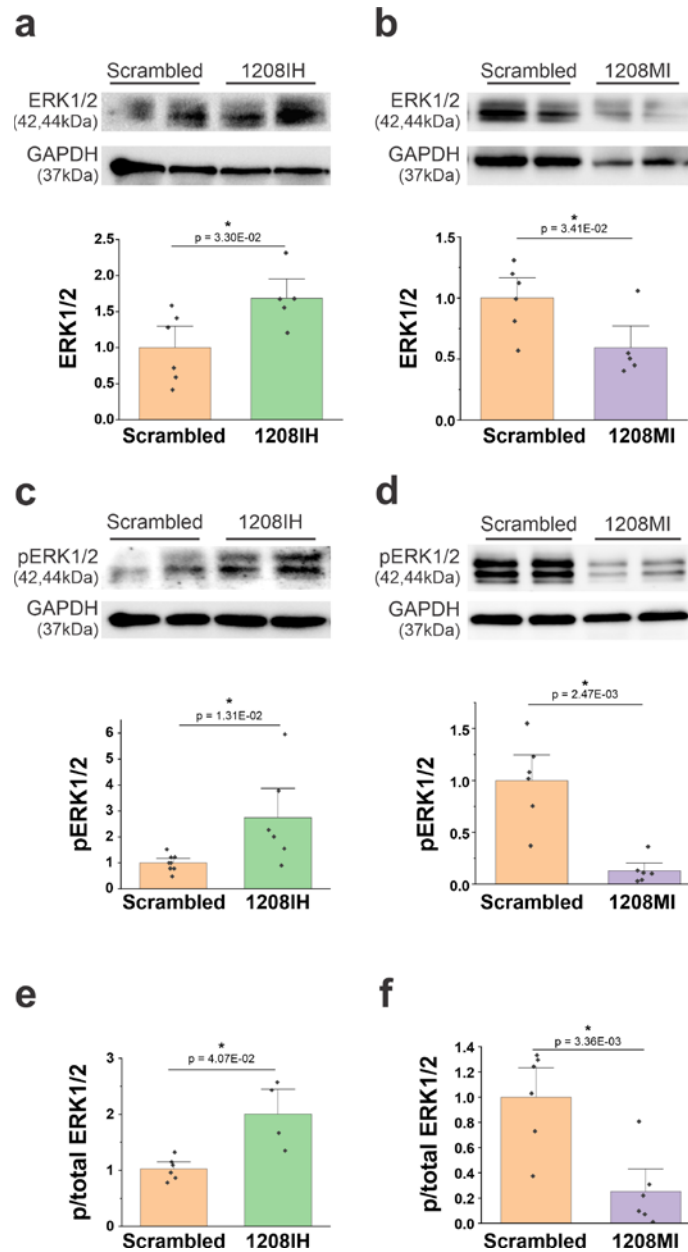


Fig. 3.4 Consequences of miR-1208 modulation on ERK1/2 and pERK1/2 levels

(a-d) Western blotting and quantification of ERK1/2 and pERK1/2 protein levels present in primary fibroblast lysates 48 h after cell seeding and transfection with either 50 nM miR-1208 inhibitor (1208IH) or 5 nM mimic (1208MI), as compared to the respective scrambled controls. 300,000 cells per well were seeded in 6-well plates. Representative Western blots from each condition are shown. (e and f) pERK1/2 to ERK1/2 ratios determined from the analysis shown in (a-d). Three experiments using fibroblasts from two donors and in different passage numbers were performed, with duplicates in each repeated experiment. Quantifications were performed by densitometry of the ERK1/2 and pERK1/2 bands normalized to GAPDH. Two-sample t-test was performed to determine statistical significance (* p-value < 0.05). Error bars indicate standard deviation.

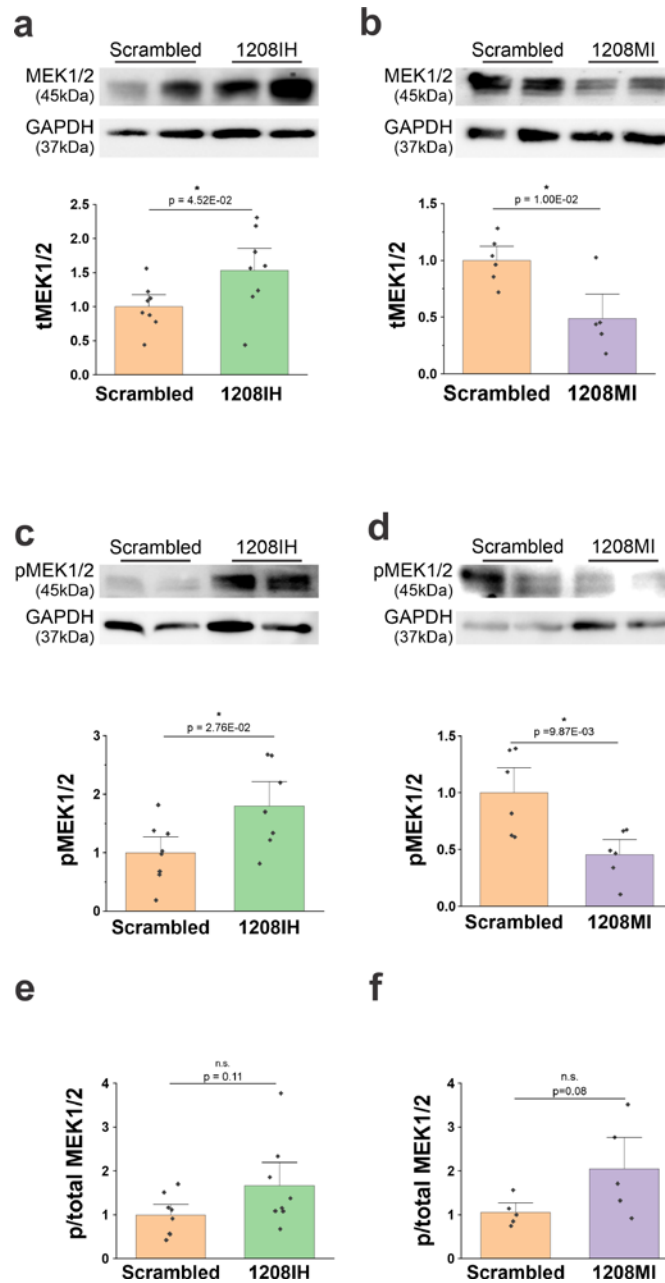


Fig. 3.5 Consequences of miR-1208 modulation on MEK1/2 and pMEK1/2 levels

(a-d) Western blotting and quantification of MEK1/2 and pMEK1/2 protein levels in primary fibroblast lysates prepared 48 h after cell seeding and transfection with either 50 nM miR-1208 inhibitor (1208IH) or 5 nM mimic (1208MI), as compared to scrambled controls. 300,000 cells per well were seeded in 6-well plates. Representative Western blots from each condition are shown. (e and f) pMEK1/2 to MEK1/2 ratios determined from the analysis shown in (a-d). Three experiments using fibroblasts from two donors and in different passage numbers were performed, with duplicates in each repeated experiment. Quantifications were performed by densitometry of the MEK1/2 and pMEK1/2 bands normalized to GAPDH. Two-sample t-test was performed to determine statistical significance (* p-value < 0.05). Error bars indicate standard deviation.

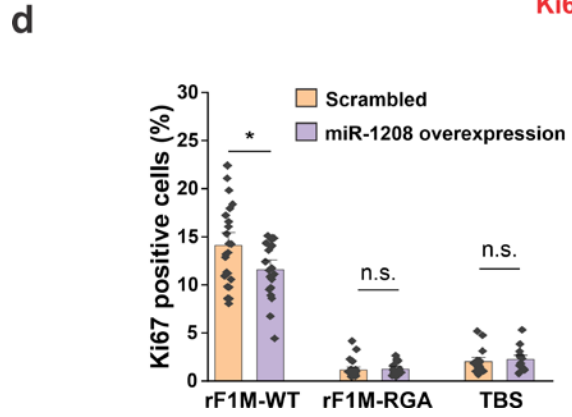
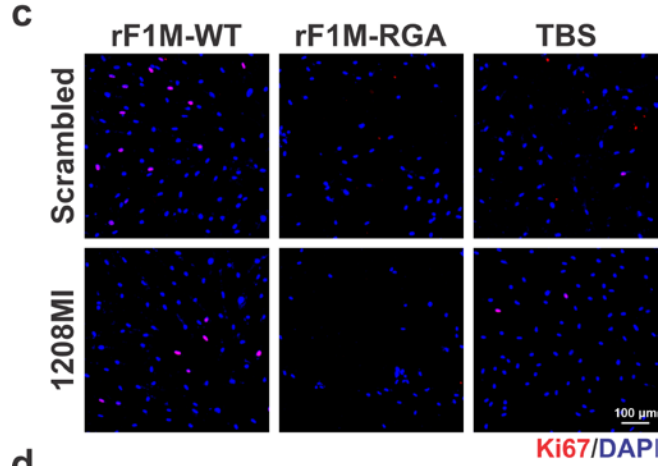
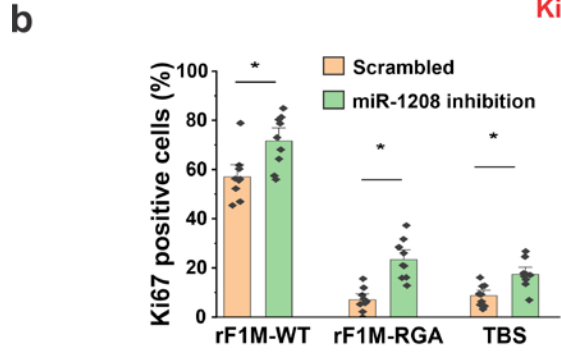
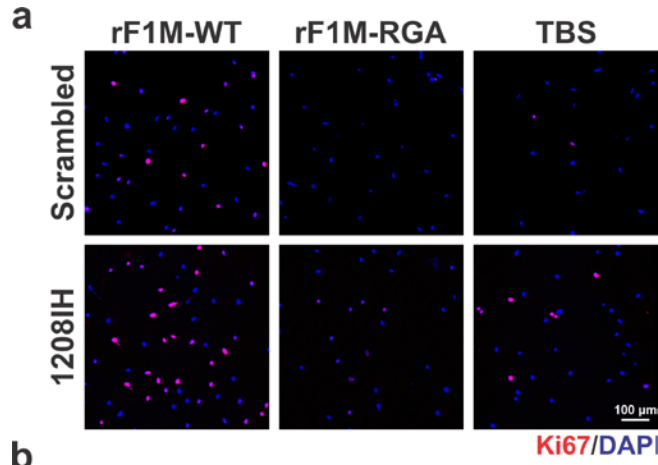


Fig. 3.6 Functional analysis of miR-1208 on fibroblast proliferation

(a and c) Representative Ki67 (red) immunofluorescence staining of fibroblasts transfected with either 50 nM miR-1208 inhibitor (1208IH) or 5 nM miR-1208 mimic (1208MI) for 48 h, compared to the respective scrambled miRNA controls. 10,000 fibroblasts were seeded per well of 8-well chamber slides coated with rF1M-WT or rF1M-RGA at 25 µg/mL or TBS buffer as a control. Cell nuclei are counterstained with DAPI (blue). **(b and d)** Quantification of Ki67 positive cells using ImageJ (45). Y-axis values show the percentage of Ki67 positive cells ± standard deviation. Two-sample t-test was performed to analyze statistical significance (* p-value < 0.05).

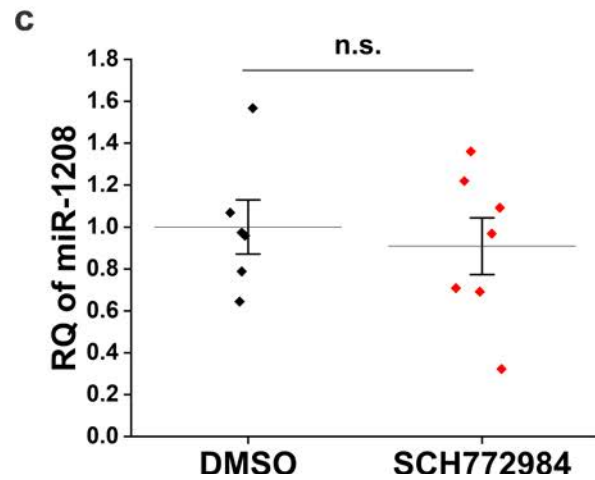
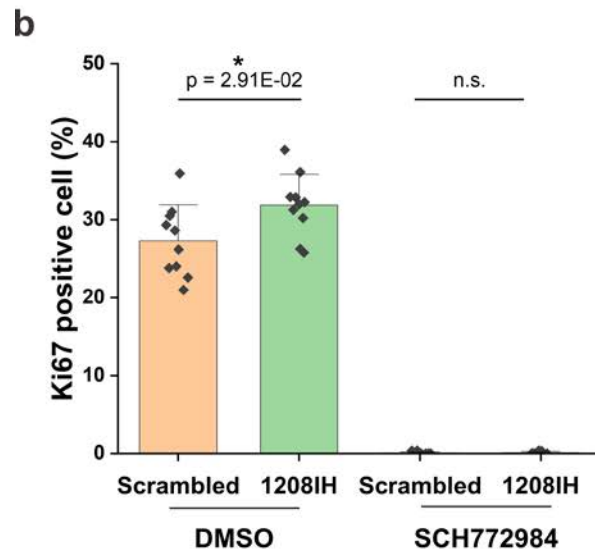
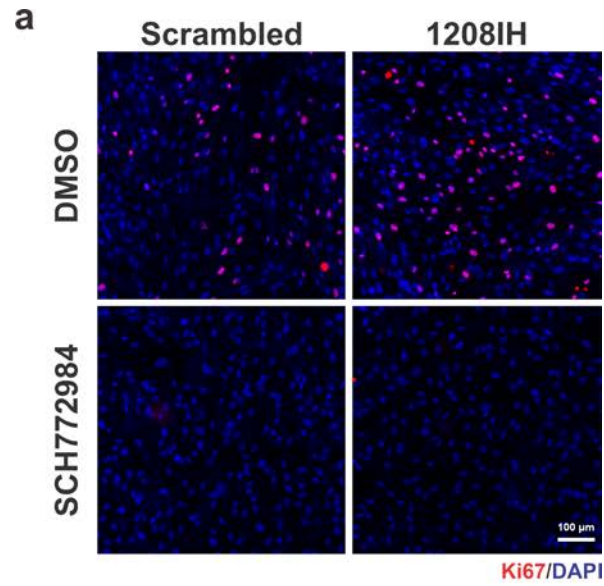


Fig. 3.7 ERK1/2 signaling is required for miR-1208 regulated proliferation

(a) Representative images of immunofluorescence staining for Ki67 (red) conducted 48 h after fibroblast seeding, in the presence of either 50 nM miR-1208 inhibitor (1208IH) or scrambled miRNA. 10 μ M SCH772984 or DMSO control (1:1,000 v/v) was added at cell seeding. Nuclei were counterstained with DAPI (blue) (b) Quantification of Ki67 positive cells shown in (a) using ImageJ, as described in [256]. Y-axis values indicate the percentage of Ki67-positive cells \pm standard deviation. Statistical significance was analyzed with the two-sample t-test (* p-value < 0.05). (c) qPCR of miR-1208 in the cell lysate 24 h after 10 μ M SCH772984 treatment, compared to the DMSO treated group (1:1,000 v/v). To obtain the RNA for qPCR, 300,000 fibroblasts per well were seeded in 6-well plates. Three experiments were performed using fibroblasts from two donors, with duplicates or triplicates of each condition. Statistical analysis was performed using the two-sample t-test (* p-value < 0.05).

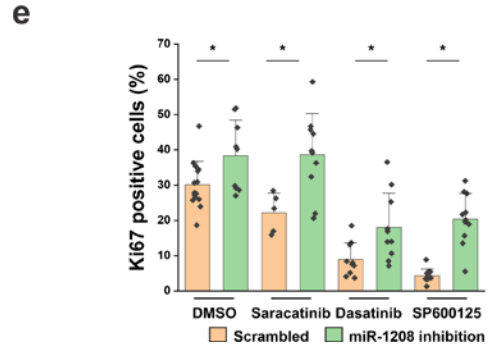
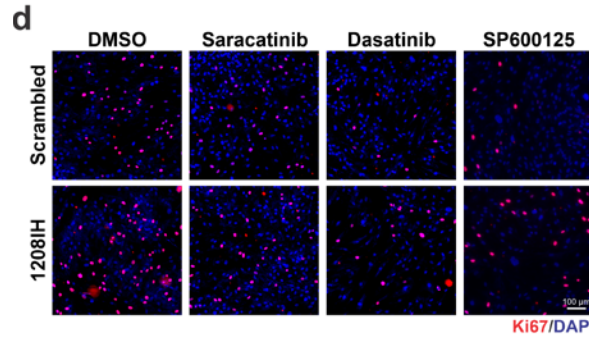
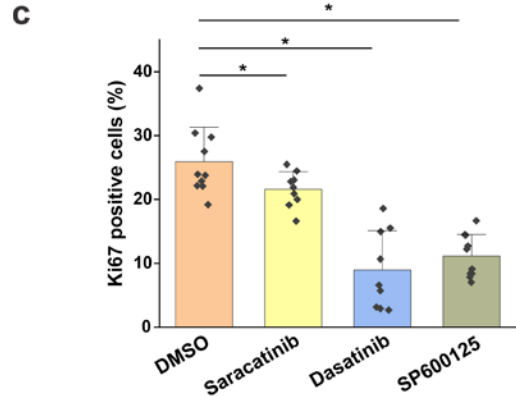
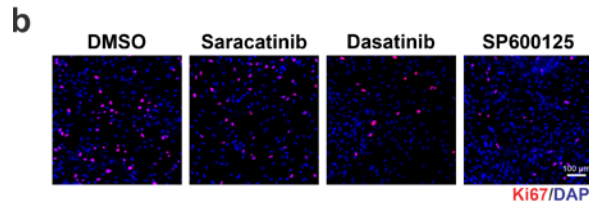
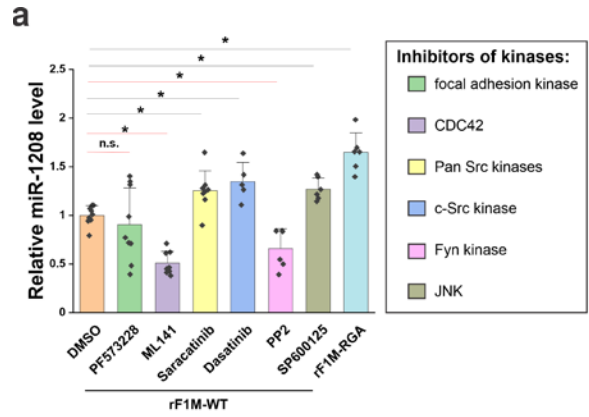


Fig. 3.8 Identification of integrin-activated signaling pathways that regulate miR-1208 expression and cell proliferation

(a) 300,000 fibroblasts were seeded per well in 6-well plates. The miR-1208 levels were determined by qPCR using the cell lysates prepared after the treatment (24 h) with specific inhibitors. FAK inhibitor (PF573228, 10 μ M), CDC42 inhibitor (ML141, 10 μ M), pan-Src kinase inhibitor (Saracatinib, 10 μ M), c-Src kinase inhibitor (Dasatinib, 10 μ M), Fyn kinase inhibitor (PP2, 10 μ M), and JNK inhibitor (SP600125, 20 μ M) were used, as compared to DMSO control (1:1,000 v/v). Three experiments were performed using fibroblasts from two different donors and in different passage numbers, with triplicates in each condition. Y-axis values show the mean (normalized to DMSO-treated condition) \pm standard deviation. Statistics were calculated using the two-sample t-test (* p-value < 0.05), with black lines on top indicating upregulated miR-1208 levels, or red lines showing downregulated levels and non-significant differences, as compared to the DMSO-treated. (b) Ki67 immunofluorescence staining (red) of fibroblasts after 48 h of treatment with Saracatinib, Dasatinib and SP600125, which can upregulate miR-1208 level as shown in (a). 20,000 fibroblasts were seeded per well in 8-well chamber slides. (c) Quantification of Ki67 positive cells in (b), as compared to DMSO control. (d) Ki67 staining images of fibroblasts treated with Saracatinib, Dasatinib and SP600125. Rescue experiments were performed with 50 nM miR-1208 inhibitor (1208IH) or miR scrambled control. DMSO (1:1,000 v/v) was used as buffer control. (e) Quantification of Ki67 positive cells in (d). Statistical analysis was performed using the two-sample t-test (* p-value < 0.05).

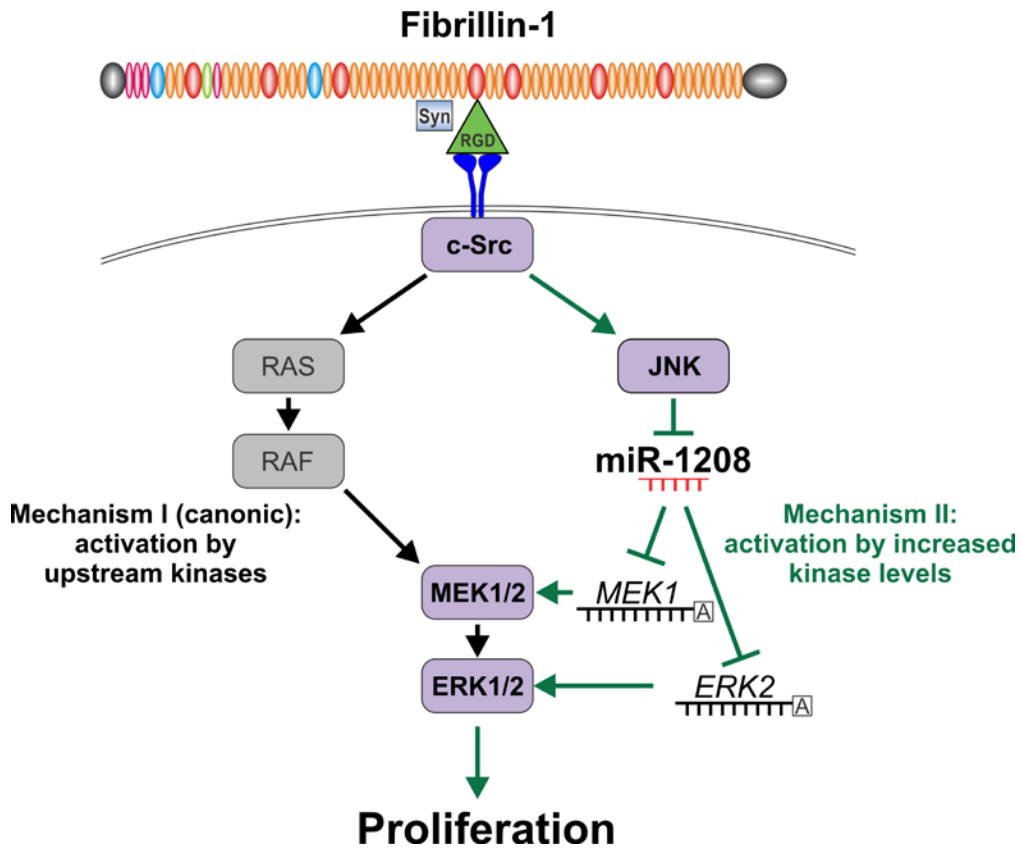


Fig. 3.9 The fibrillin-1 RGD motif activates ERK1/2 signaling and cell proliferation

The schematic shows two mechanisms of ERK1/2 activation upon fibrillin-1 RGD binding. Black arrows indicate the canonical mechanism through the RAS-RAF-MEK1/2-ERK1/2 activation cascade, in which ERK1/2 signaling is activated by the phosphorylation of upstream kinases (mechanism I). Green arrows represent a novel mechanism from the present work, showing that fibrillin-1 RGD-cell interaction can post-transcriptionally activate ERK1/2 signaling via miR-1208 suppression. In this process, fibrillin-1 RGD-cell interaction activate c-Src and JNK, which suppress miR-1208 expression. The decreased miR-1208 expression leads to elevated *ERK2* and *MEK1* mRNA levels, which in turn increase the total and phosphorylated ERK1/2 and MEK1/2 protein levels. This mechanism constitutes mechanism II, in which ERK1/2 signaling is activated by increased kinase levels.

Table S3.1 Sequences of the inserts into pmirGLO vector for dual luciferase assays

ERK2- miR1208- #1	5'-TCGAG TA GGATCC TAGT <i>ctactacctagggcactttaagtcagtga</i> AT T -3' 3'- C AT CCTAGG ATCA <i>gatgatggatcccgtgaaattcagtcact</i> TA AGATC -5'
ERK2- miR1208- #2	5'-TCGAG TA GGATCC TAGT <i>tactgtattgtgtgtgcagtgccacagtgt</i> AT T -3' 3'- C AT CCTAGG ATCA <i>atgacataaacacacacgtcacgtgtcaca</i> TA AGATC -5'
ERK2- miR1208- #3	5'-TCGAG TA GGATCC TAGT <i>gtgggtgcagatgagaagctataaacagtga</i> AT T -3' 3'- C AT CCTAGG ATCA <i>caccacgtctactcttcgatattgtcact</i> TA AGATC -5'
ERK2- miR1208- #4	5'-TCGAG TA GGATCC TAGT <i>gaaggagcagtgaggcggagaaacagtgg</i> AT T -3' 3'- C AT CCTAGG ATCA <i>cttcctcgtcactccgcctctttgtcacc</i> TA AGATC -5'
ERK2- miR1208- #5	5'-TCGAG TA GGATCC TAGT <i>ctgcccgcgctggaagggcctgcagtga</i> AT T -3' 3'- C AT CCTAGG ATCA <i>gacggggcggcacttcccggacgtcact</i> TA AGATC -5'
ERK2- miR1208- #6	5'-TCGAG TA GGATCC TAGT <i>gttgtctggggctgcctggggaactgtga</i> AT T -3' 3'- C AT CCTAGG ATCA <i>caacagaccccgcaggacccttgacact</i> TA AGATC -5'
ERK2- miR1208- #7	5'-TCGAG TA GGATCC TAGT <i>tgagaccagtttgagagtcaggcagtga</i> AT T -3' 3'- C AT CCTAGG ATCA <i>actctggtcaaacctctcagtcctcact</i> TA AGATC -5'
ERK2- miR1208- #8	5'-TCGAG TA GGATCC TAGT <i>ttgaacctgggaggtcaaggctccagtga</i> AT T -3' 3'- C AT CCTAGG ATCA <i>aacttggaccctccagttccgaggtcact</i> TA AGATC -5'
ERK2- miR1208- #9	5'-TCGAG TA GGATCC TAGT <i>acagatgactgttaacgcctccacagtgg</i> AT T -3' 3'- C AT CCTAGG ATCA <i>tgtctactgacaattgcggaggtgtcacc</i> TA AGATC -5'
ERK2- miR1208- #10	5'-TCGAG TA GGATCC TAGT <i>ttgaaccgggagggcggaggttgcagtga</i> AT T -3' 3'- C AT CCTAGG ATCA <i>aacttgggccctccgcctccaacgtcact</i> TA AGATC -5'
ERK2- miR1208- #11	5'-TCGAG TA GGATCC TAGT <i>caaaccggagaaagtcatactgtcagtga</i> AT T -3' 3'- C AT CCTAGG ATCA <i>gtttggcctctttcagtatgacagtcact</i> TA AGATC -5'
ERK2- miR1208- #12	5'-TCGAG TA GGATCC TAGT <i>acagggccccaaggctgggagcacagtgt</i> AT T -3' 3'- C AT CCTAGG ATCA <i>tgtcccggggttccgaccctcgtgtcaca</i> TA AGATC -5'
ERK2- miR1208- #13	5'-TCGAG TA GGATCC TAGT <i>ggccccggggagggagccagccacagtgt</i> AT T -3' 3'- C AT CCTAGG ATCA <i>ccggggcccctccctcggtcggtgtcaca</i> TA AGATC -5'
ERK2- miR1208- #14	5'-TCGAG TA GGATCC TAGT <i>gttgggtgggtgatagtggggtcacagtgg</i> AT T -3' 3'- C AT CCTAGG ATCA <i>caaccaccactatcaccacagtgacc</i> TA AGATC -5'
MEK1- miR1208- #1	5'-TCGAG TA GGATCC TAGT <i>aaaacctgtgccaggetgaattacagtga</i> AT T -3' 3'- C AT CCTAGG ATCA <i>ttttggacacgggtccgacttaatgtcact</i> TA AGATC -5'
MEK1- miR1208- #2	5'-TCGAG TA GGATCC TAGT <i>gctttgtcatgcctgtgaggtggcagtga</i> AT T -3' 3'- C AT CCTAGG ATCA <i>cgaaacagtacggacactccaccgtcact</i> TA AGATC -5'

The sequences of the oligonucleotides inserted into pmirGLO vector for dual luciferase assays are listed. # numbers indicated the predicted binding site of miR-1208 in *ERK2* or *MEK1* as red arrow heads indicated in Fig.2b. Sticky ends formed after annealing were *XhoI* (green) and *XbaI* (purple). The inserted *BamHI* site used for screening of positive clones are underlined. The predicted binding sequence for miR-1208 are in lower case. The remaining nucleotides were linkers.

Table S3.2 Primers used for mRNA qPCR

Gene (orientation)	Sequence 5'-3'	Reference
hERK1-forward	GCGCTACACGCAGTTGCAGTACA	Thiaville <i>et al.</i> (2008) J Biol Chem 283:10848-10857 [282]
hERK1-reverse	TGATGGCCACGCGAGTCTTG	
hERK2-forward	CGCCGAAGCACCATTCAAGTT	
hERK2-reverse	TCCTGGCTGGAATCTAGCAGTCTCT	
hMEK1-forward	TGAGAAGATCAGTGAGCTGG	Schweyer <i>et al.</i> (2004) Br J Cancer 91:589-598 [283]
hMEK1-reverse	ACTTGATCCAGAGAACCTCC	
hMEK2-forward	AACTCAAAGACGATGACTTCG	
hMEK2-reverse	CCATGCAAATGCTGATCTCC	
hGAPDH-forward	GGTCTCCTCTGACTTCAACA	Zeyer <i>et al.</i> (2019) J Mol Biol 431:401-421 [245]
hGAPDH-reverse	AGCCAAATTCGTTGTCATAC	

Supplementary Fig. 1

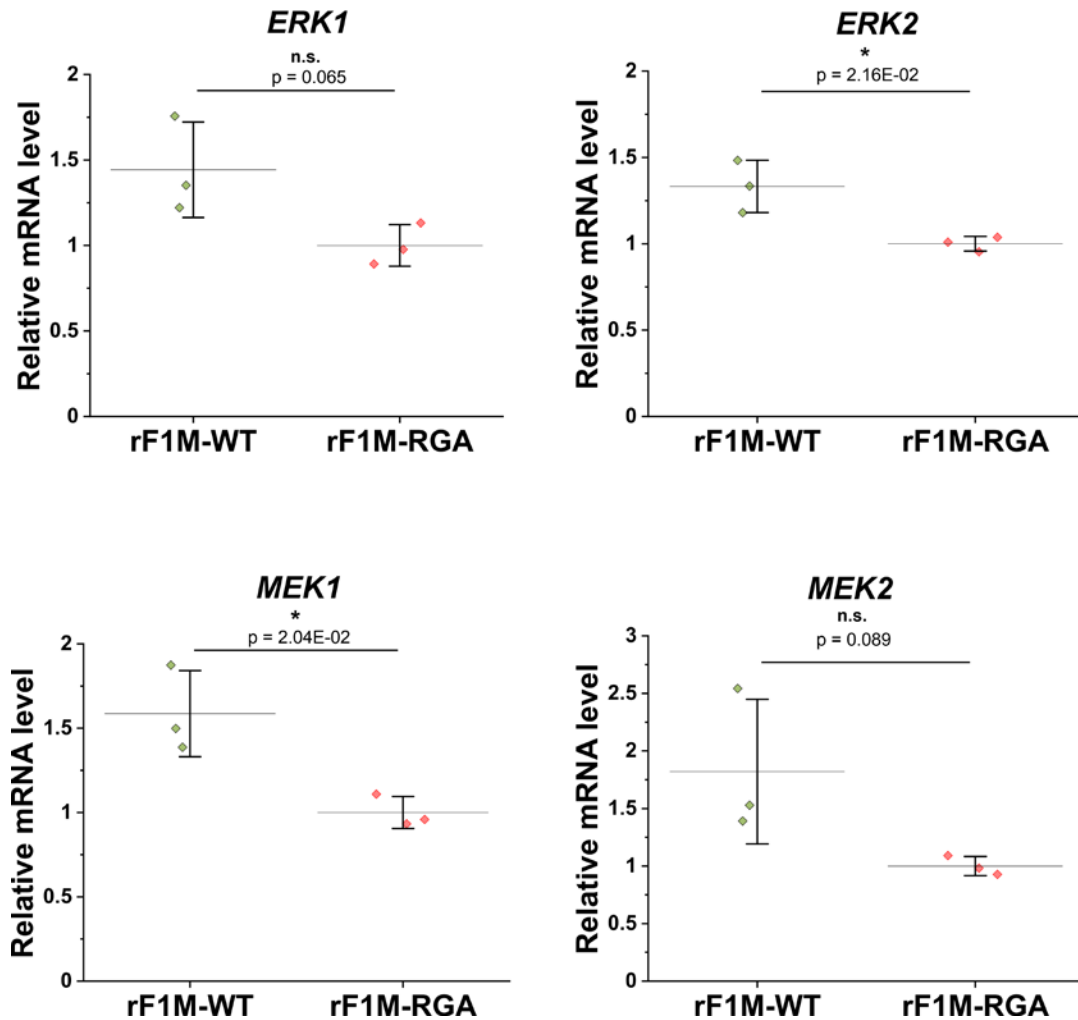


Fig. S3.1 Comparative analysis of ERK1/2 and MEK1/2 in MSU1.1 upon fibrillin-1 RGD motif binding

qPCR of ERK1, ERK2, MEK1 and MEK2 mRNAs extracted in triplicates from MSU1.1, a foreskin fibroblast cell line, seeded on the recombinant fragments for 8 h. 600,000 MSU1.1 cells were seeded per well in 6-well plate. Relative mRNA levels were normalized to rF1M-RGA. Two-sample t-tests were performed to test significance. * represents p-value less than 0.05.

Supplementary Fig. 2

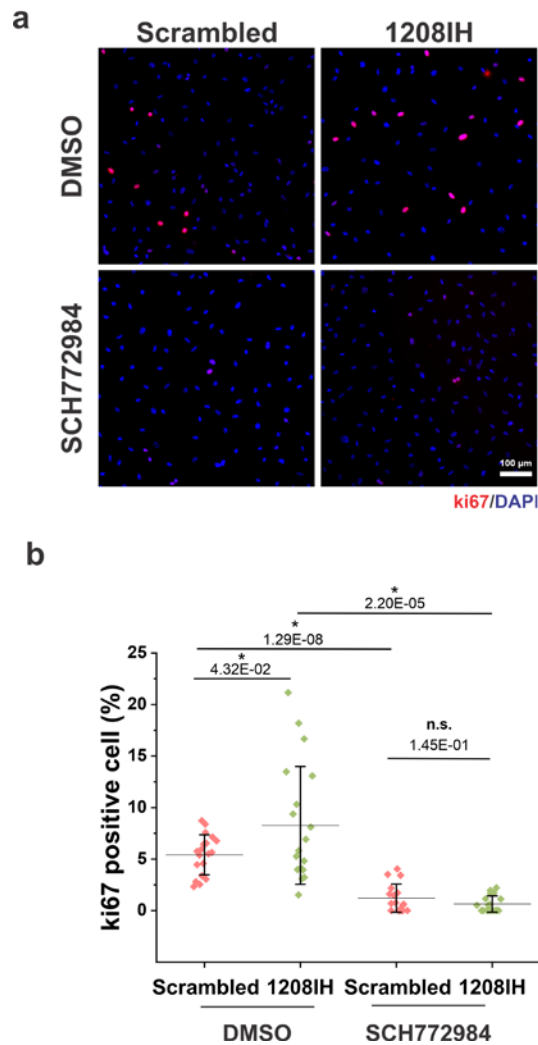


Fig. S3.2 ERK1/2 signaling is required for miR-1208 regulated proliferation under serum-free condition

(a) Representative images of immunofluorescence staining for Ki67 (red) conducted 48 h after fibroblast seeding, in the presence of either 50 nM miR-1208 inhibitor (1208IH) or scrambled miRNA, under serum-free condition. 10 μ M SCH772984 or DMSO control (1:1,000 v/v) was added at cell seeding. 20,000 fibroblasts were seeded per well in 8-well chamber slides. Nuclei are counterstained with DAPI (blue) (b) Quantification of Ki67 positive cells shown in (a) using ImageJ. Values indicate the percentage of Ki67-positive cells \pm standard deviation. Statistical significance was analyzed with the two-sample t-test (* p-value < 0.05). n.s.; not significant.

**CHAPTER 4 GENETIC PROFILING OF THORACIC AORTIC ANEURYSMS
REVEALS THE ROLE OF MIR-122 IN PATHOGENETIC INFLAMMATORY
PATHWAYS**

**Genetic profiling of thoracic aortic aneurysms reveals the role of miR-122 in
pathogenetic inflammatory pathways**

Rong-Mo Zhang,¹ Bhama Ramkhelawon,² and Dieter P. Reinhardt^{1,3*}

¹ Faculty of Medicine, McGill University, Montreal, Canada

² Department of Surgery, New York University School of Medicine, New York, USA

³ Faculty of Dentistry, McGill University, Montreal, Canada

* Correspondence to Dieter P. Reinhardt: Department of Anatomy and Cell Biology, McGill University, 3640 University Street, Montreal, Quebec, H3A 0C7, Canada. Phone: +1 514.398.4243. E-mail: dieter.reinhardt@mcgill.ca

4.1 Preface:

Chapters 2 and 3 demonstrated that fibrillin-1-controlled miRNAs participate in the fibrillin-1-promoted focal adhesion formation and fibroblast proliferation. Fibrillin-1 containing microfibrils connect aortic smooth muscle cells to the elastic laminae in the aortic tunica media. Deficiency of fibrillin-1 microfibrils causes MFS, a connective tissue disorder characterized by progressive TAA. *Fbn1^{mgR/mgR}* is a fibrillin-1 hypomorphic MFS mouse model with reduced normal fibrillin-1 containing microfibrils. Typical disease symptoms include fragmented elastic laminae and altered smooth muscle cell phenotypes in the aneurysmal aortic tissues. Given the data described in chapter 2 and 3, it is hypothesized that miRNAs are also differentially regulated in the dilated aortae of the mouse model and of human patients with TAA. To test this hypothesis, the experiments described in this chapter profiled the differentially expressed genetic networks in the ascending aortae of *Fbn1^{mgR/mgR}* mice and of human patients with TAA, and investigated the role of fibrillin-1-controlled miRNAs in TAA pathogenesis. The connections between reduced fibrillin-1 and several key phenotypes of the *Fbn1^{mgR/mgR}* aortae were explored, including inflammation, hypoxia and activated ERK1/2.

4.2 Abstract

Background: Thoracic aortic aneurysms (TAA) are characterized by elevated cytokine levels. The underlying molecular mechanisms, however, are not well understood. Although several dysregulated miRNAs were found in TAA tissue, the involvement of miRNAs in TAA inflammation was not explored. This study investigated whether dysregulated miRNAs are involved in the inflammatory responses relevant to TAA.

Methods: The hypomorphic fibrillin-1 mutant mouse model *Fbn1^{mgR/mgR}* was used to identify dysregulated miRNA networks. Common dysregulated pathways in TAA tissues of mouse and human were identified using *Fbn1^{mgR/mgR}* mRNA microarray and human RNAseq data. Bioinformatic analyses were used to predict the core miRNAs involved in the common differentially regulated pathways. Functional analyses of the selected miRNAs were performed using smooth muscle cell cultures and *ex vivo* aorta cultures.

Results: With the progression of aortic dilation, the number of dysregulated miRNAs (>2-fold) increased from 17 (4-weeks) to 129 (10-weeks). Bioinformatic analyses of those miRNAs predicted that inflammatory responses were dysregulated starting from early aortic dilation to the TAA stage. Genetic analyses showed that the inflammatory response-relevant pathways were top hits in both TAA tissues of mouse and human. Bioinformatic and functional analyses between differentially expressed miRNAs and mRNAs at 10-weeks revealed that miR-122, the most downregulated miRNA in TAA tissue, post-transcriptionally regulated the mRNA levels of pro-inflammatory cytokines, *Ccl2* and *Il1 β* . This correlated with the observed elevated inflammatory response in the aneurysmal aorta of *Fbn1^{mgR/mgR}* mice. Additionally, we identified that elevated ERK1/2 signaling, haploinsufficiency of fibrillin-1 in the matrix, and hypoxic conditions constitute the upstream regulators of miR-122.

Conclusions: Our study identified the involvement of miRNAs in inflammatory responses starting from early aortic dilation. miR-122 was the core regulatory miRNA of inflammatory responses in *Fbn1^{mgR/mgR}* aneurysmal aortae. Elevated ERK1/2 signaling, deficient fibrillin-1 in the matrix, and hypoxic conditions in aneurysmal aortae led to the downregulation of miR-122.

Keywords: thoracic aortic aneurysm; fibrillin-1 deficiency; hypoxia; miR-122; inflammation; ERK1/2 signaling

Abbreviations used:

AAA	abdominal aneurysmal aortae
DAPI	4', 6-diamidino-2-phenylindole
DIG	digoxigenin
ELISA	enzyme-linked immunosorbent assay
ERK1/2	extracellular signal-regulated kinases 1/2
FBS	fetal bovine serum
HIF-1 α	hypoxia-inducible factor 1 α
MAPK	Mitogen-activated protein kinase
MFS	Marfan syndrome
MMP	matrix metalloproteinase
PBS	phosphate-buffered saline
PSG	penicillin-streptomycin-glutamine
SDS	sodium dodecyl sulfate
SMA	smooth muscle actin
TAA	Thoracic aortic aneurysm
TGF- β	Transforming growth factor β

4.3 Introduction

Thoracic aortic aneurysm (TAA) is one of the most fatal histopathologic abnormalities in North America, characterized by fragmentation of the elastic laminae, proteoglycan accumulation, and loss of smooth muscle cells [284]. Surgical repair of the aorta is usually performed when dilation reaches approximately twice the normal diameter (5.0–5.5 cm) [92]. However, for the aneurysms detected incidentally and below the threshold for surgical repair, efficient therapeutic interventions to prevent aneurysm progression are lacking. To address this problem, elucidating the molecular mechanisms and genetic basis underlying TAA pathogenesis is essential. Although the majority of patients do not have a family history of disease, single gene mutations cause up to 20% of TAAs [285]. Marfan syndrome (MFS, MIM# 154700), an autosomal dominantly inherited connective tissue disorder caused by heterozygous mutations in the fibrillin-1 gene is characterized by progressive TAA [12] with an estimated prevalence of 2-3 in 10,000 individuals [79]. Today, more than 3,000 mutations are known in fibrillin-1 that cause MFS [80].

Fibrillin-1 is a 350 kDa glycoprotein that is secreted and assembled in the extracellular matrix of multiple connective tissues, including but not limited to aorta, skin, bone, and eye. It comprises the core of fibrillin-containing microfibrils, which provide the principal scaffold for elastic fiber formation required for elastic tissue properties. Fibrillin-1 microfibrils in the aorta connect the smooth muscle cells with elastic lamellae [286]. Disrupted smooth muscle cell mechanosensing caused by fibrillin-1 mutations is considered as primary driver of TAA formation in MFS (for review see Milewicz *et al.* [287]). This view is further supported by the fact that mutations in proteins controlling smooth muscle cell contractility, including *MYH11* [99], *ACTA2* [100], *PRKG1* [102] and *TES* [101], also lead to TAA formation. Fibrillin-1 microfibrils also regulate the bioavailability of latent TGF- β complexes [71], and TGF- β signaling is upregulated in mouse and

human MFS [70,288]. Transforming growth factor- β (TGF- β) upregulation is likely a secondary response of smooth muscle cells to correct a fibrillin-1 deficient matrix [106]. Neutralization of TGF- β results in stage-dependent consequences [289]. Blocking TGF- β signaling in young mice at early stages of TAA formation worsened aneurysm formation, whereas it ameliorated TAA progression at later stages. Thus, investigating the underlying molecular mechanisms at both early and late stages of TAA pathogenesis and the involvement of smooth muscle cells are critical to advance the development of novel therapeutic approaches to slow TAA progression.

Inflammatory cell infiltrations into the aortic adventitia and outer media were observed in *Fbn1^{mgR/mgR}* and *Fbn1^{C1039G/+}* mouse models of MFS [86,88,290,291]. Pro-inflammatory cytokines, including CCL2 [135], IL-1 β [138] and IL-6 [135,137] are upregulated in TAA mouse models or human patients. Besides the classical role as chemotaxis cues for inflammatory cells, cytokines can also induce matrix metalloproteinase (MMP) secretion and loss of the smooth muscle cells contractile phenotype. Although little is known how cytokines regulate smooth muscle cells *in vivo*, *in vitro* results have shown that IL-1 β can promote secretion of MMP1, 2, 3 or 9 [292,293]. Furthermore, fibrillin-1 fragments and elastin degradation products can serve as chemotactic stimulators [140], contributing to the inflammatory response in TAA. In regard to the differentiation of smooth muscle cells, IL-1 β was shown to suppress the expression of smooth muscle cell contractile markers, including α -smooth muscle actin (SMA), smooth muscle myosin heavy chain, calponin-1, and SM22[294]. CCL2 and IL-6 from monocytes or purified recombinant proteins also suppressed α -SMA expression, myosin heavy chain and calponin-1 in smooth muscle cells *in vitro* [295]. These data stress the detrimental role of CCL2, IL-1 β and IL-6 on aortic wall integrity and smooth muscle contractility at TAA lesions. Elevated MMP2 and MMP9 are associated with smooth muscle phenotype changes at the aneurysmal lesions in MFS patients

[296,297] and in *Fbn1^{mgR/mgR}* mice [130,298]. Thus, it is important to investigate how CCL2, IL-1 β and IL-6 are regulated during TAA pathogenesis.

Transcription factor hypoxia-inducible factor 1 α (HIF-1 α) is a master regulator of oxygen homeostasis, protecting cells under hypoxic conditions by controlling angiogenesis, erythropoiesis, and glycolysis [142]. *Hif-1 α ^{-/-}* mice die on embryonic day 10.5 with cardiac defects, vascular malformations, and impaired erythropoiesis [299]. HIF-1 α was elevated in both TAA and abdominal aneurysmal aortae (AAA) tissue on the mRNA and protein levels [147,300]. Rapamycin, an inhibitor for mTOR signaling and HIF-1 α accumulation [301], can attenuate TAA in *Fbn1^{C1039G/+}*, via suppressing extracellular signal-regulated kinases 1/2 (ERK1/2) [148]. Rapamycin also ameliorates β -aminopropionitrile-induced TAA and pancreatic elastase-induced AAA via reducing MMP-2 and 9 and mural macrophage infiltration [302,303]. Inhibition of HIF-1 α , using digoxin and 2-methoxyestradiol, have been shown to ameliorate angiotensin II induced AAA [304]. However, a smooth muscle cell specific *Hif-1 α* knockout displayed detrimental effects on β -aminopropionitrile and angiotensin II-induced aortic aneurysms by reducing lysyl oxidase and tropoelastin mRNA [149]. These data suggest that elevated HIF-1 α is closely associated with aneurysm development, but the underpinning mechanisms need to be elucidated. Moreover, while the regulatory role of hypoxia on the inflammatory response of immune cells are well described [305,306], whether and how hypoxia influences the inflammatory responses of aortic smooth muscle cells in the pathology of aneurysms are not understood.

miRNA is a family of small non-coding RNAs which promote the degradation and suppresses the translation of target mRNA via RNA-induced silencing complex [191]. miRNAs constitute a regulating network essential for the aortic homeostasis as outlined below. Vascular smooth muscle

cell-specific knockout of *Dicer*, an endoribonuclease required for miRNA maturation, results in lethality at embryonic day 16 due to severe hemorrhage and dilated vessels [157]. miRNA profiles in the tissue or plasma of patients with TAA (including MFS) were investigated, providing candidates to study their involvement in aneurysm pathogenesis or as potential markers for TAA [307-310]. Among them, several specific miRNAs have been identified to regulate aortic aneurysm formation. miR-29b, which inhibits the expression of multiple extracellular matrix (ECM) genes including *COL3A1*, is upregulated in the ascending aorta of *Fbn1^{C1039G/+}* mice [159]. Inhibition of miR-29b by locked nucleic acid oligonucleotides can rescue aneurysmal progression in both MFS and AAA mouse models [159,195]. Lentiviral overexpression of miR-21 and miR-24 slows AAA progression, by targeting the mRNA of phosphatase and tensin homolog protein and chitinase 3-like 1, respectively [161,311]. These data show that miRNAs are important players in aneurysm progression. Given the importance of intervention time in treating TAA of MFS, it is important to compare the dysregulated miRNAs between early and late stage of TAA pathogenesis. In our current study, we investigated the dysregulated miRNAs at both early (4-week) and late stages (10-week) of TAA progression in *Fbn1^{mgR/mgR}* mice.

4.4 Results

4.4.1 Characterization of the ascending aortic aneurysms in *Fbn1^{mgR/mgR}* mice

To study the genetic dysregulation during pathogenesis of TAA in MFS, we used *Fbn1^{mgR/mgR}* mice [86]. First, we investigated whether male and female *Fbn1^{mgR/mgR}* mice developed similar or different aortic aneurysms. Images of gross aortae were recorded of freshly isolated thoracic aortae at 4-weeks and 10-weeks of age from both sexes (Fig. 4.1A-D). At 4-weeks of age, male *Fbn1^{mgR/mgR}* mice already displayed ascending aortic dilations (1.2-fold enlargement) compared to wild-type mice, but not the female mice. At 10-weeks of age, the dilation in male *Fbn1^{mgR/mgR}* mice developed into aneurysms (2.1-fold enlargement). For female *Fbn1^{mgR/mgR}* mice at 10-weeks, the diameter was 1.5-fold larger than in wild-type mice. These results demonstrate that male *Fbn1^{mgR/mgR}* mice presented with a stronger phenotype in TAA progression, while female mice showed delayed aortic dilation. Since we were interested in large effect sizes, we decided to use male mice for further studies. Fig. 4.1E shows representative cross-sections of ascending aortae of 10-week old male wild-type and *Fbn1^{mgR/mgR}* mice including the autofluorescence originating from elastic laminae, the α -smooth muscle actin staining, and the fibrillin-1 staining of the tunica media. Consistent with the gross anatomical analyses, the lumen of the ascending aortae was 2-fold larger in *Fbn1^{mgR/mgR}* mice than in wild-type mice, and the aortic tunica media was 1.4-fold thicker (Fig. 4.1F). Corresponding with the hypomorphic *Fbn1* gene expression in the *Fbn1^{mgR/mgR}* mice, fibrillin-1 staining of the ascending aortae decreased at the aneurysmal site of *Fbn1^{mgR/mgR}* mice to 37% of the wild-type level.

4.4.2 Time-dependent miRNA profiling of ascending aortae of *Fbn1^{mgR/mgR}* mice

Our previous studies have shown that cell-fibrillin-1 interaction regulates miRNAs [245]. Activated ERK1/2 signaling, which are higher in aneurysmal aortae of MFS mice [271], can also control miRNA expression in multiple cell types [258]. These data suggest that miRNAs could be differentially regulated in wild-type versus *Fbn1^{mgR/mgR}* aortae, which are characterized by deficient fibrillin-1 deposition in the media (see Fig. 4.1E). To explore whether and how miRNAs are differentially regulated during the progression of aortic dilation, two time points were chosen to perform miRNA microarray analyses in male mice based on the initial characterization at the early stage of aortic dilation (4-weeks) and at the fully developed aneurysm stage (10-weeks). At 4-weeks, 3 miRNAs were downregulated and 14 upregulated more than 2-fold (Fig. 4.2A and B). At 10-weeks, the number of differentially regulated miRNAs (>2-fold) increased to 129 with 5 down- and 124 upregulated miRNAs (Fig. 4.2D). Figure 4.2E shows the top 3 down- and top 20 up-regulated miRNAs in 10-week ascending aortic tissue. miR-122 was the most downregulated with 5.8-fold lower expression in the *Fbn1^{mgR/mgR}* compared to the wild-type tissues. Bioinformatic prediction using mirPath v.3 revealed inflammatory responses (red) among the top hits regulated by the differentially expressed miRNAs at early and late stages of aneurysm formation (Fig. 4.2C and F). ECM/cell adhesion relevant pathways were marked in green. Mitogen-activated protein kinase (MAPK) related pathways were marked in orange, Contractility/cytoskeleton related pathways were in purple. Additional to profiling the differentially regulated miRNA networks, our results suggested, at the first time, that inflammatory, ECM/cell adhesion, MAPK and cell contractility relevant pathways were dysregulated before the formation of TAA, starting from early stage of aortic dilation.

4.4.3 mRNA profiling of ascending aortae of *Fbn1^{mgR/mgR}* mice

To determine differentially regulated mRNAs, we performed mRNA microarray analyses of aortic aneurysm tissue from 10-week male wild-type and *Fbn1^{mgR/mgR}* mice (Fig. 4.3A). 471 mRNAs were up-regulated (green) and 253 down-regulated (red) more than 2-fold ($p < 0.05$) in the aneurysmal versus the wild-type tissues (Fig. 4.3A). Gene ontology analyses using all 724 differentially regulated mRNAs (>2-fold) are shown in Figs. 3B and C. As was predicted from miRNA profiling, a prominent upregulation of inflammatory related pathways (red) was observed, including cytokine-cytokine receptor interaction as the top enriched pathway with 26 genes dysregulated (red, Fig. 4.3B). Multiple ECM/cell adhesion relevant pathways were also upregulated in *Fbn1^{mgR/mgR}* aortae (green, Fig. 4.3B). The contractility/cytoskeleton related pathways were clustered into both up- or downregulated group: “*Regulation of actin cytoskeleton*” was upregulated, while “*Calcium signaling pathway*” was downregulated (purple, Figs. 4.3B and C). Surprisingly, although ERK1/2 signaling, one of MAPK signaling, was reported to be upregulated in *Fbn1^{mgR/mgR}* mice [70], the overall MAPK signaling was downregulated in mRNA levels (Orange, Fig. 4.3C).

As the inflammatory responses were upregulated in enriched pathway analyses of 10-week ascending aortic tissue of *Fbn1^{mgR/mgR}* mice, we investigated immune cell infiltration at that time point. Consistent with studies on human TAA patient tissues [290], macrophages (CD68) and T cells (CD3) were present in the aortic adventitia of the *Fbn1^{mgR/mgR}* ascending aorta, but not in tissue from wild-type mice (Fig. 4.3D, white arrow heads). Typical fragmentation of elastic laminae in the aortic media was observed in the tissues from *Fbn1^{mgR/mgR}*, but not wild-type mice (Fig. 4.3D, open white arrow heads). Fig. 4.3E shows the top nine upregulated mRNAs enriched in the “*Cytokine-cytokine receptor interaction*” pathway from Fig. 4.3B, including *Ccr2* (12.4-

fold), *Ccl2* (4.05-fold) and *Il1 β* (2.92-fold). Western blotting of freshly isolated 10-week old *Fbn1^{mgR/mgR}* ascending aortae confirmed that CCR2, CCL2 and IL-1 β were upregulated at the protein level, with 1.5, 3.8 and 2.1-fold respectively (Figs. 4.3F and G). An enzyme-linked immunosorbent assay (ELISA) of aorta organ culture medium conditioned for 72 h also displayed elevated CCL2 for *Fbn1^{mgR/mgR}* versus wild-type tissues (2.8-fold) (Fig. 4.3H). (ELISA of IL-1 β in organ culture medium is still in progress)

4.4.4 RNA-seq analyses of TAA tissues from human patients

To identify differentially regulated pathways in human TAA tissues, RNAseq analyses were performed to analyze five tissue samples obtained from TAA patients (Supplementary Table 4.1), compared to three non-aneurysmal aortic control samples from donors with no evidence of aortic diseases (Fig. 4.4). Consistent with the data obtained from *Fbn1^{mgR/mgR}* mice, gene ontology analyses of the 4761 differentially (>2-fold; p<0.05) regulated RNA transcripts indicated that the “*Cytokine-cytokine receptor interaction*” pathway (Fig. 4.4A; red text) was the top hit that included 39 upregulated mRNAs. Also differentially regulated were pathways in ECM/cell adhesion and MAPK pathways (Fig. 4.4A and B; green text). Additionally, the smooth muscle phenotypes were identified to be downregulated in human TAA tissues (Fig. 4.4B; green text). Comparative analyses of the differentially regulated mRNAs from *Fbn1^{mgR/mgR}* mice and from human TAA samples revealed 8 common upregulated and 5 common downregulated pathways (Fig. 4.4C and D). “*Cytokine-cytokine receptor interaction*” was the top commonly upregulated pathway in TAA tissues from *Fbn1^{mgR/mgR}* mice and human patients including most differentially regulated mRNAs (Fig. 4.4E; red text). The green highlighted pathways in Fig. 4.4E and F show commonly upregulated cell adhesion-related pathways, and the commonly downregulated MAPK

signaling pathway. These comparative analyses confirmed the upregulation of inflammatory responses in the aneurysmal aortae of both *Fbn1^{mgR/mgR}* mice and human TAA patients. Since the cause of TAA in these patients were not clear, and the patients were without the typical phenotypes of MFS, the results suggested that inflammatory responses were likely to be elevated in the pathogenesis of TAAs with various molecular causes. We next sought to elucidate the regulators of the identified pro-inflammatory molecules.

4.4.5 Correlative analyses between miRNAs and mRNAs expression in aneurysm tissues

It is known that miRNAs are actively involved in various disorders characterized by prominent inflammatory responses, including multiple sclerosis, arthritis, and several forms of cancers [312]. However, little is known whether miRNAs participate in the regulation of the inflammatory response in TAA pathogenesis. Bioinformatic analyses predicted the involvement of miRNAs in inflammatory responses in the aortae of *Fbn1^{mgR/mgR}* mice (as shown in Fig. 4.2C and F). To further understand which mRNAs were regulated by these miRNAs, we compared the expression levels between the differentially regulated miRNAs and mRNAs detected by microarrays of aortic tissues harvested from 10-week old *Fbn1^{mgR/mgR}* mice. Since the primary function of miRNAs is to promote the degradation of mRNA targets [151], the expression level of miRNAs and their targets typically inversely correlate (here we call it “correlated”). Thus, we compared the expression levels of miRNAs and their experimentally validated mRNA targets (based on the miRNA Targets Database TarBase, which contains experimentally validated miRNA-mRNA interactions [313] and selected the pairs that are “correlated”. Blue pies in Figs. 4.5A and B show 91 miRNAs and their 354 mRNA targets were differentially regulated >2-fold. These differentially regulated miRNAs and mRNAs compose 70.5% and 49% of the total differentially regulated miRNAs or mRNAs. Among them, 89 miRNAs correlated with 109 mRNA targets (Figs. 4.5A and B, green

pies). These 109 mRNAs comprised 15% of the >2-fold dysregulated mRNAs. Pathway enrichment analyses of the 109 mRNAs revealed that inflammatory related pathways were the top hits (Fig. 4.5C; red text), including 5 differentially expressed mRNAs, *Cxcl13*, *Il6*, *Ccl2*, *Il1β* and *Bmpr1b*. All of these, except *Bmpr1b*, were upregulated in the ascending aortae of *Fbn1^{mgR/mgR}* mice (Fig. 4.5D). Based on the TarBase library, miR-122, the most downregulated miRNA in *Fbn1^{mgR/mgR}* ascending aortae, targets all 4 upregulated inflammatory related mRNAs. This strongly suggested the importance of miR-122 in regulating inflammatory responses at the sites of dilated aortic walls.

4.4.6 Functional analyses of miR-122 on inflammatory responses

In situ hybridization of ascending aortae of 10-week old wild-type male mice showed that miR-122 was primarily present in smooth muscle cells of the media with particular strong staining patterns adjacent of the elastic lamellae (Fig. 4.5E). In ascending aortae of age and sex matched *Fbn1^{mgR/mgR}* mice, miR-122 was significantly down-regulated (77.5%) (Figs. 4.5E, F). Functional consequences of downregulated miR-122 on the mRNA expression levels of *Ccl2*, *Il1β*, *Cxcl13*, and *Il6* were investigated with *ex vivo* aorta organ cultures from 10-week wild-type mice of both sexes. Fresh aortae from the same animal were cut into 1 mm small pieces, and either transfected with miR-122 inhibitor (miR122IH) or scrambled controls (Fig. 4.5G). The *Ccl2* and *Il1β* mRNAs were significantly upregulated by 2.1 and 4.4-fold, respectively, upon miR-122 inhibition, but not the *Cxcl13* and *Il6* mRNA. Analysis of the protein levels of CCL2 by ELISA showed that CCL2 was upregulated 2.2-fold in the conditioned medium of the *ex vivo* aortae (ELISA of IL-1β is still in progress) (Fig. 4.5H). These results suggested that the downregulated miR-122 in TAA tissue of *Fbn1^{mgR/mgR}* mice promoted the inflammatory response with the post-transcriptional upregulation of *Ccl2* and *Il1β*.

4.4.7 Deficient fibrillin-1 in the ECM downregulates miR-122 via decreased c-Src kinase

Our previously published data has validated that a deficient fibrillin-1-fibroblast interaction regulates a subset of miRNAs [245]. Re-analysis of the microarray data from that study showed that miR-122 was downregulated by 20% 24 h after fibroblasts were seeded on rF1M-RGA, a fibrillin-1 fragment not able to promote fibrillin-1-integrin interaction, as compared to the wild-type fibrillin-1 fragment rF1M-WT (Fig. 4.6A). Using an identical experimental setup with human aortic smooth muscle cells, we identified a larger decrease (71%) of miR-122 when the cells were seeded on rF1M-RGA for 24 h (Fig. 4.6B), as compared to rF1M-WT. Since the RGA mutation does not represent a known MFS mutation, we extended the experimental setup using cell-derived matrices produced by skin fibroblasts obtained from seven MFS patients with defined mutations in fibrillin-1 (Supplementary Table 4.2). Aortic smooth muscle cells from these MFS patients were not available for this study. There are six cysteines in one calcium-binding epidermal growth factor-like (cbEGF) domain of fibrillin-1 [17,18], which form three disulfide bonds stabilizing the domain [19]. The RGD sequence is located in the 4th TGF- β binding protein-like (TB4) domain of fibrillin-1 [13]. Fibroblast with mutations occurring in the 1st, 2nd, 3rd, 4th and 6th cysteines of various cbEGF domains, a mutation locating in the TB4 domain, and a terminal mutation happening 5 amino acid upstream of TB4 domain were chosen. These mutations were all expected to reduce the stability of fibrillin-1 to proteases or influence the RGD-cell interactions. After production of the cell-derived matrices by the MFS fibroblasts or by fibroblasts from healthy controls for 7 d, the cells were first removed from the matrices, followed by re-seeding of skin fibroblasts from healthy control subjects. qPCR analyses of the fibroblasts after 24 h revealed that miR-122 was downregulated to 39%, demonstrating that matrices containing a fibrillin-1 MFS

mutation cannot maintain miR-122 levels, at least in fibroblasts (Fig. 4.6C). We next investigated potential kinases involved in regulating miR-122 when smooth muscle cells were seeded on culture dishes. Chemical inhibitors of focal adhesion kinase (FAK) and c-Src kinase, which are known to be activated by integrin-ECM interactions, were applied to human aortic smooth cells for 48 h. Downregulation of c-Src, but not FAK, suppressed miR-122 expression (Fig. 4.6D). Together, these data demonstrate that mutations in fibrillin-1 lower the levels of miR-122. The active c-Src kinase is needed to maintain the miR-122 levels under normal culture conditions.

4.4.8 Hypoxic conditions suppress miR-122 expression and fibrillin-1 network formation

Previous studies identified elevated HIF-1 α mRNA and protein levels at sites of human acute thoracic aneurysm dissections [147]. Consistent with this finding, HIF-1 α mRNA and protein levels were upregulated in the ascending aortae of *Fbn1^{mgR/mgR}* mice (Figs. 4.6E and F). Although *HIF-1 α* mRNA was not upregulated based on the human TAA RNAseq data, it is noteworthy that “*Oxidative phosphorylation*” was one of the most downregulated pathways in human TAA with 34 downregulated genes (Fig. 4.4B, underlined). The mitochondrial respiratory chain relies on oxygen for energy production via oxidative phosphorylation [314]. Under hypoxic conditions, cells switch from oxidative phosphorylation to glycolysis as a means of ATP production [315]. The upregulated HIF-1 α in the *Fbn1^{mgR/mgR}* aneurysmal aorta and the impaired oxidative phosphorylation in human TAA tissues showed that the TAA tissues experienced hypoxic stress. To understand how hypoxic conditions and activated HIF-1 α affect miR-122, we investigated its expression levels in human aortic smooth muscle cell culture either by reducing the atmospheric oxygen to 5% or by adding CoCl₂, an activator of HIF-1 α , to the culture medium for 48 h (Figs. 4.6G, H). qPCR analyses showed that the miR-122 levels in a hypoxic atmosphere were suppressed to 15% as compared to normoxic conditions (Fig. 4.6G). CoCl₂ also downregulated miR-122 levels

significantly (Fig. 4.6H). Since HIF-1 α can regulate gene expression of multiple ECM proteins including collagens and lysyl oxidase [316], and because we have shown that fibrillin-1 and fibrillin-1 containing ECM is critical for maintaining miR-122 levels (see Figs. 4.6A-D), we investigated whether hypoxic conditions or HIF-1 α activation in smooth muscle cell cultures affected the ability of fibrillin-1 to form fibers. Fibrillin-1 immunofluorescence staining after 72 h of treatment showed that fibrillin-1 fibers were greatly diminished either under hypoxic conditions or with CoCl₂ treatment under normoxic conditions (Fig. 4.6I). Then we analyzed whether hypoxic conditions could downregulate miR-122 levels without the contribution of fibrillin-1 deficiency in the ECM. To address this question, *ex vivo* aorta cultures from 10-week old wild-type mice of both sexes were used. Aortae sections obtained from the same mice were cultured either under normoxic or hypoxic conditions for 72 h. qPCR analyses demonstrated that miR-122 levels were downregulated by 32.9% under hypoxic conditions (Fig. 4.6J). Treatment of the aortic smooth muscle cells for 48 h with digoxin, a HIF-1 α inhibitor, upregulated miR-122 levels by 2.6-fold (Fig. 4.6K). These results demonstrated that hypoxic conditions present in TAA tissues negatively regulate miR-122 expression in smooth muscle cells and in *ex vivo* aorta cultures and suppress fibrillin-1 network formation in cell cultures.

4.4.9 ERK1/2 inhibition elevated miR-122 levels

Since ERK1/2 signaling can regulate multiple miRNAs [258] and is activated in the ascending aortae of TAA mouse models, including *Fbn1*^{mgR/mgR} and *Fbn1*^{C1039G/+} mice [70,130], we investigated whether ERK1/2 also regulates miR-122. Using the selective ERK1/2 inhibitor SCH772984 in *ex vivo* aorta cultures and in smooth muscle cell cultures, miR-122 was found to be significantly upregulated (Fig. 4.6H and L).

4.5 Discussion

The present study identified differentially regulated miRNAs in TAA tissues of 4 and 10-week old male *Fbn1^{mgR/mgR}* MFS mice, as compared to wild-type mice. Pathway prediction based on these dysregulated miRNAs suggested that inflammatory responses started from early aortic dilation stages (4-weeks), and persisted to the fully developed aneurysmal stage (10-weeks) in male *Fbn1^{mgR/mgR}* aortae. Complementing mRNA levels were determined for aneurysmal aortae from 10-week old *Fbn1^{mgR/mgR}* and wild-type mice. This analysis also revealed upregulated inflammatory pathways, including elevated expression of multiple pro-inflammatory cytokines and cytokines receptors. Upregulated CCL2, IL-1 β and CCR2 in the *Fbn1^{mgR/mgR}* aortae were validated. Genetic profiles revealed upregulation of inflammatory responses in both mouse and human TAA tissues. miR-122 was demonstrated to be the most downregulated miRNA in 10-week old *Fbn1^{mgR/mgR}* aortae. Functional studies revealed that inhibition of miR-122 could upregulate *Ccl2* and *Il1b* mRNA in *ex vivo* aorta cultures, and CCL2 protein in the medium of aorta cultures (green arrows in Fig. 4.7). Fibrillin-1 deficiency was demonstrated to suppress miR-122 in both human skin fibroblasts and aortic smooth muscle cells, using either a RGA-containing recombinant fibrillin-1 fragment or matrices derived from skin fibroblasts of MFS patients. Active c-Src kinase was shown to maintain miR-122 expression in smooth muscle cells. Hypoxic conditions and elevated ERK1/2 signaling, both of which are upregulated in TAA tissues, were shown to downregulate miR-122 in smooth muscle cells and in *ex vivo* aorta cultures.

TAA was reported to occur 1.7 times more often in male compared to female individuals (reviewed by Guo [317]). Consistent with these reports, the data presented here showed that male *Fbn1^{mgR/mgR}* mice developed aortic dilation earlier than female mice (Fig. 4.1A-D). Cook *et al.* demonstrated that TGF- β neutralizing treatment of TAA in MFS mice showed a time-dependent efficacy, as

blocking TGF- β signaling at an early stage of aortic dilation worsened aortic outcomes in *Fbn1^{mgR/mgR}* mice, whereas treatment at later stages attenuated TAA formation [289]. This finding stresses the importance of analyzing dysregulated miRNA pathways at early and late stages of aortic aneurysm progression. Ascending aortic dilation (1.2-fold) occurred as early as 4-weeks of age in male *Fbn1^{mgR/mgR}* mice. This allowed us to profile the miRNAs both at the early and late stages of TAA progression. Already at 4-weeks, the miRNA profiles predicted inflammatory and ECM/cell adhesion related pathways to be dysregulated. Whether inflammatory responses at this stage are indeed dysregulated at the mRNA and protein levels, and whether inflammatory responses at this time point are beneficial or detrimental for aorta homeostasis still requires further analyses. Nevertheless, the results suggested the involvement of inflammatory pathways in TAA pathogenesis starting from early stages of aortic dilation.

At the fully developed aneurysmal stage of TAA tissues in *Fbn1^{mgR/mgR}* mice and in human patients, the ECM/cell adhesion related pathways were upregulated (green text in Fig. 4.3 and 4). The evaluated ECM/cell adhesion may be initiated by the elevated proteoglycan and fibronectin content in the dilated thoracic aortae, which was previously reported by several groups [91,318,319]. Surprisingly, pathway enrichment analyses showed the MAPK pathway was downregulated in both *Fbn1^{mgR/mgR}* mice and in human patients (orange text in Fig. 4.3 and 4.4), even though elevated phosphorylated ERK1/2, one component of the MAPK signaling pathway, was reported in MFS mice [70,130]. This may result from the limitation of mRNA profiling that the activation status of kinases cannot be detected.

Inflammatory cell infiltration into the adventitia of the aneurysmal aortae were observed in human TAA patients and two MFS mouse models, including the *Fbn1^{mgR/mgR}* mice [86,88,290,291].

Although inflammatory cell infiltration is not as prominent as in AAA, our miRNA and mRNA microarrays of *Fbn1*^{mgR/mgR} TAA tissues and RNAseq of human aneurysmal tissues displayed elevation of multiple cytokines and cytokine-receptors. With the elevation of CCR2, CCL2 and IL-1 β demonstrated in *Fbn1*^{mgR/mgR}. *Ccr2* mRNA was previously reported to be elevated in the ascending aorta of *Fbn1*^{mgR/mgR} [320]. This study first proved its upregulation at protein level. Our CCL2 results correlated with the previous studies by Ju *et al.*, which showed upregulated CCL2 and IL-6 levels in the aortic media and medium from *ex vivo* aorta culture of *Fbn1*^{mgR/mgR} mice [135]. We reported for the first time the elevation of IL-1 β in both mRNA and protein levels at the aneurysmal site of *Fbn1*^{mgR/mgR} ascending aorta. Among them, CCL2 and IL-1 β can repress the expression of smooth muscle cell contractile markers, including α -SMA, smooth muscle myosin heavy chain, calponin-1, and SM22 [294] in cell culture. IL-1 β can promote secretion of multiple MMPs from smooth muscle cells, including MMP 1, 2, 3 and 9 [292,293]. The *in vitro* literature data and our *in vivo* data presented here suggests that the upregulation of CCL2 and IL-1 β contributed to the loss of contractile smooth muscle cells, and aortic wall destruction at the aneurysmal site of *Fbn1*^{mgR/mgR} mice.

Our study identified that miR-122 negatively regulates the mRNA expression of several cytokines in *ex vivo* aorta cultures, including *Ccl2* and *Il1 β* . This data indicated that downregulation of miR-122 in TAA tissue of *Fbn1*^{mgR/mgR} mice may elevate the expression of these pro-inflammatory cytokines. Although miR-122 is primarily described in the context of liver, expression of miR-122 is also detected in other tissues and cells, including human aortic endothelial cells [176], myocardium [321] and squamous cell carcinoma [322]. Our study demonstrated by *in situ* hybridization that miR-122 is also expressed in the aorta, primarily in smooth muscle cells. In our study, we detected 26 dysregulated mRNAs enriched in the cytokine-cytokine receptor interaction

pathway in the aortae of *Fbn1^{mgR/mgR}* mice. Among these, *Ccl2*, *Il1b*, *Ccr2* and *Bmpr1b* mRNA represented targets of miR-122, and for CCL2, IL- β and CCR2 we validated that the protein levels were also elevated in the aortae of *Fbn1^{mgR/mgR}* mice. Tsai *et al.* showed that the *Ccl2* and *Il1b* mRNAs were direct targets of miR-122 in HEK293 using dual-luciferase reporter assays [173]. Consistently, our *ex vivo* organ culture studies demonstrated that miR-122 inhibition upregulated *Ccl2* by 2.1-fold, and *Il1 β* by 4.4-fold. A CCL2 ELISA in our studies showed 2.2-fold elevation in the *ex vivo* aorta culture medium when miR-122 was suppressed (green arrows in Fig. 4.7). ELISA of IL- β are not yet performed. Besides the pro-inflammatory cytokines regulated by miR-122, Beaumont *et al.* showed that miR-122 can directly target the 3' untranslated region of *TGF- β 1* mRNA [323]. In summary, the data suggest that miR-122 is a core regulator in several important pathways underlying TAA progression, including inflammation and TGF- β signaling. The results may provide the basis in the longer term to explore restoration of miR-122 levels in TAA as a novel therapeutic avenue to reduce inflammatory responses and normalize TGF- β signaling.

To understand miR-122 regulation, we investigated its upstream regulators. The results showed that miR-122 was downregulated by elevated ERK1/2 signaling, fibrillin-1 deficiency in the ECM and by hypoxic conditions (green arrows in Fig. 4.7). Inhibition of ERK1/2 signaling has been shown to ameliorate TAA progression in *Fbn1^{C10039G/+}* MFS mice [70]. It is possible that ERK1/2 signaling restored miR-122 expression levels in these studies giving rise to its benefits in TAA amelioration. Another important mechanism of miR-122 regulation is via cell-fibrillin-1 interaction. We showed that c-Src kinase positively regulates miR-122 in human smooth muscle cells in a FAK-independent manner. Since fibrillin-1 interacts with α v β 3 integrin [35,51], and β 3 integrin can activate c-Src kinase [247], the data suggest the involvement of β 3 integrin in miR-122 regulation.

The microarray and immunofluorescence data for HIF-1 α in the aneurysmal aorta of *Fbn1^{mgR/mgR}* mice, and the RNAseq data obtained from patient derived aortic tissues have indicated that the smooth muscle cells in TAA tissues are under hypoxic stress. Hypoxic conditions were shown to downregulate miR-122 expression in squamous cell carcinoma [322]. Reoxygenation after hypoxia treatment of myocardial cells can upregulate miR-122 [321]. Consistently, we demonstrated that hypoxic conditions and CoCl₂, a chemical HIF-1 α activator, can downregulate miR-122 levels in smooth muscle cells and in *ex vivo* aorta cultures. Digoxin, a HIF-1 α inhibitor, could rescue downregulated miR-122 in smooth muscle cells cultivated under hypoxic conditions. Additionally, several HIF-1 α inhibitors, including digoxin, 2-methoxyestradiol, and rapamycin have been shown to partially rescue the aortic tissue structure by reducing elastic lamina fragmentation in TAA or AAA mouse models [148,303,304]. This suggests that hypoxic conditions contribute to TAA progression. However, HIF-1 α is also reported to be essential for the mRNA expression of lysyl oxidase and tropoelastin in aortic smooth muscle cells [149]. In that study, HIF-1 α showed a protective role for TAA progression by restoring the structure of the aortic wall. The discrepancy between these studies may partly result from the fact that the available pharmacological drugs to inhibit HIF-1 α activity used in the previous studies are not HIF-1 α specific, as there is no specific pharmacological inhibitor for HIF-1 α . Digoxin, 2-methoxyestradiol and rapamycin can all inhibit HIF-1 α translation [324,325]. Addition to that, digoxin is a sodium-potassium ATPase inhibitor, which mediates cellular calcium uptake, promoting myocardial contraction in patients with atrial fibrillation, atrial flutter, and heart failure [326]. 2-methoxyestradiol, an estrogen metabolite, can additionally depolymerize microtubules by binding to the colchicine binding site in tubulin [327]. Rapamycin, a mTOR signaling inhibitor, can also influence cell survival, metabolism and proliferation [301]. Therefore, these inhibitors

experiments should be complemented with specific siRNA inhibition of HIF-1 α in cells. Because the timing of TGF- β inhibition was shown to be critical in terms of TAA prevention [289], it would be important to test the role of *Hif-1 α* at different time points on its role in TAA progression, for example with an inducible knockout of *Hif-1 α* in *Fbn1^{mgR/mgR}* mice.

In summary, our study determined the time-dependent microRNA profiles in the ascending aortae of *Fbn1^{mgR/mgR}* mice. Similarities between the genetic profiles of TAA tissues from *Fbn1^{mgR/mgR}* mice and human TAA patients were uncovered. Furthermore, we revealed a novel linkage in TAA progression between hypoxia, fibrillin-1 deficiency and inflammatory responses of smooth muscle cells, with the involvement of miR-122 as the connector (Fig. 4.7).

4.6 Materials and Methods

4.6.1 Mice and aortic tissue preparation

Heterozygous mutant mice *Fbn1^{mgR/+}* on the C57BL/6J genetic background were kindly provided by Prof. Francesco Ramirez in the department of pharmacological sciences, Icahn School of Medicine at Mt Sinai, and were bred to generate wild-type and *Fbn1^{mgR/mgR}* mice for experiments. *Fbn1^{mgR/mgR}* is a hypomorphic fibrillin-1 mouse model that expresses about 20-25% of normal fibrillin-1 compared to wild-type mice [328]. All mouse experiments strictly followed the guidelines of the Canadian Council on Animal Care and were approved by the McGill University Animal Care Committee (protocol 2017–7979). Mice were maintained in positive pressure isolators under a 12 h light-dark cycle. The mice were humanely sacrificed with an intraperitoneal injection of overdosed ketamine/xylazine/acepromazine cocktail (100/10/3 mg/kg). Aortae were freshly dissected after 2 min transcardial perfusion with phosphate-buffered saline (PBS) for gross image recording, *ex vivo* aorta cultures, smooth muscle cell explants and RNA and protein extractions. For histological analysis of aortic tissues, an additional perfusion with 2%

paraformaldehyde for 2 min was used to fixate the aortic wall tissue. More details of the procedures are described below.

4.6.2 *Ex vivo* aorta culture

After PBS perfusion, dissected thoracic aortae were washed with cold PBS two times and cut into ~1 mm long segments that were placed into serum-free DMEM/F12 (1:1) medium (Gibco) supplemented with 100 µg/mL penicillin, 100 µg/mL streptomycin, and 2 mM glutamine (PSG) at 37°C in a 5% CO₂ atmosphere. Serum was not added to avoid outgrowth of smooth muscle cells, so that the composition of different cell types in the aortic wall was preserved. Tissue segments were randomly distributed in the cultures between different treatment groups, to avoid potential variations among the locations.

4.6.3 Mouse smooth muscle cell explant

After euthanasia and PBS transcardial perfusion of 12 d old mice, the thoracic aortic media were dissected, and the adventitial fat, the adventitia and the endothelial cells lining the media were removed under a dissection microscope. About 0.5×0.5 mm thoracic aorta media segments were placed in tissue culture flasks for 1 h at 37°C in a 5% CO₂ atmosphere, with the luminal side adhered to the flask surface. After 1 h, DMEM/F12 (1:1) medium containing PSG and 10% heat inactivated fetal bovine serum (FBS) was added. The culture medium were changed every two days, until the explanted smooth muscle cells were confluent for further passaging.

4.6.4 RNA extraction and reverse transcript PCR

For RNA extraction of cells, 200,000 cells grown in 12-well plates (Sarstedt) were lysed in 100 µL Qiazol (Qiagen). For tissue RNA extraction, the ascending aorta was sonicated 3 × 5 s in 200 µL Qiazol on ice. Extraction of total RNA including both miRNAs and mRNAs were performed using the miRNeasy Mini Kit (Qiagen, cat# 217004), according to the manufacturer's instructions.

For reverse transcription of RNA into cDNA, 0.1-1 µg of total RNA was used. miScript II RT kit (Qiagen) was used to reverse transcribe miRNAs, according to the manufacturer's instructions. Super Script III First-Strand Synthesis System for RT-PCR (Life Technologies) was used to reverse transcribe mRNAs as detailed in the supplier's manual.

4.6.5 Microarray analysis of mouse ascending aorta

Microarray analysis was performed for miRNAs and mRNAs using the GeneChip miRNA 4.0 Array and the Clariom D Array, mouse from Affymetrix, respectively. The GeneChip miRNA 4.0 Array interrogates all mature miRNA sequences in the miRbase 20. Clariom D Array Mouse covers the entire transcribed mouse genome including all known coding and long non-coding RNAs, with >214,000 transcripts. RNA extraction, RNA quality control, cDNA preparation and labeling, and the arrays were conducted as standard procedures at the Genome Quebec Innovation Centre at McGill University. Four ascending aorta samples each group from 4 and 10-week old wild-type and from *Fbn1^{mgR/mgR}* mice were prepared as described above, and snap-frozen in liquid nitrogen to preserve the integrity of RNA.

The Transcriptome Analysis Console software (Affymetrix) was used to perform statistical tests, to visualize fold changes of miRNAs and mRNAs, and to analyze miRNA-mRNA interactions. Normalized intensities between the aortae from wild-type and *Fbn1^{mgR/mgR}* mice were compared using one-way ANOVA, followed by multi-testing correction using the Benjamini-Hochberg false discovery rate (FDR)-controlling procedure for all expressed genes. All p-values indicated refer to FDR-adjusted p-values.

4.6.6 Human sample collections and RNA isolation

Human samples were collected in accordance with New York University (NYU) Langone Medical Center Institutional Review Board policies. Informed consent was obtained from each patient. TAA specimen from 5 male patients (age range of 29-63 years) were collected upon open repair procedures at the NYU Langone Medical Center, New York, NY, USA. None of the patients had genetic collagen disorders, or were diagnosed with MFS. Non-aneurysmal aortic control tissues were collected from donors with no evidence of aortic diseases at autopsies provided by LiveOnNY organization, New York, NY, USA. Patient information was collected by a questionnaire or from the patient's file at the hospital (Supplementary Table 4.1). Tissue samples were oriented, formalin fixed, paraffin embedded and sectioned or kept frozen at -80 °C for RNA isolation.

4.6.7 RNA sequencing

Total RNA extractions of the specimen were performed using the RNeasy Fibrous Tissue Mini Kit according to the manufacturer's instructions (Qiagen, cat#74704). Isolated RNA samples were processed using the Clontech Low Input Kit according to manufacturer's instructions to prepare RNA-Seq libraries, followed by purification using AMPure beads (Agilent Technologies). The qualities of RNA samples were verified by a Bioanalyzer (Agilent Technologies, cat#G2939BA). The samples were analyzed on a HiSeq 2500 System (Illumina) as paired-end reads with 50 nucleotides in length. The readings were mapped against the hg19 human reference genome, using the Tophat 2.0.9. HTSeq 0.6.1 python framework and hg19 GTF gene annotation (UCSC database) to process BAM alignment files. The Bioconductor package DESeq2 (3.2) was used to identify differentially expressed genes. The Benjamin and Hochberg method was performed to control the

false discovery rate. RNA transcripts that had adjusted $p < 0.05$ were considered to be differentially expressed.

4.6.8 Pathway enrichment analyses

To discover the network of regulators and the pathways associated with transcriptomic data, significantly dysregulated transcripts from mRNA microarray and RNAseq (with fold change >2 , $p < 0.05$) were analyzed using Gene Set Enrichment Analyses (GSEA) software [329]. To identify the miRNA-regulated pathways, DIANA mirPath v.3.0 was used to analyze the dysregulated miRNAs (>2 -fold, $p < 0.05$), [DIANA TOOLS - mirPath v.3 \(grnet.gr\)](http://grnet.gr) [330]. Prediction of the dysregulated pathways with $p < 0.05$ are listed.

4.6.9 Cell Culture

Primary human smooth muscle cells, mouse smooth muscle cells and primary skin fibroblasts from healthy human and from individuals with MFS were used in the experiments. The primary human smooth muscle cells were purchased from ScienCell Research Laboratories (Cat# 6110), primary mouse smooth muscle cells were isolated from the aortae of wild-type and *Fbn1*^{mgR/mgR} mice at postnatal day 12. Human healthy skin fibroblasts were isolated from the foreskin of healthy boys (two to five years of age), following a standard circumcision procedure, approved by the Montreal Children's Hospital Research Ethics Board (PED-06-054). Skin fibroblast isolated from the abdomen and arm of healthy adults were gifts from Dr. Anie Philip at McGill University. MFS skin fibroblasts with 7 different mutations were purchased from the Coriell Institute (Camden, NJ, USA) (Supplementary Table 4.2). For all experiments, primary cells were used between passages 4 and 10. Human smooth muscle cells were cultured in 231 medium with growth supplement SMGS (Gibco) and 10% FBS. Mouse smooth muscle cells were cultured in DMEM/F12 (1:1) medium, supplemented with 10% heat inactivated FBS. Primary skin fibroblasts were cultured in DMEM medium, supplemented with 10% FBS. All media were additionally supplemented with PSG. Cells were cultured at 37°C in a 5% CO₂ atmosphere. To grow cells under hypoxic conditions, a Nuair incubator NU-4950 was adjusted to a 5% oxygen atmosphere.

For analyses of smooth muscle cells seeded on rF1M-WT and rF1M-RGA, the proteins were purified as previously described [245]. Cell culture plates or chamber slides were first pre-coated with 100 µg/mL poly-D-lysine for 2 h at room temperature, followed by coating of the recombinant proteins at a concentration of 25 µg/mL in Tris-buffered saline (TBS) containing 2 mM Ca²⁺ overnight at 4 °C. This coating concentration was previously optimized for promoting cell

adhesion [245]. We showed previously that poly-D-lysine does not affect integrin-triggered signaling [245].

Fetal bovine serum contains plasma fibronectin, which could interfere with the fibrillin-1 RGD cell binding and signaling. Thus, prior to cell experiments with coated recombinant proteins, cell derived matrices or transfection with miRNA inhibitors, smooth muscle cells or human skin fibroblasts were serum-starved for 4 h or 24 h to remove residual plasma fibronectin from the medium. For the kinase inhibitor experiments conducted without coated recombinant proteins, serum-containing medium was used, because plasma fibronectin does not interfere with this experimental setup. For trypsinization, cell monolayers were first washed twice with PBS, followed by incubation with 0.25% trypsin-EDTA (Wisent) for 3 min. DMEM medium was added to the dissociated cells and the cell suspension was centrifuged for 5 min at $1,200 \times g$. The cell pellet was resuspended in medium and centrifuged again for 5 min at $1,200 \times g$ to completely remove residual trypsin. The short incubation time with trypsin and the two centrifugation steps minimized proteolytic degradation of cell surface integrins.

4.6.10 Generation of fibroblast-derived matrix

Primary fibroblasts used for generating cell-derived matrices included normal foreskin fibroblasts, adult abdominal skin, and skin fibroblasts from adult MFS patients (Coriell Institute). with 1mL prewarmed (37°C) cell-extraction buffer (0.5% v/v Triton X-100 ; 20 mM NH_4OH in PBS). The fibroblast-derived matrices were washed twice with PBS and kept in DMEM medium with PSG for further cell culture.

4.6.11 microRNA transfection into cells and ex vivo aorta culture

The inhibitor of miR-122 were commercially obtained from Qiagen (Anti-hsa-miR-122, cat# MIMAT0000421). The inhibitor was prepared with HiPerFect transfection reagent (Qiagen, cat#301704) in serum-free DMEM medium. The solution was applied directly to the cells seeded on 6-well plates, or to the aorta cultures on 48-well plates, at a final concentration of 50 nM. qPCR analyses were performed 24 h after transfection of cells and 48 h after transfection of *ex vivo* aorta cultures.

4.6.12 Quantification of miRNA and mRNA

For quantification of miRNAs, real-time qPCR was performed using the miScript SYBR Green PCR Kit (Qiagen, cat#218073), according to the manufacturer's instructions. miScript Primer Assays were obtained from Qiagen for human miR-122 (cat#MS00014196). RNU6 (cat# MS00033740) was used as a reference. The real-time cycler (Applied Biosystems, Step-One Real-Time qPCR system) was programmed to an initial PCR activation step for 15 min at 95°C and 40 cycles of a 3-step cycling program: 1) Denaturation (94°C for 15 s), 2) Annealing (55°C for 30 s), 3) Extension (70°C for 34 s). Melting curve analysis was performed after each run to determine the specificity of the amplified products. For quantification of mRNA, cDNA was used for real-time qPCR with the SYBR Green Select Master Mix (Applied Biosystems, cat#4472908), and 200 nM forward and reverse primers (Supplementary Table 4.2). GAPDH was used as a reference. The real-time cycler was programmed to an initial PCR activation step for 2 min at 50°C and afterwards 2 min at 95°C and 40 cycles of a 3-step cycling program: 1) Denaturation (95°C for 15 s), 2) Annealing (58°C for 15 s), 3) Extension (72°C for 1 min). Melting curve analysis was performed after each run to determine the specificity of the amplified products. The delta-delta Ct method was used to compare different groups.

4.6.13 Inhibitor treatment of smooth muscle cells

Inhibitors purchased from Selleckchem were applied at the concentrations recommended by the manufacturer to fibroblasts directly after cell seeding: 10 μ M ERK1/2 inhibitor (SCH772984, cat#S7101), 10 μ M FAK inhibitor (PF573228 cat#S2013), 100 nM c-Src inhibitor (Dasatinib, cat#S1021). 1:1,000 v/v DMSO was used as buffer control. qPCR analyses were performed 48 h after treatment.

4.6.14 Western blotting

Aorta lysis was performed in 200 μ L RIPA buffer (pH 8, 50mM Tris, 150mM NaCl, 0.5% Sodium deoxycholate, 1% Triton X-100, 0.1% sodium dodecyl sulfate (SDS) including 1:50 v/v protease inhibitor cocktail (Roche, cat# 11697498001) and 1:100 v/v phosphatase inhibitor cocktail (Sigma cat# P5726). Tissues were sonicated 3 \times 5 s on ice. The lysates were transferred immediately to 1.5 mL tubes on ice and centrifuged at 9,300 \times g for 2 min to sediment non-soluble cell debris and ECM. The supernatants were denatured in SDS-containing sample buffer at 95°C for 5 min, then 50 μ L of the supernatant was loaded onto 10% SDS-PAGE gels, electrophoresed, and then transferred in 10 mM sodium tetraborate onto 0.45 μ m pore size nitrocellulose membrane (Bio-Rad, cat#1620115). The blots were blocked with 5% non-fat dry milk for 1 h at room temperature. The blot was subjected to primary antibody incubation overnight at 4°C, followed by 3 \times 5 min washes in TBST (TBS, pH 7.4 with 0.05% Tween-20). The blots were incubated with one of the following primary antibodies at a 1:1,000 dilution in 2% non-fat dry milk: anti-CCR2 (Novus Biologicals, cat #NBP1-48337), anti-CCL2 (Abcam cat#ab25124), anti-IL-1 β (Abcam, cat #ab9722) and anti-GAPDH (Cell Signaling, cat #2118). Horseradish peroxidase conjugated goat anti-rabbit secondary antibody (Thermo Fisher, cat#PI31470) was used 1:800 diluted (2 h incubation at room temperature). Chemiluminescent Western blotting substrate (Thermo,

cat#34580) was used to detect the horseradish peroxidase substrate signal. The blots were imaged using a ChemiDoc imager (Bio-Rad). Band intensities were quantified using ImageJ and normalized to GAPDH staining on the same blot, as described previously [256]. The exposure times were adjusted for each experiment to ensure non-saturation of the bands.

4.6.15 Indirect immunofluorescence of aortae

Indirect immunofluorescence was performed as previously described [188]. Briefly, cells were grown in 8-well chamber glass slides (Thermo Fisher Scientific) at densities of 20,000 cells/well. After fixation with 70% methanol/30% acetone, cells were blocked with 10% v/v normal goat serum. 1:500 dilution of primary antibody against the C-terminal half of human fibrillin-1 was applied to the cells for 1.5 h at room temperature [22]. Secondary antibody used was 1:200 diluted goat anti-rabbit conjugated to Cy3 (Jackson ImmunoResearch Laboratories, cat#111-165-003) incubated for 1 h at room temperature. Nuclear counterstaining was performed with 4', 6-diamidino-2-phenylindole (DAPI). All images were recorded using an Axio Imager M2 microscope (Zeiss) equipped with an ORCA-flash 4.0 camera (Hamamatsu). Original images in the tiff format were exported for cell counting using ImageJ [226], as previously described [256].

4.6.16 Indirect immunofluorescence of cells

After transcardial perfusion with PBS and 2% paraformaldehyde, dissected thoracic aortae were fixed in 4% paraformaldehyde for 2 h. Tissues were dehydrated in 30% sucrose solution for 48 h, and embedded in Optimal Cutting Temperature embedding medium (Tissue-Tex, cat# 4583). 5 μ m sections were cut and kept in -80 °C before staining. Sections were warmed up at room temperature for 1h, followed by TBS hydration. 1 mg/mL proteinase XXIV in 50 mM Tris, pH 7.6 solution was used to retrieve antigen epitopes followed by blocking with 2% delipidized BSA in TBS. The proteinase treatment is essential for fibrillin-1 staining in aortic mediae. Antibodies were

diluted in 1% delipidized BSA in TBS. Anti- α SMA (Dako, cat# M0851), anti-C-terminal half of mouse fibrillin-1 (93), anti-CD68 (Abcam, cat# ab5690), anti-CD3 (Abcam, cat# ab5690) and anti-HIF (Novus Biologicals, cat# NB100-479SS) were used as primary antibodies. anti-rabbit Cy5-conjugated antibody (ThermoFisher, Cat#A10534) was used as secondary antibody. Incubation time of primary and secondary antibodies and the imaging microscope were the same as described above.

4.6.17 miR-122 in situ hybridization of aorta

Cryosections were prepared as described above for immunofluorescence, with additional RNase-Zap (Invitrogen) treatment of the sectioning equipment. 10 μ m OCT embedded cryosections were used for miR-122 in situ hybridization. All buffer used were diluted in RNase-free water and autoclaved. The sections were treated with proteinase K (in 1 mM EDTA, 1 mM NaCl, pH 7.4, 5 mM Tris buffer) for 10 min at 37 °C. PBS with 0.1% Tween-20 was used for wash steps. Sections were incubated in 0.16 M 1-ethyl-3-(3-dimethylaminopropyl) carbodiimide in RNase-free water at room temperature for 1 h, which can immobilize the miRNA at its 5' phosphate and thus preserve the miRNA signal. Hybridization using the double digoxigenin (DIG) labeled miR-122 probe (Qiagen) was performed at 65 °C after two PBST washes. Stringent washes with 5 \times SSC buffer, twice with 1 \times SSC, twice with 0.2 \times SSC at 65 °C, followed by 0.2 \times SSC at room temperature, were performed to remove non-specifically bound probes. Sections were blocked with 2% delipidized BSA in TBS at room temperature for 1 h, followed by a PBST wash 2 \times 5 min. Since mouse Alex647-conjugated anti-DIG antibodies (Jackson Laboratory, 1:1000 dilution, 1 h at room temperature) were used to detect the DIG labeled probe on mouse tissue, a blocking step with mouse on mouse IgG (Abcam, 1:200 dilution, 1 h at room temperature) was included to

block non-specific interactions. Stained sections were preserved in vector shield (Vector Laboratories) after 2×5 min PBST washes.

4.6.18 Enzyme-linked immunosorbent assay

Mouse CCL2 levels in the medium of aorta organ cultures were measured with a commercially available ELISA (R&D Systems, cat# MJE00B). Conditioned media without serum were collected after 72 h of organ culture. 50 μ L Assay Diluent RD1W were added to each well of 96-well plates (R&D Systems), followed by 50 μ L of standard or sample. The plates were incubated at room temperature for 2 h and then washed with the provided Wash Buffer. 100 μ L of mouse anti-CCL2 antibody Conjugate were added to each well and incubated for 2 h at room temperature. After four washes, 100 μ L of Substrate Solution were added, followed by 30 min incubation. Reactions were stopped with 100 μ L of Stop Solution. The optical density was measured at 450 nm using a Beckman Coulter plate reader (AD 340). Readings at 540 nm were subtracted to correct for optical imperfections in the plates.

4.7 Figures and Tables

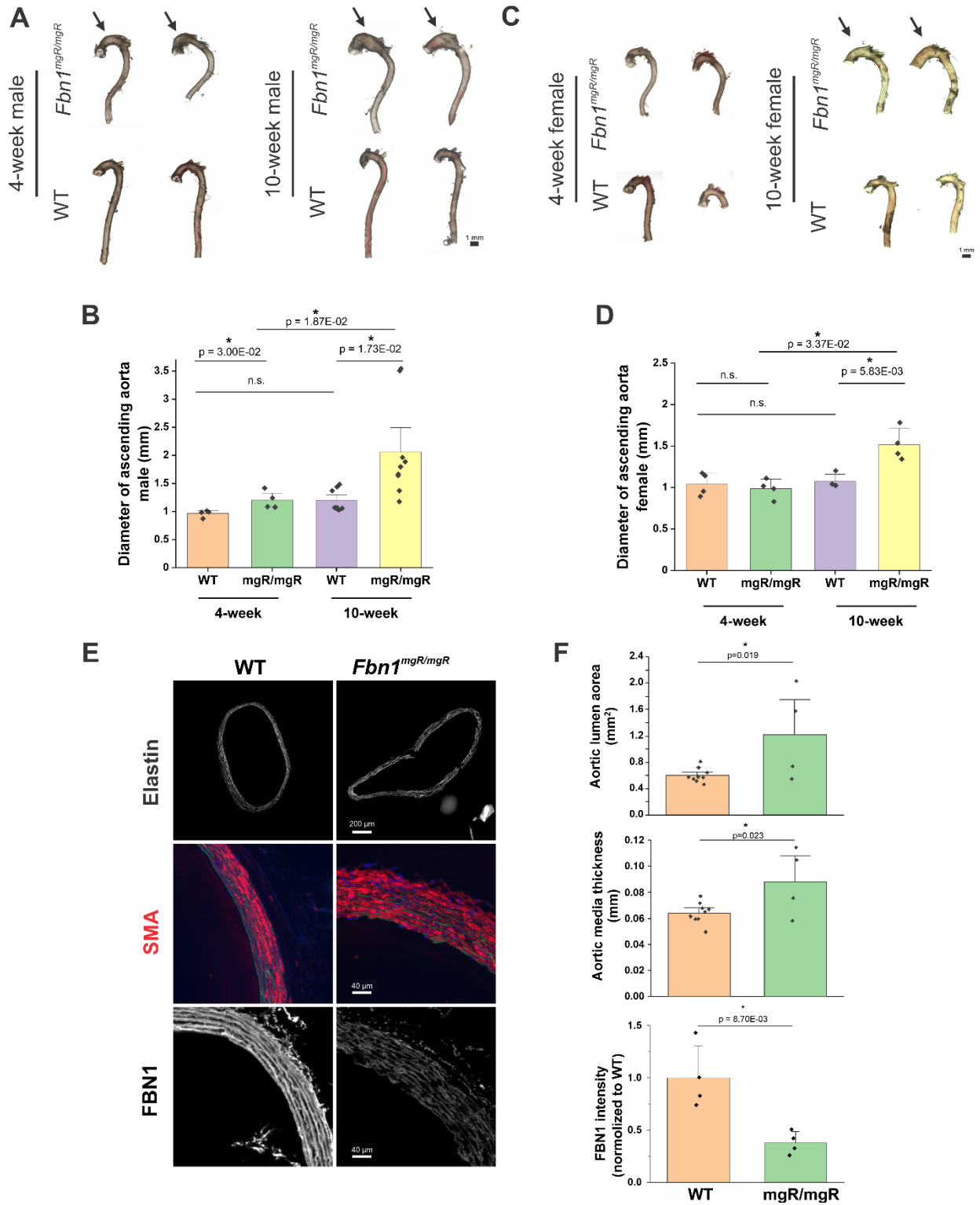


Fig. 4.1 Characterization of the ascending aortic aneurysms in *Fbn1*^{mgR/mgR} mice

(A and C) Gross view of freshly isolated thoracic aortae from male (A) and female (C) wild-type (WT) and *Fbn1*^{mgR/mgR} mice at 4 and 10-weeks of age. Arrows point to the dilated region in the ascending aortae. (B and D) Quantification of the diameters of the ascending aortae in A and C, respectively. Each data point represents the measurement from one mouse. (E) Representative images of elastic lamina auto-fluorescence (Elastin), α -smooth muscle actin staining (SMA) and fibrillin-1 staining (FBN1) of ascending aortic cross-sections from 10-week old male wild-type and *Fbn1*^{mgR/mgR} mice. (F) Quantification of the lumen area and media thickness determined from cross-sections as shown in (E). The average thickness of the aortic media was obtained from determining the perimeters of outer elastic laminae (Po) and inner elastic laminae (Pi) in the cross-sections under 50 \times magnification. Media thickness = $(Po - Pi) / 2\pi$. Intensities of fibrillin-1 staining were determined by ImageJ, and normalized to the cell number (DAPI). Each data point represents the analysis of tissue from one mouse. * indicates p-values less than 0.05.

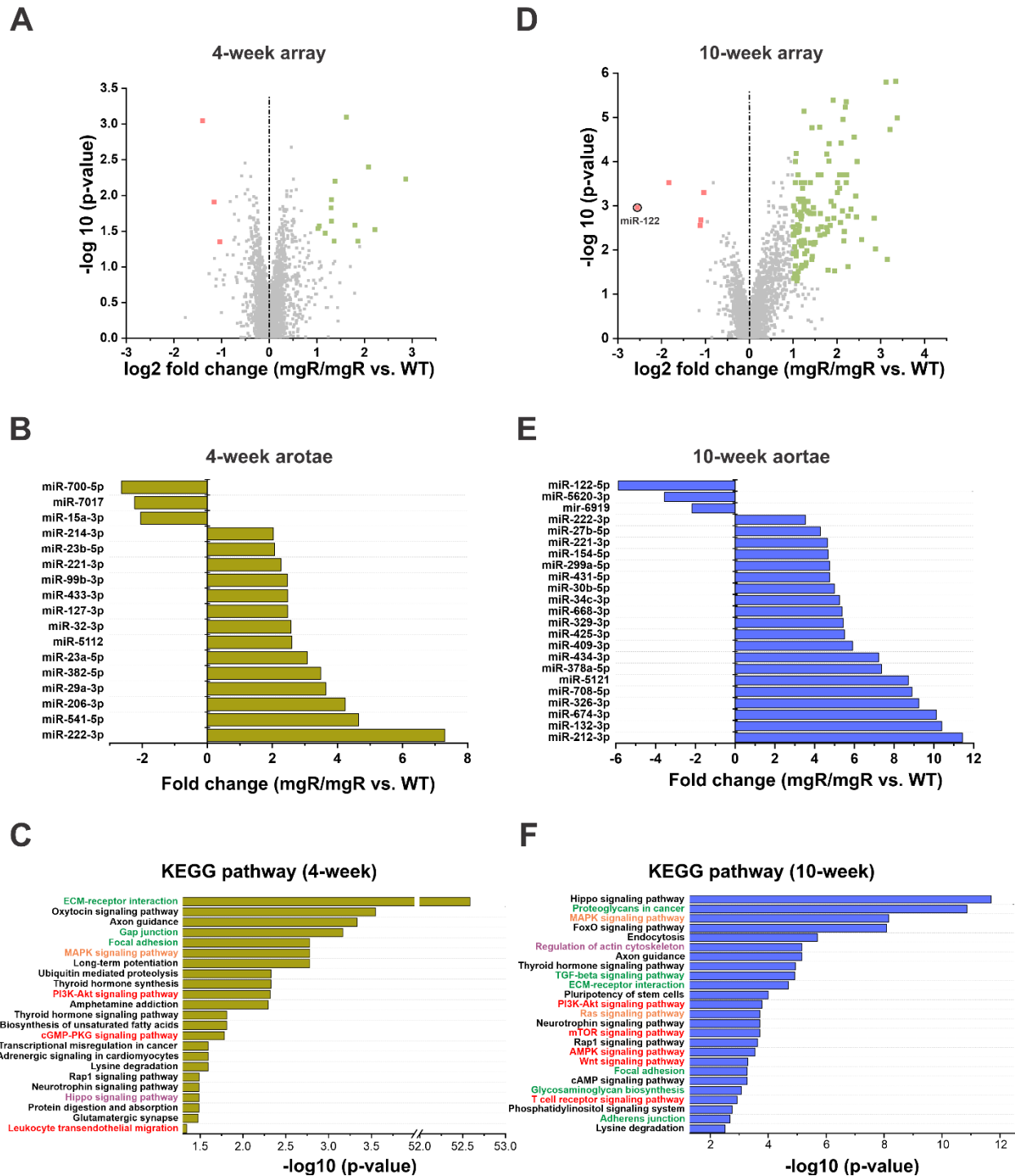


Fig. 4.2 Time-dependent miRNA profiling of ascending aortae of *Fbn1*^{mgR/mgR} mice
(A and D) Volcano plots showing differentially expressed miRNAs in the ascending aorta of *Fbn1*^{mgR/mgR} versus wild-type (WT) mice at 4 and 10-weeks of age detected by Affymetrix GeneChip miRNA 4.0 Arrays. Green data points represent upregulated miRNAs (>2-fold, p<0.05), and red data points indicate downregulated miRNAs (>2-fold, p<0.05). 4 wild-type (*continued*)

(continued from previous page) and 4 *Fbn1^{mgR/mgR}* mice were analyzed. miR-122 is indicated with a black circle. **(B and E)** Levels of all 17 differentially expressed miRNAs (>2-fold) at 4-weeks of age from (A) was plotted in (B), (E) shows the top 3 downregulated and top 20 upregulated miRNAs at 10-weeks of age from (D). Data are shown as fold change *Fbn1^{mgR/mgR}* versus WT. **(C and F)** Pathway enrichment prediction using all differentially expressed (>2-fold, p<0.05) miRNAs at 4 (C) and 10-weeks (F) of age, using the DIANA tool mirPath v.3 (<http://snf-515788.vm.okeanos.grnet.gr>)[330]. The inflammation related pathways are in red color. ECM/cell adhesion relevant pathways are in green. Orange marks the MAPK relevant pathways. Contractility/cytoskeleton related pathways are marked in purple

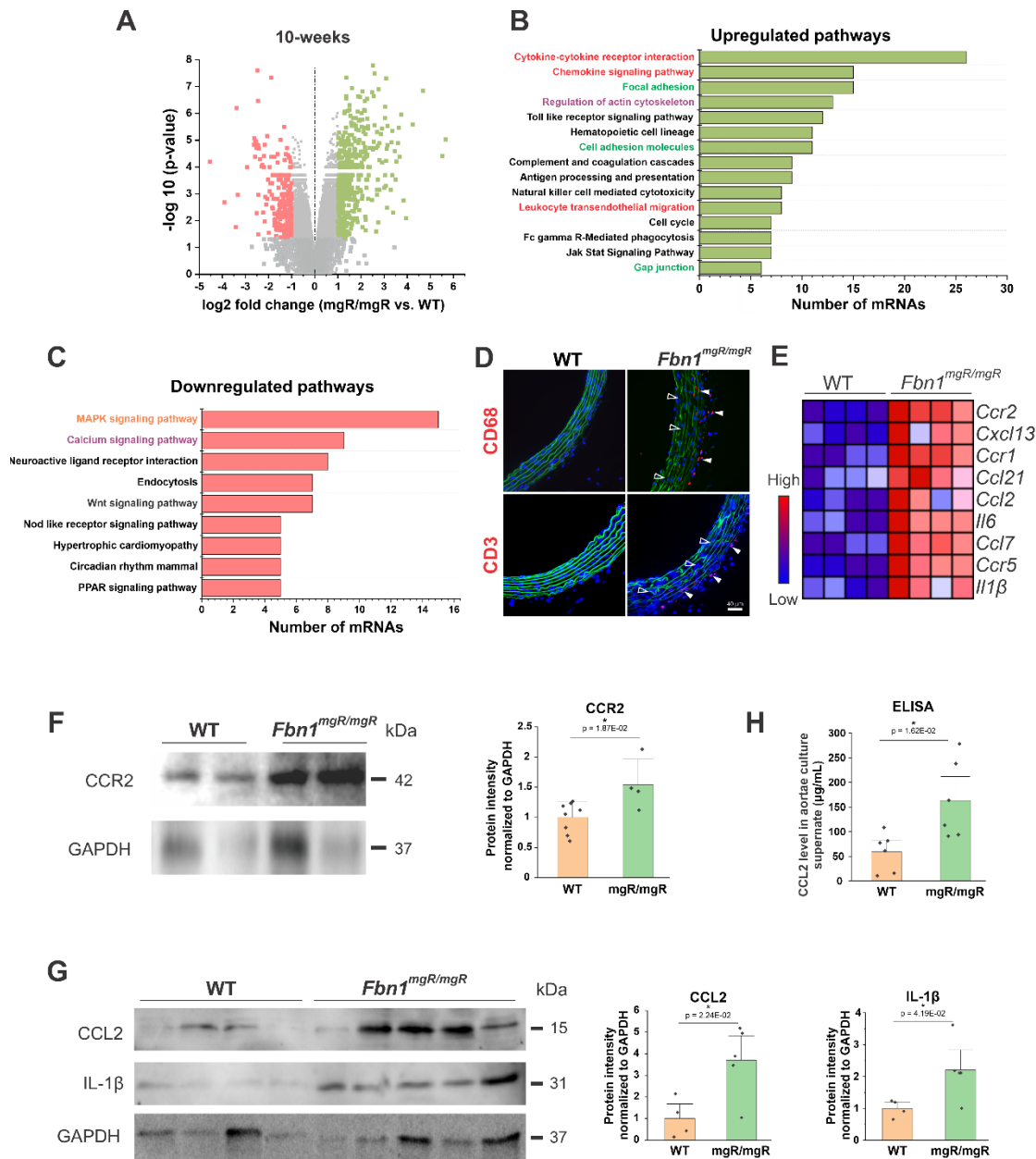


Fig. 4.3 Global mRNA analyses and selected protein levels relevant to inflammation in the ascending aortae of 10-week old *Fbn1*^{mgR/mgR} versus wild-type mice

(A) Volcano plot of differentially expressed mRNAs of 10-week old ascending aortae of *Fbn1*^{mgR/mgR} versus wild-type (WT) mice analyzed by Affymetrix Clariom D array, mouse. Green data points represent upregulated mRNAs (>2-fold, p<0.05), and red data points indicate downregulated mRNAs (>2-fold, p<0.05). (B and C) Gene Set Pathway Enrichment (GSEA; <https://www.gsea-msigdb.org>) analyses showing the upregulated (B) and downregulated (C) pathways. All >2-fold (p<0.05) differentially regulated mRNA transcripts detected were used for the analysis. Red text indicates inflammatory relevant pathways, green text indicates (continued)

(continued from previous page) ECM/cell adhesion related pathways. MAPK pathway is in orange. Contractility/cytoskeleton related pathways are in purple. **(D)** Representative macrophage (CD68) and T cell (CD3) staining of ascending aortic cross-sections from 10-week old male mice. White arrow heads indicate the infiltration of macrophages and T cells in the adventitia and outer media of the *Fbn1*^{mgR/mgR} but not the WT mice. Open white arrow heads indicate the fragmentation of elastic lamina only seen in the *Fbn1*^{mgR/mgR} mice. **(E)** Heat map of the 9 most upregulated mRNAs in the “Cytokine-cytokine receptor interaction” pathway shown in B in WT (left panel) and *Fbn1*^{mgR/mgR} (right panel) aortae. Data are shown for 4 mice in each group. **(F and G)** Analysis of CCL2, IL1 β and CCR2 protein expression levels in 10-week old WT and *Fbn1*^{mgR/mgR} aortae by Western blotting of tissue extracts. Quantifications of the bands are shown on the right. Each data point represents the analysis of one mouse. Error bars represent standard deviation. Two-sample t-test was used to test significance. * represents p-values less than 0.05.

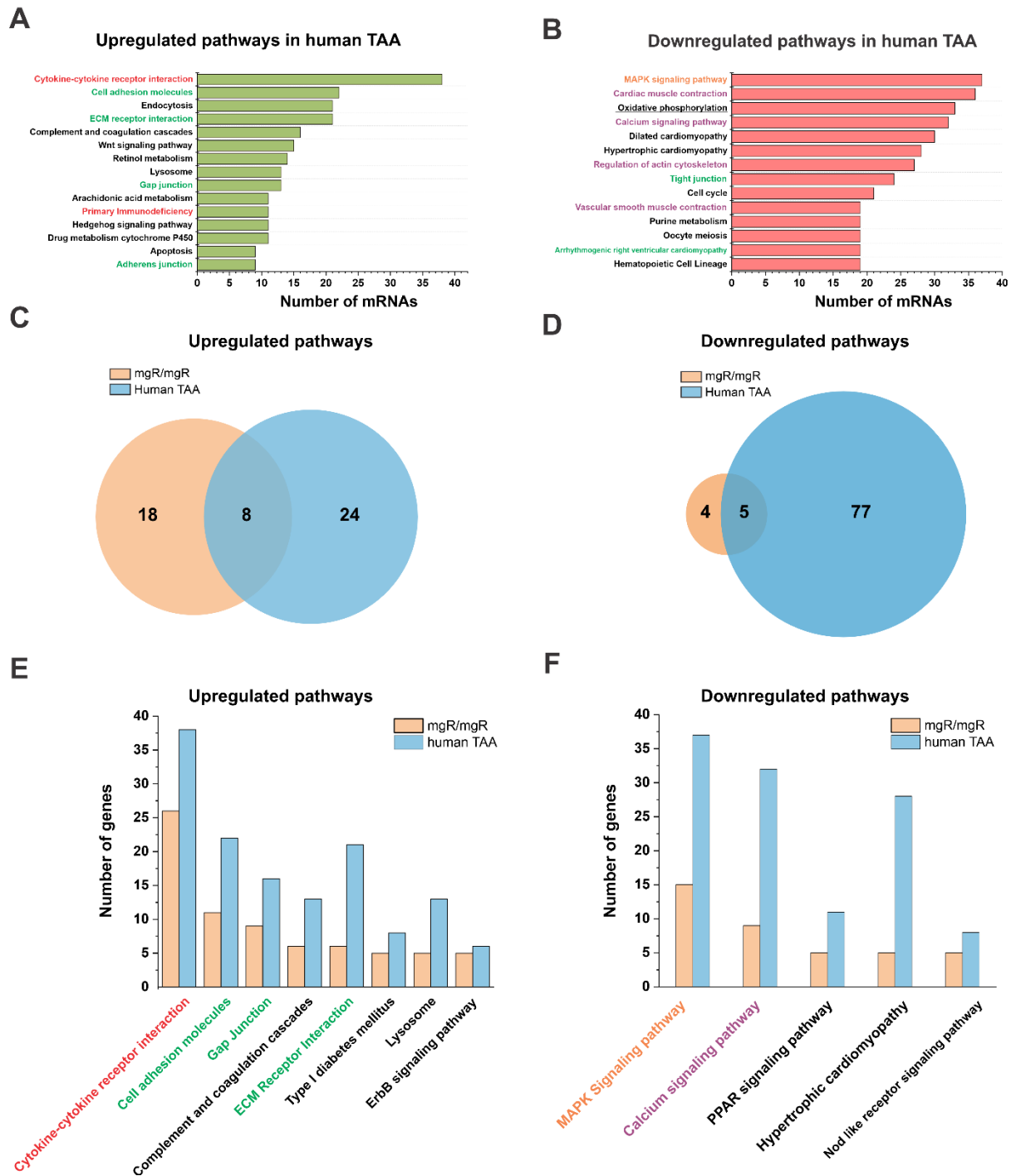


Fig. 4.4 RNA-seq analyses of human TAA patients and its comparison with *Fbn1*^{mgR/mgR}

(A and B) RNA-seq analyses was performed on five human TAA samples and compared with three normal control samples as described in the Methods. Results of GSEA analyses using all >2-fold ($p < 0.05$) differentially expressed transcripts are indicated for the upregulated (A, green bars) and the downregulated (B, red bars) KEGG pathways. Same as Fig. 4.2, inflammatory (*continued*)

(continued from previous page) relevant pathways are colored red. ECM/cell adhesion related pathways are in green. Orange text indicates MAPK pathway. Contractility/cytoskeleton related pathways are in purple. Additionally, "Oxidative phosphorylation" is underlined. **(C and D)** Venn diagrams comparing common and different pathways based on GSEA analyses of *Fbn1*^{mgR/mgR} aortic samples (beige) and human TAA samples (blue). 8 pathways were commonly upregulated (C), and 5 pathways were commonly downregulated (D) in *Fbn1*^{mgR/mgR} and human TAA samples. **(E and F)** The overlapping pathways identified in C and D are indicated in detail in E and F, respectively. The number of genes in each pathway is shown for *Fbn1*^{mgR/mgR} derived tissue (beige bars) and for human TAA derived tissue (blue bars).

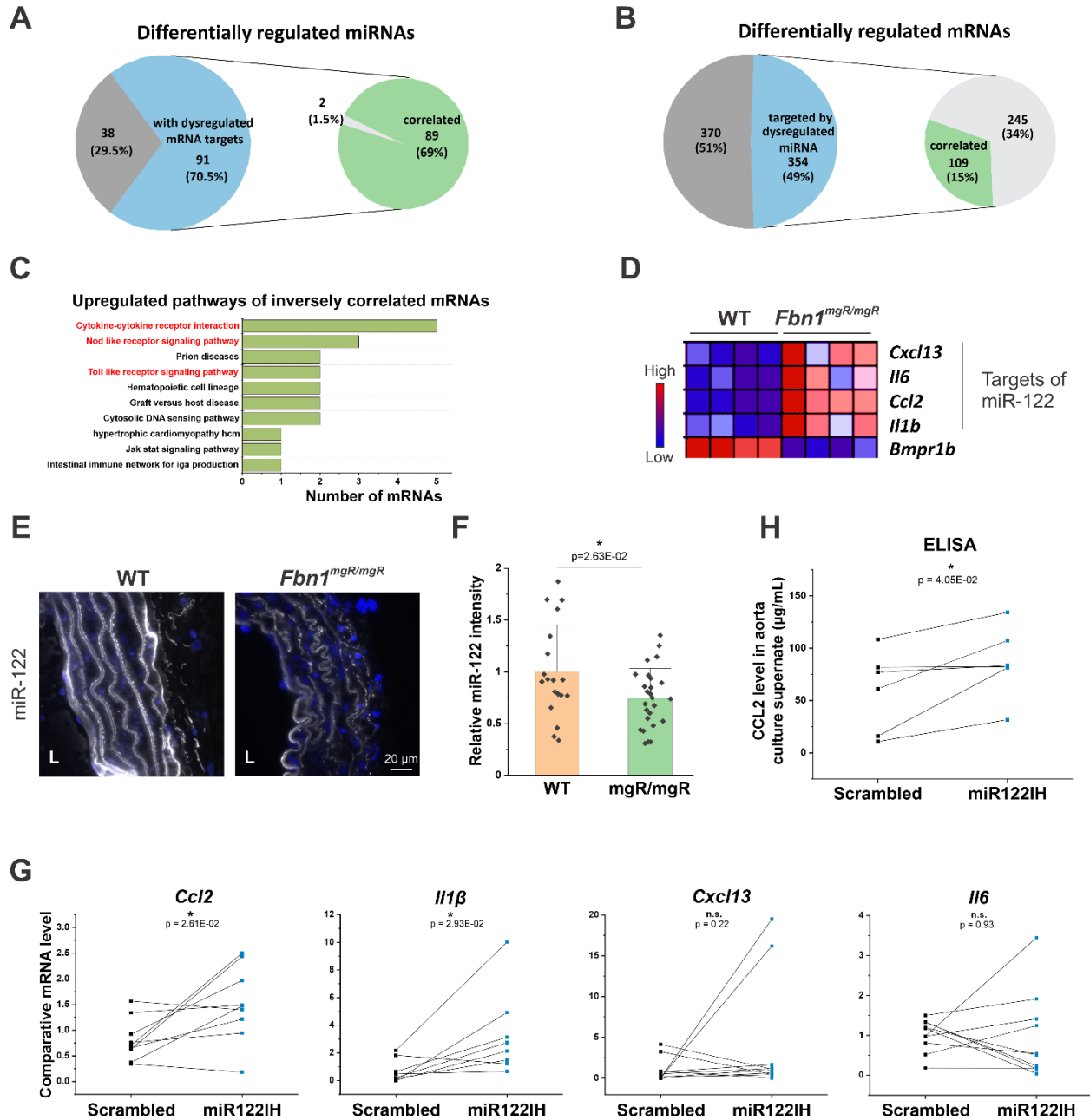


Fig. 4.5 Comparative analyses between the miRNAs and mRNAs expression in mouse tissues (A and B) Pie charts categorizing the differentially expressed 129 miRNAs and 724 mRNAs (>2-fold, $p < 0.05$) based on whether they are inversely correlated. The gray sector in A indicates the number of miRNAs (38) that had no targets in the pool of differentially expressed mRNAs. The gray sector in B shows the number of mRNAs (370) that were not targeted by dysregulated miRNAs. Blue sectors show that 91 miRNAs (A) and their 354 mRNA targets (B) were both differentially expressed. Green sectors indicate that the expression of 89 miRNAs were (*continued*)

(continued from previous page) correlated with their 109 mRNA targets. The light grey sectors show that 2 miRNAs (A) and 245 mRNAs (B) were not correlated. (C) KEGG pathway analyses of the 109 mRNAs which inversely correlated with the miRNAs that targets them (green sector in (B)), using GSEA. Only upregulated pathways were enriched. Inflammatory related pathways are shown in red text. (D) Heat map of the dysregulated mRNAs in the “*Cytokine-cytokine receptor interaction*” pathway from (C). Data are shown for 4 wild-type (WT; left) and 4 *Fbn1^{mgR/mgR}* (right) mice of 10-week male mice. (E) *In situ* hybridization of miR-122 (white signal) in ascending aortic cross-sections from 10-week male WT and *Fbn1^{mgR/mgR}* mice. Nuclei were counter-stained by DAPI (blue). The lumen side is positioned on the left, marked with “L”. (F) Quantification of the miR-122 intensity from (E), normalized to the cell numbers. Each data point represents analysis of one image. In total, 4 *Fbn1^{mgR/mgR}* and 3 WT mice were used. Error bars represent standard deviations. Two-sample t-test was used to test significance. (G) qPCR analyses of the four upregulated mRNA targets of miR-122 (shown in D) using total RNA from *ex vivo* aorta organ cultures treated with miR-122 inhibitor (miR122IH) compared to the scrambled controls. Aortae from 8 wide-type mice were used. Linked is the aorta from each mouse treated with inhibitor and control. (H) CCL2 ELISA of culture medium from *ex vivo* organ cultures treated with miR-122 inhibitor (miR122IH) or a scrambled control. Aortae from 6 mice were used at 10-week of age. Paired-sample t-test was used to test significance in (G and H). * represents p-values less than 0.05.

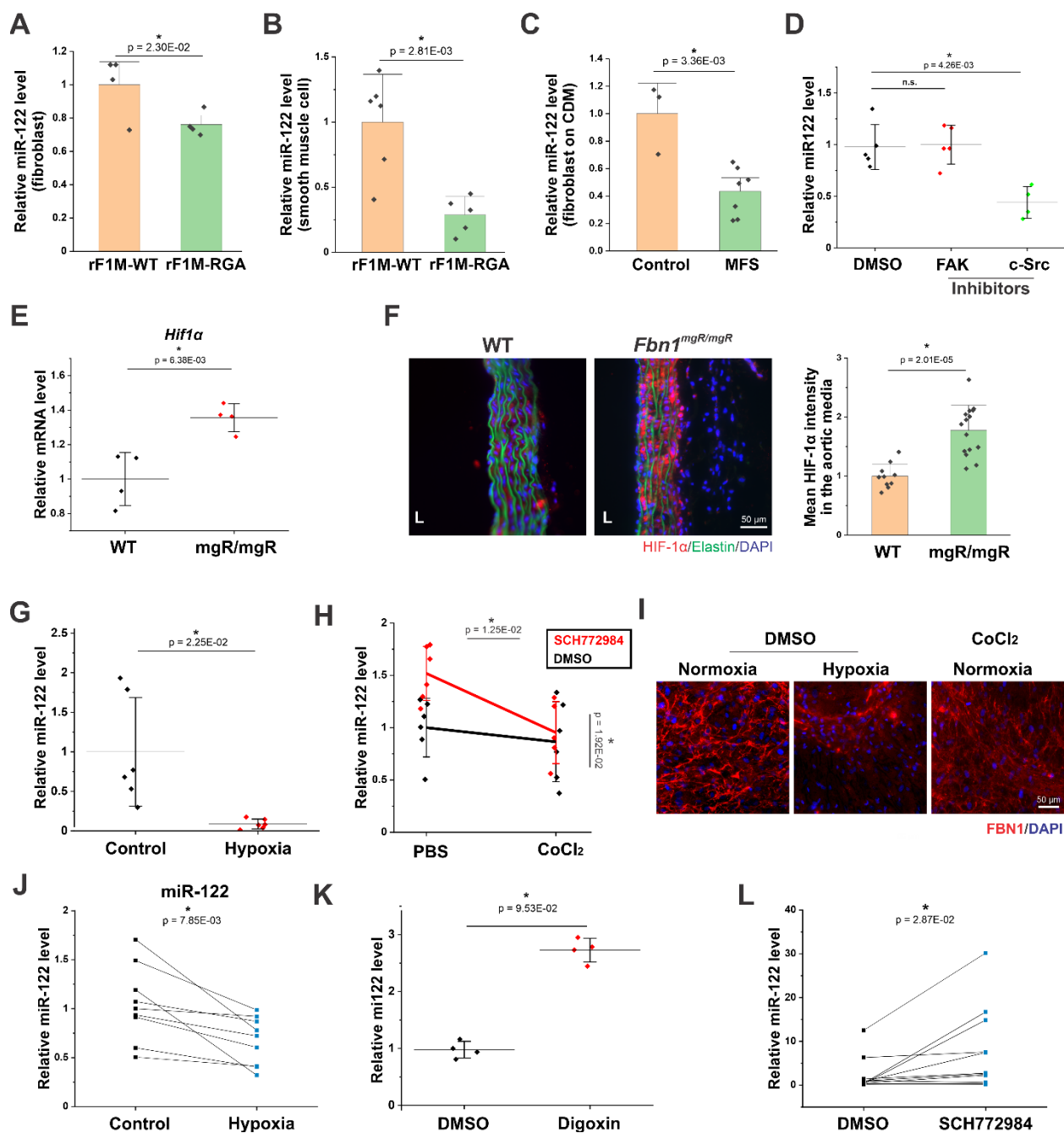


Fig. 4.6 Upstream regulators of miR-122

(A and B) qPCR analyses of miR-122 extracted from fibroblasts (A) and smooth muscle cells (B) 24 h after seeding on rF1M-WT and rF1M-RGA. (C) miR-122 qPCR analyses of normal skin fibroblasts seeded for 24 h either on cell-derived matrices from MFS fibroblasts derived from 7 patients (Supplementary Table 4.2), or on the matrices produced by fibroblasts derived from 3 healthy controls. (D) miR-122 qPCR analyses of smooth muscle cells upon treatment with inhibitors for FAK and c-Src kinase, with DMSO (1:1,000 v/v) used as control. (E) (*continued*)

(continued from previous page) Relative *Hif-1 α* mRNA levels determined by microarrays of 10-week old male mice, comparing *Fbn1^{mgR/mgR}* to wild-type (WT). **(F)** HIF-1 α immunostaining (red) of ascending aortic cross sections of 10-week old male *Fbn1^{mgR/mgR}* and WT mice. The nuclei were counterstained using DAPI (blue). Elastic laminae autofluorescence is shown in green. The lumen side is positioned on the left, marked with “L”. Quantifications of HIF-1 α staining are shown on the right. Each data point represents analysis of one image. **(G)** miR-122 qPCR of human smooth muscle cells cultivated for 48 h under normoxic (Control) or hypoxic conditions. **(H)** miR-122 expression (qPCR analysis) of human smooth muscle cells kept for 48 h under the following conditions: PBS with DMSO (control), PBS with ERK1/2 inhibitor SCH772984, CoCl₂ (activator of HIF-1 α) with DMSO, and CoCl₂ with SCH772984. **(I)** Fibrillin-1 immunostaining (red; nuclear DAPI staining in blue) of human smooth muscle cells cultivated for 48 h under normoxic or hypoxic (5% O₂) conditions. CoCl₂ was to activate HIF-1 α under normoxic condition to mimic hypoxic condition. **(J)** miR-122 qPCR of aorta organ cultures cultivated for 48 h under normoxic or hypoxic conditions. n = 8 mice **(K)** miR-122 levels of human smooth muscle cells treated for 48 h with digoxin (1 μ M) or the DMSO control. **(L)** miR-122 qPCR of aorta organ cultures treated for 48 h with SCH772984 compared to the DMSO control n = 8 mice. Two-sample t-test was used for statistical analyses in (A-G and K). Paired-sample t-test was applied in (J and L). Two-way ANOVA was used in (H). Error bars represent standard deviations. * represents p-values less than 0.05.

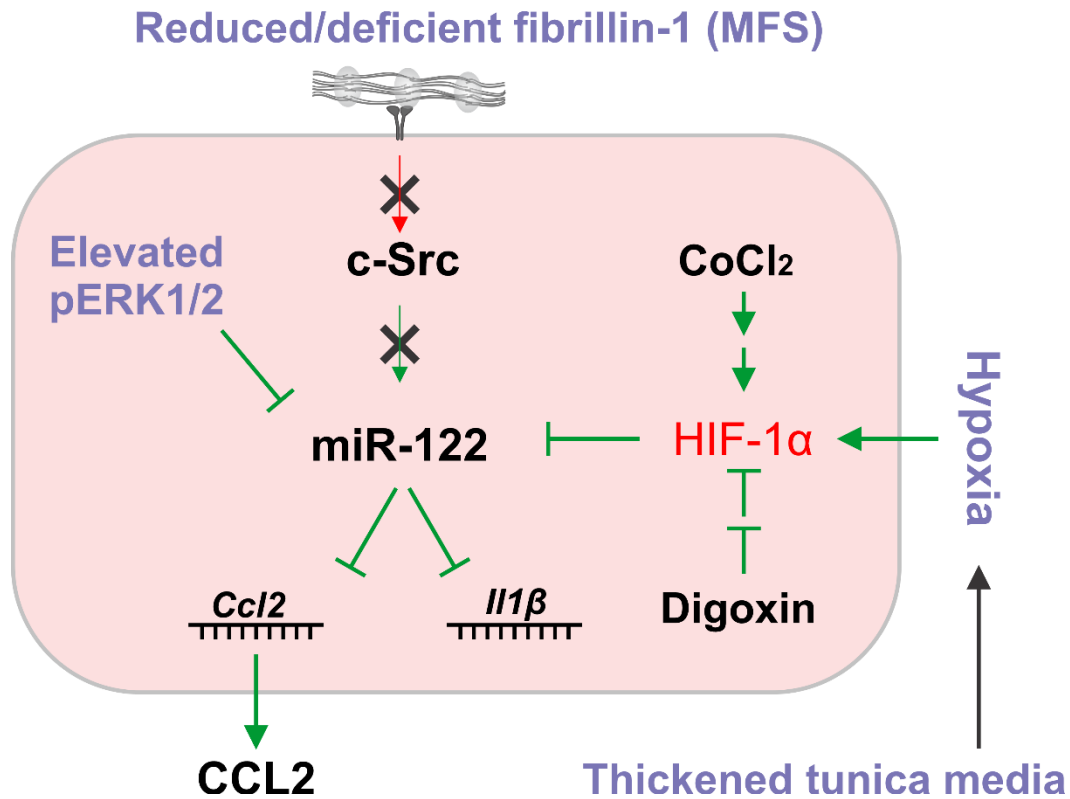


Fig. 4.7 Working model illustrating the central role of miR-122 in TAA

The present study revealed that reduced or deficient fibrillin-1 in the ECM led to downregulation of miR-122. c-Src kinase was necessary to maintain miR-122 levels in normal smooth muscle cells (green arrow). However, whether fibrillin-1-smooth muscle cell interaction can activate c-Src still needs to be further explored (red arrow), but this is expected because fibrillin-1 activates c-Src in fibroblasts (as shown in chapter 3 of this thesis). Hypoxic conditions, which was reported in TAA mouse, and the HIF-1 α activator CoCl₂ downregulated miR-122, whereas the HIF-1 α inhibitor digoxin upregulated miR-122 expression. Whether HIF-1 α (red) was the direct mediator requires further confirmation. Activated ERK1/2, which was shown to be upregulated in aneurysmal aortae of MFS mice, including *Fbn1*^{mgR/mgR}, suppressed miR-122 levels. Functional analyses elucidated that inhibition of miR-122 upregulates inflammatory components, including *Ccl2* and *Il1 β* mRNA levels, and CCL2 protein secretion. Known pathological conditions were in light blue texts. Mechanisms that are validated in this study are highlighted in green, whereas aspects that require further validation are shown in red.

Table S4.1 Information of the five TAA patients, from which the TAA tissues were used for RNAseq

Sex	Age	Smoker(Y,N,F)*	Aneurysm size	Location (R,As,Ar,D)**
M	28	F	5.7 cm	R, As
M	46	N	-	R, As
M	58	F	5.2 cm	R, Ar,D
M	63	N	5.5 cm	R, Ar
M	73	N	4.6 cm	R, As

* Y, N and F mean Yes, No, Frequent respectively

** R, As, Ar, D mean aortic root, ascending aorta, aortic arch, and descending aorta respectively.
It indicates the location where the aneurysm occurred in the patients.

Table S4.2: Information of the seven MFS patients, from which skin fibroblasts were used to generate cell-derived matrices

Mutations	Sex	Age	ID at Coriell institute
C1589F	Male	25	GM21932
G1127S	Female	36	GM21938
C1153Y	Male	-	GM21942
C1039Y	Female	30	GM21948
C1171R	Male	22	GM21950
C1672F	Male	38	GM21956
R1523X	Female	49	GM21982

**CHAPTER 5 QUANTIFICATION OF EXTRACELLULAR MATRIX FIBER SYSTEMS
RELATED TO ADAMTS PROTEINS**

Quantification of Extracellular Matrix Fiber Systems Related to ADAMTS Proteins

Rongmo Zhang¹, Heena Kumra¹, Dieter P. Reinhardt^{1,2,*}

¹Faculty of Medicine, Department of Anatomy and Cell Biology, and ²Faculty of Dentistry

McGill University, Montreal, QC H3A 0C7, Canada

***Corresponding author:**

Dieter P. Reinhardt, PhD

Department of Anatomy and Cell Biology

McGill University

3640 University Street

Montreal, Quebec, H3A 0C7

Canada

E-Mail: dieter.reinhardt@mcgill.ca

Running Head: Quantification of ECM Proteins and Fibers

5.1 Preface:

As were demonstrated in previous chapters, fibrillin-1-cell interaction and miRNAs could regulate multiple cell activities, including focal adhesion formation, cell proliferation, ECM fiber formation etc. Images from immunostainings and *in situ* hybridization are widely used to visualize these changes. In chapter 2, anti-phosphorylated FAK antibody was applied to stained focal adhesion. In chapter 3, Ki67-positive nucleus were used to indicate the proliferating fibroblasts. In chapter 4, immunofluorescence staining and *in situ* hybridization were used to indicate the levels of fibrillin-1 and miR-122 in tissue sections or smooth muscle cell cultures. To quantitatively analyze these modulations, unbiased methods were needed. This chapter presents customized methods based on an open source image processing program ImageJ.

5.2 Abstract

ADAMTS (a disintegrin-like and metalloprotease domain with thrombospondin type 1 motifs) proteins regulate tissue homeostasis and extracellular matrix (ECM)-related pathogenesis. Some ADAMTS proteins interact with or process multiple extracellular matrix (ECM) proteins, including fibrillins, fibronectin, and collagens. Therefore, characterization and quantification of these ECM fiber systems is essential to understand their functional relationship with ADAMTS proteins. Here we describe unbiased methods to quantify various aspects of ADAMTS-related ECM fiber systems in cell culture and in tissues. We focus on cell counting, overall fiber intensity, fiber length, and focal adhesion analysis in cell culture, and on the quantification of immunohistochemical and immunofluorescent tissue sections. We use ImageJ/Fiji, a widely used Java-based open source software which provides efficient and customizable quantification methods for microscopy images.

Key Words: Extracellular matrix fibers, focal adhesions, cell number, ImageJ, Fiji, cell culture, tissue sections

5.3 Introduction

ADAMTS proteins, which are secreted (non-membrane bound) proteases or ECM components, regulate homeostasis in tissues, such as blood vessels and cartilage [331,332]. They have important roles in ECM-related pathogenesis, including cancer metastasis, and in connective tissue disorders such as geleophysic dysplasia and Weill- Marchesani syndrome [333-335]. ECM protein fiber systems, such as fibronectin, fibrillins and collagens, either act as binding partner for or are processed by ADAMTS proteins [336,337]. The quantification and characterization of these ECM

fiber systems in relation to ADAMTS proteins can provide important information that allows functional conclusions. Frequently in the literature, qualitative analyses of ECM fiber systems are presented that lack thorough unbiased quantifications. Efficient methods are required to improve this situation.

ImageJ, first developed by Wayne Rasband, is a Java-based software [338]. It is compatible with multiple operation systems, including Windows, Linux and Macintosh [339]. Furthermore, ImageJ is an open-source software for which scientists and enthusiasts can develop additional plugin programs designed for specific purposes [340]. Fiji is entirely based on ImageJ and bundles multiple plugins, providing a convenient software suite to fulfill the needs for various quantification approaches [341]. Here, we describe a number of customized quantification protocols using ImageJ/Fiji useful to quantify ECM fiber systems in relation to the cells that produce them in cell culture or in tissues.

5.4 Materials

1. The image processing packages ImageJ (<https://imagej.nih.gov/ij/download.html>) [338] or Fiji (<https://imagej.net/Fiji/Downloads>) [341] can be freely downloaded from the respective websites.
2. The Skeleton plugin is already included in Fiji, but requires a separate download and installation for ImageJ (<https://imagej.net/Skeletonize3D>) [342].
3. The CLAHE (Contrast Limited Adaptive Histogram Equalization) plugin ([https://imagej.net/Enhance_Local_Contrast_\(CLAHE\)#cite_note-1](https://imagej.net/Enhance_Local_Contrast_(CLAHE)#cite_note-1)) needs to be downloaded and installed for both distributions [228].

4. Images of cells and tissue sections stained by indirect immunofluorescence or immunohistochemistry are prepared as explained in detail elsewhere [343] (see **Note 1**).
 - a. For immunofluorescence, original images (without applying RGB colors) should be exported from the epifluorescent microscope software in a lossless compression format, preferably the Tagged Image File Format (TIFF) as 8-bit grayscale images.
 - b. Existing immunofluorescence images in the 24-bit RGB format need to be converted into 8-bit grayscale in ImageJ/Fiji.
 - i. Merged 24-bit RGB images including multiple channels need to be split into individual channel images (8-bit gray scale) using “*Image - Color - Split Channels*”.
 - ii. An individual 24-bit RGB image (not merged) needs to be converted with “*Image - Type - 8-bit*”.
 - c. For tissue sections stained by immunohistochemistry, 24-bit RGB bright-field images in the TIFF format are used, which should be exported with the microscope software.

5.5 Methods

5.5.1 Quantification Procedures in Cell Culture

Mesenchymal cells, including fibroblast and smooth muscle cells, grown on tissue culture plates will secrete and organize ECM fibers. Immunofluorescence staining of these ECM fibers and interacting proteins can visualize their shape and organizational pattern in relation to the cells.

5.5.1.1 Cell Numbers

To normalize immunofluorescent signals of ECM fibers, it is often desirable to determine the number of cells for normalization. To achieve this, the cell nuclei need to be counterstained [343] (see **Note 2**).

Protocol:

1. Open image in ImageJ/Fiji. See Materials for preparation of the images.
2. Set the scale for the image with “*Analyze - Set scale*”. “*Distance in pixels*”, “*Known distance*”, and “*Unit of length*” should be obtained from the microscope software. Set the “*Pixel aspect ratio*” to 1.
3. Set threshold via “*Image - Adjust - threshold*” with the settings in the popup window “*Default*”, “*B&W*”, and “*Dark background*” checked. Set threshold max value to 255. Setting the correct min value varies, depending on the intensity of the DAPI staining. As a general rule, the shape of the nucleus should be preserved, while minimizing the background. Click “*Apply*”.
4. Click “*Process - Binary - Watershed*”, to separate potentially overlapping nuclei. Figure 5.1 shows the original and the processed DAPI stained image of human skin fibroblast nuclei (see **Note 3**).
5. Uncheck all parameters in “*Analyze - Set measurements*” and click “*OK*”.
6. To analyze the processed image, select “*Analyze - Analyze particles*”. Set range of “*Size*” (given in the units defined in set scale under #1) accordingly to exclude small particles that are not representing nuclei. We recommend using the “*Straight Line Selection Tool*” to measure the diameter of the smallest nuclei in the image, and then set the range accordingly (e.g. 4 μm^2 -Infinity). Uncheck “*Pixel units*”, define “*Circularity*” as 0-0.99, because a

perfect circle is unlikely for the shape of the nucleus. Set “*Show*” to “Nothing”. Check “*Summarize*” and click “*OK*”. The “*Summary*” window will display the “Count”, “Total Area”, “Average Size”, “%Area” of the nuclei. Use the “Count” result for the number of cells.

5.5.1.2 Intensity of ECM Fibers and Intracellular Signaling Proteins

In indirect and direct immunofluorescence, the labeling intensity of the target proteins correlates with the amount of epitopes recognized by the primary antibody (see **Note 4**). The overall pixel intensity is used to determine the total amount of fluorescence present in the image, and hence provide a relative measure for the total amount of target protein. Here we describe two commonly used methods to determine i) ECM fibers assembled by mesenchymal cells (see **Note 5**), and ii) ECM-regulated intracellular signaling protein staining (see **Note 6**).

i) Intensity of ECM Fibers

Protocol:

1. Open and, if required convert the image into 8-bit gray scale format in ImageJ/Fiji, and set the scale, as described in 5.5.1.1.
2. Select “*Analyze - Set Measurements*” to include “*Area*” and “*Mean gray value*”, click “*OK*”.
3. Click “*Analyze - Measure*”, which will provide the *Total Area* and the *Mean Total Intensity* of the entire image.
4. Select a small region including only background staining with the selection tool, and click “*Analyze - Measure*” (*Background Mean Intensity*).

5. Calculation:

- a. $\text{Mean Total Intensity} - \text{Background Mean Intensity} = \text{Mean Specific Intensity}$
(stained ECM fibers).
- b. $\text{Mean Specific Intensity} \times \text{Total Area} = \text{Total Specific Intensity}$ of the ECM fibers.

6. Normalization:

- a. Refer to 5.5.1.1, to obtain the total number of cells. Normalize the *Total Specific Intensity* to the cell number.

ii) Intensity of Intracellular Signaling Proteins

Some ECM proteins that either directly or indirectly interact with ADAMTS proteins (e.g. fibrillins, LTBPs) serve not only as structural support, but also as regulators of cell function. This can occur either via biomechanical sensing of the ECM, or by sequestering soluble growth factors, such as transforming growth factor beta and bone morphogenetic proteins [344]. These soluble growth factors can regulate multiple downstream signaling proteins, located in the cytosol and in the nucleus. Thus, quantification of the regulated intracellular signaling pathway components reveals an important effect of ADAMTS proteins. This can be quantified with entire images following the protocol i) for intensities of ECM fibers, or by analyzing individual cells described in the following (see **Note 7**).

Protocol:

1. Open and potentially convert the image into 8-bit gray scale format in ImageJ/Fiji, and set the scale as described in 5.5.1.1.

2. Select “*Analyze - Set Measurements*” to include “*Area*” and “*Mean gray value*”, click “*OK*”.
3. Outline individual cells of interest using the “*Freehand Selections Tool*”, and click “*Analyze - Measure*”. This will provide the *Cell Area* and *Mean Total Intensity* of this outlined cell.
4. Outline a region with only background staining close to the cell, and click “*Analyze - Measure*” (*Background Mean Intensity*).
5. Calculation:
 - a. $Mean\ Total\ Intensity - Background\ Mean\ Intensity = Mean\ Specific\ Intensity$
(stained intracellular signaling proteins).
 - b. $Mean\ Specific\ Intensity \times Cell\ Area = Total\ Specific\ Intensity$ of the intracellular signaling proteins.

5.5.1.3 Total Fiber Length and Branch Points

The fiber length and branch points are important indicators for ECM fiber maturity. Therefore, we provide a customized protocol to quantify these features (see **Note 8** and **9**).

Protocol:

1. Open and potentially convert the image into the 8-bit gray scale format in ImageJ/Fiji, and set the scale as described in 5.5.1.1 (see **Note 10**).
2. Adjust the threshold by “*Image - Adjust - Threshold*”. Set the threshold “Maximum” to 255, and manually set the “Minimum” to match best the fiber appearance in the original

image. Check “*Default*”, “*B&W*”, and “*Dark background*”, then click “*Apply*” (see **Note 11**).

3. Remove noise generated by small non-fibrous particles by applying three times “*Process - Noise - Despeckle*”.
4. Skeletonize the thresholded ECM fiber staining by applying “*Plugins - Skeleton - Skeletonize (2D/3D)*”, which will reduce the width of objects into single-pixel-wide shapes. Figure 5.2A and B shows an example of an original and a processed image of fibronectin staining.
5. To analyze the processed image, click “*Analyze - Skeleton - Analyze Skeleton (2D/3D)*”, with the “*Prune cycle method*” set to “none”, and “*Show detailed info*” checked. Click “*OK*”. This opens a “*Results*” window and a “*Branch information*” window. The “*Branch length*” for each individual branch is shown in the “*Branch Information*” window, and the “*Number of branches*” and “*Number of junctions*” is displayed in the “*Results*” window. The total fiber lengths, number of branches, average branch length, and the number of junctions can be conveniently calculated after copying the results into a spreadsheet software (Figure 5.2C).

5.5.1.4 Focal Adhesions

ECM proteins bind to various membrane proteins, including activated integrins and heparan sulfate containing proteoglycans [40]. These membrane proteins connect ECM fibers to the cytoskeleton via protein complexes such as focal adhesions. The assembly and disassembly of focal adhesions provide mechanical support for cell migration, and trigger multiple signaling pathways [215]. The distribution and maturation of focal adhesion complexes display a unique pattern different from

the previously discussed ECM proteins or intracellular staining of signaling components and is influenced by various factors, such as the curvature of the plasma membrane, the migration direction, or the mechanical force applied [345]. Thus, a unique quantification method is essential to reveal the properties of focal adhesion (see **Note 12**). The following protocol is adopted from Horzum et al. (2014) [227].

Protocol:

1. Due to the small sizes of focal adhesions, a microscope magnification of $\geq 600\times$ is recommended to record the images. Open and potentially convert the image into 8-bit gray scale format in ImageJ/Fiji, and set the scale as described under 5.5.1.1.
2. Run “**Process - Subtract Background**” with “*Rolling ball radius*” set to as 50.0, and “*Sliding paraboloid*” checked.
3. Run “**Plugins - CLAHE**” with “*blocksize*” of 19, “*histogram bins*” of 256, and “*maximum slope*” of 6, to enhance the local contrast.
4. Further reduce the background by running “**Process - Math - Exp**”.
5. Run “**Image - Adjust - Brightness/Contrast**”. Set “Minimum” and “Maximum” to closely match the focal adhesion signals of the original images, then “*Apply*”. The “*Auto*” setting is a good start point for the adjustment (see **Note 13**).
6. Run “**Image - Adjust - Threshold**”. Set the threshold maximum to 255, and manually set the minimum to closely represent the focal adhesions of the original image, then “*Apply*”. Figure 5.3 shows an example of the original and the processed image of phosphorylated focal adhesion kinase, which is commonly used to visualize focal adhesions (see **Note 14**).

7. To analyze the processed image, click “*Analyze - Analyze particles*”. Set the range of “*Size*” to 0-Infinity. Uncheck “*Pixel units*”, define “*Circularity*” as 0-0.99, because a perfect circle is likely to be an artifact. Set “*Show*” to “*Nothing*”. Check “*Summarize*” and click “*OK*”. The “*Summary*” window will display the “*Count*”, “*Total Area*”, “*Average Size*”, “*%Area*” of the focal adhesion.
8. The total area, total number, and the average size of focal adhesions in the entire image can be conveniently calculated after copying the results into a spreadsheet software (Figure 5.3C). The data can be normalized with the cell count method described under 5.5.1.1.

5.5.2 Quantification Procedures of Tissue Sections

Immunofluorescence or immunohistochemistry methods can detect and quantify proteins in tissues. Both techniques detect the protein using a specific primary antibody, which is then recognized by a secondary antibody labelled with either a fluorophore (immunofluorescence) or with an enzyme such as horseradish peroxidase (immunohistochemistry).

For immunofluorescence, images are obtained with an epifluorescence microscope, which uses specific wavelengths to excite and then detect the emission from a fluorophore. Images are recorded in a red, a green and a blue channel (hence RGB images). Each channel typically represents the staining with one antibody, and thus one target protein. Overlay of the three channels provides a merged image in which the colors are additively mixed (e.g. a red and a green signal results in a yellow merged signal). This allows conclusions of colocalized proteins. Importantly, the entire information for one fluorescent dye is maintained within one channel, allowing quantification of each immunostained protein after splitting the merged image into individual channels.

In immunohistochemistry, the sections are treated with substrates such as 3,3'-diaminobenzidine (DAB) or 3-amino-9-ethylcarbazole (AEC), which when converted by the enzyme, results in detectable colored products. These products absorb light in bright-field microscopy and thus the resulting colors are produced by subtracting parts of the light spectrum. The total absorbed light (and thus the signal intensity) contains parts of all three channels, and thus the channels cannot be split like in immunofluorescence images. They need to be analyzed together.

Because both techniques are based on antigen-antibody reaction, which is non-stoichiometric, these techniques do not provide an absolute quantification of the target proteins. They provide a relative quantification of the protein analyzed when compared to various experimental conditions.

5.5.2.1 Analysis of Tissue Section Stained by Immunofluorescence

Immunofluorescence stainings are performed on frozen tissue sections, which are briefly fixed for 1-2 h. This is the preferred method for staining more than one protein in tissues to determine potential colocalization. It is very important to pre-analyze the tissue sections for autofluorescence and to avoid fluorophores with emission spectra overlapping with tissue autofluorescence. For example, to analyze aortic wall sections, Fluorescein/Alexa Fluor 488 labelled secondary antibodies cannot be used as the elastic lamellae have a very strong autofluorescence in the emission range of these fluorophores (~525nm) (see **Note 15**). It is important to note that the ECM proteins and fibers in the tissues between cells always adopt a significant depth, which typically results in some areas that are not in focus when analyzed by an epifluorescent microscope. This can be improved by using confocal microscopy or structured illumination techniques.

Protocol:

1. Open an 8-bit grey scale image in ImageJ/Fiji. If the image is not in this format, convert it according to the procedure provided in “Materials” (Section 2). Figure 5.4 shows an example of a 24-bit RGB image, which is converted into an 8-bit gray scale used for quantification.
2. Set the scale of the image with “*Analyze – Set scale*”. “*Distance in pixels*”, “*Known distance*”, and “*Unit of length*” should be obtained from the microscope software. Set the “*Pixel aspect ratio*” to 1.
3. Outline the area to be quantified using one of the selection tools (mouse over to see the description). If the entire image needs to be quantified omit this step and proceed to #4.
4. Click on “*Analyze - Set Measurements*”. Check “*Area*”, and “*Mean gray value*”. Click “*OK*”. This step only needs to be performed once to set the parameters of interest.
5. Click on “*Analyze - Measure*”. A result window will open, providing the values for the *Area* and the *Mean Total Intensity* of the outlined region.
6. Select a background area on the image where there is no tissue with one of the selection tools and click on “*Analyze - Measure*”. This provides the *Background Mean Intensity*.
7. Calculation:
 - a. $Mean\ Total\ Intensity - Background\ Mean\ Intensity = Mean\ Specific\ Intensity$ (of the stained protein)
 - b. $Mean\ Specific\ Intensity \times Area = Total\ Specific\ Intensity$ of the protein stained.
8. Proceed to section 5.5.3 “Explanation of Quantification Parameters”.

5.5.2.2 Analysis of Tissue Section Stained by Immunohistochemistry

IHC staining procedures are usually performed with paraformaldehyde/formalin fixed paraffin sections. This allows detection of a specific protein in sections where the tissue histology is completely maintained. The colored products typically used in immunohistochemistry (DAB, or AEC based) require recording of the images by bright-field microscopy and cannot be split into various channels (see explanation in 3.2). What can be determined is the optical density resulting from the colored product. Counterstains such as hematoxylin also contribute to the optical density of an image. Therefore, sections used for quantifying immunohistochemistry signals should not be counterstained. Similar to the antigen-antibody reaction, the deposition of colored products is a non-stoichiometric reaction. Therefore, this procedure allows quantification of the protein of interest relative to other experimental conditions.

Protocol:

1. Open a 24-bit RGB image (without counterstain) in ImageJ/Fiji obtained through bright-field microscopy. Figure 5.5 shows a typical immunohistochemistry stained image with the counterstain (hematoxylin), which needs to be omitted for quantification.
2. Set the scale for the image with “*Analyze - Set scale*”. “*Distance in pixels*”, “*Known distance*”, and “*Unit of length*” should be obtained from the microscope software. Set the “*Pixel aspect ratio*” to 1.
3. Outline the area to be quantified with one of the selection tools (mouse over to see the description).
4. Click on “*Analyze - Set Measurements*”. Check “*Area*”, and “*Mean gray value*”. Click “*OK*”. This step only needs to be done once to set the parameters measured.

5. Click on “*Analyze – Measure*”.
6. A result window will open, providing the values for the *Area* and the *Mean Total Intensity* of the outlined region.
7. Select a background area on the image, where there is no tissue, with one of the selection tools and click on “*Analyze - Measure*”. This provides the *Background Mean Intensity*
8. Calculation:
 - a. $Mean\ Total\ Intensity - Background\ Mean\ Intensity = Mean\ Specific\ Intensity$ (of the stained protein)
 - b. $Mean\ Specific\ Intensity \times Area = Total\ Specific\ Intensity$ of the protein stained.
9. Proceed to section 5.5.3 “Explanation of Quantification Parameters”.

5.5.3 Explanation of Quantification Parameters

Depending on the research question, different parameters are used for the quantification.

1. “Area” is displayed in the dimensions as defined with the “*Set scale*” procedure. It allows determination of the area selected between the different analyzed images.
2. “Mean” provides the average intensity of the staining (averaged gray value of all pixels selected) irrespective of the area of the selected region. Pixel gray values range from 0 to 255 where 0 represents black and 255 represents white. To obtain positive values for increasing staining intensities, the “Mean” values should be inverted (“Mean” value subtracted from 255).
3. *Mean Specific Intensity* is used when analyzing the distribution of a protein in the tissue. But if the focus is on the total protein content, then *Total Specific Intensity* is the parameter

analyzed. For immunohistochemistry, the *Mean Specific Intensity* is the commonly used parameter for quantification.

5.6 Notes

1. In general, to be able to compare various conditions, it is of utmost importance to acquire the images with exactly the same exposure times and other microscopes settings, e.g., exposure time, gain.
2. The DNA-binding fluorescent dye, 4', 6-diamidino-2-phenylindole (DAPI) is commonly used for nuclei counterstaining, because it can cross the intact plasma membrane and the nuclear envelope to bind stoichiometrically to AT-rich regions of intact DNA. The DNA–DAPI complex is stable and the fluorescence at 365 nm excitation is 20-fold increased as compared to non-bound DAPI [346]. One stained nucleus represents one cell, because the number of dividing cells containing two nuclei is typically low. Other nuclei counterstaining dyes will work similarly well.
3. Cells forming clusters or significantly overlapping will cause problems for the watershed procedure.
4. Methanol:acetone (70:30) fixation permeabilizes the cell membrane and thus allows staining of intracellular aspects. When intracellular staining needs to be excluded, 4% paraformaldehyde (PFA) fixation can be used. However, PFA mediated protein cross-linking can destroy antibody epitopes, and thus may reduce the reactivity of some antibodies (especially monoclonal antibodies) [343].
5. For ECM fibers, analysis of 20-30 images taken at ~400× magnification should provide statistically robust results, depending on the signal variations.

6. For intracellular signaling proteins, depending on the signal variations, about 50-150 cells should be analyzed, which should provide a statistically robust analysis.
7. To achieve precise outlines of the cells, a draw pad is recommended that allows drawing with a pen instead of the computer mouse.
8. For quantification of the total fiber length and branch points, the green fluorescent dyes (e.g. FITC, Alexa 488) work better than red dyes (e.g. Cy3) as they provide sharper signals and thus a better resolution. However, if the protein to be quantified is present only in low amounts, then red dyes generally provide stronger signals.
9. When intracellular staining needs to be excluded, 4% paraformaldehyde (PFA) fixation should be used [343].
10. High quality measurements require a low background. If required, a high background can be reduced with “*Process - Subtract Background*” prior to step #2.
11. When quantifying total fiber lengths and branch points, it is of utmost importance to keep the “Minimum” of “*Image - Adjust - Threshold*” (Step #2) consistent for all analyzed images, so that the parameters from different experimental conditions can be compared. We recommended to use the average optimized “Minimum” values from several images.
12. Measuring the entire image provides a convenient way to quantify focal adhesions on slides containing confluent cells. Analysis of 15-30 images taken at $\geq 600\times$ magnification should provide statistically robust results.
13. To be able to compare the quantified parameters with other experimental conditions, it is of utmost importance to keep the “Minimum” and “Maximum” of “*Image - Adjust - Brightness/Contrast*” (Step #5), and the “Minimum” of “*Image - Adjust - Threshold*”

(Step #6) consistent for all analyzed images. Averages of optimized parameters from multiple images can be used.

14. For experiments with a much lower cell density where cells are clearly separated from each other, a more detailed analysis can be obtained by outlining each cell using the selection tools after step #6. Then perform the procedure under step #7, which provides the total number, the total area, and the average size of focal adhesions after outlining a cell. In this case, normalization in step #8 is not required. Depending on the variations, about 30-100 cells should be analyzed, which should provide a statistically robust analysis.
15. If it is not possible to avoid the fluorophore overlapping with tissue autofluorescence, then a counterstain with Pontamine Sky Blue is recommended which reduces the tissue autofluorescence [347].

5.7 Figures

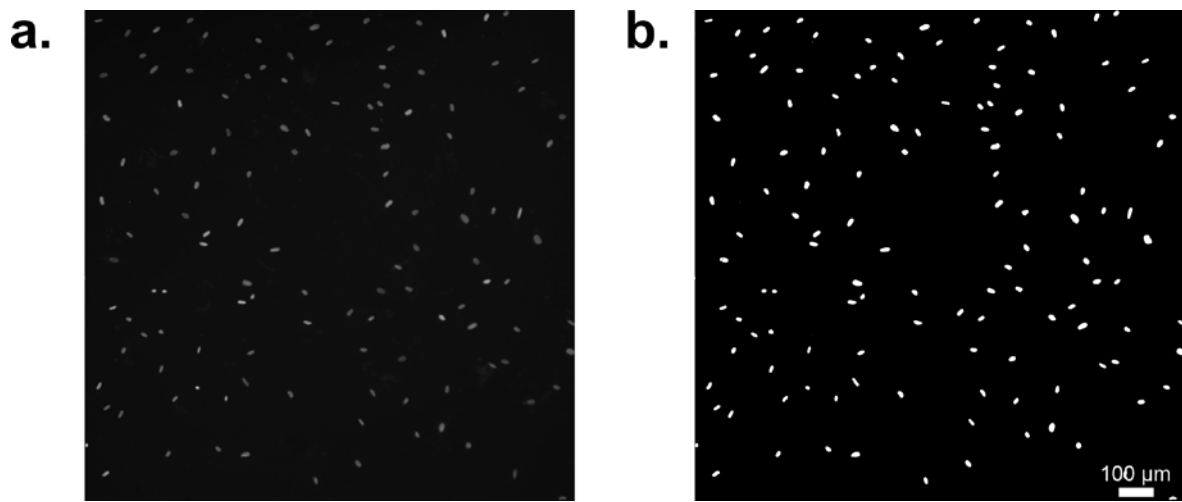
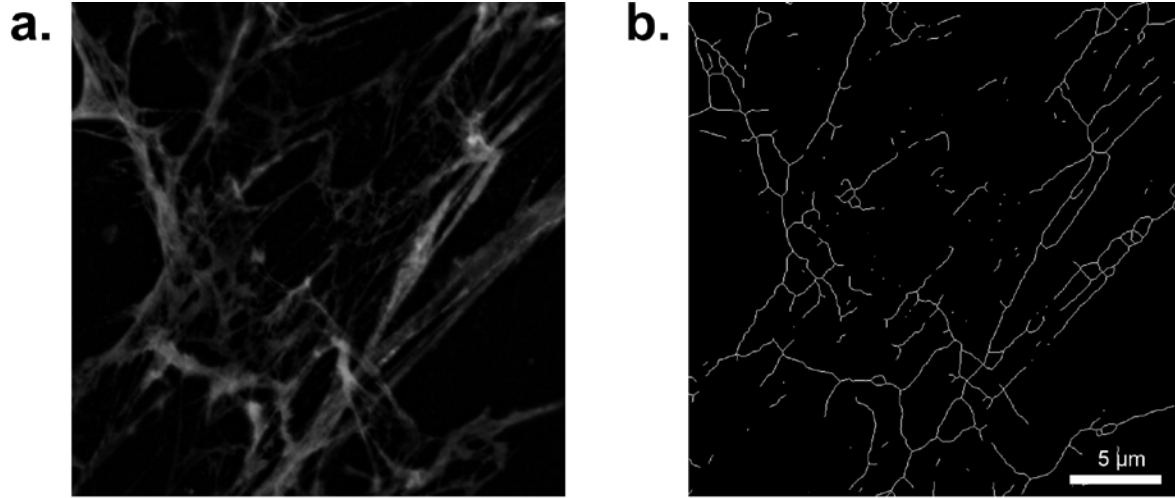


Fig. 5.1 Processing of DAPI-stained nuclei

A) Shown is the original DAPI staining of human skin fibroblast at 100× magnification. B) DAPI staining after processing using the protocol in 3.1.1.

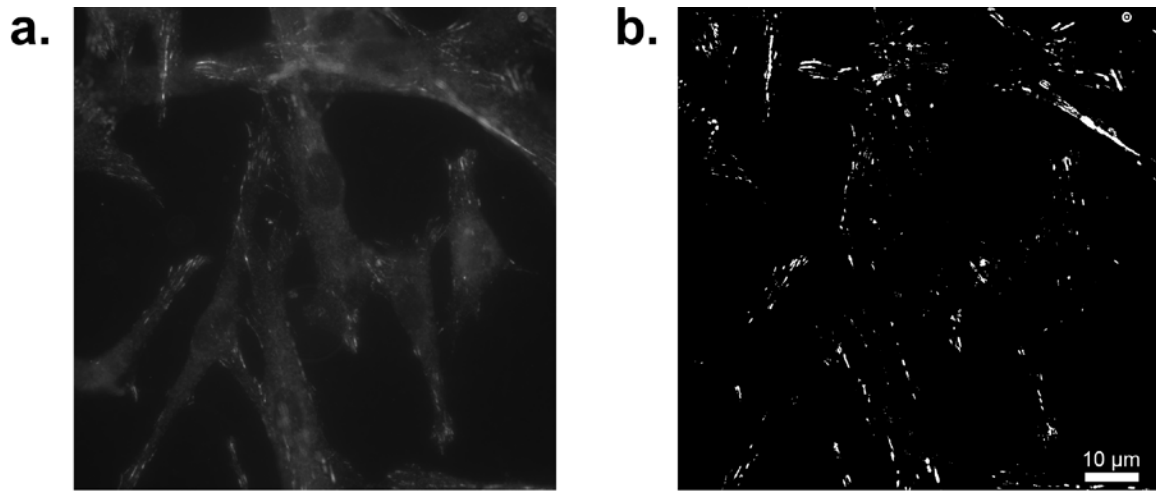


C.

Total Fiber Length (μm)	Number of Branches	Average Branch Length (μm)	Number of Junctions
776.6	319	2.4	120

Fig. 5.2 Skeletonization of fibronectin fibers and quantification results

A) Shown is the zoomed original fibronectin staining of mouse smooth muscle cells using anti-mouse fibronectin antibody (Millipore, cat# ab2033). The image is recorded at 630× magnification. B) The zoomed image after processing it with the protocol described in 3.1.3. C) Quantification results of the processed image in B). The total fiber length, number of branches, average branch length and number of junctions are shown.



C.

Total Area of Focal Adhesions (μm^2)	Number of Focal Adhesions	Average Size of Focal Adhesions (μm^2)
597.1	573	1.0

Fig. 5.3 Image processing after focal adhesion kinase staining and quantification results

A) Shown is the original phosphorylated focal adhesion staining of human fibroblast using an anti-focal adhesion kinase antibody (Abcam, cat# ab812980). The image is recorded at 630 \times magnification. B) The image of the phosphorylated focal adhesion kinase staining in A) after processing using the protocol described in 3.1.4. C) Quantification results of the processed image in B). The total area, total number, and average size of focal adhesions are indicated.

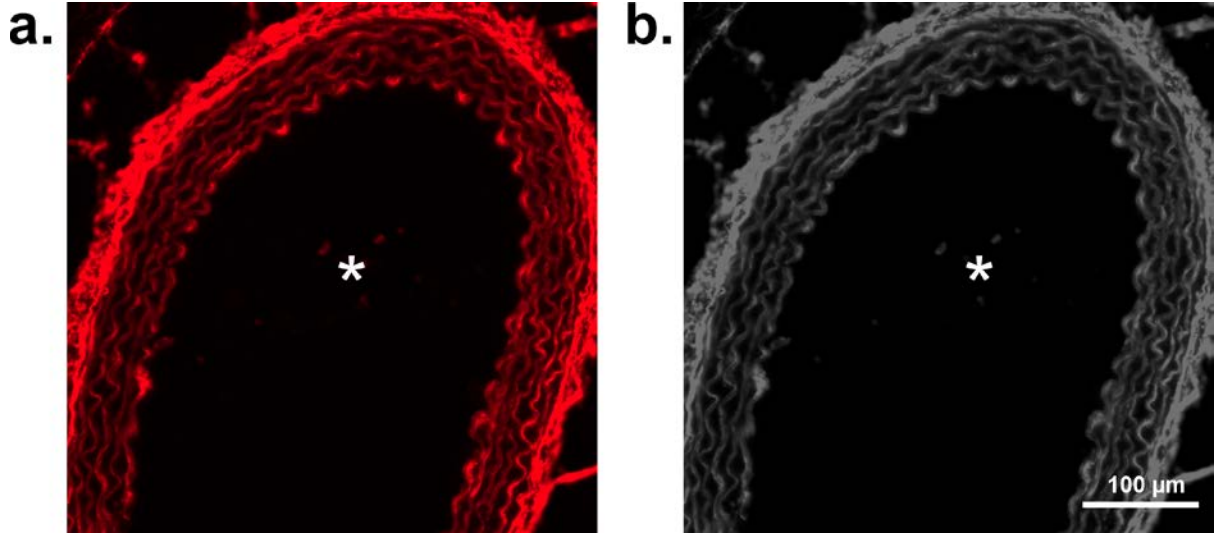


Fig. 5.4 Immunofluorescence staining of fibrillin-1 in the descending aorta of an 8-day old mouse using Cy5 labeled secondary antibodies

A) Individual red channel image showing fibrillin-1 specific staining. The image is recorded at 400× magnification. B) 8-bit gray scale image obtained after converting the 24-bit RGB image shown in (A). Scale bar represents 100 μm. * represents the lumen of the aorta.

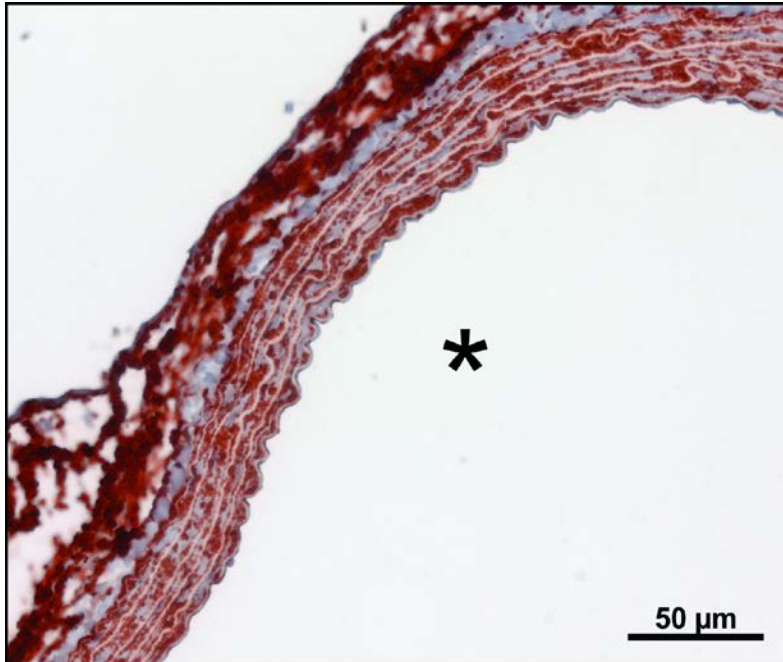


Fig. 5.5 Immunohistochemical staining of fibrillin-1 in the descending aorta of an 8-month old mouse

The image shows fibrillin-1-specific staining (AEC based colored product; red-brown signal) and counterstain hematoxylin (blue). Note that hematoxylin or other counterstains should be avoided because they interfere with image quantification. The image is recorded at 400× magnification. Scale bar represents 50 μm. * represents the lumen of the aorta.

CHAPTER 6 CONCLUSION AND DISCUSSION

The present study elucidated novel outside-in signaling mechanisms involving fibrillin-1 RGD-controlled miRNAs. The investigated molecular mechanisms include focal adhesion formation and cell proliferation, as well as cytokine expression. Fibrillin-1 RGD was identified to promote focal adhesion formation and proliferation in normal skin fibroblasts via downregulation of miR-612 and miR-3185. When seeded on a fibrillin-1 RGD-containing fragment, fibroblasts exhibited increased proliferation through elevated ERK1/2 signaling. This enhanced ERK1/2 signaling was identified to be post-transcriptionally activated by downregulation of miR-1208 (Fig. 3.9). *In vivo* studies using the fibrillin-1 hypomorphic mouse model *Fbn1^{mgR/mgR}* identified differentially regulated miRNA profiles from early aortic dilation stage at 4 weeks to the fully developed aneurysmal stage at 10 weeks. miR-122, a fibrillin-1-controlled miRNA, was identified as the most downregulated miRNA at the aneurysmal stage. Downregulation of miR-122 caused upregulation of *Ccl2* and *Ili1β* mRNA levels post-transcriptionally in *ex vivo* aorta cultures. Moreover, analyses of the upstream regulators in smooth muscle cells and *ex vivo* organ cultures demonstrated that several important dysregulated signaling pathways were involved in the downregulation of miR-122 (Fig. 4.7). These pathways include hypoxia and elevated ERK1/2.

Bax *et al.* identified that fibrillin-1 RGD was critical for focal adhesion formation in fibroblasts, with the assist of a synergy site located in the upstream cbEGF domains of the RGD-containing TB4 domain [40]. This thesis presents novel outside-in signaling initiated by the fibrillin-1 RGD-fibroblast interaction, which promotes focal adhesion by suppressing miR-612 and miR-3185. Downregulation of miR-612 and miR-3185 altered the focal adhesion kinase activities from the intracellular side: miR-612 partially rescued the focal adhesion on non-integrin binding controls, and overexpression of miR-3185 using miRNA mimics suppressed focal adhesion formation when fibroblasts were seeded on RGD-containing fragments. It is also

noteworthy that miR-612 and miR-3185 did not work exactly in the same pattern. Inhibition of miR-612 upregulated both the number and the average size of focal adhesions, while inhibition of miR-3185 only upregulated the average size. The size of focal adhesion indicates the maturation status. Therefore, these results suggested that miR-3185 inhibition only promotes focal adhesion formation. Whereas miR-612 inhibition promotes both focal adhesion formation as well as maturation. To determine the cause for the identified molecular difference between miR-612 and miR-3185, their targets relevant to focal adhesion formation were analyzed. Talin and vinculin mRNA were the predicted targets of both miR-612 and miR-3185. Calponin-1 (a myofibroblast marker) mRNA was only identified to be targeted by miR-612, but not miR-3185. Stress fibers are needed for the maturation of focal adhesion in fibroblasts [112]. Antagonists of myosin contraction disrupt focal adhesion formation [113]. These data suggest that downregulated miR-612 may promote focal adhesion maturation by elevating calponin-1, but this requires further investigation.

Proliferation of mesangial and endothelial cells were previously shown to be promoted by fibrillin-1 RGD-containing fragments [232,233]. Even though this was not shown in fibroblasts before, a similar outcome was expected. This project confirmed this outcome, and additionally identified a novel underlying molecular mechanism. Downregulation of miR-1208 promotes fibroblast proliferation via increased *ERK2* and *MEK1* mRNA levels. This displayed a novel activation mechanism (as discussed in detail in Chapter 3), by which the ERK1/2 and MEK1/2 was activated post-transcriptionally and not just via the upstream RAS-RAF kinases. As demonstrated in chapter 2, the RGD motif in fibronectin could also regulate some fibrillin-1-controlled miRNAs. miR-1208, for example, was commonly downregulated in fibroblast interacting with RGD motifs in either fibrillin-1 or fibronectin. Thus, similar elevating effects on *ERK2* and *MEK1* and fibroblast proliferation are expected when fibroblast interact with the

fibronectin RGD motif. Differences are expected in focal adhesion formation when fibroblasts are seeded on fibrillin-1 versus fibronectin RGD, since the two ECM proteins differentially regulated both, miR-612 and miR-3185. Fibrillin-1 RGD downregulated both miR-612 and miR-3185, whereas fibronectin upregulated miR-612 and did not change the level of miR-3185. These results suggested that the RGD motifs from fibrillin-1 and fibronectin share some common intracellular signaling consequences, but differ in others. The different effects on regulating miRNAs may result from the different contexts adjacent to the RGD motifs of fibrillin-1 and fibronectin. The different upstream synergy sites and the presence of heparin/heparan sulfate binding sites adjacent to the fibrillin-1 TB4 domain (see Fig. 1.1) could be contributing to the functional differences to fibronectin.

Isolated smooth muscle cells from SSS patients showed decreased focal adhesion formations [11]. Beneficial effects of either activating $\beta 1$ integrin or deactivating $\beta 3$ integrin in *Fbn1*^{RGE/+} mice proved the involvement of fibrillin-1 RGD-cell interaction in skin fibrosis pathogenesis [76]. The ERK1/2 inhibitor RDEA119 or TGF- β neutralizing antibodies prevented aggressive skin fibrosis in the *Fbn1*^{RGE/+} mice. As we have shown in chapter 2 and 3, fibrillin-1 RGD tightly regulated focal adhesion formation and ERK1/2 signaling through miRNAs (miR-612, miR-3185 and miR-1208). These results are especially pertinent to SSS, GD, AD and WMS, which are pathological conditions resulting from mutations in or around the RGD-containing TB4 domain. However, limited by the fact that miR-612, miR-3185 and miR-1208 are not reported in mouse [162], the SSS mouse models and Tsk mouse model (Fig. 1.3) can not be used to explore their role in fibrosis pathogenesis. Human skin tissues or cells from relevant disorders are required to explore their role *in vivo*.

Other than miR-612, miR-3185 and miR-1208, another fibrillin-1 RGD controlled miRNA which was identified in fibroblasts was miR-122. miR-122 was observed to be upregulated in fibroblasts when the fibrillin-1 RGD motif was present in the ECM. In other words, miR-122 was decreased when there was a deficiency of fibrillin-1-cell interaction. As MFS fibroblasts produced deficient functional fibrillin-1 microfibrils [85], we extended the studies using cell-derived matrices produced by skin fibroblasts obtained from seven MFS patients with different mutations in fibrillin-1. miR-122 was downregulated in healthy fibroblasts when seeded on MFS cell derived matrices. One major difference between cell-derived matrices versus the coating of purified recombinant fibrillin-1 fragments is the presence of other ECM proteins in the former condition. Therefore, these results strongly suggested that miR-122 was mainly regulated by fibrillin-1 despite the presence of other ECM proteins in the cell derived matrices. However, whether MFS cell derived matrix and RGA non-integrin binding fibrillin-1 fragment cause similar effects for all other fibrillin-1-controlled miRNAs need to be further studied.

Chapter 4 further extends the analyses of fibrillin-1 RGD controlled miR-122 to human aortic smooth muscle cells. miR-122 was also downregulated in smooth muscle cells when there was deficiency of fibrillin-1 RGD-cell interaction. Similar to the regulation of miR-1208, c-Src also regulated miR-122 in a FAK-independent manner, but in the opposite direction: c-Src inhibitor upregulated miR-1208 levels in skin fibroblast, but downregulated miR-122 in smooth muscle cells. Although c-Src kinase is generally known to dock on activated FAK [348], it can also be recruited by $\beta 3$ integrins [247]. Integrins $\alpha 5\beta 1$, $\alpha \nu\beta 3$ and $\alpha \nu\beta 6$ have been reported to interact with the RGD in fibrillin-1 [35,51-53]. The results suggested the involvement of integrin $\alpha \nu\beta 3$ in the regulation of both miR-1208 and miR-122. Further validation using specific integrin blocking antibodies or siRNA for $\beta 3$ integrins is needed to test this hypothesis.

This project validated that the fibrillin-1 RGD motif regulates miRNA expression in both skin fibroblasts and smooth muscle cells. However, whether there is cell-type specificity in this regulation is not entirely clear yet. The outside-in signaling is jointly regulated by the ECM protein ligands, the expression profile of integrins, and the intracellular regulatory mediators. Different cells have been shown to present different dominant integrins on fibrillin-1 binding [52]. Thus, cell-specific expression of integrins and intracellular regulatory mediators are expected in primary fibroblasts and aortic smooth muscle cells. To explore global differences on miRNA expression, the miRNA profiling from different cells seeded on the same fibrillin-1 fragments can be performed. In addition, specific integrin blocking/activating antibodies or kinase inhibitors can also be applied to explore the cell-specific regulatory mechanisms.

Different from the cell culture conditions, in which the variables other than the coated proteins or cell derived matrices are well controlled, the *in vivo* aneurysmal tissues of *Fbn1*^{mgR/mgR} mice possess multiple other dysregulated signaling pathways in addition to disrupted fibrillin-1 microfibrils. This project demonstrated two additional pathogenic stimuli in the aneurysmal tunica media that also suppressed miR-122 expression: elevated ERK1/2 signaling and hypoxic conditions. ERK1/2 signaling is reported to be activated in the aneurysmal aorta of MFS mice [70,349]. Our results proved that the elevated ERK1/2 reduces miR-122 level, as an ERK1/2 inhibitor upregulated miR-122 levels in smooth muscle cells and in aorta cultures. Beneficial effects of inhibiting MEK1/2 signaling has been shown for TAA progression of *Fbn1*^{C1039G/+} mice [70]. Although not reported in the previous study, our results suggested that restoration of miR-122 by the MEK1/2 inhibitor may be one of the underlying beneficial mechanisms. Consistent with previous studies showing upregulation of HIF-1 α in both human TAA and AAA tissues [147,300], our results displayed reduced oxidative phosphorylation pathways based on the

RNAseq data of human TAA samples. Upregulated HIF-1 α was also observed in the smooth muscle cells of *Fbn1*^{mgR/mgR} ascending aortae, which may result from the thickened tunica media. Another potential activator of HIF-1 α could be reactive oxygen species [350], which was found increased in aortic tissue of two different TAA mouse models (*Fbn1*^{C1039G/+} and *Acta2*^{-/-}) [351,352], and in smooth muscle cell cultures from MFS patients [353]. Angiotensin II, which is also upregulated in TAA mice and in patients [271,354,355], could be another activator for HIF-1 α . Our *in vitro* experiments showed that CoCl₂, an activator of HIF-1 α could downregulate miR-122. Digoxin, an inhibitor of HIF-1 α , upregulated miR-122 in smooth muscle cells. These data suggest that HIF-1 α could upregulate miR-122. However, specific *HIF-1 α* siRNA is needed to validate this hypothesis. miR-3185 is another fibrillin-1-controlled miRNA associated with hypoxic conditions, which is reported to be elevated in mechanical asphyxia of cardiac tissues.

miR-122 was previously validated to target *Ccl2* and *Il1 β* mRNA in HEK293 cells [173]. Consistently, functional analyses in our study demonstrated significant elevation of *Ccl2* and *Il1 β* mRNA upon miR-122 inhibition in aorta cultures. CCL2 and IL-1 β protein can suppress the expression of smooth muscle cell contractile markers, including α -SMA, smooth muscle myosin heavy chain, calponin-1, and SM22 in smooth muscle cell culture [295]. IL-1 β can promote the secretion of multiple MMP-2 and 9 [293]. These results suggested that the downregulation of miR-122 in 10-week old *Fbn1*^{mgR/mgR} ascending aortae might contribute to the loss of smooth muscle cell contractility and aortic wall integrity in TAA tissues. As miR-122 was demonstrated to be regulated by fibrillin-1 and by hypoxic conditions, our studies complement current knowledge in TAA pathogenesis with the involvement of ECM, hypoxia and inflammatory responses.

Overall, this thesis project extends our understanding of how miRNAs are involved in the outside-in signaling initiated by fibrillin-1. Our data revealed that fibrillin-1-controlled miRNAs (miR-612, miR-3185 and miR-1208) participate in multiple key functions triggered by fibrillin-1-fibroblast interaction, including focal adhesion formation and cell proliferation. These novel regulatory mechanisms complemented to the classical kinase activation upon RGD-integrin binding. Furthermore, our study reveals the involvement of fibrillin-1 controlled miRNA (miR-122) in the pathogenesis of TAA. Upstream regulator identification and functional analyses for miR-122 reveals a novel connection among fibrillin-1 deficiency, activated ERK1/2 signaling, hypoxic conditions and elevated inflammatory responses in the aneurysmal aortae. This project not only promotes our understanding on cell-ECM interaction, but also provides some promising therapeutical perspectives on fibrillinopathies, especially on TAA pathogenesis.

REFERENCES

1. Aumailley M, Gayraud B. (1998). Structure and biological activity of the extracellular matrix. *J Mol Med (Berl)* **76**, 253-265
2. Rozario T, DeSimone DW. (2010). The extracellular matrix in development and morphogenesis: a dynamic view. *Dev Biol* **341**, 126-140
3. Tsang KY, Cheung MC, Chan D, Cheah KS. (2010). The developmental roles of the extracellular matrix: beyond structure to regulation. *Cell Tissue Res* **339**, 93-110
4. Hynes RO. (2009). The extracellular matrix: not just pretty fibrils. *Science* **326**, 1216-1219
5. Jia LX, Zhang WM, Zhang HJ, Li TT, Wang YL, Qin YW, Gu H, Du J. (2015). Mechanical stretch-induced endoplasmic reticulum stress, apoptosis and inflammation contribute to thoracic aortic aneurysm and dissection. *J Pathol* **236**, 373-383
6. Costa AM, Peyrol S, Porto LC, Comparin JP, Foyatier JL, Desmouliere A. (1999). Mechanical forces induce scar remodeling. Study in non-pressure-treated versus pressure-treated hypertrophic scars. *Am J Pathol* **155**, 1671-1679
7. Todorovic V, Rifkin DB. (2012). LTBPs, more than just an escort service. *J Cell Biochem* **113**, 410-418
8. Muthu ML, Reinhardt DP. (2020). Fibrillin-1 and fibrillin-1-derived asprosin in adipose tissue function and metabolic disorders. *J Cell Commun Signal* **14**, 159-173
9. Kawecki C, Hezard N, Bocquet O, Poitevin G, Rabenoelina F, Kauskot A, Duca L, Blaise S, Romier B, Martiny L, Nguyen P, Debelle L, Maurice P. (2014). Elastin-derived peptides are new regulators of thrombosis. *Arterioscler Thromb Vasc Biol* **34**, 2570-2578
10. Urban Z, Davis EC. (2014). Cutis laxa: Intersection of elastic fiber biogenesis, TGFbeta signaling, the secretory pathway and metabolism. *Matrix Biol* **33**, 16-22
11. Loeys BL, Gerber EE, Riegert-Johnson D, Iqbal S, Whiteman P, McConnell V, Chillakuri CR, Macaya D, Coucke PJ, De Paepe A, Judge DP, Wigley F, Davis EC, Mardon HJ, Handford P, Keene DR, Sakai LY, Dietz HC. (2010). Mutations in fibrillin-1 cause congenital scleroderma: stiff skin syndrome. *Sci Transl Med* **2**, 23ra20-23ra20
12. Dietz HC, Cutting GR, Pyeritz RE, Maslen CL, Sakai LY, Corson GM, Puffenberger EG, Hamosh A, Nanthakumar EJ, Curristin SM, Stetten G, Meyers DA, Francomano CA. (1991). Marfan syndrome caused by a recurrent de novo missense mutation in the fibrillin gene. *Nature* **352**, 337-339
13. Piha-Gossack A, Sossin WS, Reinhardt DP. (2012). The evolution of extracellular fibrillins and their functional domains. *PLoS One* **7**, e33560
14. Reber-Müller S, Spissinger T, Schuchert P, Spring J, Schmid V. (1995). An extracellular matrix protein of jellyfish homologous to mammalian fibrillins forms different fibrils depending on the life stage of the animal. *Dev Biol* **169**, 662-672
15. Thurmond FA, Trotter JA. (1996). Morphology and biomechanics of the microfibrillar network of sea cucumber dermis. *J Exp Biol* **199**, 1817-1828
16. Davison IG, Wright GM, DeMont ME. (1995). The structure and physical properties of invertebrate and primitive vertebrate arteries. *J Exp Biol* **198**, 2185-2196
17. Downing AK, Knott V, Werner JM, Cardy CM, Campbell ID, Handford PA. (1996). Solution structure of a pair of calcium-binding epidermal growth factor-like domains: implications for the Marfan syndrome and other genetic disorders. *Cell* **85**, 597-605

18. Smallridge RS, Whiteman P, Werner JM, Campbell ID, Handford PA, Downing AK. (2003). Solution structure and dynamics of a calcium binding epidermal growth factor-like domain pair from the neonatal region of human fibrillin-1. *J Biol Chem* **278**, 12199-12206
19. Reinhardt DP, Ono RN, Sakai LY. (1997). Calcium stabilizes fibrillin-1 against proteolytic degradation. *J Biol Chem* **272**, 1231-1236
20. Marson A, Rock MJ, Cain SA, Freeman LJ, Morgan A, Mellody K, Shuttleworth CA, Baldock C, Kielty CM. (2005). Homotypic fibrillin-1 interactions in microfibril assembly. *J Biol Chem* **280**, 5013-5021
21. Reinhardt DP, Keene DR, Corson GM, Pöschl E, Bächinger HP, Gambée JE, Sakai LY. (1996). Fibrillin 1: Organization in microfibrils and structural properties. *J Mol Biol* **258**, 104-116
22. Tiedemann K, Bätge B, Müller PK, Reinhardt DP. (2001). Interactions of fibrillin-1 with heparin/heparan sulfate: Implications for microfibrillar assembly. *J Biol Chem* **276**, 36035-36042
23. Rock MJ, Cain SA, Freeman LJ, Morgan A, Mellody K, Marson A, Shuttleworth CA, Weiss AS, Kielty CM. (2004). Molecular basis of elastic fiber formation. Critical interactions and a tropoelastin-fibrillin-1 cross-link. *J Biol Chem* **279**, 23748-23758
24. Pereira L, D'Alessio M, Ramirez F, Lynch JR, Sykes B, Pangilinan T, Bonadio J. (1993). Genomic organization of the sequence coding for fibrillin, the defective gene product in Marfan syndrome. *Hum Mol Genet* **2**, 961-968
25. Yuan X, Downing AK, Knott V, Handford PA. (1997). Solution structure of the transforming growth factor β -binding protein-like module, a domain associated with matrix fibrils. *EMBO J* **16**, 6659-6666
26. Corson GM, Chalberg SC, Dietz HC, Charbonneau NL, Sakai LY. (1993). Fibrillin binds calcium and is coded by cDNAs that reveal a multidomain structure and alternatively spliced exons at the 5' end. *Genomics* **17**, 476-484
27. Jensen SA, Iqbal S, Lowe ED, Redfield C, Handford PA. (2009). Structure and interdomain interactions of a hybrid domain: a disulphide-rich module of the fibrillin/LTBP superfamily of matrix proteins. *Structure* **17**, 759-768
28. Nagase T, Nakayama M, Nakajima D, Kikuno R, Ohara O. (2001). Prediction of the coding sequences of unidentified human genes. XXII. The complete sequences of 100 new cDNA clones from brain which code for large proteins in vitro. *DNA Res* **8**, 85-95
29. Lönnqvist L, Reinhardt DP, Sakai LY, Peltonen L. (1998). Evidence for furin-type activity-mediated C-terminal processing of profibrillin-1 and interference in the processing by certain mutations. *Hum Mol Genet* **7**, 2039-2044
30. Ritty TM, Broekelmann T, Tisdale C, Milewicz DM, Mecham RP. (1999). Processing of the fibrillin-1 carboxyl-terminal domain. *J Biol Chem* **274**, 8933-8940
31. Raghunath M, Putnam EA, Ritty T, Hamstra D, Park ES, Tschödrich-Rotter M, Peters R, Rehemtulla A, Milewicz DM. (1999). Carboxy-terminal conversion of profibrillin to fibrillin at a basic site by PACE/furin-like activity required for incorporation in the matrix. *J Cell Sci* **112**, 1093-1100
32. Mariencheck MC, Davis EC, Zhang H, Ramirez F, Rosenbloom J, Gibson MA, Parks WC, Mecham RP. (1995). Fibrillin-1 and fibrillin-2 show temporal and tissue-specific regulation of expression in developing elastic tissues. *Connect Tissue Res* **31**, 87-97

33. Sabatier L, Miosge N, Hubmacher D, Lin G, Davis EC, Reinhardt DP. (2011). Fibrillin-3 expression in human development. *Matrix Biol* **30**, 43-52
34. Pierschbacher MD, Ruoslahti E. (1984). Variants of the cell recognition site of fibronectin that retain attachment-promoting activity. *Proc Natl Acad Sci USA* **81**, 5985-5988
35. Sakamoto H, Broekelmann T, Cheresch DA, Ramirez F, Rosenbloom J, Mecham RP. (1996). Cell-type specific recognition of RGD- and non-RGD-containing cell binding domains in fibrillin-1. *J Biol Chem* **271**, 4916-4922
36. Ruoslahti E, Pierschbacher MD. (1987). New perspectives in cell adhesion: RGD and integrins. *Science* **238**, 491-497
37. Pfaff M, Sasaki T, Tangemann K, Chu ML, Timpl R. (1995). Integrin-binding and cell-adhesion studies of fibulins reveal a particular affinity for alpha IIb beta 3. *Exp Cell Res* **219**, 87-92
38. Pierschbacher MD, Ruoslahti E. (1987). Influence of stereochemistry of the sequence Arg-Gly-Asp-Xaa on binding-specificity in cell-adhesion. *J Biol Chem* **262**, 17294-17298
39. Hautanen A, Gailit J, Mann DM, Ruoslahti E. (1989). Effects of modifications of the RGD sequence and its context on recognition by the fibronectin receptor. *J Biol Chem* **264**, 1437-1442
40. Bax DV, Mahalingam Y, Cain S, Mellody K, Freeman L, Younger K, Shuttleworth CA, Humphries MJ, Couchman JR, Kielty CM. (2007). Cell adhesion to fibrillin-1: Identification of an Arg-Gly-Asp-dependent synergy region and a heparin-binding site that regulates focal adhesion formation. *J Cell Sci* **120**, 1383-1392
41. Xiong JP, Stehle T, Goodman SL, Arnaout MA. (2003). Integrins, cations and ligands: making the connection. *J Thromb Haemost* **1**, 1642-1654
42. Danen EHJ, Aota SI, van Kraats AA, Yamada KM, Ruitter DJ, van Muijen GN. (1995). Requirement for the synergy site for cell adhesion to fibronectin depends on the activation state of integrin alpha 5 beta 1. *J Biol Chem* **270**, 21612-21618
43. Lee SS, Knott V, Jovanovic J, Harlos K, Grimes JM, Choulier L, Mardon HJ, Stuart DI, Handford PA. (2004). Structure of the integrin binding fragment from fibrillin-1 gives new insights into microfibril organization. *Structure* **12**, 717-729
44. Hynes RO. (2002). Integrins: bidirectional, allosteric signaling machines. *Cell* **110**, 673-687
45. Giancotti FG, Ruoslahti E. (1999). Integrin signaling. *Science* **285**, 1028-1032
46. Hughes PE, O'Toole TE, Ylanne J, Shattil SJ, Ginsberg MH. (1995). The conserved membrane-proximal region of an integrin cytoplasmic domain specifies ligand binding affinity. *J Biol Chem* **270**, 12411-12417
47. Shimaoka M, Springer TA. (2003). Therapeutic antagonists and conformational regulation of integrin function. *Nat Rev Drug Discov* **2**, 703-716
48. Barczyk M, Carracedo S, Gullberg D. (2010). Integrins. *Cell Tissue Res* **339**, 269-280
49. Takagi J, Erickson HP, Springer TA. (2001). C-terminal opening mimics 'inside-out' activation of integrin alpha5beta1. *Nat Struct Biol* **8**, 412-416
50. Calderwood DA. (2004). Integrin activation. *J Cell Sci* **117**, 657-666
51. Pfaff M, Reinhardt DP, Sakai LY, Timpl R. (1996). Cell adhesion and integrin binding to recombinant human fibrillin-1. *FEBS Lett* **384**, 247-250

52. Bax DV, Bernard SE, Lomas A, Morgan A, Humphries J, Shuttleworth A, Humphries MJ, Kielty CM. (2003). Cell adhesion to fibrillin-1 molecules and microfibrils is mediated by alpha5 beta1 and alpha5 beta3 integrins. *J Biol Chem* **278**, 34605-34616
53. Jovanovic J, Takagi J, Choulier L, Abrescia NG, Stuart DI, van der Merwe PA, Mardon HJ, Handford PA. (2007). α V β 6 is a novel receptor for human fibrillin-1: Comparative studies of molecular determinants underlying integrin-RGD affinity and specificity. *J Biol Chem* **282**, 6743-6751
54. Cain SA, Baldwin AK, Mahalingam Y, Raynal B, Jowitt TA, Shuttleworth CA, Couchman JR, Kielty CM. (2008). Heparan sulfate regulates fibrillin-1 N- and C-terminal interactions. *J Biol Chem* **283**, 27017-27027
55. Yadin DA, Robertson IB, McNaught-Davis J, Evans P, Stoddart D, Handford PA, Jensen SA, Redfield C. (2013). Structure of the fibrillin-1 N-terminal domains suggests that heparan sulfate regulates the early stages of microfibril assembly. *Structure* **21**, 1743-1756
56. Baldock C, Koster AJ, Ziese U, Rock MJ, Sherratt MJ, Kadler KE, Shuttleworth CA, Kielty CM. (2001). The supramolecular organization of fibrillin-rich microfibrils. *J Cell Biol* **152**, 1045-1056
57. Kielty CM, Cummings C, Whittaker SP, Shuttleworth CA, Grant ME. (1991). Isolation and ultrastructural analysis of microfibrillar structures from foetal bovine elastic tissues. *J Cell Sci* **99**, 797-807
58. Keene DR, Maddox BK, Kuo HJ, Sakai LY, Glanville RW. (1991). Extraction of extendable beaded structures and their identification as fibrillin-containing extracellular matrix microfibrils. *J Histochem Cytochem* **39**, 441-449
59. Kielty CM, Shuttleworth CA. (1995). Fibrillin-containing microfibrils: structure and function in health and disease. *Int J Biochem Cell Biol* **27**, 747-760
60. Kumra H, Nelea V, Hakami H, Pagliuzza A, Djokic J, Xu J, Yanagisawa H, Reinhardt DP. (2019). Fibulin-4 exerts a dual role in LTBP-4L-mediated matrix assembly and function. *Proc Natl Acad Sci USA* **116**, 20428-20437
61. Freeman LJ, Lomas A, Hodson N, Sherratt MJ, Mellody KT, Weiss AS, Shuttleworth A, Kielty CM. (2005). Fibulin-5 interacts with fibrillin-1 molecules and microfibrils. *Biochem J* **388**, 1-5
62. Kielty CM, Sherratt MJ, Marson A, Baldock C. (2005). Fibrillin microfibrils. *Adv Protein Chem* **70**, 405-436
63. Wagenseil JE, Mecham RP. (2007). New insights into elastic fiber assembly. *Birth Defects Res C Embryo Today* **81**, 229-240
64. Carta L, Pereira L, Arteaga-Solis E, Lee-Arteaga SY, Lenart B, Starcher B, Merkel CA, Sukoyan M, Kerkis A, Hazeki N, Keene DR, Sakai LY, Ramirez F. (2006). Fibrillins 1 and 2 perform partially overlapping functions during aortic development. *J Biol Chem* **281**, 8016-8023
65. Streeten BW, Licari PA. (1983). The zonules and the elastic microfibrillar system in the ciliary body. *Invest Ophthalmol Vis Sci* **24**, 667-681
66. Raviola G. (1971). The fine structure of the ciliary zonule and ciliary epithelium. *Invest Ophthalmol* **10**, 851-869
67. Kriz W, Elger M, Lemley K, Sakai T. (1990). Structure of the glomerular mesangium: a biomechanical interpretation. *Kidney Int Suppl* **30**, S2-S9

68. Nistala H, Lee-Arteaga S, Smaldone S, Siciliano G, Carta L, Ono RN, Sengle G, Arteaga-Solis E, Levasseur R, Ducey P, Sakai LY, Karsenty G, Ramirez F. (2010). Fibrillin-1 and -2 differentially modulate endogenous TGF-beta and BMP bioavailability during bone formation. *J Cell Biol* **190**, 1107-1121
69. Isogai Z, Ono RN, Ushiro S, Keene DR, Chen Y, Mazzieri R, Charbonneau NL, Reinhardt DP, Rifkin DB, Sakai LY. (2003). Latent transforming growth factor beta-binding protein 1 interacts with fibrillin and is a microfibril-associated protein. *J Biol Chem* **278**, 2750-2757
70. Holm TM, Habashi JP, Doyle JJ, Bedja D, Chen Y, van Erp C, Lindsay ME, Kim D, Schoenhoff F, Cohn RD, Loeys BL, Thomas CJ, Patnaik S, Marugan JJ, Judge DP, Dietz HC. (2011). Noncanonical TGFbeta signaling contributes to aortic aneurysm progression in Marfan syndrome mice. *Science* **332**, 358-361
71. Neptune ER, Frischmeyer PA, Arking DE, Myers L, Bunton TE, Gayraud B, Ramirez F, Sakai LY, Dietz HC. (2003). Dysregulation of TGF-beta activation contributes to pathogenesis in Marfan syndrome. *Nat Genet* **33**, 407-411
72. Faivre L, Gorlin RJ, Wirtz MK, Godfrey M, Dagonneau N, Samples JR, Le Merrer M, Collod-Beroud G, Boileau C, Munnich A, Cormier-Daire V. (2003). In frame fibrillin-1 gene deletion in autosomal dominant Weill-Marchesani syndrome. *J Med Genet* **40**, 34-36
73. Tsipouras P, Del Mastro R, Sarfarazi M, Lee B, Vitale E, Child AH, Godfrey M, Devereux RB, Hewett D, Steinmann B, Viljoen D, Sykes BC, Kilpatrick M, Ramirez F, The International Marfan Syndrome Collaborative S. (1992). Genetic linkage of the Marfan syndrome, ectopia lentis, and congenital contractural arachnodactyly to the fibrillin genes on chromosomes 15 and 5. *N Engl J Med* **326**, 905-909
74. Le Goff C, Mahaut C, Wang LW, Allali S, Abhyankar A, Jensen S, Zylberberg L, Collod-Beroud G, Bonnet D, Alanay Y, Brady AF, Cordier MP, Devriendt K, Genevieve D, Kiper PO, Kitoh H, Krakow D, Lynch SA, Le Merrer M, Megarbane A, Mortier G, Odent S, Polak M, Rohrbach M, Sillence D, Stolte-Dijkstra I, Superti-Furga A, Rimoin DL, Topouchian V, Unger S, Zabel B, Bole-Feysot C, Nitschke P, Handford P, Casanova JL, Boileau C, Apte SS, Munnich A, Cormier-Daire V. (2011). Mutations in the TGFβ binding-protein-like domain 5 of FBN1 are responsible for acromicric and geleophysic dysplasias. *Am J Hum Genet* **89**, 7-14
75. Viljoen D. (1994). Congenital contractural arachnodactyly. *J Med Genet* **31**, 640-643
76. Gerber EE, Gallo EM, Fontana SC, Davis EC, Wigley FM, Huso DL, Dietz HC. (2013). Integrin-modulating therapy prevents fibrosis and autoimmunity in mouse models of scleroderma. *Nature* **503**, 126-130
77. Siracusa LD, McGrath R, Ma Q, Moskow JJ, Manne J, Christner PJ, Buchberg AM, Jimenez SA. (1996). A tandem duplication within the fibrillin 1 gene is associated with the mouse tight skin mutation. *Genome Res* **6**, 300-313
78. Gayraud B, Keene DR, Sakai LY, Ramirez F. (2000). New insights into the assembly of extracellular microfibrils from the analysis of the fibrillin 1 mutation in the tight skin mouse. *J Cell Biol* **150**, 667-680
79. Pyeritz R, Dietz H. (2002) Marfan syndrome and other microfibrillar disorders. In *Connective Tissue and its Heritable Disorders* (Royce PM, Steinmann B eds.), Wiley-Liss, Inc., New York. pp 585-626

80. Collod-Beroud G, Le Bourdelles S, Ades L, Ala-Kokko L, Booms P, Boxer M, Child A, Comeglio P, De Paepe A, Hyland JC, Holman K, Kaitila I, Loeys B, Matyas G, Nuytinck L, Peltonen L, Rantamaki T, Robinson P, Steinmann B, Junien C, Beroud C, Boileau C. (2003). Update of the UMD-FBN1 mutation database and creation of an FBN1 polymorphism database. *Hum Mutat* **22**, 199-208
81. Schrijver I, Liu W, Brenn T, Furthmayr H, Francke U. (1999). Cysteine Substitutions in Epidermal Growth Factor-Like Domains of Fibrillin-1: Distinct Effects on Biochemical and Clinical Phenotypes. *Am J Hum Genet* **65**, 1007-1020
82. Tiedemann K, Bätge B, Reinhardt DP. (2004) Assembly of Microfibrils. In *Marfan Syndrome: A Primer for Clinicians and Scientists* (Robinson PN, Godfrey M eds.), Landes Bioscience, Georgetown, Texas, USA. pp 130-142
83. Kirschner R, Hubmacher D, Iyengar G, Kaur J, Fagotto-Kaufmann C, Brömme D, Bartels R, Reinhardt DP. (2011). Classical and neonatal Marfan syndrome mutations in fibrillin-1 cause differential protease susceptibilities and protein function. *J Biol Chem* **286**, 32810-32823
84. Chung AWY, Yang HHC, Radomski MW, van Breemen C. (2008). Long-term doxycycline is more effective than atenolol to prevent thoracic aortic aneurysm in Marfan syndrome through the inhibition of matrix metalloproteinase-2 and-9. *Circ Res* **102**, E73-E85
85. Hollister DW, Godfrey M, Sakai LY, Pyeritz RE. (1990). Immunohistologic abnormalities of the microfibrillar-fiber system in the Marfan syndrome. *N Engl J Med* **323**, 152-159
86. Pereira L, Lee SY, Gayraud B, Andrikopoulos K, Shapiro SD, Bunton T, Biery NJ, Dietz HC, Sakai LY, Ramirez F. (1999). Pathogenetic sequence for aneurysm revealed in mice underexpressing fibrillin-1. *Proc Natl Acad Sci USA* **96**, 3819-3823
87. Lima BL, Santos EJ, Fernandes GR, Merkel C, Mello MR, Gomes JP, Soukoyan M, Kerkis A, Massironi SM, Visintin JA, Pereira LV. (2010). A new mouse model for marfan syndrome presents phenotypic variability associated with the genetic background and overall levels of Fbn1 expression. *PLoS One* **5**, e14136
88. Judge DP, Biery NJ, Keene DR, Geubtner J, Myers L, Huso DL, Sakai LY, Dietz HC. (2004). Evidence for a critical contribution of haploinsufficiency in the complex pathogenesis of Marfan syndrome. *J Clin Invest* **114**, 172-181
89. Charbonneau NL, Carlson EJ, Tufa S, Sengle G, Manalo EC, Carlberg VM, Ramirez F, Keene DR, Sakai LY. (2010). In vivo studies of mutant fibrillin-1 microfibrils. *J Biol Chem* **285**, 24943-24955
90. Pannu H, Tran-Fadulu V, Milewicz DM. (2005). Genetic basis of thoracic aortic aneurysms and aortic dissections. *Am J Med Genet C Semin Med Genet* **139**, 10-16
91. Cikach FS, Koch CD, Mead TJ, Galatioto J, Willard BB, Emerton KB, Eagleton MJ, Blackstone EH, Ramirez F, Roselli EE, Apte SS. (2018). Massive aggrecan and versican accumulation in thoracic aortic aneurysm and dissection. *JCI Insight* **3**
92. Hiratzka LF, Bakris GL, Beckman JA, Bersin RM, Carr VF, Casey DE, Jr., Eagle KA, Hermann LK, Isselbacher EM, Kazerooni EA, Kouchoukos NT, Lytle BW, Milewicz DM, Reich DL, Sen S, Shinn JA, Svensson LG, Williams DM, American College of Cardiology Foundation/American Heart Association Task Force on Practice G, American Association for Thoracic S, American College of R, American Stroke A, Society of Cardiovascular A, Society for Cardiovascular A, Interventions, Society of Interventional R, Society of

- Thoracic S, Society for Vascular M. (2010). 2010 ACCF/AHA/AATS/ACR/ASA/SCA/SCAI/SIR/STS/SVM guidelines for the diagnosis and management of patients with Thoracic Aortic Disease: a report of the American College of Cardiology Foundation/American Heart Association Task Force on Practice Guidelines, American Association for Thoracic Surgery, American College of Radiology, American Stroke Association, Society of Cardiovascular Anesthesiologists, Society for Cardiovascular Angiography and Interventions, Society of Interventional Radiology, Society of Thoracic Surgeons, and Society for Vascular Medicine. *Circulation* **121**, e266-369
93. Lacro RV, Dietz HC, Wruck LM, Bradley TJ, Colan SD, Devereux RB, Klein GL, Li JS, Minich LL, Paridon SM, Pearson GD, Printz BF, Pyeritz RE, Radojewski E, Roman MJ, Saul JP, Stylianou MP, Mahony L. (2007). Rationale and design of a randomized clinical trial of beta-blocker therapy (atenolol) versus angiotensin II receptor blocker therapy (losartan) in individuals with Marfan syndrome. *Am Heart J* **154**, 624-631
 94. Forteza A, Evangelista A, Sanchez V, Teixido-Tura G, Sanz P, Gutierrez L, Gracia T, Centeno J, Rodriguez-Palomares J, Rufilanchas JJ, Cortina J, Ferreira-Gonzalez I, Garcia-Dorado D. (2016). Efficacy of losartan vs. atenolol for the prevention of aortic dilation in Marfan syndrome: a randomized clinical trial. *Eur Heart J* **37**, 978-985
 95. Pope FM, Burrows NP. (1997). Ehlers-Danlos syndrome has varied molecular mechanisms. *J Med Genet* **34**, 400-410
 96. Barbier M, Gross MS, Aubart M, Hanna N, Kessler K, Guo DC, Tosolini L, Ho-Tin-Noe B, Regalado E, Varret M, Abifadel M, Milleron O, Odent S, Dupuis-Girod S, Faivre L, Edouard T, Dulac Y, Busa T, Gouya L, Milewicz DM, Jondeau G, Boileau C. (2014). MFAP5 loss-of-function mutations underscore the involvement of matrix alteration in the pathogenesis of familial thoracic aortic aneurysms and dissections. *Am J Hum Genet* **95**, 736-743
 97. Guo DC, Regalado ES, Gong L, Duan X, Santos-Cortez RL, Arnaud P, Ren Z, Cai B, Hostetler EM, Moran R, Liang D, Estrera A, Safi HJ, University of Washington Center for Mendelian G, Leal SM, Bamshad MJ, Shendure J, Nickerson DA, Jondeau G, Boileau C, Milewicz DM. (2016). LOX mutations predispose to thoracic aortic aneurysms and dissections. *Circ Res* **118**, 928-934
 98. Sheen VL, Jansen A, Chen MH, Parrini E, Morgan T, Ravenscroft R, Ganesh V, Underwood T, Wiley J, Leventer R, Vaid RR, Ruiz DE, Hutchins GM, Menasha J, Willner J, Geng Y, Gripp KW, Nicholson L, Berry-Kravis E, Bodell A, Apse K, Hill RS, Dubeau F, Andermann F, Barkovich J, Andermann E, Shugart YY, Thomas P, Viri M, Veggiotti P, Robertson S, Guerrini R, Walsh CA. (2005). Filamin A mutations cause periventricular heterotopia with Ehlers-Danlos syndrome. *Neurology* **64**, 254-262
 99. Khau Van Kien P, Mathieu F, Zhu L, Lalande A, Betard C, Lathrop M, Brunotte F, Wolf JE, Jeunemaitre X. (2005). Mapping of familial thoracic aortic aneurysm/dissection with patent ductus arteriosus to 16p12.2-p13.13. *Circulation* **112**, 200-206
 100. Guo DC, Pannu H, Tran-Fadulu V, Papke CL, Yu RK, Avidan N, Bourgeois S, Estrera AL, Safi HJ, Sparks E, Amor D, Ades L, McConnell V, Willoughby CE, Abuelo D, Willing M, Lewis RA, Kim DH, Scherer S, Tung PP, Ahn C, Buja LM, Raman CS, Shete SS, Milewicz DM. (2007). Mutations in smooth muscle alpha-actin (ACTA2) lead to thoracic aortic aneurysms and dissections. *Nat Genet* **39**, 1488-1493

101. Li Y, Gao S, Han Y, Song L, Kong Y, Jiao Y, Huang S, Du J, Li Y. (2021). Variants of Focal Adhesion Scaffold Genes Cause Thoracic Aortic Aneurysm. *Circ Res* **128**, 8-23
102. Guo DC, Regalado E, Casteel DE, Santos-Cortez RL, Gong L, Kim JJ, Dyack S, Horne SG, Chang G, Jondeau G, Boileau C, Coselli JS, Li Z, Leal SM, Shendure J, Rieder MJ, Bamshad MJ, Nickerson DA, Gen TACRC, National Heart L, Blood Institute Grand Opportunity Exome Sequencing P, Kim C, Milewicz DM. (2013). Recurrent gain-of-function mutation in PRKG1 causes thoracic aortic aneurysms and acute aortic dissections. *Am J Hum Genet* **93**, 398-404
103. Boileau C, Guo DC, Hanna N, Regalado ES, Detaint D, Gong L, Varret M, Prakash SK, Li AH, d'Indy H, Braverman AC, Grandchamp B, Kwartler CS, Gouya L, Santos-Cortez RL, Abifadel M, Leal SM, Muti C, Shendure J, Gross MS, Rieder MJ, Vahanian A, Nickerson DA, Michel JB, National Heart L, Blood Institute Go Exome Sequencing P, Jondeau G, Milewicz DM. (2012). TGFB2 mutations cause familial thoracic aortic aneurysms and dissections associated with mild systemic features of Marfan syndrome. *Nat Genet* **44**, 916-921
104. Bertoli-Avella AM, Gillis E, Morisaki H, Verhagen JMA, de Graaf BM, van de Beek G, Gallo E, Kruithof BPT, Venselaar H, Myers LA, Laga S, Doyle AJ, Oswald G, van Cappellen GWA, Yamanaka I, van der Helm RM, Beverloo B, de Klein A, Pardo L, Lammens M, Evers C, Devriendt K, Dumoulein M, Timmermans J, Bruggenwirth HT, Verheijen F, Rodrigus I, Baynam G, Kempers M, Saenen J, Van Craenenbroeck EM, Minatoya K, Matsukawa R, Tsukube T, Kubo N, Hofstra R, Goumans MJ, Bekkers JA, Roos-Hesselink JW, van de Laar I, Dietz HC, Van Laer L, Morisaki T, Wessels MW, Loeys BL. (2015). Mutations in a TGF-beta ligand, TGFB3, cause syndromic aortic aneurysms and dissections. *J Am Coll Cardiol* **65**, 1324-1336
105. Loeys BL, Schwarze U, Holm T, Callewaert BL, Thomas GH, Pannu H, De Backer JF, Oswald GL, Symoens S, Manouvrier S, Roberts AE, Faravelli F, Greco MA, Pyeritz RE, Milewicz DM, Coucke PJ, Cameron DE, Braverman AC, Byers PH, De Paepe AM, Dietz HC. (2006). Aneurysm syndromes caused by mutations in the TGF-beta receptor. *N Engl J Med* **355**, 788-798
106. Milewicz DM, Prakash SK, Ramirez F. (2017). Therapeutics targeting drivers of thoracic aortic aneurysms and acute aortic dissections: insights from predisposing genes and mouse models. *Annu Rev Med* **68**, 51-67
107. Schaller MD, Borgman CA, Cobb BS, Vines RR, Reynolds AB, Parsons JT. (1992). pp125FAK a structurally distinctive protein-tyrosine kinase associated with focal adhesions. *Proc Natl Acad Sci USA* **89**, 5192-5196
108. Kleinschmidt EG, Schlaepfer DD. (2017). Focal adhesion kinase signaling in unexpected places. *Curr Opin Cell Biol* **45**, 24-30
109. Chen HC, Appeddu PA, Parsons JT, Hildebrand JD, Schaller MD, Guan JL. (1995). Interaction of focal adhesion kinase with cytoskeletal protein talin. *J Biol Chem* **270**, 16995-16999
110. Crichtley DR, Gingras AR. (2008). Talin at a glance. *J Cell Sci* **121**, 1345-1347
111. Turner CE. (1998). Molecules in focus paxillin. *Int J Biochem Cell Biol* **30**, 955-959
112. Oakes PW, Beckham Y, Stricker J, Gardel ML. (2012). Tension is required but not sufficient for focal adhesion maturation without a stress fiber template. *J Cell Biol* **196**, 363-374

113. Dugina V, Fontao L, Chaponnier C, Vasiliev J, Gabbiani G. (2001). Focal adhesion features during myofibroblastic differentiation are controlled by intracellular and extracellular factors. *J Cell Sci* **114**, 3285-3296
114. Ren XD, Kiosses WB, Sieg DJ, Otey CA, Schlaepfer DD, Schwartz MA. (2000). Focal adhesion kinase suppresses Rho activity to promote focal adhesion turnover. *J Cell Sci* **113**, 3673-3678
115. Sieg DJ, Hauck CR, Ilic D, Klingbeil CK, Schaefer E, Damsky CH, Schlaepfer DD. (2000). FAK integrates growth-factor and integrin signals to promote cell migration. *Nat Cell Biol* **2**, 249-256
116. Owen LM, Adhikari AS, Patel M, Grimmer P, Leijnse N, Kim MC, Notbohm J, Franck C, Dunn AR. (2017). A cytoskeletal clutch mediates cellular force transmission in a soft, three-dimensional extracellular matrix. *Mol Biol Cell* **28**, 1959-1974
117. Hu K, Ji L, Applegate KT, Danuser G, Waterman-Storer CM. (2007). Differential transmission of actin motion within focal adhesions. *Science* **315**, 111-115
118. Owen JD, Ruest PJ, Fry DW, Hanks SK. (1999). Induced focal adhesion kinase (FAK) expression in FAK-null cells enhances cell spreading and migration requiring both auto- and activation loop phosphorylation sites and inhibits adhesion-dependent tyrosine phosphorylation of Pyk2. *Mol Cell Biol* **19**, 4806-4818
119. Sieg DJ, Hauck CR, Schlaepfer DD. (1999). Required role of focal adhesion kinase (FAK) for integrin-stimulated cell migration. *J Cell Sci* **112** (Pt 16), 2677-2691
120. Greenberg RS, Bernstein AM, Benezra M, Gelman IH, Taliana L, Masur SK. (2006). FAK-dependent regulation of myofibroblast differentiation. *FASEB J* **20**, 1006-1008
121. Chen HC, Appeddu PA, Isoda H, Guan JL. (1996). Phosphorylation of tyrosine 397 in focal adhesion kinase is required for binding phosphatidylinositol 3-kinase. *J Biol Chem* **271**, 26329-26334
122. Calalb MB, Polte TR, Hanks SK. (1995). Tyrosine phosphorylation of focal adhesion kinase at sites in the catalytic domain regulates kinase-activity - a role for Src family kinases. *Mol Cell Biol* **15**, 954-963
123. Slack-Davis JK, Eblen ST, Zecevic M, Boerner SA, Tarcsafalvi A, Diaz HB, Marshall MS, Weber MJ, Parsons JT, Catling AD. (2003). PAK1 phosphorylation of MEK1 regulates fibronectin-stimulated MAPK activation. *J Cell Biol* **162**, 281-291
124. Wary KK, Mainiero F, Isakoff SJ, Marcantonio EE, Giancotti FG. (1996). The adaptor protein Shc couples a class of integrins to the control of cell cycle progression. *Cell* **87**, 733-743
125. Lin TH, Aplin AE, Shen Y, Chen Q, Schaller M, Romer L, Aukhil I, Juliano RL. (1997). Integrin-mediated activation of MAP kinase is independent of FAK: evidence for dual integrin signaling pathways in fibroblasts. *J Cell Biol* **136**, 1385-1395
126. Ilic D, Kovacic B, Johkura K, Schlaepfer DD, Tomasevic N, Han Q, Kim JB, Howerton K, Baumbusch C, Ogiwara N, Strelbow DN, Nelson JA, Dazin P, Shino Y, Sasaki K, Damsky CH. (2004). FAK promotes organization of fibronectin matrix and fibrillar adhesions. *J Cell Sci* **117**, 177-187
127. Nolasco P, Fernandes CG, Ribeiro-Silva JC, Oliveira PVS, Sacrini M, de Brito IV, De Bessa TC, Pereira LV, Tanaka LY, Alencar A, Laurindo FRM. (2020). Impaired vascular smooth muscle cell force-generating capacity and phenotypic deregulation in Marfan Syndrome mice. *Biochimica et Biophysica Acta. Molecular Basis of Disease* **1866**, 165587

128. Chen Z, Gibson TB, Robinson F, Silvestro L, Pearson G, Xu B, Wright A, Vanderbilt C, Cobb MH. (2001). MAP kinases. *Chem Rev* **101**, 2449-2476
129. Roskoski R. (2012). ERK1/2 MAP kinases: structure, function, and regulation. *Pharmacol Res* **66**, 105-143
130. Xiong W, Meisinger T, Knispel R, Worth JM, Baxter BT. (2012). MMP-2 regulates Erk1/2 phosphorylation and aortic dilatation in Marfan syndrome. *Circ Res* **110**, e92-e101
131. Medzhitov R. (2008). Origin and physiological roles of inflammation. *Nature* **454**, 428-435
132. He R, Guo DC, Sun W, Papke CL, Duraisamy S, Estrera AL, Safi HJ, Ahn C, Buja LM, Arnett FC, Zhang J, Geng YJ, Milewicz DM. (2008). Characterization of the inflammatory cells in ascending thoracic aortic aneurysms in patients with Marfan syndrome, familial thoracic aortic aneurysms, and sporadic aneurysms. *J Thorac Cardiovasc Surg* **136**, 922-929
133. Zhang L, Liao MF, Tian L, Zou SL, Lu QS, Bao JM, Pei YF, Jing ZP. (2011). Overexpression of interleukin-1beta and interferon-gamma in type I thoracic aortic dissections and ascending thoracic aortic aneurysms: possible correlation with matrix metalloproteinase-9 expression and apoptosis of aortic media cells. *Eur J Cardiothorac Surg* **40**, 17-22
134. Liu C, Zhang C, Jia L, Chen B, Liu L, Sun J, Zhang W, You B, Li Y, Li P, Du J. (2018). Interleukin-3 stimulates matrix metalloproteinase 12 production from macrophages promoting thoracic aortic aneurysm/dissection. *Clin Sci* **132**, 655-668
135. Ju X, Ijaz T, Sun H, Lejeune W, Vargas G, Shilagard T, Recinos A, 3rd, Milewicz DM, Brasier AR, Tilton RG. (2014). IL-6 regulates extracellular matrix remodeling associated with aortic dilation in a fibrillin-1 hypomorphic mgR/mgR mouse model of severe Marfan syndrome. *J Am Heart Assoc* **3**, e000476
136. Artemiou P, Charokopos N, Rouska E, Sabol F, Chrysogonidis I, Tsavdaridou V, Paschalidis G. (2012). C-reactive protein/interleukin-6 ratio as marker of the size of the uncomplicated thoracic aortic aneurysms. *Interact Cardiovasc Thorac Surg* **15**, 871-877
137. Pope NH, Salmon M, Johnston WF, Lu G, Lau CL, Upchurch GR, Jr., Ailawadi G. (2015). Interleukin-6 receptor inhibition prevents descending thoracic aortic aneurysm formation. *Ann Thorac Surg* **100**, 1620-1626
138. Johnston WF, Salmon M, Pope NH, Meher A, Su G, Stone ML, Lu G, Owens GK, Upchurch GR, Jr., Ailawadi G. (2014). Inhibition of interleukin-1beta decreases aneurysm formation and progression in a novel model of thoracic aortic aneurysms. *Circulation* **130**, S51-S59
139. Senior RM, Griffin GL, Mecham RP, Wrenn DS, Prasad KU, Urry DW. (1984). Val-Gly-Val-Ala-Pro-Gly, a repeating peptide in elastin, is chemotactic for fibroblasts and monocytes. *J Cell Biol* **99**, 870-874
140. Guo G, Booms P, Halushka M, Dietz HC, Ney A, Stricker S, Hecht J, Mundlos S, Robinson PN. (2006). Induction of macrophage chemotaxis by aortic extracts of the mgR Marfan mouse model and a GxxPG-containing fibrillin-1 fragment. *Circulation* **114**, 1855-1862
141. Guo G, Munoz-Garcia B, Ott CE, Grunhagen J, Mousa SA, Pletschacher A, von Kodolitsch Y, Knaus P, Robinson PN. (2013). Antagonism of GxxPG fragments ameliorates manifestations of aortic disease in Marfan syndrome mice. *Hum Mol Genet* **22**, 433-443

142. Semenza GL. (2012). Hypoxia-inducible factors in physiology and medicine. *Cell* **148**, 399-408
143. Kaelin WG, Jr., Ratcliffe PJ. (2008). Oxygen sensing by metazoans: the central role of the HIF hydroxylase pathway. *Mol Cell* **30**, 393-402
144. Mahon PC, Hirota K, Semenza GL. (2001). FIH-1: a novel protein that interacts with HIF-1alpha and VHL to mediate repression of HIF-1 transcriptional activity. *Genes Dev* **15**, 2675-2686
145. Hong KH, Yoo SA, Kang SS, Choi JJ, Kim WU, Cho CS. (2006). Hypoxia induces expression of connective tissue growth factor in scleroderma skin fibroblasts. *Clin Exp Immunol* **146**, 362-370
146. Beyer C, Schett G, Gay S, Distler O, Distler JH. (2009). Hypoxia in the pathogenesis of systemic sclerosis. *Arthritis Res Ther* **11**, 220
147. Liu K, Fang C, Shen Y, Liu Z, Zhang M, Ma B, Pang X. (2017). Hypoxia-inducible factor 1a induces phenotype switch of human aortic vascular smooth muscle cell through PI3K/AKT/AEG-1 signaling. *Oncotarget* **8**, 33343-33352
148. Liu M, Li L, Zhu J, He C, Xu Q, Sun A, Kong W, Li W, Zhang X. (2019). Rapamycin attenuates a murine model of thoracic aortic aneurysm by downregulating the miR-126-3p mediated activation of MAPK/ERK signalling pathway. *Biochem Biophys Res Commun* **512**, 498-504
149. Imanishi M, Chiba Y, Tomita N, Matsunaga S, Nakagawa T, Ueno M, Yamamoto K, Tamaki T, Tomita S. (2016). Hypoxia-inducible factor-1alpha in smooth muscle cells protects against aortic aneurysms-Brief Report. *Arterioscler Thromb Vasc Biol* **36**, 2158-2162
150. Filipowicz W, Bhattacharyya SN, Sonenberg N. (2008). Mechanisms of post-transcriptional regulation by microRNAs: are the answers in sight? *Nat Rev Genet* **9**, 102-114
151. Eichhorn SW, Guo H, McGeary SE, Rodriguez-Mias RA, Shin C, Baek D, Hsu SH, Ghoshal K, Villen J, Bartel DP. (2014). mRNA destabilization is the dominant effect of mammalian microRNAs by the time substantial repression ensues. *Mol Cell* **56**, 104-115
152. Grimson A, Farh KK, Johnston WK, Garrett-Engel P, Lim LP, Bartel DP. (2007). MicroRNA targeting specificity in mammals: determinants beyond seed pairing. *Mol Cell* **27**, 91-105
153. Paraskevopoulou MD, Georgakilas G, Kostoulas N, Vlachos IS, Vergoulis T, Reczko M, Filippidis C, Dalamagas T, Hatzigeorgiou AG. (2013). DIANA-microT web server v5.0: service integration into miRNA functional analysis workflows. *Nucleic Acids Res* **41**, W169-173
154. Ha M, Kim VN. (2014). Regulation of microRNA biogenesis. *Nat Rev Mol Cell Biol* **15**, 509-524
155. Hashimoto Y, Akiyama Y, Otsubo T, Shimada S, Yuasa Y. (2010). Involvement of epigenetically silenced microRNA-181c in gastric carcinogenesis. *Carcinogenesis* **31**, 777-784
156. Bernstein E, Kim SY, Carmell MA, Murchison EP, Alcorn H, Li MZ, Mills AA, Elledge SJ, Anderson KV, Hannon GJ. (2003). Dicer is essential for mouse development. *Nat Genet* **35**, 215-217

157. Pan Y, Balazs L, Tigyi G, Yue J. (2011). Conditional deletion of Dicer in vascular smooth muscle cells leads to the developmental delay and embryonic mortality. *Biochem Biophys Res Commun* **408**, 369-374
158. Babalola O, Mamalis A, Lev-Tov H, Jagdeo J. (2013). The role of microRNAs in skin fibrosis. *Arch Dermatol Res* **305**, 763-776
159. Merk DR, Chin JT, Dake BA, Maegdefessel L, Miller MO, Kimura N, Tsao PS, Iosef C, Berry GJ, Mohr FW, Spin JM, Alvira CM, Robbins RC, Fischbein MP. (2012). miR-29b participates in early aneurysm development in Marfan syndrome. *Circ Res* **110**, 312-324
160. Jafarinejad-Farsangi S, Farazmand A, Gharibdoost F, Karimizadeh E, Noorbakhsh F, Faridani H, Mahmoudi M, Jamshidi AR. (2016). Inhibition of microRNA-21 induces apoptosis in dermal fibroblasts of patients with systemic sclerosis. *Int J Dermatol* **55**, 1259-1267
161. Maegdefessel L, Azuma J, Toh R, Deng A, Merk DR, Raiesdana A, Leeper NJ, Raaz U, Schoelmerich AM, McConnell MV, Dalman RL, Spin JM, Tsao PS. (2012). MicroRNA-21 blocks abdominal aortic aneurysm development and nicotine-augmented expansion. *Sci Transl Med* **4**, 122ra122
162. Kozomara A, Birgaoanu M, Griffiths-Jones S. (2019). miRBase: from microRNA sequences to function. *Nucleic Acids Res* **47**, D155-D162
163. Tao ZH, Wan JL, Zeng LY, Xie L, Sun HC, Qin LX, Wang L, Zhou J, Ren ZG, Li YX, Fan J, Wu WZ. (2013). miR-612 suppresses the invasive-metastatic cascade in hepatocellular carcinoma. *J Exp Med* **210**, 789-803
164. Tang J, Tao ZH, Wen D, Wan JL, Liu DL, Zhang S, Cui JF, Sun HC, Wang L, Zhou J, Fan J, Wu WZ. (2014). MiR-612 suppresses the stemness of liver cancer via Wnt/beta-catenin signaling. *Biochem Biophys Res Commun* **447**, 210-215
165. Liu M, Chen Y, Huang B, Mao S, Cai K, Wang L, Yao X. (2018). Tumor-suppressing effects of microRNA-612 in bladder cancer cells by targeting malic enzyme 1 expression. *Int J Oncol* **52**, 1923-1933
166. Han L, Zhang H, Zeng Y, Lv Y, Tao L, Ma J, Xu H, Ma K, Shi Q, Xiao B, Chen L. (2020). Identification of the miRNA-3185/CYP4A11 axis in cardiac tissue as a biomarker for mechanical asphyxia. *Forensic Sci Int* **311**, 110293
167. Huppi K, Volfovsky N, Runfola T, Jones TL, Mackiewicz M, Martin SE, Mushinski JF, Stephens R, Caplen NJ. (2008). The identification of microRNAs in a genomically unstable region of human chromosome 8q24. *Mol Cancer Res* **6**, 212-221
168. Anauate AC, Leal MF, Wisnieski F, Santos LC, Gigeck CO, Chen ES, Calcagno DQ, Assumpcao PP, Demachki S, Arasaki CH, Artigiani R, Rasmussen LT, Payao SM, Burbano RR, MA CS. (2019). Analysis of 8q24.21 miRNA cluster expression and copy number variation in gastric cancer. *Future Med Chem* **11**, 947-958
169. Kim EA, Jang JH, Sung EG, Song IH, Kim JY, Lee TJ. (2019). MiR-1208 increases the sensitivity to cisplatin by targeting TBCK in renal cancer cells. *Int J Mol Sci* **20**
170. Wienholds E, Kloosterman WP, Miska E, Alvarez-Saavedra E, Berezikov E, de Bruijn E, Horvitz HR, Kauppinen S, Plasterk RH. (2005). MicroRNA expression in zebrafish embryonic development. *Science* **309**, 310-311
171. Jopling C. (2012). Liver-specific microRNA-122: Biogenesis and function. *RNA Biol* **9**, 137-142

172. Wen J, Friedman JR. (2012). miR-122 regulates hepatic lipid metabolism and tumor suppression. *J Clin Invest* **122**, 2773-2776
173. Tsai WC, Hsu SD, Hsu CS, Lai TC, Chen SJ, Shen R, Huang Y, Chen HC, Lee CH, Tsai TF, Hsu MT, Wu JC, Huang HD, Shiao MS, Hsiao M, Tsou AP. (2012). MicroRNA-122 plays a critical role in liver homeostasis and hepatocarcinogenesis. *J Clin Invest* **122**, 2884-2897
174. Li J, Ghazwani M, Zhang Y, Lu J, Li J, Fan J, Gandhi CR, Li S. (2013). miR-122 regulates collagen production via targeting hepatic stellate cells and suppressing P4HA1 expression. *J Hepatol* **58**, 522-528
175. He S, Chu JH, Wu LC, Mao HY, Peng Y, Alvarez-Breckenridge CA, Hughes T, Wei M, Zhang JY, Yuan SZ, Sandhu S, Vasu S, Benson DM, Hofmeister CC, He XM, Ghoshal K, Devine SM, Caligiuri MA, Yu JH. (2013). MicroRNAs activate natural killer cells through Toll-like receptor signaling. *Blood* **121**, 4663-4671
176. Wu X, Du X, Yang Y, Liu X, Liu X, Zhang N, Li Y, Jiang X, Jiang Y, Yang Z. (2021). Inhibition of miR-122 reduced atherosclerotic lesion formation by regulating NPAS3-mediated endothelial to mesenchymal transition. *Life Sci* **265**, 118816
177. Li Y, Yang N, Dong B, Yang J, Kou L, Qin Q. (2019). MicroRNA-122 promotes endothelial cell apoptosis by targeting XIAP: Therapeutic implication for atherosclerosis. *Life Sci* **232**, 116590
178. Song JJ, Yang M, Liu Y, Song JW, Wang J, Chi HJ, Liu XY, Zuo K, Yang XC, Zhong JC. (2020). MicroRNA-122 aggravates angiotensin II-mediated apoptosis and autophagy imbalance in rat aortic adventitial fibroblasts via the modulation of SIRT6-elabela-ACE2 signaling. *Eur J Pharmacol* **883**, 173374
179. Sakai LY, Keene DR, Engvall E. (1986). Fibrillin, a new 350-kD glycoprotein, is a component of extracellular microfibrils. *J Cell Biol* **103**, 2499-2509
180. Lee B, Godfrey M, Vitale E, Hori H, Mattei MG, Sarfarazi M, Tsipouras P, Ramirez F, Hollister DW. (1991). Linkage of Marfan syndrome and a phenotypically related disorder to two different fibrillin genes. *Nature* **352**, 330-334
181. Zhang H, Hu W, Ramirez F. (1995). Developmental expression of fibrillin genes suggests heterogeneity of extracellular microfibrils. *J Cell Biol* **129**, 1165-1176
182. Corson GM, Charbonneau NL, Keene DR, Sakai LY. (2004). Differential expression of fibrillin-3 adds to microfibril variety in human and avian, but not rodent, connective tissues. *Genomics* **83**, 461-472
183. Humphries JD, Byron A, Humphries MJ. (2006). Integrin ligands at a glance. *J Cell Sci* **119**, 3901-3903
184. Ross TD, Coon BG, Yun S, Baeyens N, Tanaka K, Ouyang M, Schwartz MA. (2013). Integrins in mechanotransduction. *Curr Opin Cell Biol* **25**, 613-618
185. Horton ER, Astudillo P, Humphries MJ, Humphries JD. (2016). Mechanosensitivity of integrin adhesion complexes: role of the consensus adhesome. *Exp Cell Res* **343**, 7-13
186. Ritty TM, Broekelmann TJ, Werneck CC, Mecham RP. (2003). Fibrillin-1 and -2 contain heparin-binding sites important for matrix deposition and that support cell attachment. *Biochem J* **375**, 425-432
187. Cain SA, Baldock C, Gallagher J, Morgan A, Bax DV, Weiss AS, Shuttleworth CA, Kiely CM. (2005). Fibrillin-1 interactions with heparin: Implications for microfibril and elastic fibre assembly. *J Biol Chem* **280**, 30526-30537

188. Hubmacher D, Bergeron E, Fagotto-Kaufmann C, Sakai LY, Reinhardt DP. (2014). Early fibrillin-1 assembly monitored through a modifiable recombinant cell approach. *Biomacromolecules* **15**, 1456-1468
189. Sengle G, Charbonneau NL, Ono RN, Sasaki T, Alvarez J, Keene DR, Bachinger HP, Sakai LY. (2008). Targeting of bone morphogenetic protein growth factor complexes to fibrillin. *J Biol Chem* **283**, 13874-13888
190. Habashi JP, Judge DP, Holm TM, Cohn RD, Loeys BL, Cooper TK, Myers L, Klein EC, Liu G, Calvi C, Podowski M, Neptune ER, Halushka MK, Bedja D, Gabrielson K, Rifkin DB, Carta L, Ramirez F, Huso DL, Dietz HC. (2006). Losartan, an AT1 antagonist, prevents aortic aneurysm in a mouse model of Marfan syndrome. *Science* **312**, 117-121
191. Bartel DP. (2004). MicroRNAs: genomics, biogenesis, mechanism, and function. *Cell* **116**, 281-297
192. Rutnam ZJ, Wight TN, Yang BB. (2013). miRNAs regulate expression and function of extracellular matrix molecules. *Matrix Biol* **32**, 74-85
193. Climent M, Quintavalle M, Miragoli M, Chen J, Condorelli G, Elia L. (2015). TGFbeta triggers miR-143/145 transfer from smooth muscle cells to endothelial cells, thereby modulating vessel stabilization. *Circ Res* **116**, 1753-1764
194. Xin M, Small EM, Sutherland LB, Qi X, McAnally J, Plato CF, Richardson JA, Bassel-Duby R, Olson EN. (2009). MicroRNAs miR-143 and miR-145 modulate cytoskeletal dynamics and responsiveness of smooth muscle cells to injury. *Genes Dev* **23**, 2166-2178
195. Maegdefessel L, Azuma J, Toh R, Merk DR, Deng A, Chin JT, Raaz U, Schoelmerich AM, Raiesdana A, Leeper NJ, McConnell MV, Dalman RL, Spin JM, Tsao PS. (2012). Inhibition of microRNA-29b reduces murine abdominal aortic aneurysm development. *J Clin Invest* **122**, 497-506
196. Hubmacher D, El-Hallous E, Nelea V, Kaartinen MT, Lee ER, Reinhardt DP. (2008). Biogenesis of extracellular microfibrils: Multimerization of the fibrillin-1 C-terminus into bead-like structures enables self-assembly. *Proc Natl Acad Sci USA* **105**, 6548-6553
197. Vlachos IS, Kostoulas N, Vergoulis T, Georgakilas G, Reczko M, Maragkakis M, Paraskevopoulou MD, Prionidis K, Dalamagas T, Hatzigeorgiou AG. (2012). DIANA miRPath v.2.0: investigating the combinatorial effect of microRNAs in pathways. *Nucleic Acids Res* **40**, W498-W504
198. Betel D, Koppal A, Agius P, Sander C, Leslie C. (2010). Comprehensive modeling of microRNA targets predicts functional non-conserved and non-canonical sites. *Genome Biol* **11**, R90
199. Cambronne XA, Shen R, Auer PL, Goodman RH. (2012). Capturing microRNA targets using an RNA-induced silencing complex (RISC)-trap approach. *Proc Natl Acad Sci USA* **109**, 20473-20478
200. Hartmann P, Zhou Z, Natarelli L, Wei Y, Nazari-Jahantigh M, Zhu M, Grommes J, Steffens S, Weber C, Schober A. (2016). Endothelial Dicer promotes atherosclerosis and vascular inflammation by miRNA-103-mediated suppression of KLF4. *Nat Commun* **7**, 10521
201. Wilson R, Espinosa-Diez C, Kanner N, Chatterjee N, Ruhl R, Hipfinger C, Advani SJ, Li J, Khan OF, Franovic A, Weis SM, Kumar S, Coussens LM, Anderson DG, Chen CC, Cheresch DA, Anand S. (2016). MicroRNA regulation of endothelial TREX1 reprograms the tumour microenvironment. *Nat Commun* **7**, 13597

202. Braun JE, Huntzinger E, Izaurralde E. (2013). The role of GW182 proteins in miRNA-mediated gene silencing. *Adv Exp Med Biol* **768**, 147-163
203. Takagi J, Strokovich K, Springer TA, Walz T. (2003). Structure of integrin $\alpha 5\beta 1$ in complex with fibronectin. *EMBO J* **22**, 4607-4615
204. Aota S, Nomizu M, Yamada KM. (1994). The short amino acid sequence Pro-His-Ser-Arg-Asn in human fibronectin enhances cell-adhesive function. *J Biol Chem* **269**, 24756-24761
205. Johansson S, Svineng G, Wennerberg K, Armulik A, Lohikangas L. (1997). Fibronectin-integrin interactions. *Front Biosci* **2**, d126-146
206. Chaudhry SS, Cain SA, Morgan A, Dallas SL, Shuttleworth CA, Kielty CM. (2007). Fibrillin-1 regulates the bioavailability of TGF-beta1. *J Cell Biol* **176**, 355-367
207. van Rooij E, Sutherland LB, Thatcher JE, DiMaio JM, Naseem RH, Marshall WS, Hill JA, Olson EN. (2008). Dysregulation of microRNAs after myocardial infarction reveals a role of miR-29 in cardiac fibrosis. *Proc Natl Acad Sci USA* **105**, 13027-13032
208. Maurer B, Stanczyk J, Jungel A, Akhmetshina A, Trenkmann M, Brock M, Kowal-Bielecka O, Gay RE, Michel BA, Distler JH, Gay S, Distler O. (2010). MicroRNA-29, a key regulator of collagen expression in systemic sclerosis. *Arthritis Rheum* **62**, 1733-1743
209. Kriegel AJ, Liu Y, Fang Y, Ding X, Liang M. (2012). The miR-29 family: genomics, cell biology, and relevance to renal and cardiovascular injury. *Physiol Genomics* **44**, 237-244
210. Yang JS, Phillips MD, Betel D, Mu P, Ventura A, Siepel AC, Chen KC, Lai EC. (2011). Widespread regulatory activity of vertebrate microRNA* species. *RNA* **17**, 312-326
211. Bell S, Terentjev EM. (2017). Focal adhesion kinase: the reversible molecular mechanosensor. *Biophys J* **112**, 2439-2450
212. Wipff PJ, Hinz B. (2008). Integrins and the activation of latent transforming growth factor beta1 - an intimate relationship. *Eur J Cell Biol* **87**, 601-615
213. Duband JL, Gimona M, Scatena M, Sartore S, Small JV. (1993). Calponin and Sm22 as differentiation markers of smooth-muscle - spatiotemporal distribution during avian embryonic development. *Differentiation* **55**, 1-11
214. Hinz B, Dugina V, Ballestrem C, Wehrle-Haller B, Chaponnier C. (2003). Alpha-smooth muscle actin is crucial for focal adhesion maturation in myofibroblasts. *Mol Biol Cell* **14**, 2508-2519
215. Geiger B, Bershadsky A, Pankov R, Yamada KM. (2001). Transmembrane crosstalk between the extracellular matrix--cytoskeleton crosstalk. *Nat Rev Mol Cell Biol* **2**, 793-805
216. Lin G, Tiedemann K, Vollbrandt T, Peters H, Bätge B, Brinckmann J, Reinhardt DP. (2002). Homo- and heterotypic fibrillin-1 and -2 interactions constitute the basis for the assembly of microfibrils. *J Biol Chem* **277**, 50795-50804
217. Melody KT, Freeman LJ, Baldock C, Jowitt TA, Siegler V, Raynal BD, Cain SA, Wess TJ, Shuttleworth CA, Kielty CM. (2006). Marfan syndrome-causing mutations in fibrillin-1 result in gross morphological alterations and highlight the structural importance of the second hybrid domain. *J Biol Chem* **281**, 31854-31862
218. Cardy CM, Handford PA. (1998). Metal ion dependency of microfibrils supports a rod-like conformation for fibrillin-1 calcium-binding epidermal growth factor-like domains. *J Mol Biol* **276**, 855-860
219. Kaur J, Reinhardt DP. (2012). Immobilized metal affinity chromatography co-purifies TGF-beta1 with histidine-tagged recombinant extracellular proteins. *PLoS One* **7**, e48629

220. Morgan TL, Yang DJ, Fry DG, Hurlin PJ, Kohler SK, Maher VM, McCormick JJ. (1991). Characteristics of an infinite life span diploid human fibroblast cell strain and a near-diploid strain arising from a clone of cells expressing a transfected v-myc oncogene. *Exp Cell Res* **197**, 125-136
221. Wegener J, Keese CR, Giaever I. (2000). Electric cell-substrate impedance sensing (ECIS) as a noninvasive means to monitor the kinetics of cell spreading to artificial surfaces. *Exp Cell Res* **259**, 158-166
222. Benjamini Y, Hochberg Y. (1995). Controlling the false discovery rate - a practical and powerful approach to multiple testing. *J R Stat Soc Series B Stat Methodol* **57**, 289-300
223. Edgar R, Domrachev M, Lash AE. (2002). Gene expression omnibus: NCBI gene expression and hybridization array data repository. *Nucleic Acids Res* **30**, 207-210
224. Barrett T, Wilhite SE, Ledoux P, Evangelista C, Kim IF, Tomashevsky M, Marshall KA, Phillippy KH, Sherman PM, Holko M, Yefanov A, Lee H, Zhang N, Robertson CL, Serova N, Davis S, Soboleva A. (2013). NCBI GEO: archive for functional genomics data sets--update. *Nucleic Acids Res* **41**, D991-D995
225. Huang DW, Sherman BT, Lempicki RA. (2009). Systematic and integrative analysis of large gene lists using DAVID bioinformatics resources. *Nat Protoc* **4**, 44-57
226. Schneider CA, Rasband WS, Eliceiri KW. (2012). NIH Image to ImageJ: 25 years of image analysis. *Nat Methods* **9**, 671-675
227. Horzum U, Ozdil B, Pesen-Okvur D. (2014). Step-by-step quantitative analysis of focal adhesions. *MethodsX* **1**, 56-59
228. Zuiderveld K. (1994) Contrast limited adaptive histogram equalization. In *Graphics gems IV* (Heckbert PS ed.), Academic Press Professional. pp 474-485
229. Huang DW, Sherman BT, Lempicki RA. (2009). Bioinformatics enrichment tools: paths toward the comprehensive functional analysis of large gene lists. *Nucleic Acids Res* **37**, 1-13
230. Sakai LY, Keene DR, Glanville RW, Bächinger HP. (1991). Purification and partial characterization of fibrillin, a cysteine-rich structural component of connective tissue microfibrils. *J Biol Chem* **266**, 14763-14770
231. Cleary EG, Gibson MA. (1983). Elastin-associated microfibrils and microfibrillar proteins. *Int Rev Connect Tissue Res* **10**, 97-209
232. Porst M, Plank C, Bieritz B, Konik E, Fees H, Dötsch J, Hilgers KF, Reinhardt DP, Hartner A. (2006). Fibrillin-1 regulates mesangial cell attachment, spreading, migration and proliferation. *Kidney Int* **69**, 450-456
233. Mariko B, Ghandour Z, Raveaud S, Quentin M, Usson Y, Verdetti J, Huber P, Kielty C, Faury G. (2010). Microfibrils and fibrillin-1 induce integrin-mediated signaling, proliferation and migration in human endothelial cells. *Am J Physiol Cell Physiol* **299**, C977-C987
234. Pages G, Lenormand P, L'Allemain G, Chambard JC, Meloche S, Pouyssegur J. (1993). Mitogen-activated protein kinases p42mapk and p44mapk are required for fibroblast proliferation. *Proc Natl Acad Sci USA* **90**, 8319-8323
235. Meloche S, Pouyssegur J. (2007). The ERK1/2 mitogen-activated protein kinase pathway as a master regulator of the G1- to S-phase transition. *Oncogene* **26**, 3227-3239
236. Lefloch R, Pouyssegur J, Lenormand P. (2009). Total ERK1/2 activity regulates cell proliferation. *Cell Cycle* **8**, 705-711

237. Gabrielli A, Avvedimento EV, Krieg T. (2009). Scleroderma. *N Engl J Med* **360**, 1989-2003
238. Kantlehner M, Schaffner P, Finsinger D, Meyer J, Jonczyk A, Diefenbach B, Nies B, Holzemann G, Goodman SL, Kessler H. (2000). Surface coating with cyclic RGD peptides stimulates osteoblast adhesion and proliferation as well as bone formation. *ChemBioChem* **1**, 107-114
239. Li B, Chen J, Wang JH. (2006). RGD peptide-conjugated poly(dimethylsiloxane) promotes adhesion, proliferation, and collagen secretion of human fibroblasts. *J Biomed Mater Res A* **79**, 989-998
240. Wohlrab S, Muller S, Schmidt A, Neubauer S, Kessler H, Leal-Egana A, Scheibel T. (2012). Cell adhesion and proliferation on RGD-modified recombinant spider silk proteins. *Biomaterials* **33**, 6650-6659
241. Gospodarowicz D, Delgado D, Vlodavsky I. (1980). Permissive effect of the extracellular matrix on cell proliferation in vitro. *Proc Natl Acad Sci USA* **77**, 4094-4098
242. Bitterman PB, Rennard SI, Adelberg S, Crystal RG. (1983). Role of fibronectin as a growth factor for fibroblasts. *J Cell Biol* **97**, 1925-1932
243. Garcia AJ, Vega MD, Boettiger D. (1999). Modulation of cell proliferation and differentiation through substrate-dependent changes in fibronectin conformation. *Mol Biol Cell* **10**, 785-798
244. Schwartz MA, Assoian RK. (2001). Integrins and cell proliferation: regulation of cyclin-dependent kinases via cytoplasmic signaling pathways. *J Cell Sci* **114**, 2553-2560
245. Zeyer KA, Zhang RM, Kumra H, Hassan A, Reinhardt DP. (2019). The fibrillin-1 RGD integrin binding site regulates gene expression and cell function through microRNAs. *J Mol Biol* **431**, 401-421
246. Huveneers S, Danen EH. (2009). Adhesion signaling - crosstalk between integrins, Src and Rho. *J Cell Sci* **122**, 1059-1069
247. Arias-Salgado EG, Lizano S, Sarkar S, Brugge JS, Ginsberg MH, Shattil SJ. (2003). Src kinase activation by direct interaction with the integrin beta cytoplasmic domain. *Proc Natl Acad Sci USA* **100**, 13298-13302
248. Wary KK, Mariotti A, Zurzolo C, Giancotti FG. (1998). A requirement for caveolin-1 and associated kinase Fyn in integrin signaling and anchorage-dependent cell growth. *Cell* **94**, 625-634
249. Scaffidi AK, Petrovic N, Moodley YP, Fogel-Petrovic M, Kroeger KM, Seeber RM, Eidne KA, Thompson PJ, Knight DA. (2004). alpha(v)beta(3) Integrin interacts with the transforming growth factor beta (TGFbeta) type II receptor to potentiate the proliferative effects of TGFbeta1 in living human lung fibroblasts. *J Biol Chem* **279**, 37726-37733
250. Schneller M, Vuori K, Ruoslahti E. (1997). Alphavbeta3 integrin associates with activated insulin and PDGFbeta receptors and potentiates the biological activity of PDGF. *EMBO J* **16**, 5600-5607
251. Bartel DP. (2009). MicroRNAs: target recognition and regulatory functions. *Cell* **136**, 215-233
252. Thum T, Gross C, Fiedler J, Fischer T, Kissler S, Bussen M, Galuppo P, Just S, Rottbauer W, Frantz S, Castoldi M, Soutschek J, Koteliensky V, Rosenwald A, Basson MA, Licht JD, Pena JT, Rouhanifard SH, Muckenthaler MU, Tuschl T, Martin GR, Bauersachs J,

- Engelhardt S. (2008). MicroRNA-21 contributes to myocardial disease by stimulating MAP kinase signalling in fibroblasts. *Nature* **456**, 980-984
253. Polioudakis D, Bhinge AA, Killion PJ, Lee BK, Abell NS, Iyer VR. (2013). A Myc-microRNA network promotes exit from quiescence by suppressing the interferon response and cell-cycle arrest genes. *Nucleic Acids Res* **41**, 2239-2254
254. Suh EJ, Remillard MY, Legesse-Miller A, Johnson EL, Lemons JM, Chapman TR, Forman JJ, Kojima M, Silberman ES, Collier HA. (2012). A microRNA network regulates proliferative timing and extracellular matrix synthesis during cellular quiescence in fibroblasts. *Genome Biol* **13**, R121
255. Jin Y, Chen Z, Liu X, Zhou X. (2013). Evaluating the microRNA targeting sites by luciferase reporter gene assay. *Methods Mol Biol* **936**, 117-127
256. Zhang RM, Kumra H, Reinhardt DP. (2019). Quantification of extracellular matrix fiber systems related to ADAMTS proteins. *Methods Mol Biol* **2043**, 237-250
257. Nissan MH, Rosen N, Solit DB. (2013). ERK pathway inhibitors: how low should we go? *Cancer Discov* **3**, 719-721
258. Terasawa K, Ichimura A, Sato F, Shimizu K, Tsujimoto G. (2009). Sustained activation of ERK1/2 by NGF induces microRNA-221 and 222 in PC12 cells. *FEBS J* **276**, 3269-3276
259. Paroo Z, Ye X, Chen S, Liu Q. (2009). Phosphorylation of the human microRNA-generating complex mediates MAPK/Erk signaling. *Cell* **139**, 112-122
260. O'Connell RM, Taganov KD, Boldin MP, Cheng G, Baltimore D. (2007). MicroRNA-155 is induced during the macrophage inflammatory response. *Proc Natl Acad Sci USA* **104**, 1604-1609
261. Schwartz MA, Ginsberg MH. (2002). Networks and crosstalk: integrin signalling spreads. *Nat Cell Biol* **4**, E65-E68
262. Boulton TG, Nye SH, Robbins DJ, Ip NY, Radziejewska E, Morgenbesser SD, DePinho RA, Panayotatos N, Cobb MH, Yancopoulos GD. (1991). ERKs: a family of protein-serine/threonine kinases that are activated and tyrosine phosphorylated in response to insulin and NGF. *Cell* **65**, 663-675
263. Yao Y, Li W, Wu J, Germann UA, Su MS, Kuida K, Boucher DM. (2003). Extracellular signal-regulated kinase 2 is necessary for mesoderm differentiation. *Proc Natl Acad Sci USA* **100**, 12759-12764
264. Pages G, Guerin S, Grall D, Bonino F, Smith A, Anjuere F, Auberger P, Pouyssegur J. (1999). Defective thymocyte maturation in p44 MAP kinase (Erk 1) knockout mice. *Science* **286**, 1374-1347
265. Lefloch R, Pouyssegur J, Lenormand P. (2008). Single and combined silencing of ERK1 and ERK2 reveals their positive contribution to growth signaling depending on their expression levels. *Mol Cell Biol* **28**, 511-527
266. Vantaggiato C, Formentini I, Bondanza A, Bonini C, Naldini L, Brambilla R. (2006). ERK1 and ERK2 mitogen-activated protein kinases affect Ras-dependent cell signaling differentially. *J Biol* **5**, 14
267. Chong YP, Mulhern TD, Cheng HC. (2005). C-terminal Src kinase (CSK) and CSK-homologous kinase (CHK)--endogenous negative regulators of Src-family protein kinases. *Growth Factors* **23**, 233-244
268. Ussar S, Voss T. (2004). MEK1 and MEK2, different regulators of the G1/S transition. *J Biol Chem* **279**, 43861-43869

269. Skarpen E, Flinder LI, Rosseland CM, Orstavik S, Wierod L, Oksvold MP, Skalhegg BS, Huitfeldt HS. (2008). MEK1 and MEK2 regulate distinct functions by sorting ERK2 to different intracellular compartments. *FASEB J* **22**, 466-476
270. Weston CR, Davis RJ. (2007). The JNK signal transduction pathway. *Curr Opin Cell Biol* **19**, 142-149
271. Habashi JP, Doyle JJ, Holm TM, Aziz H, Schoenhoff F, Bedja D, Chen Y, Modiri AN, Judge DP, Dietz HC. (2011). Angiotensin II type 2 receptor signaling attenuates aortic aneurysm in mice through ERK antagonism. *Science* **332**, 361-365
272. Li Z, Rana TM. (2014). Therapeutic targeting of microRNAs: current status and future challenges. *Nat Rev Drug Discov* **13**, 622-638
273. Asano Y, Ihn H, Yamane K, Jinnin M, Mimura Y, Tamaki K. (2005). Increased expression of integrin alpha(v)beta3 contributes to the establishment of autocrine TGF-beta signaling in scleroderma fibroblasts. *J Immunol* **175**, 7708-7718
274. Juliano RL, Varner JA. (1993). Adhesion molecules in cancer: the role of integrins. *Curr Opin Cell Biol* **5**, 812-818
275. Agrez M, Chen A, Cone RI, Pytela R, Sheppard D. (1994). The alpha v beta 6 integrin promotes proliferation of colon carcinoma cells through a unique region of the beta 6 cytoplasmic domain. *J Cell Biol* **127**, 547-556
276. Hoshino R, Chatani Y, Yamori T, Tsuruo T, Oka H, Yoshida O, Shimada Y, Ari-i S, Wada H, Fujimoto J, Kohno M. (1999). Constitutive activation of the 41-/43-kDa mitogen-activated protein kinase signaling pathway in human tumors. *Oncogene* **18**, 813-822
277. Arihiro K, Kaneko M, Fujii S, Inai K, Yokosaki Y. (2000). Significance of alpha 9 beta 1 and alpha v beta 6 integrin expression in breast carcinoma. *Breast Cancer* **7**, 19-26
278. Felding-Habermann B, O'Toole TE, Smith JW, Fransvea E, Ruggeri ZM, Ginsberg MH, Hughes PE, Pampori N, Shattil SJ, Saven A, Mueller BM. (2001). Integrin activation controls metastasis in human breast cancer. *Proc Natl Acad Sci USA* **98**, 1853-1858
279. Mierke CT, Frey B, Fellner M, Herrmann M, Fabry B. (2011). Integrin alpha5beta1 facilitates cancer cell invasion through enhanced contractile forces. *J Cell Sci* **124**, 369-383
280. Breuksch I, Prossinger F, Baehr F, Engelhardt FP, Bauer HK, Thuroff JW, Heimes AS, Hasenburger A, Prawitt D, Brenner W. (2017). Integrin alpha5 triggers the metastatic potential in renal cell carcinoma. *Oncotarget* **8**, 107530-107542
281. Brandt R, Sell T, Luthen M, Uhlitz F, Klinger B, Riemer P, Giesecke-Thiel C, Schulze S, El-Shimy IA, Kunkel D, Fauler B, Mielke T, Mages N, Herrmann BG, Sers C, Bluthgen N, Morkel M. (2019). Cell type-dependent differential activation of ERK by oncogenic KRAS in colon cancer and intestinal epithelium. *Nat Commun* **10**, 2919
282. Thiaville MM, Pan YX, Gjymishka A, Zhong C, Kaufman RJ, Kilberg MS. (2008). MEK signaling is required for phosphorylation of eIF2alpha following amino acid limitation of HepG2 human hepatoma cells. *J Biol Chem* **283**, 10848-10857
283. Schweyer S, Soruri A, Meschter O, Heintze A, Zschunke F, Miosge N, Thelen P, Schlott T, Radzun HJ, Fayyazi A. (2004). Cisplatin-induced apoptosis in human malignant testicular germ cell lines depends on MEK/ERK activation. *Br J Cancer* **91**, 589-598
284. Milewicz DM, Ramirez F. (2019). Therapies for thoracic aortic aneurysms and acute aortic dissections. *Arterioscler Thromb Vasc Biol* **39**, 126-136

285. Milewicz DM, Guo DC, Tran-Fadulu V, Lafont AL, Papke CL, Inamoto S, Kwartler CS, Pannu H. (2008). Genetic basis of thoracic aortic aneurysms and dissections: focus on smooth muscle cell contractile dysfunction. *Annual Review of Genomics and Human Genetics* **9**, 283-302
286. Davis EC. (1993). Smooth muscle cell to elastic lamina connections in developing mouse aorta. *Lab Invest* **68**, 89-99
287. Milewicz DM, Trybus KM, Guo DC, Sweeney HL, Regalado E, Kamm K, Stull JT. (2017). Altered smooth muscle cell force generation as a driver of thoracic aortic aneurysms and dissections. *Arterioscler Thromb Vasc Biol* **37**, 26-34
288. Nataatmadja M, West J, West M. (2006). Overexpression of transforming growth factor-beta is associated with increased hyaluronan content and impairment of repair in Marfan syndrome aortic aneurysm. *Circulation* **114**, I371-377
289. Cook JR, Clayton NP, Carta L, Galatioto J, Chiu E, Smaldone S, Nelson CA, Cheng SH, Wentworth BM, Ramirez F. (2015). Dimorphic effects of transforming growth factor-beta signaling during aortic aneurysm progression in mice suggest a combinatorial therapy for Marfan syndrome. *Arterioscler Thromb Vasc Biol* **35**, 911-917
290. He R, Guo DC, Estrera AL, Safi HJ, Huynh TT, Yin Z, Cao SN, Lin J, Kurian T, Buja LM, Geng YJ, Milewicz DM. (2006). Characterization of the inflammatory and apoptotic cells in the aortas of patients with ascending thoracic aortic aneurysms and dissections. *J Thorac Cardiovasc Surg* **131**, 671-678
291. Dinesh NEH, Reinhardt DP. (2019). Inflammation in thoracic aortic aneurysms. *Herz* **44**, 138-146
292. Lee E, Grodzinsky AJ, Libby P, Clinton SK, Lark MW, Lee RT. (1995). Human vascular smooth muscle cell-monocyte interactions and metalloproteinase secretion in culture. *Arterioscler Thromb Vasc Biol* **15**, 2284-2289
293. Galis ZS, Muszynski M, Sukhova GK, Simon-Morrissey E, Unemori EN, Lark MW, Amento E, Libby P. (1994). Cytokine-stimulated human vascular smooth muscle cells synthesize a complement of enzymes required for extracellular matrix digestion. *Circ Res* **75**, 181-189
294. Alexander MR, Murgai M, Moehle CW, Owens GK. (2012). Interleukin-1beta modulates smooth muscle cell phenotype to a distinct inflammatory state relative to PDGF-DD via NF-kappaB-dependent mechanisms. *Physiol Genomics* **44**, 417-429
295. Battiston KG, Ouyang B, Labow RS, Simmons CA, Santerre JP. (2014). Monocyte/macrophage cytokine activity regulates vascular smooth muscle cell function within a degradable polyurethane scaffold. *Acta Biomater* **10**, 1146-1155
296. Nataatmadja M, West M, West J, Summers K, Walker P, Nagata M, Watanabe T. (2003). Abnormal extracellular matrix protein transport associated with increased apoptosis of vascular smooth muscle cells in marfan syndrome and bicuspid aortic valve thoracic aortic aneurysm. *Circulation* **108 Suppl 1**, II329-II334
297. Segura AM, Luna RE, Horiba K, Stetler-Stevenson WG, McAllister HA, Jr., Willerson JT, Ferrans VJ. (1998). Immunohistochemistry of matrix metalloproteinases and their inhibitors in thoracic aortic aneurysms and aortic valves of patients with Marfan's syndrome. *Circulation* **98**, II331-II337

- 298.** Bunton TE, Biery NJ, Myers L, Gayraud B, Ramirez F, Dietz HC. (2001). Phenotypic alteration of vascular smooth muscle cells precedes elastolysis in a mouse model of Marfan syndrome. *Circ Res* **88**, 37-43
- 299.** Yoon D, Pastore YD, Divoky V, Liu E, Mlodnicka AE, Rainey K, Ponka P, Semenza GL, Schumacher A, Prchal JT. (2006). Hypoxia-inducible factor-1 deficiency results in dysregulated erythropoiesis signaling and iron homeostasis in mouse development. *J Biol Chem* **281**, 25703-25711
- 300.** Wang W, Xu B, Xuan H, Ge Y, Wang Y, Wang L, Huang J, Fu W, Michie SA, Dalman RL. (2018). Hypoxia-inducible factor 1 in clinical and experimental aortic aneurysm disease. *J Vasc Surg* **68**, 1538-1550 e1532
- 301.** Li J, Kim SG, Blenis J. (2014). Rapamycin: one drug, many effects. *Cell Metab* **19**, 373-379
- 302.** Zhou B, Li W, Zhao G, Yu B, Ma B, Liu Z, Xie N, Fu Y, Gong Z, Dai R, Zhang X, Kong W. (2018). Rapamycin prevents thoracic aortic aneurysm and dissection in mice. *J Vasc Surg*
- 303.** Lawrence DM, Singh RS, Franklin DP, Carey DJ, Elmore JR. (2004). Rapamycin suppresses experimental aortic aneurysm growth. *J Vasc Surg* **40**, 334-338
- 304.** Tsai SH, Huang PH, Hsu YJ, Peng YJ, Lee CH, Wang JC, Chen JW, Lin SJ. (2016). Inhibition of hypoxia inducible factor-1alpha attenuates abdominal aortic aneurysm progression through the down-regulation of matrix metalloproteinases. *Sci Rep* **6**, 28612
- 305.** Eltzschig HK, Carmeliet P. (2011). Hypoxia and inflammation. *N Engl J Med* **364**, 656-665
- 306.** Murdoch C, Muthana M, Lewis CE. (2005). Hypoxia regulates macrophage functions in inflammation. *J Immunol* **175**, 6257-6263
- 307.** Liao M, Zou S, Weng J, Hou L, Yang L, Zhao Z, Bao J, Jing Z. (2011). A microRNA profile comparison between thoracic aortic dissection and normal thoracic aorta indicates the potential role of microRNAs in contributing to thoracic aortic dissection pathogenesis. *J Vasc Surg* **53**, 1341-1349 e1343
- 308.** Gasiule S, Stankevicius V, Patamsyte V, Razanskas R, Zukovas G, Kapustina Z, Zaliaduonyte D, Benetis R, Lesauskaite V, Vilkaitis G. (2019). Tissue-Specific miRNAs Regulate the Development of Thoracic Aortic Aneurysm: The Emerging Role of KLF4 Network. *J Clin Med* **8**
- 309.** Moushi A, Pillar N, Keravnou A, Soteriou M, Shomron N, Cariolou MA, Bashiardes E. (2020). MicroRNAs in ascending thoracic aortic aneurysms. *Biosci Rep* **40**
- 310.** Abu-Halima M, Kahraman M, Henn D, Radle-Hurst T, Keller A, Abdul-Khaliq H, Meese E. (2018). Deregulated microRNA and mRNA expression profiles in the peripheral blood of patients with Marfan syndrome. *J Transl Med* **16**, 60
- 311.** Maegdefessel L, Spin JM, Raaz U, Eken SM, Toh R, Azuma J, Adam M, Nakagami F, Heymann HM, Chernogubova E, Jin H, Roy J, Hultgren R, Caidahl K, Schrepfer S, Hamsten A, Eriksson P, McConnell MV, Dalman RL, Tsao PS. (2014). miR-24 limits aortic vascular inflammation and murine abdominal aneurysm development. *Nat Commun* **5**, 5214
- 312.** Singh RP, Massachi I, Manickavel S, Singh S, Rao NP, Hasan S, Mc Curdy DK, Sharma S, Wong D, Hahn BH, Rehimi H. (2013). The role of miRNA in inflammation and autoimmunity. *Autoimmunity Reviews* **12**, 1160-1165

313. Karagkouni D, Paraskevopoulou MD, Chatzopoulos S, Vlachos IS, Tastsoglou S, Kanellos I, Papadimitriou D, Kavakiotis I, Maniou S, Skoufos G, Vergoulis T, Dalamagas T, Hatzigeorgiou AG. (2018). DIANA-TarBase v8: a decade-long collection of experimentally supported miRNA-gene interactions. *Nucleic Acids Res* **46**, D239-D245
314. Chance B. (1965). Reaction of oxygen with the respiratory chain in cells and tissues. *J Gen Physiol* **49**, Suppl:163-195
315. Goda N, Kanai M. (2012). Hypoxia-inducible factors and their roles in energy metabolism. *Int J Hematol* **95**, 457-463
316. Semenza GL. (2011). Oxygen sensing, homeostasis, and disease. *N Engl J Med* **365**, 537-547
317. Guo DC, Papke CL, He R, Milewicz DM. (2006). Pathogenesis of thoracic and abdominal aortic aneurysms. *Ann N Y Acad Sci* **1085**, 339-352
318. Paloschi V, Kurtovic S, Folkersen L, Gomez D, Wagsater D, Roy J, Petrini J, Eriksson MJ, Caidahl K, Hamsten A, Liska J, Michel JB, Franco-Cereceda A, Eriksson P. (2011). Impaired splicing of fibronectin is associated with thoracic aortic aneurysm formation in patients with bicuspid aortic valve. *Arterioscler Thromb Vasc Biol* **31**, 691-697
319. Della Corte A, Quarto C, Bancone C, Castaldo C, Di Meglio F, Nurzynska D, De Santo LS, De Feo M, Scardone M, Montagnani S, Cotrufo M. (2008). Spatiotemporal patterns of smooth muscle cell changes in ascending aortic dilatation with bicuspid and tricuspid aortic valve stenosis: focus on cell-matrix signaling. *J Thorac Cardiovasc Surg* **135**, 8-18, 18 e11-12
320. Schwill S, Seppelt P, Grunhagen J, Ott CE, Jugold M, Ruhparwar A, Robinson PN, Karck M, Kallenbach K. (2013). The fibrillin-1 hypomorphic mgR/mgR murine model of Marfan syndrome shows severe elastolysis in all segments of the aorta. *J Vasc Surg* **57**, 1628-1636, 1636 e1621-1623
321. Liang W, Guo J, Li J, Bai C, Dong Y. (2016). Downregulation of miR-122 attenuates hypoxia/reoxygenation (H/R)-induced myocardial cell apoptosis by upregulating GATA-4. *Biochem Biophys Res Commun* **478**, 1416-1422
322. Hebert C, Norris K, Scheper MA, Nikitakis N, Sauk JJ. (2007). High mobility group A2 is a target for miRNA-98 in head and neck squamous cell carcinoma. *Mol Cancer* **6**, 5
323. Beaumont J, Lopez B, Hermida N, Schroen B, San Jose G, Heymans S, Valencia F, Gomez-Doblas JJ, De Teresa E, Diez J, Gonzalez A. (2014). microRNA-122 down-regulation may play a role in severe myocardial fibrosis in human aortic stenosis through TGF-beta1 up-regulation. *Clin Sci* **126**, 497-506
324. Abud EM, Maylor J, Udem C, Punjabi A, Zaiman AL, Myers AC, Sylvester JT, Semenza GL, Shimoda LA. (2012). Digoxin inhibits development of hypoxic pulmonary hypertension in mice. *Proc Natl Acad Sci USA* **109**, 1239-1244
325. Xia Y, Choi HK, Lee K. (2012). Recent advances in hypoxia-inducible factor (HIF)-1 inhibitors. *Eur J Med Chem* **49**, 24-40
326. Eichhorn EJ, Gheorghide M. (2002). Digoxin--new perspective on an old drug. *N Engl J Med* **347**, 1394-1395
327. Mueck AO, Seeger H. (2010). 2-Methoxyestradiol--biology and mechanism of action. *Steroids* **75**, 625-631

328. Pereira L, Lee SY, Gayraud B, Andrikopoulos K, Shapiro SD, Bunton T, Biery NJ, Dietz HC, Sakai LY, Ramirez F. (1999). Pathogenetic sequence for aneurysm revealed in mice underexpressing fibrillin-1. *Proc Natl Acad Sci USA* **96**, 3819-3823
329. Subramanian A, Tamayo P, Mootha VK, Mukherjee S, Ebert BL, Gillette MA, Paulovich A, Pomeroy SL, Golub TR, Lander ES, Mesirov JP. (2005). Gene set enrichment analysis: a knowledge-based approach for interpreting genome-wide expression profiles. *Proc Natl Acad Sci USA* **102**, 15545-15550
330. Vlachos IS, Zagganas K, Paraskevopoulou MD, Georgakilas G, Karagkouni D, Vergoulis T, Dalamagas T, Hatzigeorgiou AG. (2015). DIANA-miRPath v3.0: deciphering microRNA function with experimental support. *Nucleic Acids Res* **43**, W460-466
331. Liu CJ. (2009). The role of ADAMTS-7 and ADAMTS-12 in the pathogenesis of arthritis. *Nat Clin Pract Rheumatol* **5**, 38-45
332. Rodriguez-Manzaneque JC, Fernandez-Rodriguez R, Rodriguez-Baena FJ, Iruela-Arispe ML. (2015). ADAMTS proteases in vascular biology. *Matrix Biol* **44-46**, 38-45
333. Hubmacher D, Apte SS. (2015). ADAMTS proteins as modulators of microfibril formation and function. *Matrix Biol* **47**, 34-43
334. Hubmacher D, Apte SS. (2011). Genetic and functional linkage between ADAMTS superfamily proteins and fibrillin-1: a novel mechanism influencing microfibril assembly and function. *Cell Mol Life Sci* **68**, 3137-3148
335. Liu YJ, Xu Y, Yu Q. (2006). Full-length ADAMTS-1 and the ADAMTS-1 fragments display pro- and antimetastatic activity, respectively. *Oncogene* **25**, 2452-2467
336. Hashimoto G, Shimoda M, Okada Y. (2004). ADAMTS4 (aggrecanase-1) interaction with the C-terminal domain of fibronectin inhibits proteolysis of aggrecan. *J Biol Chem* **279**, 32483-32491
337. Apte SS. (2009). A disintegrin-like and metalloprotease (reprolysin-type) with thrombospondin type 1 motif (ADAMTS) superfamily: functions and mechanisms. *J Biol Chem* **284**, 31493-31497
338. Rueden CT, Schindelin J, Hiner MC, DeZonia BE, Walter AE, Arena ET, Eliceiri KW. (2017). ImageJ2: ImageJ for the next generation of scientific image data. *BMC Bioinformatics* **18**, 529
339. Collins TJ. (2007). ImageJ for microscopy. *BioTechniques* **43**, 25-30
340. Schindelin J, Rueden CT, Hiner MC, Eliceiri KW. (2015). The ImageJ ecosystem: An open platform for biomedical image analysis. *Mol Reprod Dev* **82**, 518-529
341. Schindelin J, Arganda-Carreras I, Frise E, Kaynig V, Longair M, Pietzsch T, Preibisch S, Rueden C, Saalfeld S, Schmid B, Tinevez JY, White DJ, Hartenstein V, Eliceiri K, Tomancak P, Cardona A. (2012). Fiji: an open-source platform for biological-image analysis. *Nat Methods* **9**, 676-682
342. Lee TC, Kashyap RL, Chu CN. (1994). Building skeleton models via 3-D medial surface axis thinning algorithms. *CVGIP. Graphical Models and Image Processing* **56**, 462-478
343. Kumra H, Reinhardt DP. (2018). Fibrillins. *Methods Cell Biol* **143**, 223-246
344. Doyle JJ, Gerber EE, Dietz HC. (2012). Matrix-dependent perturbation of TGFbeta signaling and disease. *FEBS Lett* **586**, 2003-2015
345. Kim DH, Wirtz D. (2013). Focal adhesion size uniquely predicts cell migration. *FASEB J* **27**, 1351-1361

346. Thornthwaite JT, Thomas RA. (1990). High-resolution DNA measurements using the nuclear isolation medium, DAPI, with the RATCOM flow cytometer. *Methods Cell Biol* **33**, 111-119
347. Cowen T, Haven AJ, G. B. (1985). Pontamine sky blue: a counterstain for background autofluorescence in fluorescence and immunofluorescence histochemistry. *Histochemistry* **82**, 205-208
348. Mitra SK, Hanson DA, Schlaepfer DD. (2005). Focal adhesion kinase: in command and control of cell motility. *Nat Rev Mol Cell Biol* **6**, 56-68
349. Xiong W, Knispel RA, Dietz HC, Ramirez F, Baxter BT. (2008). Doxycycline delays aneurysm rupture in a mouse model of Marfan syndrome. *J Vasc Surg* **47**, 166-172
350. Kaelin WG, Jr. (2005). ROS: really involved in oxygen sensing. *Cell Metab* **1**, 357-358
351. Carta L, Smaldone S, Zilberberg L, Loch D, Dietz HC, Rifkin DB, Ramirez F. (2009). p38 MAPK is an early determinant of promiscuous Smad2/3 signaling in the aortas of fibrillin-1 (Fbn1)-null mice. *J Biol Chem* **284**, 5630-5636
352. Chen J, Peters A, Papke CL, Villamizar C, Ringuette LJ, Cao J, Wang S, Ma S, Gong L, Byanova KL, Xiong J, Zhu MX, Madonna R, Kee P, Geng YJ, Brasier AR, Davis EC, Prakash S, Kwartler CS, Milewicz DM. (2017). Loss of Smooth Muscle alpha-Actin Leads to NF-kappaB-Dependent Increased Sensitivity to Angiotensin II in Smooth Muscle Cells and Aortic Enlargement. *Circ Res* **120**, 1903-1915
353. Crosas-Molist E, Meirelles T, Lopez-Luque J, Serra-Peinado C, Selva J, Caja L, Gorbenko Del Blanco D, Uriarte JJ, Bertran E, Mendizabal Y, Hernandez V, Garcia-Calero C, Busnadiago O, Condom E, Toral D, Castilla M, Forteza A, Navajas D, Sarri E, Rodriguez-Pascual F, Dietz HC, Fabregat I, Egea G. (2015). Vascular smooth muscle cell phenotypic changes in patients with Marfan syndrome. *Arterioscler Thromb Vasc Biol* **35**, 960-972
354. Brooke BS, Habashi JP, Judge DP, Patel N, Loeys B, Dietz HC. (2008). Angiotensin II blockade and aortic-root dilation in Marfan's syndrome. *N Engl J Med* **358**, 2787-2795
355. Ejiri J, Inoue N, Tsukube T, Munezane T, Hino Y, Kobayashi S, Hirata K, Kawashima S, Imajoh-Ohmi S, Hayashi Y, Yokozaki H, Okita Y, Yokoyama M. (2003). Oxidative stress in the pathogenesis of thoracic aortic aneurysm: protective role of statin and angiotensin II type 1 receptor blocker. *Cardiovasc Res* **59**, 988-996

APPENDIX

Karina A. Zeyer
Reutebachgasse 38 G
79108 Freiburg
Germany

Freiburg, March 28th 2021

Agreement on the use of a manuscript in a manuscript-based thesis at McGill

I hereby confirm that I will not use the manuscript listed below for a manuscript-based thesis at McGill. In this manuscript, Rongmo Zhang and I are listed as co-first authors. I agree to my co-first author Rongmo Zhang using it in his manuscript-based thesis.

Zeyer KA, *Zhang RM, Kumra H, Hassan A, Reinhardt DP, *Co-first authors contributed equally to this work. (2019). The fibrillin-1 RGD integrin binding site regulates gene expression and cell function through microRNAs. **J Mol Biol 431: 401-421*



Karina A. Zeyer



April 3, 2020

Animal Certificate

This is to certify that **Dr Dieter Reinhardt**, Faculty of Dentistry, currently holds an approved **Animal Use Protocol #2017-7979** with McGill University and its Affiliated Hospital's Research Institutes for the following project:

Animal Use Protocol Title: Extracellular matrix mediated regulation of microRNAs and chemokine receptors in health and disease.

Start date: March 1, 2020

Expiration date: February 28, 2021

McGill University and Affiliated Hospitals Research Institutes recognize the importance of animal research in our efforts to further our knowledge of natural processes, diseases and conservation. Research, educational and testing projects are conducted with full commitment to the wellbeing of the animal subjects. In order to limit animal use to meritorious research or educational projects, the institution relies on stringent peer review processes, along with assessment of ethical issues by the Animal Care Committee. McGill University recognizes that the use of animals in research, teaching and testing carries significant responsibilities. The institution will continue to develop and maintain guidelines and regulations, following the high standards established by the Canadian Council on Animal Care. It is committed to conducting the highest-quality research and to providing animals with the best care.

A handwritten signature in blue ink, appearing to read "Suzanne Smith".

Suzanne Smith

Director, Animal Compliance Office

Office of Vice-Principal (Research and Innovation)

Suite 325, James Administration Building, McGill University

845 Sherbrooke Street West, Montreal, Quebec, Canada H3A 0G4

suzanne.smith@mcgill.ca

McGill University

Environmental Health and Safety

Room 426, McTavish 3610 Montreal, Quebec H3A 1Y2

THIS IS TO CERTIFY THAT

Rongmo Zhang

Department of Anatomy and Cell Biology

SUCCESSFULLY COMPLETED CORE TRAINING IN

Introduction to Biosafety

ON 25-Oct-18



Joseph Vincelli
EHS Operations Manager

Valid Until Sunday, October 24, 2021



Wayne Wood
Director, EHS

Supervisor/Permit Holder:
Reinhardt, Dieter P.

Training Session ID: 2786

Trainer Name: Christina Jarabek

McGill University

Environmental Health and Safety

Room 426, McTavish 3610 Montreal, Quebec H3A 1Y2

THIS IS TO CERTIFY THAT

Rongmo Zhang

Department of Anatomy and Cell Biology

SUCCESSFULLY COMPLETED CORE TRAINING IN

Safe Use of Biological Safety Cabinets

ON 20-Sep-18



Joseph Vincelli
EHS Operations Manager



Wayne Wood
Director, EHS

Valid Until Sunday, September 19, 2021

Supervisor/Permit Holder:
Reinhardt, Dieter P.

Training Session ID: 2771

Trainer Name: Christina Jarabek

McGill University

Environmental Health and Safety

Room 426, McTavish 3610 Montreal, Quebec H3A 1Y2

THIS IS TO CERTIFY THAT

Rongmo Zhang

Department of Anatomy and Cell Biology

SUCCESSFULLY COMPLETED CORE TRAINING IN

Workplace Hazardous Materials Information System
(W.H.M.I.S.) 2015

ON 13-Sep-18



Joseph Vincelli
EHS Operations Manager



Wayne Wood
Director, EHS

Valid Until Sunday, September 12, 2021

Supervisor/Permit Holder:

Reinhardt, Dieter P.

Training Session ID:

2763

Trainer Name: Teodor Mocanu